

Die approbierte Originalversion dieser Dissertation ist an der Hauptbibliothek der Technischen Universität Wien aufgestellt (<http://www.ub.tuwien.ac.at>).

The approved original version of this thesis is available at the main library of the Vienna University of Technology (<http://www.ub.tuwien.ac.at/englweb/>).



TECHNISCHE
UNIVERSITÄT
WIEN
Vienna University of Technology

DISSERTATION

Multi-Entanglement in Neutron Interferometric and Polarimetric Experiments

ausgeführt zum Zwecke der Erlangung des akademischen Grades eines
Doktors der technischen Wissenschaften unter der Leitung von

Assistant Prof. Priv.-Doz. Dipl.-Ing. Dr. Yuji Hasegawa

E141 - Atominstitut

eingereicht an der Technischen Universität Wien

Fakultät für Physik

von

Dipl.-Ing. Stephan Sponar

Matrikelnummer 9525997

Steinklammerg.19, A-1130 Wien

Wien, am 10. Februar 2011

Abstract

Entanglement is a remarkable peculiarity in quantum mechanics. It occurs in quantum systems that consist of space-like separated parts, or in systems whose observables belong to disjoint Hilbert spaces. The latter is the case in single-neutron systems. Entangled states are renowned for exhibiting non-classical correlations between observables of individual sub-systems. In this thesis the concept of entanglement is studied via two established experimental methods. First in a perfect Si-crystal interferometer experiment entanglement between degrees of freedom in a single-neutron system is created. The prepared entanglement of spin, path and energy degree of freedom, which is referred to as a triply entangled Greenberger-Horne-Zeilinger state, is analyzed with an inequality derived by Mermin. The entanglement is induced by interaction with an oscillating magnetic field. For this purpose a radio-frequency (RF) spin-flipper, which is placed in one arm of the interferometer, has been developed. In addition, the influence of the geometric phase on a Bell measurement of a spin-path entangled state, expressed by the Clauser-Horne-Shimony-Holt inequality, is studied in detail. In the second part neutron polarimetric experiments with respect to quantum entanglement are presented. In these measurements the advantages of neutron polarimetry, such as high contrast or insensitivity to ambient disturbances, are utilized. Violations of a Bell-like inequality for a spin-energy entangled neutron state, as well as of a Mermin-like inequality for a spin-energy-momentum entanglement are demonstrated.

Kurzfassung

Verschränkung ist eine bemerkenswerte Eigenschaft der Quantenmechanik. Sie tritt einerseits in Quantensystemen auf, die aus mehreren örtlich voneinander getrennten Teilen bestehen, aber auch in Systemen, deren Observablen in disjunkten Hilbert Räumen zu finden sind. Letzteres trifft auch auf Neutronen zu. Verschränkte Zustände sind bekannt dafür, dass sie sogenannte nichtklassische Korrelationen bei Messungen an ihren Teilsystemen aufweisen. Diese Dissertation untersucht das Konzept der Verschränkung mittels zweier bewährter experimenteller Methoden. Der erste Teil beschreibt eine Messung, in der mittels eines Silizium-Perfektkristall-Neutroneninterferometers eine Verschränkung mehrerer innerer Freiheitsgrade des Neutrons hergestellt wird. Die Verschränkung von Spin, Pfad und Energie, in der Literatur üblicherweise als Greenberger-Horne-Zeilinger Zustand bezeichnet, wird mit Hilfe einer von Mermin hergeleiteten Ungleichung analysiert. Die Quelle der Verschränkung ist eine Wechselwirkung mit einem zeitlich veränderlichen Magnetfeld. Für diesen Zweck wurde eigens ein Radio-Frequenz Spinflipper entwickelt, der in einem Arm des Interferometers platziert wurde. Zusätzlich wird der Einfluss einer geometrischen Phase auf eine Bell Messung an einem Spin-Pfad verschränkten Zustand, mittels einer Clauser-Horne-Shimony-Holt Ungleichung, im Detail analysiert. Im zweiten Teil der vorliegenden Arbeit werden Experimente am Neutronen Polarimeter vorgestellt, die sich mit dem Thema der Quantenverschränkung auseinandersetzen. Die Vorteile dieser Messmethode begründen sich einerseits in einem hohen Kontrastvermögen, aber auch in der Unempfindlichkeit gegenüber äußeren Störeinflüssen. Verletzungen einer Bellschen Ungleichung für einen Spin-Energie verschränkten Zustand, so wie einer Ungleichung von Mermin für eine Verschränkung von Spin, Energie und Impuls werden nachgewiesen.

Acknowledgements

First of all, I want take the opportunity here to thank my thesis supervisor and mentor Yuji Hasegawa for his awesome support over the years and for the chance to participate in his projects. I am grateful for his drive and patience in supporting me, and for helpful discussions.

Likewise, most of the present thesis would not have been possible without the commitment and patronage of my colleagues at the Atominstitut, especially of Jürgen Klepp, who contributed in countless fruitful discussions and tireless help during the experiments. And of Rudi Loidl, whose experimental experience at the S18 ILL/Grenoble was essential. I also want to say thanks to Katharina Durstberger-Rennhofer, Stefan Filipp, Hartmut Lemmel, Josef Springer, Georg Sulyok, and Halit Tatlisu for their encouragement during my work. I want to thank Peter Pataki, Erich Tischler and Franz Foret for their support and patience when it came to the realization of various components required for experimental setups.

Finally, my thanks go to the long term members of the Atominstitut Gerald Badurek, Erwin Jericha, Helmut Rauch and Mario Villa for the kind reception in his house.

This thesis is dedicated with loving appreciation to my parents, whose guidance and words of encouragement supported me all the time.

This work has been supported by the Austrian Science Fund (FWF), project No. P17803-N02.

Contents

| | |
|---|-----------|
| Preface | xi |
| 1 Can Quantum Theory be considered complete ? | 1 |
| 1.1 Uncertainty Relation | 1 |
| 1.2 The Einstein-Podolsky-Rosen (EPR) Paradox | 2 |
| 1.2.1 Polarization states | 7 |
| 1.2.2 Entangled states and joint (correlation) measurements | 8 |
| 1.3 Bell-type Inequalities and Local Hidden Variable Theories | 17 |
| 1.3.1 Hidden variable formalism | 20 |
| 1.3.2 The original Bell inequality | 23 |
| 1.3.3 The Clauser-Horne-Shimony-Holt (CHSH) inequality | 24 |
| 1.3.4 The Greenberger-Horne-Zeilinger (GHZ) state | 27 |
| 1.3.5 Loopholes | 30 |
| 1.4 Non-Locality or Contextuality | 31 |
| 1.5 Related Experiments | 33 |
| 1.5.1 Celebrated CHSH-Bell experiments with photons | 33 |
| 1.5.2 Three-photon GHZ entanglement | 40 |
| 2 Neutron - Magnetic Field Interaction | 43 |
| 2.1 Semiclassical Theory - Manipulating a Neutron Spin with a Classical Field | 43 |
| 2.1.1 Larmor precession | 44 |
| 2.1.2 The time-dependence of magnetic fields | 49 |
| 2.2 Coupling a Spin 1/2 to Quantized Field | 60 |
| 2.2.1 Quantum theory of radiation | 60 |

| | | |
|----------|---|------------|
| 2.2.2 | Fock and coherent states | 62 |
| 2.2.3 | Mach-Zehnder and Ramsey interferometer | 72 |
| 2.2.4 | The Jaynes-Cummings model and the dressed states | 75 |
| 2.3 | Geometric Phase for Two-Level Systems | 83 |
| 2.3.1 | Classic analogue of Berry's phase | 84 |
| 2.3.2 | Derivation of Berry's phase | 85 |
| 2.3.3 | The geometric phase of Aharonov and Anandan | 89 |
| 2.3.4 | Related experiments | 92 |
| 3 | Interferometric Experiments | 101 |
| 3.1 | Neutron Interferometry | 101 |
| 3.1.1 | Functional principle | 102 |
| 3.1.2 | Spin path entanglement preparation | 115 |
| 3.2 | Coherent Energy Manipulation | 118 |
| 3.2.1 | Theoretical Background | 118 |
| 3.2.2 | Radio frequency (RF) coil construction | 122 |
| 3.2.3 | Interferometric setup | 125 |
| 3.3 | GHZ-States in Neutron Interferometry | 139 |
| 3.3.1 | State preparation | 139 |
| 3.3.2 | Mermin-like inequality | 139 |
| 3.3.3 | Measurement process and modification of the setup | 141 |
| 3.3.4 | Experimental results | 143 |
| 3.4 | Geometric Phase in Entangled Systems | 146 |
| 3.4.1 | Theory | 146 |
| 3.4.2 | Geometric phase in a single-neutron interferometer experiment . . . | 152 |
| 3.4.3 | Data analysis and experimental results | 166 |
| 4 | Polarimetric Experiments | 175 |
| 4.1 | Zero Field Precession in Neutron Polarimetry | 176 |
| 4.1.1 | Theorie | 176 |
| 4.1.2 | Polarimetric setup | 177 |
| 4.1.3 | Experimental results | 179 |

- 4.2 Violation of Bell’s Inequality in Neutron Polarimetry 184
 - 4.2.1 Theory 184
 - 4.2.2 Measurement procedure 187
- 4.3 GHZ-States in Neutron Polarimetry 193
 - 4.3.1 Theoretical Background 193
 - 4.3.2 Polarimetric experiment 195
 - 4.3.3 Experimental results 197
- 5 Conclusion and Outlook 201**
- Bibliography 203**
- Curriculum Vitae, Publications 215**

Preface

Quantum mechanics is probably the most successful theory ever. No other theory has yet given more accurate predictions from elementary-particle physics to the early stages of our universe. However, quantum mechanics only gives probabilistic predictions for individual events. Consequently, according to Einstein, a more complete, deterministic, hidden physics must underlie quantum mechanics [Einstein et al., 1935]. Einstein, Podolsky and Rosen (EPR) argued based on the assumption of local realism, that quantum mechanics is not a complete theory: “*While we have thus shown that the wavefunction does not provide a complete description of the physical reality, we left open the question of whether or not such a description exists. We believe, however, that such a theory is possible*” [Einstein et al., 1935]. Such theories, based on objective properties of physical systems, are referred to as hidden variable theories. In 1951 Bohm reformulated the EPR argument for spin observables of two spatially separated entangled particles to illuminate the essential features of the EPR paradox [Bohm, 1951]. After this, Bell proved in his celebrated theorem that all hidden variable theories, which are based on the joint assumption of locality and realism, conflict with the predictions of quantum mechanics [Bell, 1964]. Therefore Bell introduced inequalities which hold for the predictions of any local hidden variable theory applied, but are violated by quantum mechanics. Violation of a Bell inequality proves the presence of *entanglement* and thus, according to Bell’s theorem, non-local characteristics of the quantum systems. From this, one can conclude that quantum mechanics cannot be reproduced by local hidden variable theories.

Only five years later Clauser, Horne, Shimony and Holt (CHSH) reformulated Bell’s inequalities pertinent for the first practical test of quantum non-locality [Clauser et al., 1969]. Polarization measurements with correlated photon pairs [Bertlmann and Zeilinger, 2002], produced by atomic cascade [Freedman and Clauser, 1972, Aspect et al., 1982b] and parametric down-conversion of

lasers [Kwiat et al., 1995, Weihs et al., 1998, Tittel et al., 1998], demonstrated violation of the CHSH inequality. Up to date many physical systems [Rowe et al., 2001, Moehring et al., 2004, Sakai et al., 2006, Matsukevich et al., 2008] have been examined, including neutrons [Hasegawa et al., 2003].

Not a statistical violation, but a contradiction between quantum mechanics and local hidden variable theories was found by Greenberger, Horne and Zeilinger (GHZ) in 1989, for at least, a tripartite entanglement [Greenberger et al., 1989, Greenberger et al., 1990]. The GHZ argument is independent of the Bell approach, thereby demonstrating in a non-statistic manner that quantum mechanics and local realism are mutually incompatible.

Local hidden variable theories are a subset of a more general class of hidden variable theories, namely the noncontextual hidden variable theories. Noncontextuality implies that the value of a dynamical variable is determined and independent of the experimental context, i.e. of previous or simultaneous measurements of a commuting observable [Bell, 1966, Mermin, 1993]. Noncontextuality is a more stringent demand than locality because it requires mutual independence of the results for commuting observables even if there is no spacelike separation [Simon et al., 2000].

Another distinctive feature in the field of quantum mechanics is the concept of the *geometric phase*. The total phase acquired during an evolution of a quantal system generally consists of two components: the usual dynamical phase $-1/\hbar \int H(t)dt$, which depends on the dynamical properties, like energy or time, and a geometric phase γ , which is, considering a spin $\frac{1}{2}$ system, minus half the solid angle ($\Omega/2$) of the curve traced out in ray space. The peculiarity of this phase, first discovered by M.V. Berry in 1984 [Berry, 1984], lies in the fact that it does not depend on the dynamics of the system, but purely on the evolution path of the state in parameter space. The geometric phase in a single-particle system has been studied widely over the past two and a half decades. Nevertheless its effect on entangled quantum systems is less investigated. The geometric phase is an excellent candidate to be utilized for logic gate operations in quantum communication [Nielsen and Chuang, 2000], due to its robustness against noise. On the other hand entanglement is the basis for quantum communication and quantum information processing. Thus studies on systems combining both quantum phenomena, the geometric phase and quantum entanglement, are of great importance [Bertlmann et al., 2004, Tong et al., 2003]

In the case of neutrons entanglement is not achieved between particles but between different degrees of freedom. Since the observables of one Hilbert spaces, describing a certain degree of freedom, commute with observables of a different Hilbert space, the single-neutron system is suitable for studying noncontextual hidden variable theories with multiple degrees of freedom.

The fundamental quantum-mechanical concept of treating propagating particles as waves is demonstrated in the wide field of *matter-wave interferometry*. Starting from interferometers for electrons [Marton et al., 1953], neutron interferometry [Rauch et al., 1974], provides a macroscopic separation of two coherent sub-beams resulting in high-contrast interference patterns when recombined. After developing techniques to control atom waves, in a next step atom interferometer have been realized [Cronin et al., 2009]. Since atomic properties (such as mass, magnetic moment, and polarizability) can be selected over wide ranges atom interferometry has become a flexible, powerful tool for studying fundamental quantum-mechanical phenomena as well as probing atomic and material properties. Since the first atom interferometers were built 1991 (for instance for Na [Keith et al., 1991]) the development of molecules interferometers [Arndt et al., 1999, Nairz et al., 2004] promises future scientific gain.

Using neutron interferometry [Rauch and Werner, 2000], single-particle entanglement between the spinor and the spatial part of the neutron wave function [Hasegawa et al., 2003], as well as full tomographic state analysis [Hasegawa et al., 2007], have already been accomplished. In addition, the contextual nature of quantum theory [Hasegawa et al., 2006, Bartosik et al., 2009] has been demonstrated.

Neutron polarimetry has several advantages compared to perfect crystal interferometry. It is insensitive to ambient-mechanical and thermal disturbances and therefore provides better phase stability. Efficiencies of the manipulations, including state splitting and recombination, are considerably high resulting in a better contrast compared to interferometry. In addition, Single-crystal interferometers accept neutrons only within an angular range of a few arcseconds, which leads to a significant decrease in intensity. Neutron polarimetry has been used to demonstrate the noncommutation properties of the Pauli spin operator [Hasegawa and Badurek, 1999], and for geometric phase measurements [Wagh et al., 2000, Klepp et al., 2005, Klepp et al., 2008]. However, experimental studies of entanglement related phenomena in neutron polarimetry can be barely found.

Outline

Chapter one contains an introduction to the properties of entangled systems. With the EPR Paradox as point of origin correlation measurements and Bell inequalities are introduced.

Chapter two focuses on typical properties of the neutron, when exposed to magnetic field of different types, thereby especially discussing the coupling to quantized magnetic fields.

Within the scope of the third Chapter, measurements by means of Si-perfect crystal interferometry are presented. Creation and manipulation of an entanglement between three degrees of freedom in a single-neutron system i.e. spin, path and energy degrees of freedom, is demonstrated. The prepared GHZ-like state is analyzed with an inequality derived by Mermin: the obtained value clearly exhibits a violation of the classical limit. The entanglement is induced by interaction with an oscillating magnetic field in one path of the interferometer. The total system is characterized by an entangled state vector, consisting of neutron and radiation fields, governed by a Jaynes-Cummings Hamiltonian. The methods and results are published in [Sponar et al., 2008b] and [Hasegawa et al., 2010]. Moreover, in this Section the influence of the geometric phase on a Bell measurement of a spin-path entanglement, expressed by the Clauser-Horne-Shimony-Holt inequality, is analyzed in detail. The experiment follows in most instances the proposal given in [Bertlmann et al., 2004] and the results are summarized in [Sponar et al., 2010a].

Motivated by the lack of experimental work in the field of entanglement in neutron polarimetry, the fourth Chapter presents an experimental confirmation for the violation of a Bell-like CHSH inequality. In this particular experiment the neutrons wavefunction exhibits entanglement between the spinor and energy degree of freedom. Each degree of freedom has to be addressed independently for projective measurements required for the violation of the CHSH inequality. Experimental methods and results are published in [Sponar et al., 2008a] and [Sponar et al., 2010b], respectively. Finally a triply entangled GHZ-like state is generated utilizing a suitable combination of two radio-frequency fields in a neutron polarimeter setup. The proposed Mermin-like inequality relies on correlations between the spin, energy and momentum degree of freedom.

1

Can Quantum Theory be considered complete ?

1.1 Uncertainty Relation

Measurements disturb microscopic systems inevitably. This is reflected in the famous uncertainty principle, which has been known as one of the most fundamental principles in quantum mechanics. It was Werner Heisenberg who first proposed a relation for the measurement of noise and disturbance in his celebrated paper [Heisenberg, 1927], published in 1927. Heisenberg's uncertainty relation can be summarized as follows: For every measurement of the position Q of a mass with root-mean-square error $\epsilon(Q)$, the root-mean-square disturbance $\eta(P)$ of the momentum P of the mass caused by the interaction of this measurement always satisfies the relation

$$\epsilon(Q)\eta(P) \leq \frac{\hbar}{2}. \quad (1.1)$$

Considering Heisenberg's famous *X-ray Gedankenexperiment*, the smallest separation Δx , that can still be resolved, is given by

$$\Delta x \sim \lambda/2 \sin \theta, \quad (1.2)$$

with λ being the wavelength and θ the angle subtended by the lens. Hence for measuring the position of an object with accuracy Δx at least a wavelength $\lambda > 2(\Delta x) \sin \theta$ is required. In quantum physics, according to de Broglie's relation $p = \hbar/\lambda$, short wavelengths corresponds to quanta with high momentum. A high momentum photon scatters off the measured object, thereby altering its momentum up to an amount $\pm \hbar/2\Delta x$. This is the meaning of the Heisenberg uncertainty relation

1.2 The Einstein-Podolsky-Rosen (EPR) Paradox

In their famous paper [Einstein et al., 1935] entitled "*Can quantum-mechanical description of physical reality be considered complete*", the authors consider quantum mechanics to be incomplete. They argue that a complete theory must represent *both* the position and the momentum of a particle at any time with arbitrary accuracy. Quantum mechanics indeed does not; hence it is incomplete.

Their key argument, as summarized in Bohr's reply [Bohr, 1935], is the following: Two particles that had interacted in the past, are now far apart and no more interaction is present. So, according to the authors, a measurement of one particle does not affect the other, spacelike separated particle. Using an apparatus as shown in Fig.1.1 (left), one can measure the height of one particle relative to the other. The experiment has to be repeated, until both particles pass through the two slots, which are a distance L apart. The result is denoted as $x_2 - x_1$. Now the height of one particle (e.g. x_1) is measured after passing the board. With this setup the height of one particle is measured directly and the height of the other particle is measured indirectly, without affecting it.

In a next step the position measurement is combined with a momentum measurement, which is depicted in Fig.1.1 (right). Initially $p_1 = p_2 = 0$, since the initial momenta are horizontal. Since the total momentum of board and particles is unchanged during the passage, this measurement yields the total momentum of the particles denoted as $p_1 + p_2$. Actually the vertical recoil of the board measures the change in $p_1 + p_2$, since p_1 and p_2 may change by knocking against the slots as the particles pass through. When the particles pass through the slots the vertical recoil is measured yielding $p_1 + p_2$. Again after passing the slots one can infer p_2 from a direct measurement of p_1 . However measuring p_1 may affect x_1 .

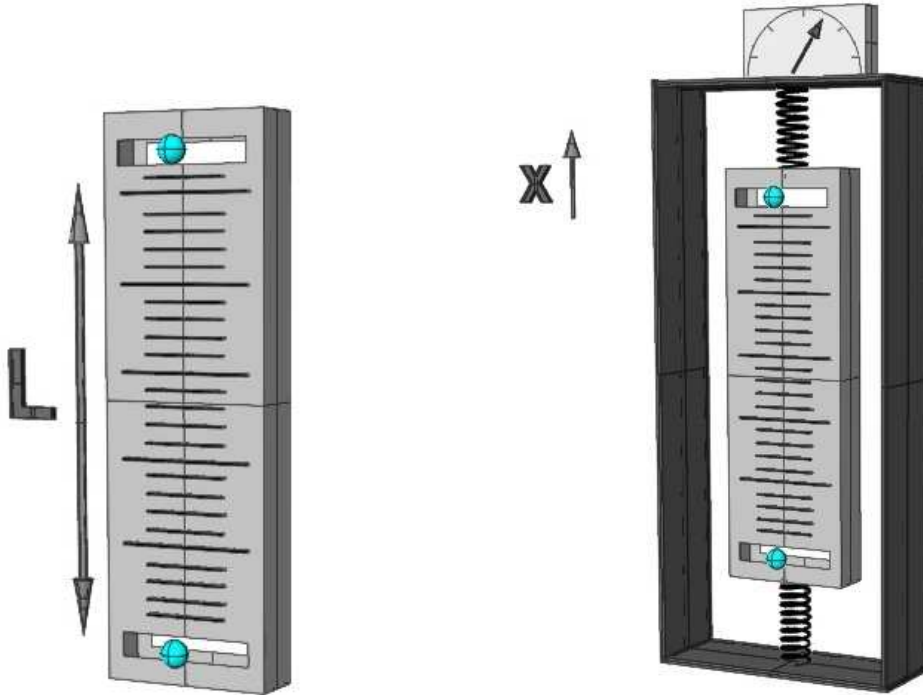


Figure 1.1: Apparatus for Einstein-Podolsky-Rosen Gedankenexperiment allowing for simultaneous measurement of $x_2 - x_1$ (relative height with distance L) and $p_1 + p_2$, measured by the vertical recoil of the board. A direct measurement of p_2 is carried out first (which is an indirect measurement of p_1), followed either by a x_1 or p_1 measurement. If a x_1 measurement is carried out p_1 cannot be measured and quantum mechanics does not predict the result of the p_2 . Since quantum mechanics does not predict the result for p_1 quantum theory is incomplete.

If the board does not recoil up or down the apparatus measures $p_1 + p_2 = 0$ and $x_2 - x_1 = l$. Next a direct measurement is of p_2 and either x_1 or p_1 is performed. Since there is no interaction between the two particles the result of the p_2 measurement cannot depend on whether p_1 or x_1 is measured. If the result is $p_2 = P$ the result $p_1 = -P$ follows from $p_1 + p_2 = 0$. But if a x_1 measurement is carried out p_1 cannot be measured and quantum mechanics does not predict the result of the p_2 measurement. But the results of the p_2 measurement cannot depend on whether x_1 or p_1 is measured, by assumption. But still p_2 is given by $-P$, a predetermined value independent of what is measured on the other particle. Since quantum mechanics does not predict this result quantum theory is incomplete. This is the EPR claim.

To be more precise the EPR paradox refers to a Gedankenexperiment challenging the dogma that the description of reality, given by the wave function, is complete: *"In a complete theory there is an element corresponding to each element of reality"*, or as states in the paper: *"every element of the physical reality must have a counterpart in the physical theory."* The authors thereby claim that the outcome of a measurement, which already exist before the actual measurement takes place, is determined by an *element of reality*, a part of the real physical world: *"If without in any way disturbing the system, we can predict with certainty the value of a physical quantity, then there exists an element of reality corresponding to this physical quantity"* Furthermore the systems properties are independent of which interventions are carried out on spatially separated systems: *"...since at the time of the measurement the two systems no longer interact, no real change can take place in the second system in consequence of anything that may be done to the first system"* [Einstein et al., 1935]. So the *elements of reality* are *local*, in the sense that they can only be influenced by an event which is located in the past light cone of the elements point in spacetime. These are the two main assumptions in the EPR claim, namely **locality** and **realism**, which are often referred to just as **local realism**.

In quantum mechanics the behavior of a particle is described by the concept of states. It is completely characterized by a wave function ψ , which is a function of variables such as x and p to describe the particles behavior. Corresponding to each physical observable quantity A there is an operator (may be assigned the same letter, but hatted). If ψ is an eigenstate of \hat{A} , which is if

$$\hat{A}\psi = a\psi, \tag{1.3}$$

where a is a real number, then the physical quantity A has with certainty the value a whenever the particle is in state ψ .

Since $[\hat{P}, \hat{X}] = h/(2\pi i)$ a precise measurement of p will result in an equally distributed probability of x . The authors concluded from that: *"... when the momentum of a particle is known, its coordinate has no physical reality... From this follows either (1) the quantum-mechanical description of reality given by the wave function is not complete or (2) when the operators corresponding to two physical quantities do not commute the two quantities cannot have simultaneous reality."*

This is the authors starting point used to derive a contradiction with quantum me-

chanics. Showing that it is possible to *assign two different wave functions to the same reality (the second system after the interaction with the first)*:

The system is characterized by a two particle wave function denoted as

$$\Psi(x_1, x_2) = \int_{-\infty}^{\infty} e^{(2\pi i/h)(x_1 - x_2 + x_0)} dp, \quad (1.4)$$

where x_0 is a constant. If the observable A is now the momentum of the first particle, according to Eq.(1.3), which becomes

$$\frac{h}{2\pi i} \frac{\partial}{\partial x_1} \psi = p\psi, \quad (1.5)$$

where its eigenfunction, corresponding to the eigenvalue p , is given by

$$u_p(x_1) = e^{(2\pi i/h)px_1}. \quad (1.6)$$

Consequently Eq.(1.4) can be rewritten as

$$\Psi(x_1, x_2) = \int_{-\infty}^{\infty} \psi_p(x_2) u_p(x_1) dp, \quad (1.7)$$

where

$$\psi_p(x_2) = e^{(2\pi i/h)(x_2 - x_0)p} \quad (1.8)$$

is the eigenfunction of the operator $\hat{P} = \frac{h}{2\pi i} \frac{\partial}{\partial x_2}$ corresponding to the eigenvalue $-p$ of the momentum of the second particle.

On the other hand if the measured observable is the coordinate of the first particle, with eigenfunction

$$v_x(x_1) = \delta(x_1 - x), \quad (1.9)$$

corresponding to the eigenvalue x , Eq.(1.4) becomes

$$\Psi(x_1, x_2) = \int_{-\infty}^{\infty} \varphi_x(x_2) v_x(x_1) dp, \quad (1.10)$$

where

$$\varphi_x(x_2) = \int_{-\infty}^{\infty} e^{(2\pi i/h)(x - x_2 + x_0)p} dp = h\delta(x - x_2 + x_0). \quad (1.11)$$

Here $\varphi_x(x_2)$ is eigenfunction of the operator $\hat{Q} = x_2$. Since

$$\hat{Q}\hat{P} - \hat{P}\hat{Q} = \frac{2\pi i}{h} \quad (1.12)$$

it is possible for ψ_k and φ_r to be eigenfunctions of two noncommuting observables, corresponding to physical quantities. So in the first case \hat{P} is considered to be an element of reality, whereas in the second case \hat{Q} is considered to be an element of reality. But both wavefunctions ψ_k and φ_r belong to the same reality.

So depending on which measurement is performed on the first system, the second system is left in different wavefunctions (this mechanism is commonly referred to as *collapse of wavefunction*). On the other hand since the particles no longer interact, no real change can take place in the second system (same reality).

So it is stated explicitly in the paper "*Previously we proved that either (1) the quantum-mechanical description of reality given by the wave function is not complete or (2) when the operators corresponding to two physical quantities do not commute the two quantities cannot have simultaneous reality.*" The consequence of (1) would be that quantum mechanics is local and there must be some unknown underlying mechanism acting on these variables to give rise to the observed effects of "noncommuting quantum observables", i.e. the Heisenberg uncertainty principle. Such a theory is called a hidden variable theory. If quantum mechanics were complete (first option failed) then the second option would hold, that is, incompatible quantities (operators corresponding to two physical quantities do not commute) cannot have real values simultaneously. But if quantum mechanics were complete, then incompatible quantities could indeed have simultaneous, real values. Thus the negation of (1) leads to the negation of the only alternative (2), concluding that the quantum-mechanical description using wave functions is incomplete.

The problem within the EPR claim is that the two main assumptions are incompatible with quantum mechanics. So basically EPR shows that quantum mechanics is not a classical theory.

If position and momentum in the EPR Gedankenexperiment are replaced by spin or polarization measurements it becomes experimentally testable. In 1951 Bohm reformulated the EPR argument for the polarization of two spatially separated entangled particles to illuminate the essential features of the EPR paradox [Bohm, 1951].

1.2.1 Polarization states

According to classical theory light is an electromagnetic wave and therefore described either by a single monochromatic or by a superposition of several monochromatic waves. Any monochromatic wave is defined by its propagation vector \vec{k} , thereby fixing the angular frequency $\omega = c|\vec{k}|$ and a polarization, which determines the direction of the electric field $\vec{E}(\vec{x}, t)$ denoted as

$$\vec{E}(\vec{x}, t) = E_1 \cos(\vec{k} \cdot \vec{x} - \omega t + \phi_1) \vec{e}_1 + E_2 \cos(\vec{k} \cdot \vec{x} - \omega t + \phi_2) \vec{e}_2, \quad (1.13)$$

with (real) phases ϕ_1, ϕ_2 and amplitudes E_1, E_2 . There are two independent directions for \vec{E} , which are perpendicular to \vec{k} . These directions are commonly known as polarizations (oscillation planes), with unit vectors \vec{e}_1 and \vec{e}_2 , with $\vec{e}_1 \cdot \vec{e}_2 = \vec{e}_1 \cdot \vec{k} = \vec{e}_2 \cdot \vec{k} = 0$. If $\phi_1 = \phi_2$ the polarization is linear. Otherwise its elliptic. In important special case of elliptic is circular polarization where $|E_1| = |E_2|$ and $\phi_1 - \phi_2 = \pm\pi/2$.

$\vec{E}(x, t)$ can be expressed as the real part of a complex wave given by

$$\vec{E}(x, t) = \text{Re}((E_1 e^{i\phi_1} \vec{e}_1 + E_2 e^{i\phi_2} \vec{e}_2) e^{i\vec{k}\vec{x} - \omega t}). \quad (1.14)$$

In the case of linear polarization the electromagnetic wave are therefore given by

$$\vec{E}_H \sim \vec{e}_H e^{i\vec{k}\vec{x} - \omega t}, \quad \vec{E}_V \sim \vec{e}_V e^{i\vec{k}\vec{x} - \omega t}, \quad (1.15)$$

where the indices H and V refer to horizontal and vertical polarization (see Fig 1.2).

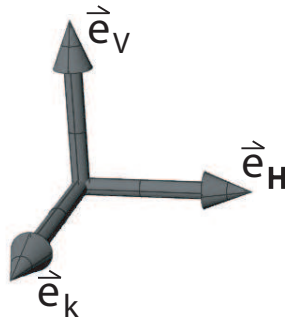


Figure 1.2: Polarization vectors and the propagation vector (wavevektor k) for linearly polarized photons.

Another frequently used basis is given by

$$\vec{e}_{H'} = \vec{e}_{+45^\circ} = \frac{1}{\sqrt{2}}(\vec{e}_H + \vec{e}_V), \quad \vec{e}_{V'} = \vec{e}_{-45^\circ} = \frac{1}{\sqrt{2}}(\vec{e}_H - \vec{e}_V). \quad (1.16)$$

The right-hand and left-hand circularly polarized electromagnetic waves are defined as

$$\vec{E}(R, L) \sim \vec{e}(R, L)e^{i\vec{k}\cdot\vec{x}-\omega t}, \quad (1.17)$$

using $\phi_1 - \phi_2 = \pm\pi/2$ (phase factor $e^{\pm\pi/2} = \pm i$)

$$\vec{e}(R) = \frac{1}{\sqrt{2}}(\vec{e}_H + i\vec{e}_V), \quad \vec{e}(L) = \frac{1}{\sqrt{2}}(\vec{e}_H - i\vec{e}_V). \quad (1.18)$$

The state vectors of the quantum system photon corresponding to these polarizations are described by vectors in a two dimensional complex Hilbert space \mathcal{H}_2 :

$$\begin{aligned} \vec{e}_H &\longleftrightarrow |H\rangle = |0\rangle, & \vec{e}_V &\longleftrightarrow |V\rangle = |1\rangle \\ \vec{e}_{H'} &\longleftrightarrow |H'\rangle = | + 45^\circ \rangle = \frac{1}{\sqrt{2}}(|H\rangle + |V\rangle) = |0_x\rangle \\ \vec{e}_{V'} &\longleftrightarrow |V'\rangle = | - 45^\circ \rangle = \frac{1}{\sqrt{2}}(|H\rangle - |V\rangle) = |1_x\rangle \\ \vec{e}_R &\longleftrightarrow |R\rangle = \frac{1}{\sqrt{2}}(|H\rangle + i|V\rangle) = |0_y\rangle \\ \vec{e}_L &\longleftrightarrow |L\rangle = \frac{1}{\sqrt{2}}(|H\rangle - i|V\rangle) = |1_y\rangle \end{aligned} \quad (1.19)$$

Note the connection with the eigenvectors of the Pauli operators, indicated by the indices x and y , being basis vectors of the two dimensional complex Hilbert space \mathcal{H}_2 .

1.2.2 Entangled states and joint (correlation) measurements

A pion at rest decays into two photons, which fly in opposite directions with equal but opposite momenta. So what is their polarization state? As seen before right-handed and left-handed circular polarized states with fixed propagation \vec{k} form a basis in the Hilbert space \mathcal{H}_2 of polarizations. So the polarization state has to be a combination of the four basis vectors, spanned by $|R\rangle$ and $|L\rangle$ of the individual systems A and B , denoted as $|R^A, R^B\rangle$, $|R^A, L^B\rangle$, $|L^A, R^B\rangle$ and $|L^A, L^B\rangle$. But which combination? The same question arises for the emission of photons in an atomic cascade, which is described in more detail

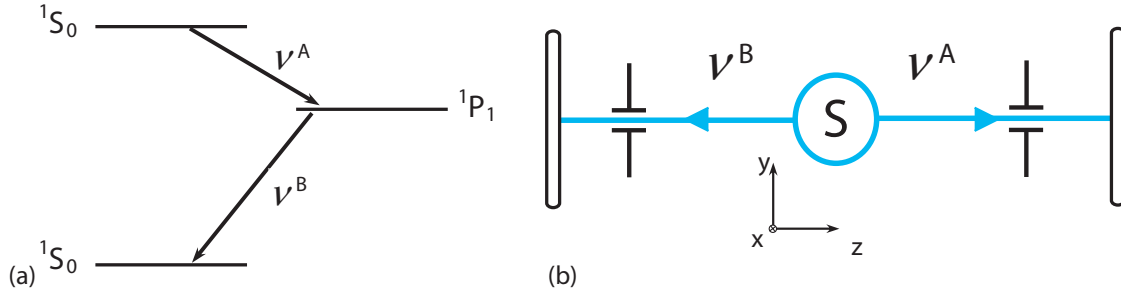


Figure 1.3: (a) Atomic cascade emitting pairs of photons correlated in polarization. (b) Ideal configuration with infinitely small solid angles.

later in this Section. The possible states are denoted as

$$\begin{aligned}
 |\Psi_-^{AB}\rangle &= \frac{1}{\sqrt{2}}(|R^A, L^B\rangle - |L^A, R^B\rangle) \\
 |\Psi_+^{AB}\rangle &= \frac{1}{\sqrt{2}}(|R^A, L^B\rangle + |L^A, R^B\rangle) \\
 |\Phi_+^{AB}\rangle &= \frac{1}{\sqrt{2}}(|R^A, R^B\rangle + |L^A, L^B\rangle) \\
 |\Phi_-^{AB}\rangle &= \frac{1}{\sqrt{2}}(|R^A, R^B\rangle - |L^A, L^B\rangle).
 \end{aligned} \tag{1.20}$$

First, only $|\Psi_-^{AB}\rangle$ and $|\Phi_+^{AB}\rangle$ are invariant under rotations around the axis of symmetry (the direction of propagation of the photons). Therefore the polarization state must be either $|\Psi_-^{AB}\rangle$ or $|\Phi_+^{AB}\rangle$. Second, the parity of $|\Psi_-^{AB}\rangle$ is odd, whereas the parity of $|\Phi_+^{AB}\rangle$ is even. Pions have odd parity and therefore they decay by emitting photons in the polarization state $|\Psi_-^{AB}\rangle = \frac{1}{\sqrt{2}}(|R^A, L^B\rangle - |L^A, R^B\rangle)$. Hence photons emitted in a pion decay have *opposite* polarizations. An experiment performed in 1949 confirmed the anticorrelated polarization of photons pairs from pion (as well as positron) decay [Wu and Shaknov, 1950]

A different physical situation arises from an atomic cascade [Freedman and Clauser, 1972, Aspect et al., 1981]. In an atomic cascade (for example calcium) an atom decays via two sequential transitions from an excited state via an intermediate state to the ground state. The two emitted photons have wavelengths of $\lambda_A = 551,3 \text{ nm}$ and $\lambda_B = 422,7 \text{ nm}$, which is schematically illustrated in Fig. 1.3(a). Generally they are not emitted in opposite direction (see Fig. 1.3(b)), but for experimental

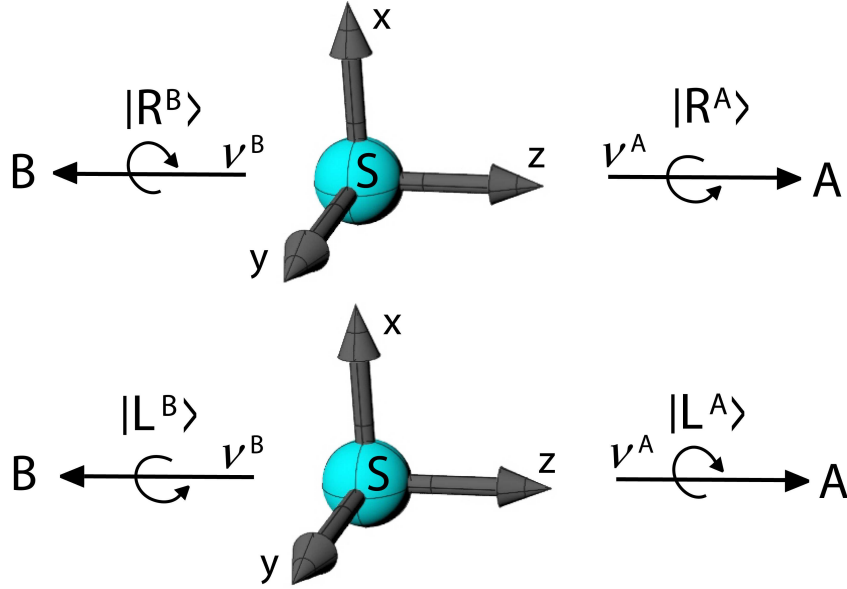


Figure 1.4: Polarization of the cascade photons in respect to the propagation directions.

convenience only photons propagating in $\pm z$ -direction are selected. This is the main reason for the so called *detection loophole*, which is explained in detail in Sec.1.3.5. Since in the $J = 0 \rightarrow J = 1 \rightarrow J = 0$ transition the total angular momentum remains unchanged the emitted photons must have circular polarization with opposite angular momentum. The wavevector \vec{k} is in one case proportional to $+\hat{e}_z$ and in the other case proportional to $-\hat{e}_z$. According to the vanishing total angular momentum, and since the two-photon state must have even parity (change of coordinate system right to left-handed state remains unchanged) in an atomic cascade the only choice yields

$$|\Phi_+^{AB}\rangle = \frac{1}{\sqrt{2}}(|R^A, R^B\rangle + |L^A, L^B\rangle), \quad (1.21)$$

which is known as a Bell state. Hence photons emitted in an atomic cascade have the *same* polarization. Since the intermediate state is degenerated the ground state can be arrived via two different intermediate states (like paths in a two-slit experiment). This, together with the superposition, gives rise to the entanglement.

For a joint measurement it is convenient to calculate the linear polarizations in the x and y direction of the laboratory frame (instead of the k -dependent polarization directions R and L), which is illustrated in Fig.1.4. Using Eq.(1.17) and Eq.(1.17), and keeping in

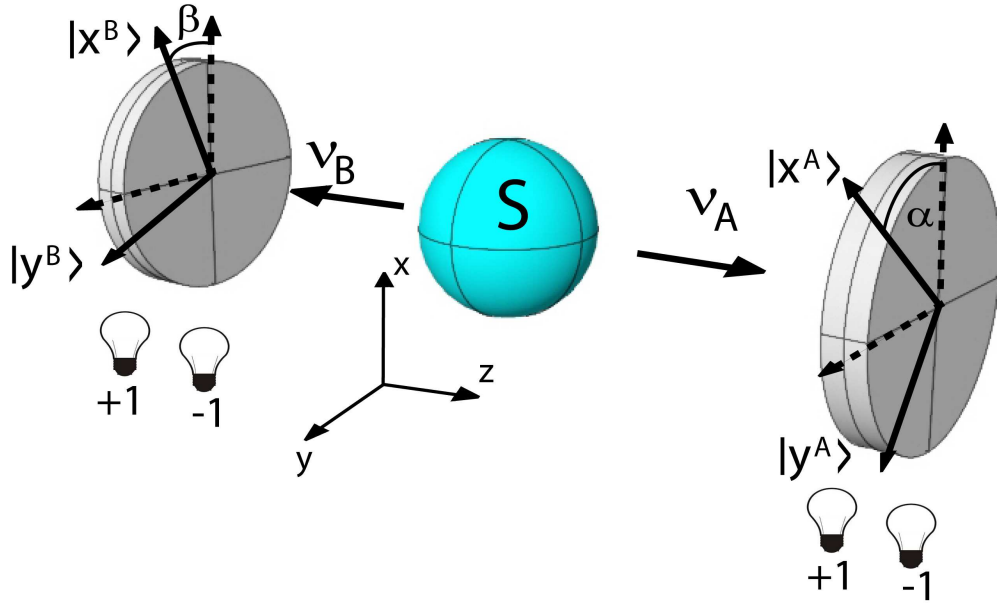


Figure 1.5: Schematic sketch of the *Einstein-Podolsky-Rosen-Bohm Gedankenexperiment* with photons. The two photons ν_A and ν_B , emitted in the state $|\Psi_+^{AB}\rangle$ are analyzed by linear polarizers in orientations α and β .

mind the convention for the propagation direction, one finds

$$\begin{aligned}
 |R^A\rangle &= \frac{1}{\sqrt{2}}(|x^A\rangle + i|y^A\rangle) \\
 |L^A\rangle &= \frac{1}{\sqrt{2}}(|x^A\rangle - i|y^A\rangle) \\
 |R^B\rangle &= \frac{1}{\sqrt{2}}(|x^B\rangle - i|y^B\rangle) \\
 |L^B\rangle &= \frac{1}{\sqrt{2}}(|x^B\rangle + i|y^B\rangle),
 \end{aligned} \tag{1.22}$$

and thus

$$|\Phi_+^{AB}\rangle = \frac{1}{\sqrt{2}}(|x^A, x^B\rangle + |y^A, y^B\rangle), \tag{1.23}$$

for the entangled rotationally-symmetric Bell-state $|\Phi_+^{AB}\rangle$.

Next two detectors, which observe the linear polarization, are placed along the trajectories of ν^A and ν^B , which is schematically illustrated in Fig 1.5 (the distance may be

very long). They can be rotated by an angle α for the polarization analysis for ν^A (β for ν^B) around the z -axis (propagation direction). The detectors register counts, when the polarization $|x^A\rangle$ or $|y^A\rangle$ is found respectively. Hereby the polarization $|x^A\rangle$ is attributed to measure the value $+1$ whereas $|y^A\rangle$ corresponds to -1 . For ν^B the scheme is the same. The observables for the local photon measurement are defined by the projection operators denoted as

$$\begin{aligned}\hat{P}_x(\alpha) &= |\alpha^x\rangle\langle\alpha^x| \\ \hat{P}_y(\alpha) &= |\alpha^y\rangle\langle\alpha^y|,\end{aligned}\tag{1.24}$$

with

$$\begin{aligned}|\alpha^x\rangle &= \cos\alpha|x\rangle + \sin\alpha|y\rangle \\ |\alpha^y\rangle &= -\sin\alpha|x\rangle + \cos\alpha|y\rangle.\end{aligned}\tag{1.25}$$

Using Eq.(1.24) and Eq.(1.25) one can calculate the following probabilities for single measurements, with polarization analysis along α for ν^A (and β for ν^B):

$$\begin{aligned}P_+(\alpha) &= \langle\Phi_+^{AB}|\hat{P}_x(\alpha)|\Phi_+^{AB}\rangle = \langle\Phi_+^{AB}|\alpha^x\rangle\langle\alpha^x|\Phi_+^{AB}\rangle = \frac{1}{2} \\ P_-(\alpha) &= \langle\Phi_+^{AB}|\hat{P}_y(\alpha)|\Phi_+^{AB}\rangle = \langle\Phi_+^{AB}|\alpha^y\rangle\langle\alpha^y|\Phi_+^{AB}\rangle = \frac{1}{2} \\ P_+(\beta) &= \langle\Phi_+^{AB}|\hat{P}_x(\beta)|\Phi_+^{AB}\rangle = \langle\Phi_+^{AB}|\beta^x\rangle\langle\beta^x|\Phi_+^{AB}\rangle = \frac{1}{2} \\ P_-(\beta) &= \langle\Phi_+^{AB}|\hat{P}_y(\beta)|\Phi_+^{AB}\rangle = \langle\Phi_+^{AB}|\beta^y\rangle\langle\beta^y|\Phi_+^{AB}\rangle = \frac{1}{2}.\end{aligned}\tag{1.26}$$

So each individual polarization measurement gives a *random* result. Now considering the probabilities for joint detection

$$\begin{aligned}P_{++}(\alpha, \beta) &= \langle\Phi_+^{AB}|\hat{P}_x(\alpha)\hat{P}_x(\beta)|\Phi_+^{AB}\rangle = \langle\Phi_+^{AB}|\alpha^x, \beta^x\rangle\langle\alpha^x, \beta^x|\Phi_+^{AB}\rangle = \frac{1}{2}\cos^2(\beta - \alpha) \\ P_{+-}(\alpha, \beta) &= \langle\Phi_+^{AB}|\hat{P}_x(\alpha)\hat{P}_y(\beta)|\Phi_+^{AB}\rangle = \langle\Phi_+^{AB}|\alpha^x, \beta^y\rangle\langle\alpha^x, \beta^y|\Phi_+^{AB}\rangle = \frac{1}{2}\sin^2(\beta - \alpha) \\ P_{-+}(\alpha, \beta) &= \langle\Phi_+^{AB}|\hat{P}_y(\alpha)\hat{P}_x(\beta)|\Phi_+^{AB}\rangle = \langle\Phi_+^{AB}|\alpha^y, \beta^x\rangle\langle\alpha^y, \beta^x|\Phi_+^{AB}\rangle = \frac{1}{2}\sin^2(\beta - \alpha) \\ P_{--}(\alpha, \beta) &= \langle\Phi_+^{AB}|\hat{P}_y(\alpha)\hat{P}_y(\beta)|\Phi_+^{AB}\rangle = \langle\Phi_+^{AB}|\alpha^y, \beta^y\rangle\langle\alpha^y, \beta^y|\Phi_+^{AB}\rangle = \frac{1}{2}\cos^2(\beta - \alpha).\end{aligned}\tag{1.27}$$

So the probability of finding both photons in the same polarization is given by

$$P_{\text{equal}}(\alpha, \beta) = P_{++}(\alpha, \beta) + P_{--}(\alpha, \beta) = \cos^2(\beta - \alpha), \quad (1.28)$$

and the probability of finding both photons in the different polarization is

$$P_{\text{diff}}(\alpha, \beta) = P_{+-}(\alpha, \beta) + P_{-+}(\alpha, \beta) = \sin^2(\beta - \alpha). \quad (1.29)$$

Correlations

Considering the particular situation for $|\Phi_+^{AB}\rangle$, where polarizers are parallel ($\alpha = \beta$). Then the predictions for the joint detection probabilities are the following:

$$\begin{aligned} P_{++}(\alpha, \alpha) &= P_{--}(\alpha, \alpha) = \frac{1}{2} \\ P_{+-}(\alpha, \alpha) &= P_{-+}(\alpha, \alpha) = 0 \end{aligned} \quad (1.30)$$

Hence when the photon ν_A is found in the + channel of polarizer A , ν_B is found with certainty in the + channel of polarizer B . For parallel oriented polarizers, there is thus a *full correlation* between the individually random results of measurements of polarization on the two photons ν_A and ν_B . A method to measure the amount of correlations between random quantities, is to calculate the correlation coefficient. For the polarization measurements it is equal to

$$\begin{aligned} E_{\text{QM}}(\alpha, \beta) &= P_{++}(\alpha, \beta) + P_{--}(\alpha, \beta) - P_{+-}(\alpha, \beta) - P_{-+}(\alpha, \beta) \\ &= P_{\text{equal}}(\alpha, \beta) - P_{\text{diff}}(\alpha, \beta) = \cos(2(\beta - \alpha)). \end{aligned} \quad (1.31)$$

The correlation coefficient is an expectation value for a joint measurement of the polarizations of ν^A and ν^B . In the particular case of parallel polarizers ($\alpha = \beta$), $E(\alpha, \beta) = 1$ is found, conforming that the correlation is full.

Formally the same result can be achieved by introducing the observables

$$\begin{aligned} \hat{A}(\alpha) &= \hat{P}_x(\alpha) - \hat{P}_y(\alpha) \\ \hat{B}(\beta) &= \hat{P}_x(\beta) - \hat{P}_y(\beta), \end{aligned} \quad (1.32)$$

with

$$E_{\text{QM}}(\alpha, \beta) = \langle \Phi_+^{AB} | A(\alpha) B(\beta) | \Phi_+^{AB} \rangle = \cos(2(\beta - \alpha)). \quad (1.33)$$

At this point it should be mentioned that for the polarization state $|\Psi_-^{AB}\rangle$ the correlation function only differs in sign and reads

$$E'_{\text{QM}}(\alpha, \beta) = \langle \Psi_-^{AB} | A(\alpha) B(\beta) | \Psi_-^{AB} \rangle = -\cos(2(\beta - \alpha)). \quad (1.34)$$

To sum up, the quantum-mechanical calculations show that although each individual measurement gives a random result, these random results are correlated, as expressed by Eqs.(1.31,1.34). Hence for parallel analyzers ($\alpha = \beta$) *anti-correlation* is observed.

Spin $\frac{1}{2}$ -objects

For polarization measurements with two spin $\frac{1}{2}$ -particles the correlation coefficient is calculated in an analogous manner. The state is denoted as, for instance,

$$|\Phi_+^{AB}\rangle = \frac{1}{\sqrt{2}}(|\uparrow^A, \uparrow^B\rangle + |\downarrow^A, \downarrow^B\rangle). \quad (1.35)$$

Again the projection operators are given by

$$\begin{aligned} \hat{P}_+(\alpha) &= |+\alpha\rangle\langle+\alpha| \\ \hat{P}_-(\alpha) &= |-\alpha\rangle\langle-\alpha|, \end{aligned} \quad (1.36)$$

where $|+\alpha\rangle$ and $|-\alpha\rangle$ are defined as

$$\begin{aligned} |+\alpha\rangle &= \cos\frac{\alpha}{2}|\uparrow\rangle + \sin\frac{\alpha}{2}|\downarrow\rangle \\ |-\alpha\rangle &= -\sin\frac{\alpha}{2}|\uparrow\rangle + \cos\frac{\alpha}{2}|\downarrow\rangle. \end{aligned} \quad (1.37)$$

As before in Eq.(1.27) the probabilities yield

$$P_{++}^{S=\frac{1}{2}} = P_{--}^{S=\frac{1}{2}} = \frac{1}{2} \cos^2\left(\frac{\beta - \alpha}{2}\right) \quad (1.38)$$

and

$$P_{+-}^{S=\frac{1}{2}} = P_{-+}^{S=\frac{1}{2}} = \frac{1}{2} \sin^2\left(\frac{\beta - \alpha}{2}\right) \quad (1.39)$$

with

$$P_{\text{equal}}^{S=\frac{1}{2}} = P_{++}^{S=\frac{1}{2}} + P_{--}^{S=\frac{1}{2}} = \cos^2\left(\frac{\beta - \alpha}{2}\right) \quad (1.40)$$

and

$$P_{\text{diff}}^{S=\frac{1}{2}} = P_{+-}^{S=\frac{1}{2}} + P_{-+}^{S=\frac{1}{2}} = \sin^2\left(\frac{\beta - \alpha}{2}\right). \quad (1.41)$$

Finally the correlation coefficient, which is the quantum-mechanical expectation values for a projective joint measurement along α and β , $E^{S=\frac{1}{2}}(\alpha, \beta)$ is calculated as

$$E_{\text{QM}}^{S=\frac{1}{2}}(\alpha, \beta) = P_{\text{equal}}^{S=\frac{1}{2}} - P_{\text{diff}}^{S=\frac{1}{2}} = \langle \Phi_+^{AB} | A(\alpha)B(\beta) | \Phi_+^{AB} \rangle = \cos(\beta - \alpha). \quad (1.42)$$

As seen above, for spin $\frac{1}{2}$ -particles the angles are typically half as large compared to photons. In practise this state exhibits when a $J = 0$ systems spontaneously disintegrates into two spin $\frac{1}{2}$ -particles. An example for this process is the decay of a η meson into a muon pair

$$\eta \rightarrow \mu^+ + \mu^-, \quad (1.43)$$

or the decay of ^2He , where entangled proton pairs are produced. They are formed in the $^1\text{H}(d, ^2\text{He})n$ reaction using a deuteron beam in conjunction with a liquid hydrogen target [Sakai et al., 2006]. Both systems are found in the spin spin-singlet state

$$|\Psi_-^{AB}\rangle = \frac{1}{\sqrt{2}}(|\uparrow^A, \downarrow^B\rangle - |\downarrow^A, \uparrow^B\rangle). \quad (1.44)$$

The correlation coefficient projective joint measurement along α and β is given by

$$E_{\text{QM}}'^{S=\frac{1}{2}}(\alpha, \beta) = \langle \Psi_-^{AB} | A(\alpha)B(\beta) | \Psi_-^{AB} \rangle = -\cos(\beta - \alpha), \quad (1.45)$$

which again is half as large as in the photon case.

Collapse of the state vector

By applying the postulate of *reduction of the state vector*, introduced by Heisenberg [Heisenberg, 1927] and later postulated by von Neumann [von Neumann, 1932], a surprising picture of the scenario derived on the last few pages can be constructed. Without loss of generality, it is possible to identify separately the two measurements happening on both sides of the measurement apparatus of Fig 1.5, by splitting up the joint measurement in two steps. Suppose the measurement on photon ν_A takes place first, and gives the result yields $+$, with the polarizer A in orientation α . This result is found with a probability of $1/2$. Now using the concept of reduction of the state vector, from which follows, that after this measurement, the new state vector $|\Phi_+^{*AB}\rangle$ is obtained by projection of the initial state vector $|\Phi_+^{AB}\rangle$ onto the eigenspace associated to the result $+$. Using the corresponding projector the system is found in the state

$$|\Phi_+^{*AB}\rangle = |\alpha, \alpha\rangle. \quad (1.46)$$

This equation states that immediately after the first measurement, photon ν^A takes the polarization α . This is somehow obvious, since ν^A has been measured with a polarizer A oriented along α , and the result $+$ has been obtained. What is more surprisingly, is that the distant photon ν^B , which has not yet interacted with any polarizer, has also been projected into the state $|\alpha\rangle$ with a well defined polarization, parallel to the one found for photon ν^A . However this gives the correct final result (Eq.(1.27)), applying *Malus' law* (cosine dependence of the intensity of a polarized beam after an ideal polarizer) for a subsequent measurement of ν^B performed along β yields

$$P_{++}(\alpha, \beta) = \frac{1}{2} \cos^2(\beta - \alpha). \quad (1.47)$$

Proving that a calculation in two steps yields the same result as the direct calculation.

It should be mentioned that the change in the description of ν^B happens instantaneously, whatever the distance between ν^A and ν^B , at the moment of the first measurement. This seems to be in contradiction with relativity. According to Einstein, what happens in a given region of space-time cannot be influenced by an event happening in a region space-like separated region. So it is reasonable to try to find more acceptable pictures of the EPR correlations, which is presented in the next Section.

1.3 Bell-type Inequalities and Local Hidden Variable Theories

The *spooky action at a distance* or *spukhafte Fernwirkung*, as it was called originally by Einstein in his correspondence with various physicists, can be explained if the measurement outcome is already pre-determined at the time of the states creation. However this information is not part of the quantum-mechanical description. But before going into detail the two major assumptions of the EPR claim, namely *reality* and *locality* (or just *local realism*), are summarized as it was done in the original paper:

Physical reality: Properties of physical systems are those physical quantities whose value can be predicted with certainty before carrying out the corresponding measurement. These properties are in reality already determined before they are measured. They are *elements of reality*. This concept is called **Einstein reality**: "*If without in any way disturbing the system, we can predict with certainty the value of a physical quantity, then there exists an element of reality corresponding to this physical quantity*" [Einstein et al., 1935]. This means that this physical quantity has a value independent of whether it is measured or not.

Locality: Physical reality can be described locally. Meaning that the properties of a physical system (i.e. the value of a measurement) is independent of which interventions (measurements) are carried out on an other spatially separated system. This concept is called **Einstein locality**: "*The real factual situation of a system A is independent of what is done with system B, which is spatially separated from the former.*" [Einstein et al., 1935]

The authors of the EPR paper argued based on local realism that quantum mechanics is not structured finely enough to capture all the elements of the physical reality (which are always present, whether measured or not). They concluded from this assumption that quantum mechanics is not incorrect but *incomplete*. There are elements of reality that do not appear in quantum theory, and therefore they are **hidden variables** for quantum theory.

A simple example using pre-defined values

Now the most simple example is constructed, based on local realism, leading to predictions different from quantum mechanics. Polarization measurements along three axes, denoted as \hat{a} , \hat{b} and \hat{c} are carried out. Each photon belongs to a certain type, for example $(\hat{a}-, \hat{b}+, \hat{c}+)$ would yield -1 for a measurement along \hat{a} and +1 for \hat{b} and \hat{c} . Again there must be a perfect matching in the sense that the other particle must also be of type $(\hat{a}+, \hat{b}+, \hat{c}+)$, according to the state Ψ_+^{AB} . All eight possible particle type are listed in Tab. 1.1.

If a measurement along \hat{a} of particle A ($S_1 \cdot \hat{a}$) yields +1 and along \hat{b} of particle B ($S_2 \cdot \hat{b}$) yields -1 the pair obviously belongs either to type 3 or type 4. So the total number of particles which possible for this event is given by $N_3 + N_4$. The possibility that in a random selection of particles ($S_1 \cdot \hat{a}$) results in +1 and ($S_2 \cdot \hat{b}$) in -1 is denoted as

$$P(\hat{a}+; \hat{b}-) = \frac{N_3 + N_4}{\sum_i^8 N_i}. \quad (1.48)$$

Table 1.1: The 8 possible particle types, including their pre-defined values for polarization measurements along directions \hat{a} , \hat{b} and \hat{c} .

| type | Population | Photon A | Photon B |
|------|------------|----------------------------------|----------------------------------|
| 1 | N_1 | $(\hat{a}+, \hat{b}+, \hat{c}+)$ | $(\hat{a}+, \hat{b}+, \hat{c}+)$ |
| 2 | N_2 | $(\hat{a}+, \hat{b}+, \hat{c}-)$ | $(\hat{a}+, \hat{b}+, \hat{c}-)$ |
| 3 | N_3 | $(\hat{a}+, \hat{b}-, \hat{c}+)$ | $(\hat{a}+, \hat{b}-, \hat{c}+)$ |
| 4 | N_4 | $(\hat{a}+, \hat{b}-, \hat{c}-)$ | $(\hat{a}+, \hat{b}-, \hat{c}-)$ |
| 5 | N_5 | $(\hat{a}-, \hat{b}+, \hat{c}+)$ | $(\hat{a}-, \hat{b}+, \hat{c}+)$ |
| 6 | N_6 | $(\hat{a}-, \hat{b}+, \hat{c}-)$ | $(\hat{a}-, \hat{b}+, \hat{c}-)$ |
| 7 | N_7 | $(\hat{a}-, \hat{b}-, \hat{c}+)$ | $(\hat{a}-, \hat{b}-, \hat{c}+)$ |
| 8 | N_8 | $(\hat{a}-, \hat{b}-, \hat{c}-)$ | $(\hat{a}-, \hat{b}-, \hat{c}-)$ |

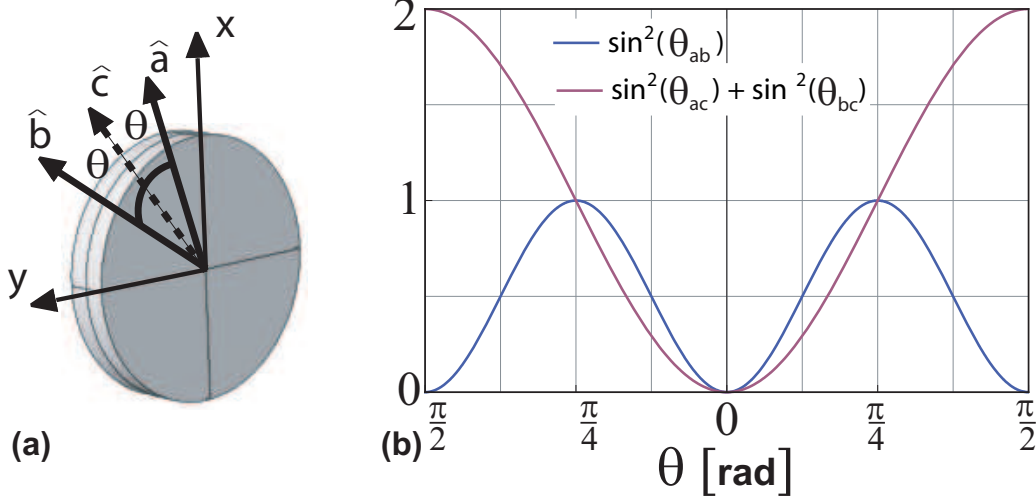


Figure 1.6: (a) Direction for polarization measurements along orientations \hat{a} , \hat{b} and \hat{c} , defined by their common relative angle θ . (b) Left and right side of Eq.(1.53) with maximal violation of Bell's inequality at $\theta = \pi/8$.

For measurement along \hat{c} the probabilities for different results is given by

$$P(\hat{a}+; \hat{c}-) = \frac{N_2 + N_4}{\sum_i^8 N_i} \quad \text{and} \quad P(\hat{b}+; \hat{c}-) = \frac{N_2 + N_6}{\sum_i^8 N_i} \quad (1.49)$$

Since N_i is positive the following inequality holds:

$$N_3 + N_4 \leq (N_3 + N_2) + (N_4 + N_6) \quad (1.50)$$

Using Eq.(1.48) and Eq.(1.49) the inequality introduced in Eq.(1.50) can be written as

$$P(\hat{a}+; \hat{b}-) \leq P(\hat{a}+; \hat{c}-) + P(\hat{b}+; \hat{c}-), \quad (1.51)$$

which is known as **Bell's inequality**.

What are the predictions of quantum mechanics for this particular situation? As defined in Eq.(1.27) the probability of finding particle 1 in + polarization along \hat{a} and particle 2 in - polarization along \hat{b} is $P_{+-} = \frac{1}{2} \sin^2(\theta_{ab})$ for photons. So Bell's inequality can be rewritten as

$$\sin^2(\theta_{ab}) \leq \sin^2(\theta_{ac}) + \sin^2(\theta_{cb}). \quad (1.52)$$

For simplicity \hat{c} is chosen such that it bisects the two directions \hat{a} and \hat{b} , which is depicted in Fig. 1.6:

$$\theta_{ab} = 2\theta \quad \text{and} \quad \theta_{ac} = \theta_{cb} = \theta. \quad (1.53)$$

Hence Inequality Eq.(1.52) is violated for $0 < \theta < \frac{\pi}{4}$, for example $\theta = \pi/8$ yields

$$0.5 < 0.292893. \quad (1.54)$$

For spin $\frac{1}{2}$ -particles the angles are half as large. As shown in this simple example, quantum-mechanical predictions are not compatible with Bell's inequality - they violate Bell's inequality.

1.3.1 Hidden variable formalism

Now a somehow more general way to derive Bell's inequality is presented: A set of supplementary parameters (hidden variables) denoted λ represents all *elements of reality* which occur in connection with the polarization measurement. All properties of an object are characterized by a certain set of variables λ . Particles with values of the variables λ are emitted by a source with a probability $\rho(\lambda)$ with

$$\int \rho(\lambda) d\lambda = 1, \quad \text{for } \rho(\lambda) \geq 0. \quad (1.55)$$

Again the only possible outcomes of a polarization measurement at A for an angle of rotation α of the analyzer are $+1$ or -1 . Then there exists an unambiguous function $S_A^\lambda(\alpha)$, which for a given λ and α (β) determines the measurement value definitely as $+1$ or -1 , which are the only two possible results of $S_A^\lambda(\alpha)$. The same is valid for the polarization measurement at B along β , expressed as

$$S_A^\lambda(\alpha) = \left\{ \begin{array}{c} +1 \\ -1 \end{array} \right\} \quad S_B^\lambda(\beta) = \left\{ \begin{array}{c} +1 \\ -1 \end{array} \right\}. \quad (1.56)$$

A particular hidden variable theory is completely defined by the explicit form of the function $\rho(\lambda)$, $S_A^\lambda(\alpha)$ and $S_B^\lambda(\beta)$. Now one can express the probabilities of the various results of measurements. For instance, noting that the function $\frac{1}{2}(S_A^\lambda(\alpha) + 1)$ assumes the value $+1$ for the $+$ result, and 0 for the $-$ result. In the same manner the function

$\frac{1}{2}(1 - S_B^\lambda(\beta))$ assumes the value +1 for the - result, and 0 otherwise. So the probability to measure +1 at polarizer A , at the angle α is given by

$$P_+^{\text{cl}}(\alpha) = \int \rho(\lambda) \frac{(S_A^\lambda(\alpha) + 1)}{2} d\lambda, \quad (1.57)$$

or for the joint probability to measure +1 at polarizer A , at the angle α and -1 at polarizer B , at the angle β

$$P_{+-}^{\text{cl}}(\alpha, \beta) = \int \rho(\lambda) \frac{(S_A^\lambda(\alpha) + 1)}{2} \frac{(1 - S_B^\lambda(\beta))}{2} d\lambda, \quad (1.58)$$

The classical correlation function is then expressed as

$$E_{\text{cl}}(\alpha, \beta) = \int \rho(\lambda) S_A^\lambda(\alpha) S_B^\lambda(\beta) d\lambda. \quad (1.59)$$

The fact that the correlation is given by a product of the two functions $S_A^\lambda(\alpha)$ and $S_B^\lambda(\beta)$ expresses *locality*. So result of $S_A^\lambda(\alpha)$ does not depend on the measurement settings at B , and vice versa.

A naive example of a local hidden variable model

At this point it is informative to introduce a simple example of supplementary parameters theory: Here each photon pair is supposed to have a well defined linear polarization, determined by its angle λ_A or λ_B with the x -axis. To account for the strong correlation,

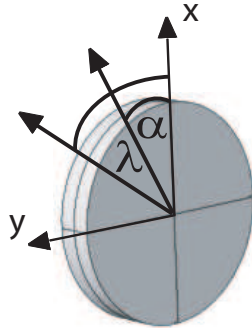


Figure 1.7: Each pair of photons has a predefined *direction of polarization*, which is defined by λ , being the supplementary parameter of the model. Polarizer A carries out a polarization measurement along α .

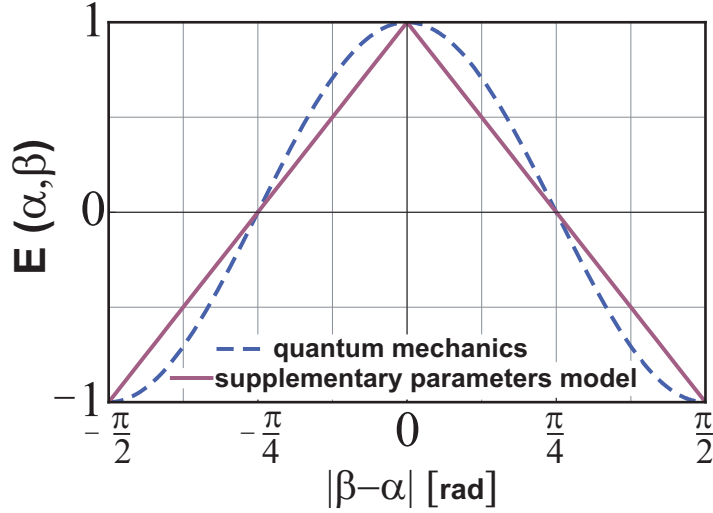


Figure 1.8: Polarization correlation coefficient, as a function of the relative orientation of the polarizers ($\beta - \alpha$). Dotted line: Predictions of quantum mechanics. Solid line: Supplementary parameter model.

the two photons of a same pair are emitted with the same linear polarization, defined by the common angle λ (see Fig 1.7). The polarization of the various pairs should be randomly distributed, consequently the probability distribution is assumed to be rotationally invariant:

$$\rho(\lambda) = \frac{1}{2\pi} \quad (1.60)$$

Next to complete this model an explicit form of the functions $S_A^\lambda(\alpha)$ and $S_B^\lambda(\beta)$ has to be defined such as

$$\begin{aligned} S_A^\lambda(\alpha) &= \text{sign}(\cos 2(\alpha - \lambda)) \\ S_B^\lambda(\beta) &= \text{sign}(\cos 2(\beta - \lambda)). \end{aligned} \quad (1.61)$$

$S_A^\lambda(\alpha)$ assumes the value +1 when the polarization of photon ν^A encloses an angle less than $\pi/4$ with the direction of analysis α , and -1 for the complementary case, where the polarization is closer to the perpendicular to α .

With this explicit model and Eq.(1.58) the various probabilities of the polarization

measurements can be compared with the predictions of quantum mechanics:

$$P_+^{\text{cl}}(\alpha) = P_-^{\text{cl}}(\alpha) = P_+^{\text{cl}}(\beta) = P_-^{\text{cl}}(\beta) = \frac{1}{2} \quad (1.62)$$

As seen these results are identical to the quantum-mechanical results from Eq.(1.26) for the state $|\Phi_+^{AB}\rangle$. By applying Eq.(1.59) joint probabilities, or equivalently the correlation function, can be calculated, which yields

$$E_{\text{cl}}(\alpha, \beta) = 1 - 4 \frac{|\beta - \alpha|}{\pi}, \quad (1.63)$$

for

$$-\frac{\pi}{2} \leq \beta - \alpha \leq \frac{\pi}{2}, \quad (1.64)$$

which is depicted in Fig. 1.8. This is a remarkable result. First that $E^{\text{cl}}(\alpha, \beta)$ depends only on the relative angle between α and β , such as the predictions of quantum mechanics $E(\alpha, \beta) = \cos(2(\beta - \alpha))$. Second, as can be seen in Fig. 1.8 the difference between the predictions of this simple supplementary parameters model and the quantum-mechanical predictions is always small. This could suggest that a more sophisticated model could be able to reproduce exactly the quantum-mechanical predictions. But this is not the case! *Bell's discovery is the fact that the search for such local realistic models is hopeless.*

1.3.2 The original Bell inequality

Now back to a more general derivation of Eq.(1.51) using supplementary parameters. From Eq.(1.55) and Eq.(1.56) follows that

$$S_A^\lambda(\delta) = S_B^\lambda(\delta) = S^\lambda(\delta), \quad (1.65)$$

indicating, that the two observables have the same functional dependence on the hidden variables λ and the angle δ (of course this is an experimental limitation, which will be obsolete in the CHSH formulation of Bell's inequality, which is discussed later).

Next measurements for pairs of angles for the analyzers A and B are considered. With the three pairs of angles (α, β) , (α, γ) and (β, γ) , the following identity is introduced:

$$S^\lambda(\alpha)S^\lambda(\beta) - S^\lambda(\alpha)S^\lambda(\gamma) = \underbrace{S^\lambda(\alpha)S^\lambda(\beta)}_{\pm 1} \underbrace{[1 - S^\lambda(\beta)S^\lambda(\gamma)]}_{\geq 0}, \quad (1.66)$$

since $S^\lambda(\beta)S^\lambda(\beta)=1$. Integration together with Eq.(1.55) yields

$$\begin{aligned} \left| \int \rho(\lambda) \{S^\lambda(\alpha)S^\lambda(\beta) - S^\lambda(\alpha)S^\lambda(\gamma)\} d\lambda \right| &= \left| \rho(\lambda) S^\lambda(\alpha) S^\lambda(\beta) \{1 - S^\lambda(\beta) S^\lambda(\gamma)\} d\lambda \right| \\ &\leq \int \rho(\lambda) \underbrace{[1 - S^\lambda(\beta) S^\lambda(\gamma)]}_{\geq 0} d\lambda = 1 - \int \rho(\lambda) S^\lambda(\beta) S^\lambda(\gamma) d\lambda. \end{aligned} \quad (1.67)$$

Using the definitions for the classical correlation coefficients introduced in Eq.(1.59) Bell's inequality reads [Bell, 1964]

$$|E_{\text{cl}}(\alpha, \beta) - E_{\text{cl}}(\alpha, \gamma)| \leq 1 - E_{\text{cl}}(\beta, \gamma). \quad (1.68)$$

This inequality again conflicts with quantum mechanics which predicts, say, for the following angles $\alpha = 60^\circ$, $\beta = 120^\circ$ and $\gamma = 180^\circ$

$$E_{\text{QM}}^{S=\frac{1}{2}}(\alpha, \beta) = \frac{1}{2}, \quad E_{\text{QM}}^{S=\frac{1}{2}}(\alpha, \gamma) = -\frac{1}{2}, \quad E_{\text{QM}}^{S=\frac{1}{2}}(\beta, \gamma) = \frac{1}{2}, \quad (1.69)$$

which leads to

$$1 \leq \frac{1}{2}, \quad (1.70)$$

a violation of Bell's inequality, defined in Eq.(1.68) (accordingly for photons the angles would be $\alpha = 30^\circ$, $\beta = 60^\circ$ and $\gamma = 90^\circ$).

1.3.3 The Clauser-Horne-Shimony-Holt (CHSH) inequality

Now an additional combination of rotation angles of the analyzers is present, where references to experimental results (like in Eq.(1.65)) are no longer required. In 1969 Clauser, Horne, Shimony and Holt (CHSH) reformulated Bell's inequalities pertinent for the first practical test of quantum non-locality [Clauser et al., 1969]: At analyzer A measurements are carried out with the orientations α and α' and at B with β and β' accordingly. Assuming local realism all four measurements have predefined values denoted as $\epsilon_\alpha, \epsilon_{\alpha'}, \epsilon_\beta$ and $\epsilon_{\beta'}$ which can only take the values $+1$ or -1 . The identity

$$(\epsilon_\beta - \epsilon_{\beta'})\epsilon_\alpha + (\epsilon_\beta + \epsilon_{\beta'})\epsilon_{\alpha'} = \pm 2 \quad (1.71)$$

holds for any random set of the four values. By accumulating data one can average the four terms and construct the algebraic sum S_{av} , corresponding to the quantum-mechanical

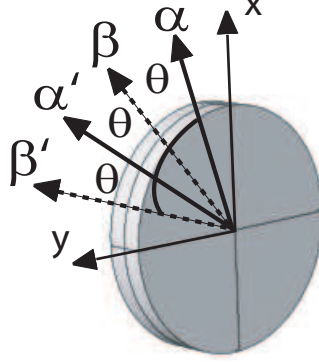


Figure 1.9: Orientations yielding the largest conflict between Bells inequalities and quantum mechanics are found at $\theta = \pi/8$ for photons and $\theta = \pi/4$ for spin 1/2-particles.

expectation values, which yields

$$S_{\text{av}} = \langle \sigma_{\alpha}^A \sigma_{\beta}^B \rangle - \langle \sigma_{\alpha}^A \sigma_{\beta'}^B \rangle + \langle \sigma_{\alpha'}^A \sigma_{\beta}^B \rangle + \langle \sigma_{\alpha'}^A \sigma_{\beta'}^B \rangle. \quad (1.72)$$

Since S_{av} is the average of a quantity which can take only the values ± 2 , it must be bounded within these limits:

$$-2 \leq S_{\text{av}} \leq 2 \quad (1.73)$$

On the other hand quantum mechanics predicts for the expectation value $E^{S=\frac{1}{2}}(\alpha, \beta) = \cos(\beta - \alpha) = \cos(\theta_{(\alpha, \beta)})$. Hence the algebraic sum can be written as

$$S(\theta) = \cos \theta_{\alpha\beta} - \cos \theta_{\alpha\beta'} + \cos \theta_{\alpha'\beta} + \cos \theta_{\alpha'\beta'}. \quad (1.74)$$

As shown in Fig. 1.9 the relative angles between the measurement directions are given by $\theta_{\alpha\beta} = \theta_{\alpha'\beta} = \theta_{\alpha'\beta'} = \theta$ and $\theta_{\alpha\beta'} = \theta_{\alpha'\beta'} + \theta_{\alpha'\beta} + \theta_{\alpha\beta} = 3\theta$, which leads to

$$S(\theta) = 3 \cos(\theta) - \cos(3\theta). \quad (1.75)$$

A maximal violation of the CHSH-Bell inequality is found for $\theta = \pi/4$ (for photons at $\pi/8$) where $\sum(\theta) = 2\sqrt{2} \not\leq 2$, which can be seen in Fig. 1.10. A value of $-2\sqrt{2}$ is found for $\theta = 3\pi/4$ (for photons at $3\pi/8$).

Let us see in more detail. Considering a combination of functions S , as defined in

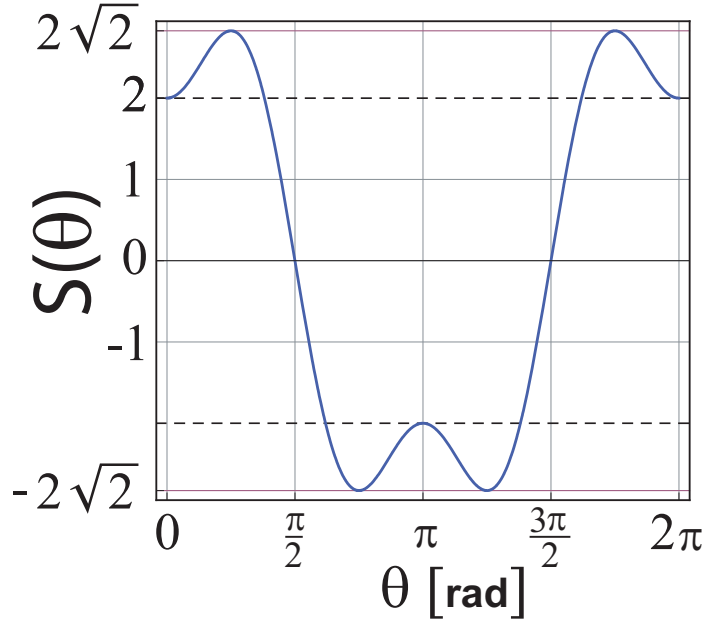


Figure 1.10: $S(\theta)$ as predicted by quantum mechanics. A conflict with Bells inequalities happens when $|S(\theta)|$ is larger than 2, indicated by the horizontal dashed lines. A maximum violation is found at $\pi/4$ for spin $\frac{1}{2}$ -particles, which corresponds to $\pi/8$ for photons.

Eq.(1.56) with the only possible values $S_{A,B}^\lambda = \pm 1$:

$$\underbrace{[S_B^\lambda(\beta) - S_B^\lambda(\beta')]}_{\pm 2} S_A^\lambda(\alpha) + \underbrace{[S_B^\lambda(\beta) + S_B^\lambda(\beta')]}_0 S_A^\lambda(\alpha'), \quad (1.76)$$

$$\begin{array}{ccc} \pm 2 & \longleftrightarrow & 0 \\ 0 & & \pm 2 \end{array}$$

with

$$|[S_B^\lambda(\beta) - S_B^\lambda(\beta')]S_A^\lambda(\alpha) + [S_B^\lambda(\beta) + S_B^\lambda(\beta')]S_A^\lambda(\alpha')| = 2, \quad (1.77)$$

and consequently, using Eq.(1.55),

$$\begin{aligned} & |\int \rho(\lambda)[S_B^\lambda(\beta) - S_B^\lambda(\beta')]S_A^\lambda(\alpha) + [S_B^\lambda(\beta) + S_B^\lambda(\beta')]S_A^\lambda(\alpha')d\lambda| \\ & \leq \int \rho(\lambda)|[S_B^\lambda(\beta) - S_B^\lambda(\beta')]S_A^\lambda(\alpha) + [S_B^\lambda(\beta) + S_B^\lambda(\beta')]S_A^\lambda(\alpha')|d\lambda \\ & = 2 \int \rho(\lambda)d\lambda = 2. \end{aligned} \quad (1.78)$$

Using the classical correlation coefficients, defined in Eq.(1.59) one obtains

$$S_{cl} = |E_{cl}(\alpha, \beta) - E_{cl}(\alpha, \beta') + E_{cl}(\alpha', \beta) + E_{cl}(\alpha', \beta')| \leq 2. \quad (1.79)$$

However quantum mechanics predicts for the corresponding measurement on correlated spins, with angles $\alpha = 0$, $\alpha' = \pi/2$, $\beta = \pi/4$ and $\beta' = 3\pi/4$ (again for photons half of these angles)

$$E_{\text{QM}}^{S=\frac{1}{2}}(\alpha, \beta) = E_{\text{QM}}^{S=\frac{1}{2}}(\alpha', \beta) = E_{\text{QM}}^{S=\frac{1}{2}}(\alpha', \beta') = \frac{1}{\sqrt{2}} \quad \text{and} \quad E_{\text{QM}}^{S=\frac{1}{2}}(\alpha', \beta) = -\frac{1}{\sqrt{2}}, \quad (1.80)$$

therefore the correlation functions, defined in Eq.(1.79), yields

$$S(\theta) = 2\sqrt{2}, \quad (1.81)$$

which violates the CHSH-Bell inequality derived in Eq.(1.72).

The correlation coefficient $E(\alpha, \beta)$ consists of 4 coincidence rates $N_{\pm\pm}(\alpha, \beta)$ with detectors in the output channels of the polarizers, for polarizers in orientations α and β :

$$E(\alpha, \beta) = \frac{N_{++}(\alpha, \beta) - N_{+-}(\alpha, \beta) - N_{-+}(\alpha, \beta) + N_{--}(\alpha, \beta)}{N_{++}(\alpha, \beta) + N_{+-}(\alpha, \beta) + N_{-+}(\alpha, \beta) + N_{--}(\alpha, \beta)}, \quad (1.82)$$

By performing four measurements of this type in orientations (α, β) , (α, β') , (α', β) and (α', β') one obtains a measured value $S^{\text{exp}}(\alpha, \alpha', \beta, \beta')$, as defined in Eq.(1.79).

To sum up: All inequalities for correlation measurements in local variable theories, which are based on the joint assumptions of locality and realism (all these theories are subsumed as Bell inequalities), are at variance with quantum mechanics. Quantum mechanics cannot be reproduced by local-realistic hidden variables theories, which has been demonstrated in numerous experiments [Bertlmann and Zeilinger, 2002].

1.3.4 The Greenberger-Horne-Zeilinger (GHZ) state

Not a statistical violation, but a contradiction between quantum mechanics and local hidden variable theories was found by D. M. Greenberger, M. A. Horne and A. Zeilinger for a tripartite entanglement [Greenberger et al., 1989, Greenberger et al., 1990] in 1989. The GHZ argument is independent of the Bell approach, and shows in a non-statistic manner that quantum mechanics and local realism are mutually incompatible. The GHZ state for a tripartite spin-entangled system, where the objects are spatially separated, is an element of the product Hilbert space $\mathcal{H}_2^A \otimes \mathcal{H}_2^B \otimes \mathcal{H}_2^C$ and given by

$$|\psi_{\text{GHZ}}^{ABC}\rangle = \frac{1}{\sqrt{2}}(|0^A, 0^B, 0^C\rangle + |1^A, 1^B, 1^C\rangle). \quad (1.83)$$

Here $|0\rangle$ and $|1\rangle$ are the eigenstates of σ_z with the corresponding eigenvalues $+1$ and -1 . Next local spin measurements, for different orientations, are performed. For example for a yyx -measurement, the observables σ_y^A , σ_y^B and σ_x^C are measured on the corresponding composite system. An easy way to calculate the expectation value is to decompose the GHZ-state in the eigenfunctions of the measurement operator (in this case system A in y -basis, B in y -basis and C in x -basis). This can be done by using the inverse transformation of Eq.(1.19)

$$\begin{aligned} |H'\rangle = |0_x\rangle &= \frac{1}{\sqrt{2}}(|H\rangle + |V\rangle) & |V'\rangle = |1_x\rangle &= \frac{1}{\sqrt{2}}(|H\rangle - |V\rangle) = \\ \longrightarrow |H\rangle &= \frac{1}{\sqrt{2}}(|1_x\rangle + |0_x\rangle) & |V\rangle &= \frac{1}{\sqrt{2}}(|1_x\rangle - |0_x\rangle) \end{aligned} \quad (1.84)$$

and

$$\begin{aligned} |R\rangle = |0_y\rangle &= \frac{1}{\sqrt{2}}(|H\rangle + i|V\rangle) & |L\rangle = |1_y\rangle &= \frac{1}{\sqrt{2}}(|H\rangle - i|V\rangle) \\ \longrightarrow |H\rangle &= \frac{1}{\sqrt{2}i}(|1_y\rangle + |0_y\rangle) & |V\rangle &= \frac{1}{\sqrt{2}i}(|1_y\rangle - |0_y\rangle). \end{aligned} \quad (1.85)$$

Thus the GHZ state can be expressed in a $y^A y^B x^C$ -basis as

$$\begin{aligned} |\psi_{\text{GHZ}}^{ABC}\rangle &= \frac{1}{\sqrt{2}}(|0^A, 0^B, 0^C\rangle + |1^A, 1^B, 1^C\rangle) \\ &= \frac{1}{2} \left(|1_y^A, 0_y^B, 1_x^C\rangle + |0_y^A, 1_y^B, 1_x^C\rangle + |1_y^A, 1_y^B, 0_x^C\rangle + |0_y^A, 0_y^B, 0_x^C\rangle \right). \end{aligned} \quad (1.86)$$

The quantum-mechanical expectation value can be calculated easily ($+1$ for every $|1_j^i\rangle$ and -1 for every $|0_j^i\rangle$), with $i = A, B, C$ and $j = x, y$):

$$E(\sigma_y^A, \sigma_y^B, \sigma_x^C) = \langle \psi_{\text{GHZ}}^{ABC} | \sigma_y^A, \sigma_y^B, \sigma_x^C | \psi_{\text{GHZ}}^{ABC} \rangle = \frac{-4}{4} = -1 \quad (1.87)$$

Due to the symmetry of the state the result remains the same for the other two measurements (xyx and xyy), only with different indices. For example for the xyx -measurement:

$$\begin{aligned} |\psi_{\text{GHZ}}^{ABC}\rangle &= \frac{1}{\sqrt{2}}(|0^A, 0^B, 0^C\rangle + |1^A, 1^B, 1^C\rangle) \\ &= \frac{1}{2} \left(|1_y^A, 0_x^B, 1_y^C\rangle + |0_y^A, 1_x^B, 1_y^C\rangle + |1_y^A, 1_x^B, 0_y^C\rangle + |0_y^A, 0_x^B, 0_y^C\rangle \right). \end{aligned} \quad (1.88)$$

The two measurements resulting in

$$E(\sigma_y^A, \sigma_x^B, \sigma_y^C) = -1, \quad E(\sigma_x^A, \sigma_y^B, \sigma_y^C) = 1 \quad (1.89)$$

The unique property of this system is that the result of the x -measurement of one system can be predicted with certain, when the results of the y -measurement of the other systems are known. Analogously, the result of one y -measurement can be predicted of the results of the other y -measurement and the x -measurement are known.

From the point of view of a local realistic theory this behaviour can be reproduced simply by addressing predefined value to the individual spin measurements. Let for example s_y^A be the predefined result of the σ_x^A measurement, which can only be +1 or -1. A simple combination of values, reproducing Eq.(1.87) and Eq.(1.89) is given by

$$\begin{aligned} s_x^A = 1 & \quad s_x^B = 1 & \quad s_x^C = -1 \\ s_y^A = -1 & \quad s_y^B = -1 & \quad s_y^C = 1, \end{aligned} \quad (1.90)$$

yielding

$$\begin{aligned} s_y^A s_y^B s_x^C &= -1 \\ s_y^A s_x^B s_y^C &= -1 \\ s_x^A s_y^B s_y^C &= -1. \end{aligned} \quad (1.91)$$

Now multiplying the left and right sides of Eq.(1.91) gives

$$(s_x^A s_y^A s_y^A)(s_y^B s_y^B s_x^B)(s_x^C s_y^C s_y^A) = -1, \quad (1.92)$$

with $s_y^A s_y^A = s_y^B s_y^B = s_y^C s_y^C = 1$ finally

$$s_x^A s_x^B s_x^C = -1 \quad (1.93)$$

is obtained.

However the predictions of quantum mechanics are not only different, but the complete opposite: Now the GHZ state is expressed in a $x^A x^B x^C$ -basis as

$$\begin{aligned} |\psi_{\text{GHZ}}^{ABC}\rangle &= \frac{1}{\sqrt{2}}(|0^A, 0^B, 0^C\rangle + |1^A, 1^B, 1^C\rangle) \\ &= \frac{1}{2} \left(|1_x^A, 1_x^B, 1_x^C\rangle + |0_x^A, 0_x^B, 1_x^C\rangle + |1_x^A, 0_x^B, 0_x^C\rangle + |0_x^A, 1_x^B, 0_x^C\rangle \right) \end{aligned} \quad (1.94)$$

which yields

$$E(\sigma_x^A, \sigma_x^B, \sigma_x^C) = \langle \psi_{\text{GHZ}}^{ABC} | \sigma_x^A, \sigma_x^B, \sigma_x^C | \psi_{\text{GHZ}}^{ABC} \rangle = \frac{+4}{4} = +1. \quad (1.95)$$

Here a rigorous contradiction between the predictions of local-realistic theories and quantum mechanics has been disclosed. Since all experiments confirm the quantum predictions ([Bouwmeester et al., 1999, Zhao et al., 2004, Walther et al., 2005, Lu et al., 2007], [Leibfried et al., 2005], [Häffner et al., 2005]) local realism is refuted once again.

1.3.5 Loopholes

Up to date numerous experiments testing the EPR claim have been carried out. However, all experiments to date have shown a remarkable agreement with the predictions of quantum mechanics, giving very strong evidence that quantum mechanics cannot be reproduced by local realistic theories. However some researchers still question these experimental tests due to perceived *loopholes*, i.e, the detection loophole (not all particles are detected), and the locality loophole (the outcomes or settings of one measurement could influence the outcomes of the another measurement).

Detection loophole

In particular, a common problem for all the experiments seems to be the detection efficiency, given by the ratio between the number of detected events and the number of tested quantum systems. This is referred to as the detection loophole. The detection loophole arises from the following assumption: the sample over which the statistic is measured is fair, commonly known as *fair sampling assumption*. However, as pointed out by Clauser, Horne, Shimony, and Holt [Clauser et al., 1969]:” *in view of the difficulty of an experimental check, the assumption could be challenged by an advocate of hidden variable theories in case the outcome of the proposed experiment favours quantum mechanics*”. This indicates, that the fair sampling assumption is not trivial from the point of view of a local hidden variables theory. One could for instance postulate a variable that triggers the detector. Consequently a threshold efficiency $\eta_{\text{crit}} = 2(\sqrt{2}-1) \sim 0.83$ is required to close the detection loophole with maximally entangled states [Garg and Mermin, 1987, Larsson, 1998].

In an atomic cascade photons generally are not emitted in opposite direction, but for experimental convenience only photons propagation in $\pm z$ -direction are selected (see

Fig. 1.3(b)). This problem of weak correlation in direction was solved by a new type of source called parametric down conversion (which will be introduced later).

Since the first successful Bell experiment by Freedman and Clauser [Freedman and Clauser, 1972] implementations have been tested aiming to close the detection loophole [Rowe et al., 2001, Grangier, 2001].

Locality or "light-cone" loophole

To close the second famous loophole, which is called locality loophole, polarizers are required that can be independently reorientated at random times. Here the reorientation autocorrelation time has to be shorter than the space separation L/c between the polarizers. This assured that the settings of the local measurements are randomly chosen in space-like separated regions. Experimental implementations to close the locality loophole, by using time-varying analyzers, have been performed since the early 1980's [Aspect et al., 1982a, Weihs et al., 1998, Zeilinger, 1986, Aspect, 1999].

1.4 Non-Locality or Contextuality

Bell's original inequality is based on the joint assumptions of locality and realism. However it is possible to derive a Bell inequality without the need of locality, by introducing the concept of noncontextuality. Noncontextuality implies that the value of a dynamical variable is pre-defined and independent of the experimental context, i.e. of previous or simultaneous measurements of a commuting observable [Mermin, 1993]: "*...such a theory should assign to each observable $A, B, C...$ a numerical value $v(A), v(B), v(C)...$, so that if any observable is measured on a individual system the result of the measurement will be the corresponding value.*"

Noncontextuality is a more stringent demand than locality because it requires mutual independence of the results for commuting observables even if there is no spacelike separation [Simon et al., 2000]. Einstein-locality is a special case of this noncontextual hidden variable hypothesis. This more general class of hidden variable theories is characterized as noncontextual hidden variable theories. Local hidden variable theories are only a subset of this class of hidden variable theories.

A formulation of a Bell-like inequality derived without the assumption of locality using noncontextuality can be found for example in [Basu et al., 2001] or [Home and Sengupta, 1984]: Let A_1, A_2 and B_1, B_2 be two pairs of noncommuting dynamical variables pertaining to a spin-1/2 particle such that A_i ($i = 1, 2$) commute with B_j ($j = 1, 2$), where A_i and B_j belong to mutually disjoint Hilbert spaces corresponding to mutually commuting degrees of freedom (say, spin and position momentum). Each of A_1, A_2 and B_1, B_2 is assumed to be valued either $+1$ or -1 . If one considers the outcomes of joint measurements of four commuting pairs A_1B_1, A_1B_2, A_2B_1 , and A_2B_2 , the following equality holds:

$$A_1B_1 - A_1B_2 + A_2B_1 - A_2B_2 = \pm 2. \quad (1.96)$$

Taking the ensemble averages, it follows from Eq.(1.96):

$$|A_1B_1 - A_1B_2 + A_2B_1 - A_2B_2| \leq 2. \quad (1.97)$$

Thus Eq.(1.97) is a CHSH-Bell-like inequality, that can be viewed as a testable consequence of noncontextuality.

The single-neutron system is an optimal system for testing noncontextual hidden variable theories. Here entanglement is achieved between different degrees of freedom and not between different particles. Since the observables of one Hilbert spaces, describing a certain degree of freedom, commute with observables of a different Hilbert spaces, the single-neutron system is suitable for studying noncontextual hidden variable theories with multiple degrees of freedom.

1.5 Related Experiments

1.5.1 Celebrated CHSH-Bell experiments with photons

CHSH-Bell experiments with one-channel polarizers

After the CHSH paper [Clauser et al., 1969] was published in 1969 two groups started working on an experimental realization, one at Berkeley, and one at Harvard. After their conflicting results, a third experiment was carried out in College Station (Texas). All three experiments used a simplified experimental scheme, different from the ideal situation introduced in Sec.1.3.3, since one-channel polarizers were involved.

A mannerism of a one-channel polarizer is that it only transmits light polarized parallel to α (or β), with a typical transmittance of ~ 0.95 , but blocks the orthogonal one. Thus one can only detect the +1 results, and the coincidence measurements only yield the coincidence rates $N_{++}(\alpha, \beta)$. To recover the missing settings additional measurements have to be performed, with one or both polarizers removed. This orientation shall be denoted as ∞ . The relations between the measured coincidence rates $N_{++}(\alpha, \beta)$, $N_{++}(\alpha, \infty)$ and $N_{++}(\infty, \beta)$ and coincidence rates which are not measured :

$$\begin{aligned} N_{++}(\infty, \infty) &:= N(\infty, \infty) = N_{++}(\alpha, \beta) + N_{+-}(\alpha, \beta) + N_{-+}(\alpha, \beta) + N_{--}(\alpha, \beta) \\ N_{++}(\alpha, \infty) &:= N(\alpha, \infty) = N_{++}(\alpha, \beta) + N_{+-}(\alpha, \beta) \\ N_{++}(\infty, \beta) &:= N(\infty, \beta) = N_{++}(\alpha, \beta) + N_{-+}(\alpha, \beta) \end{aligned} \quad (1.98)$$

By plugging in the results from above into the polarization correlation coefficient from Eq.(1.82), combined with the inequalities defined in Eq.(1.79), one can eliminate all the quantities which are not measured, thereby obtaining the following CHSH-Bell inequality:

$$-1 \leq S' \leq 0, \quad (1.99)$$

where the quantity S is given by

$$S' = \frac{N(\alpha, \beta) - N(\alpha, \beta') + N(\alpha', \beta) + N(\alpha', \beta') - N(\alpha', \infty) - N(\infty, \beta)}{N(\infty, \infty)}. \quad (1.100)$$

In the Berkeley experiment [Freedman and Clauser, 1972], Freedman and Clauser built a source where calcium atoms were excited to highly lying states by ultraviolet radiation,

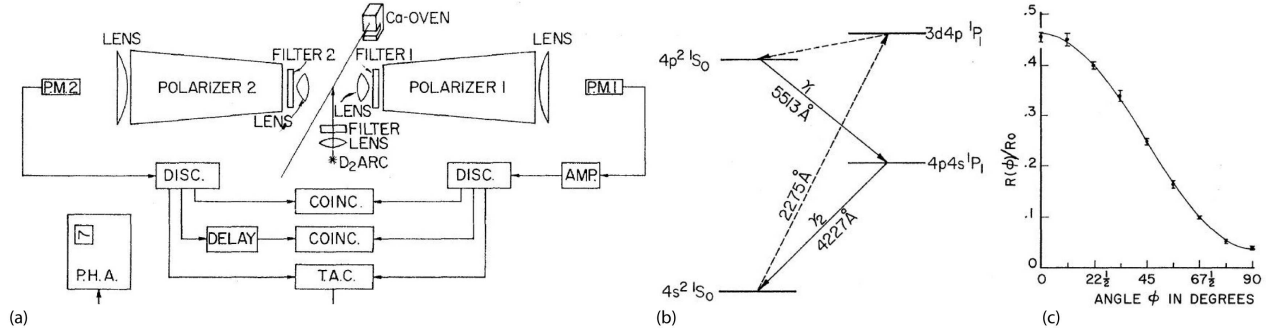


Figure 1.11: (a) Schematic diagram of measurement apparatus for counting coincidences in the experiment of Freedman and Clauser in Berkeley [Freedman and Clauser, 1972]. (b) level schema of calcium. (c) coincidence rate (divided by rate with polarizers removed), plotted versus the angle between the polarizers. The solid line represents predictions of quantum mechanics, including efficiency of polarizers and solid angle of photon emittance.

followed by a decay among the various desexcitation routes (see Fig. 1.11 (b) for details). The results were found in agreement with quantum mechanics, and a violation of the relevant Bell inequalities (1.99) was observed, due to final value of $S' = 0.050 \pm 0.008$. Measurement apparatus and results are summarized in Fig. 1.11.

At the same time, at Harvard, Holt and Pipkin [Pipkin, 1978] found a result in disagreement with quantum mechanics, and in agreement with Bell's Inequalities. They obtained a final value of $S' = -0.034 \pm 0.013$. Their source was based on $(9^1P_1 \rightarrow 7^3P_1 \rightarrow 6^3P_0)$ cascade of Mercury (isotope 200). Clauser subsequently repeated their experiment, but with Mercury 202. He found an agreement with Quantum Mechanics, and a significant violation of Bell's Inequality [Clauser, 1976]: $S' = 0.0385 \pm 0.0093$ (the result of Clausers measurements is shown in Fig. 1.12 (a))

In 1976, in Houston, Fry and Thompson [Fry and Thompson, 1976] built a much improved source of correlated photons, emitted in the $7^3S_1 \rightarrow 6^3P_1 \rightarrow 6^3S_0$ cascade of Mercury 200, different from the one used in Havard by Holt and Pipkin. The signal was several order of magnitude larger than in previous experiments, allowing them to collect the relevant data in a shorter time. Their result was in excellent agreement with quantum mechanics, and they found a violation of Bell's inequality by $S' = 0.046 \pm 0.014$. A plot of the results can be seen in Fig. 1.12 (b).

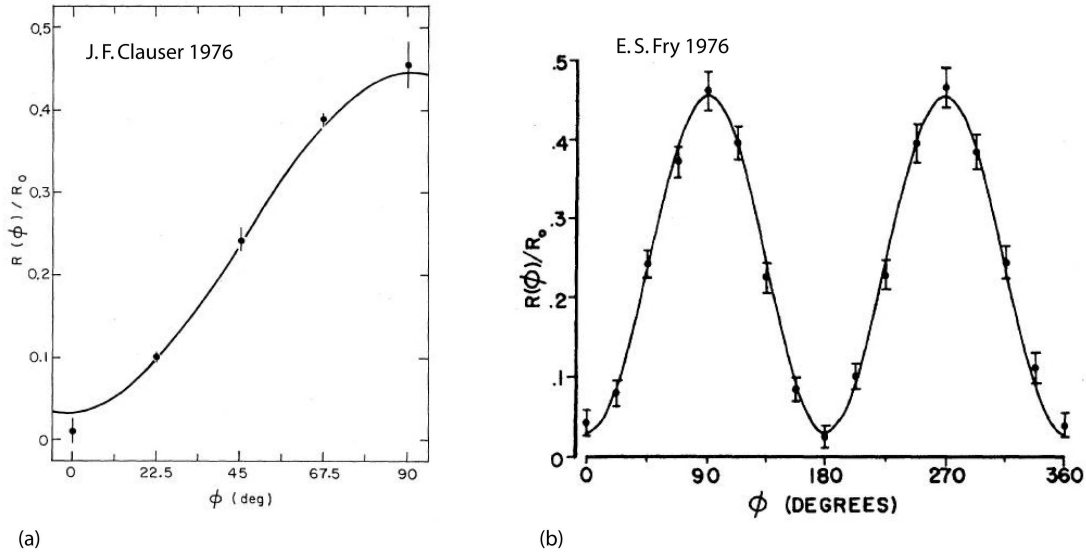


Figure 1.12: (a) Coincidence rate versus the angle between the polarizers in the experiment carried out by Clauser [Clauser, 1976] to confute the results of a similar measurement of Holt and Pipkin from Harvard. (b) Normalized polarization coincidences versus angle between the polarizers in the Fry experiment [Fry and Thompson, 1976]. This experiment was performed since the results of Clauser, Freedman in Berkeley and Holt, Pipkin in Havard contradicted each other. Finally a clear accordance with the predictions of quantum mechanics was bought to light.

A further experiment which should be mentioned at this point is a measurement carried out by A. Aspect and his co-workers in 1981 [Aspect et al., 1981]. A new developed high-efficiency source, emitting photons from an atomic cascade of calcium, allowed to achieve an excellent statistical accuracy. For the quantity S' they found $S' = 0.126 \pm 0.014$, violating the inequalities by 9 standard deviations.

CHSH-Bell experiments with two-channel polarizers

Using one-channel polarizers, the measurements of polarization are inherently incomplete, since when a photon pair has been emitted, if no count is obtained, there is no way to know if "it has been missed" by the detector or if it has been blocked by the polarizer (only the later case corresponds to a result). This is why further measurements have to

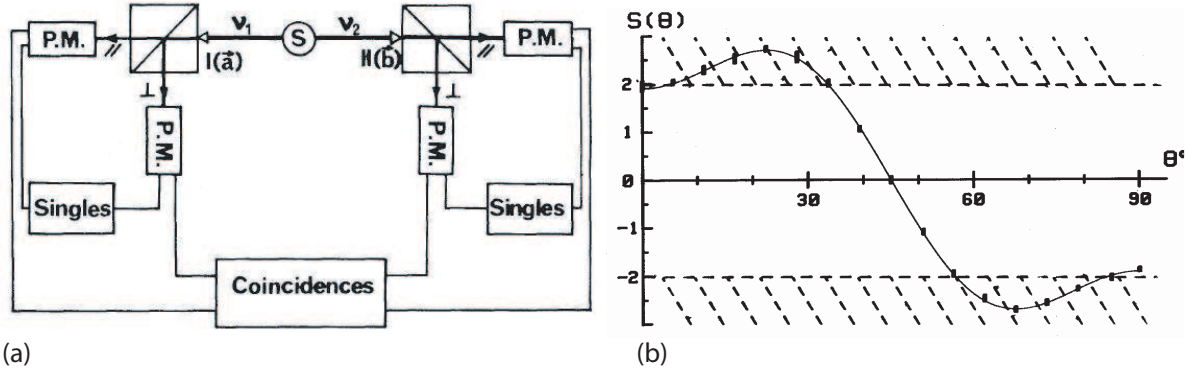


Figure 1.13: (a) Experimental apparatus for true dichotomic polarization measurement from [Aspect et al., 1982b]. (b) Quantity $S(\theta)$, tested by Bell's inequalities ($-2 \leq S \leq 2$), as a function of the relative angle θ between the polarizers. A clear violation of Bell's inequality can be seen (dash area), within a certain range of θ .

be carried out. With the use of two-channel polarizers experiments can be performed, that is much more similar to the ideal scheme of Fig 1.5. With polarizers orientations α and β the four coincidence rates $N_{\pm}(\alpha, \beta)$ can be measured within a single run, and plugged in Eq.(1.82). However a supporter of hidden variable theories could still argue one cannot be sure that the selected sample, remains the same when the orientations of the polarimeters are changed. A so called "fair sampling assumption" in which one assumes that the ensemble of detected pairs is a fair sample of the ensemble of all emitted pairs, has to be checked experimentally. The final result of this measurement, carried out by A. Aspect and his co-workers in 1982 [Aspect et al., 1982b], yields $S = 2.697 \pm 0.015$. This result is in excellent agreement with the predictions of quantum mechanics and violating the inequalities by more than 40 standard deviations! A schematic plot of the setup and the final S values, in respect to a change in the angle between the polarizers, is given in Fig. 1.13.

CHSH-Bell experiments with timing devices (closing locality loophole)

An ideal test of Bell's inequalities should involve the possibility of switching at random times the orientation of each polarizer. In their experimental modification in 1982

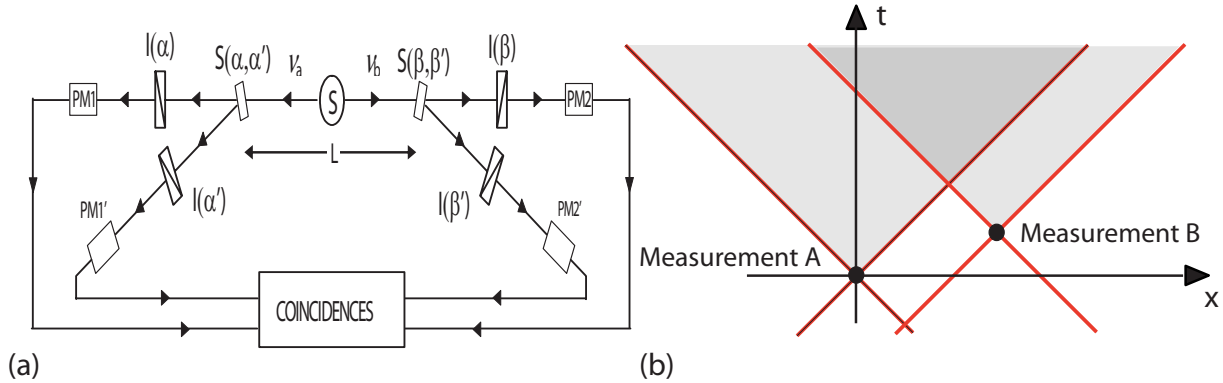


Figure 1.14: (a) Timing-experiment with optical switches $S(\alpha, \alpha')$ ($S(\beta, \beta')$), redirecting the incident light either to the polarizer in orientation $\alpha(\beta)$ or $\alpha'(\beta')$, used in [Aspect et al., 1982a]. (b) space-time diagram for space-like separated measurements.

[Aspect et al., 1982a] A. Aspect and his co-workers made use of optical switches. These devices are able to rapidly redirect the incident light either to the polarizer in orientation $\alpha(\beta)$, or to the polarizer in orientation $\alpha'(\beta')$ respectively). This procedure is equivalent to a switching of the directions of the polarizers. The distance L between the switches was chosen large enough (13 m) that the time of travel of a signal between the switches at the velocity of light (43 ns) was significantly larger than the delay between two switchings (about 10 ns). The modified scheme is shown on Fig. 1.14. Finally a value of $S' = 0.101 \pm 0.020$ was obtained.

CHSH-Bell experiments using parametric down-conversion (first step to close the detection loophole)

In the late 80s a new sources of pairs of correlated photons has been developed. With these sources, a pair of red photons is produced by parametric down conversion of a U.V. photon. Due to the phase matching condition in the non linear crystal used for this process, there is a strong correlation between the directions of emission of the two photons of a pair. By spatial selection with two diaphragms positioned in conjugate positions, one can in principle be sure to get the two photons of a pair. This is the main advantages compared to atomic radiative cascades, which produce photons only weakly

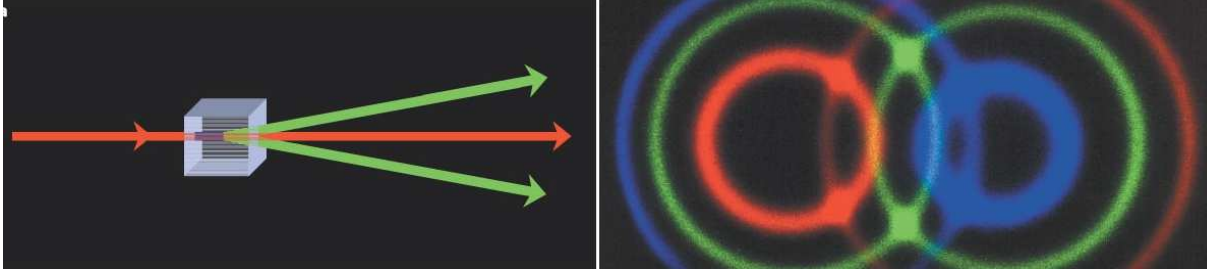


Figure 1.15: (a) An ultraviolet photon incident on a non linear crystal can split spontaneously into two photons. These photons are emitted on opposite sides of the pump beam along two cones. One photon is horizontal polarized, whereas the other of is polarized. (b) Photon pairs emitted along the intersections of the two cones are entangled in polarization.

correlated in direction (the coincidence rate may be more than one order of magnitude larger). The perfect correlation between the directions of emission, together with photon detectors with efficiency close to unity, is expected to offer the possibility to close the loophole related to the low detection efficiency (detection loophole). The principle of the parametric down-conversion is schematically illustrated in Fig 1.15.

This new source of entangled photon pairs has lead to a series of tests of Bells inequalities. All experiments up to today have confirmed the predictions of quantum mechanics. Clear violations of Bells inequalities, up to 100 standard deviations [Kwiat et al., 1995] have been found. Also an experiment where a clear violation of Bells inequalities has been observed with one leg of the apparatus made of 4 kilometers of optical fiber [Tapster et al., 1994]. More recently, EPR correlations have been observed with photons propagating in several tens of kilometers of commercial telecommunication fibers [Tittel et al., 1998].

Violation of Bells inequality under strict Einstein locality conditions

The first experiment that fully enforced Bell's requirement for strict relativistic separation between measurements, was performed at the University of Innsbruck in the 1998 [Weihs et al., 1998], by a group around A. Zeilinger. The necessary spacelike separation of the observations is achieved by sufficient physical distance between the measurement stations, by ultrafast and random setting of the analyzers, and by completely independent

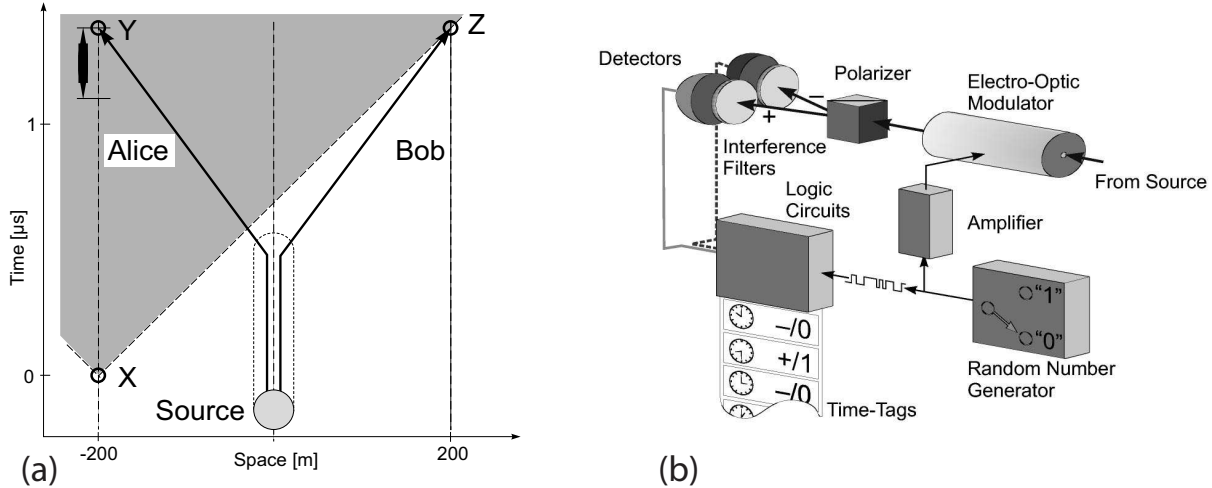


Figure 1.16: (a) Spacetime diagram of the Bell experiment under strict Einstein locality conditions from [Weihs et al., 1998]. Selecting a random analyzer direction, setting the analyzer, and finally detecting a photon constitute the measurement process. (b) One of the two observer stations. A random number generator is driving the electro-optic modulator. Silicon avalanche photodiodes are used as detectors.

data registration. In this particular experiment for the first time, any mutual influence between the two observations was excluded within the realism of Einstein locality. The two observers were spatially separated by 400 m across the Innsbruck University science campus, which in turn means that the individual measurements had to be shorter than $1.3 \mu\text{s}$. The source was provided by degenerate type-II parametric down-conversion, where a BBO (beta- BaB_2O_4) crystal with 400 mW of 351 nm light was pumped from an argon-ion laser. Afterwards the polarization entangled photon pairs were sent to the observers through optical fibers having a length of 500 meters. Each of the observers switched the direction of local polarization analysis with a transverse electro-optic modulator, before detecting the photons. However, an ultimate experiment should also have higher detection efficiency, which was in this experiment 5%. A graphical representation of the setup, as well as the corresponding spacetime diagram are given in Fig. 1.16.

With a visibility of 97 per cent a final value of $S = 2.73 \pm 0.02$ for 14 700 coincidence events collected in 10 seconds was achieved. This corresponds to a violation of the CHSH inequality of 30 standard deviations.

1.5.2 Three-photon GHZ entanglement

The first experimental test of quantum non-locality in three-photon Greenberger-Horne-Zeilinger entanglement was carried out by a group of A. Zeilinger in the year 1999 [Bouwmeester et al., 1999, Pan et al., 2000].

The corresponding entangled three-photon GHZ state is given by:

$$|\psi_{\text{GHZ}}^{ABC}\rangle = \frac{1}{\sqrt{2}}(|H^A, H^B, H^C\rangle + |V^A, V^B, V^C\rangle), \quad (1.101)$$

where H and V denote horizontal and vertical linear polarizations respectively. Considering measurements of linear polarization along directions H', V' rotated by 45° with respect to the original H, V directions, or of circular polarization L, R (left-handed, righthanded). These new polarizations can be expressed in terms of the original ones as already demonstrated in Sec. 1.3.4:

$$\begin{aligned} |H'\rangle &= \frac{1}{\sqrt{2}}(|H\rangle + |V\rangle) & |V'\rangle &= \frac{1}{\sqrt{2}}(|H\rangle - |V\rangle) \\ |R\rangle &= \frac{1}{\sqrt{2}}(|H\rangle + i|V\rangle) & |L\rangle &= \frac{1}{\sqrt{2}}(|H\rangle - i|V\rangle) \end{aligned} \quad (1.102)$$

Thus the GHZ state can be expressed in a $y^A y^B x^C$ -basis as

$$|\psi_{\text{GHZ}}^{ABC}\rangle = \frac{1}{2} \left(|R^A, L^B, H'^C\rangle + |L^A, R^B, H'^C\rangle + |R^A, R^B, V'^C\rangle + |L^A, L^B, V'^C\rangle \right). \quad (1.103)$$

As already discussed Sec. 1.3.4 Eq.(1.103) implies, first that any result obtained in any individual or in any two-photon joint measurement is maximally random. For example, photon A will exhibit polarization R or L with the same probability of $1/2$, or photons A and B will exhibit polarizations RL, LR, RR or LL with the same probability of $1/4$. Second, given any two results of measurements on any two photons, one can predict with certainty the result of the corresponding measurement performed on the third photon (e.g. photons A and B both exhibit right-handed R circular polarization, photon C will assuredly be V' polarized.) Consequently every one of the three $y^A y^B x^C$, $y^A x^B y^C$, and $x^A y^B y^C$ joint polarization measurements yields -1, according to quantum mechanics.

Assuming local realism, each photon carries elements of reality for both x and y polarization measurements. These elements of reality X_i with predefined values of $+1$ or

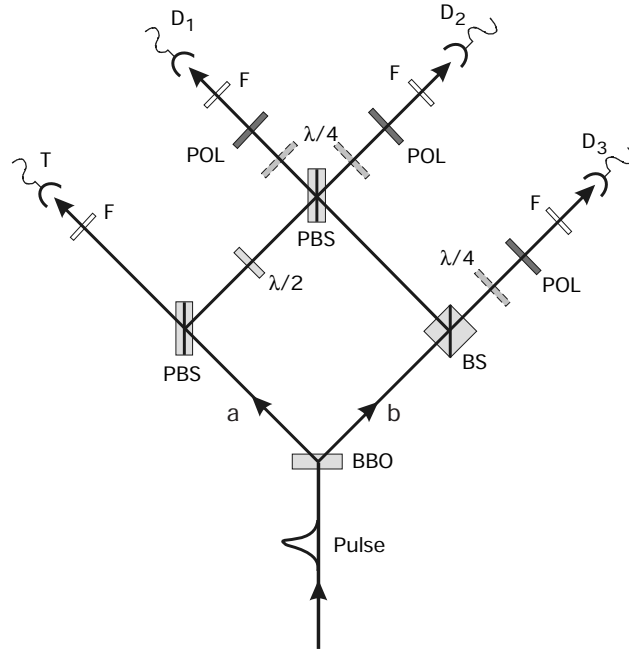


Figure 1.17: Experimental setup for 3 photon GHZ tests of quantum non-locality from [Bouwmeester et al., 1999]. Pairs of polarization-entangled photons (one photon H polarized and the other V) are generated by a short pulse of ultraviolet light. The photon registered at T is always H , thus its partner in b must be V . The photon reflected at the polarizing beam-splitter (PBS) in arm a is always V , being turned into equal superposition of V and H by the $\lambda/2$ plate. Its partner in arm b is H . If all four detectors register at the same time, the two photons in $D1$ and $D2$ must either both have been V, V and reflected by the last PBS or H, H and transmitted. The photon at $D3$ was therefore H or V , respectively. Both possibilities are made indistinguishable by having equal path lengths via a and b to $D1$ ($D2$). Polarizers oriented at 45° and $\lambda/4$ plates in front of the detectors allow measurement of linear H', V' (circular R, L) polarization.

-1 for H, V polarizations and Y_i also with values +1 or -1 for R, L polarization. For the combination of polarization measurements $Y^A Y^B X^C = -1$, $Y^A X^B Y^C = -1$ and $X^A Y^B Y^C = -1$, one can address values to each measurement X^i, Y^i , in order to reproduce the quantum predictions given above. Since $Y^i Y^i = 1$, one finds $X^A X^B X^C = (X^A Y^B Y^C)(Y^A X^B Y^C)(Y^A Y^B X^C)$, resulting in $X^A X^B X^C = 1$. Hence from a local realist point of view the only possible results for an xxx -experiment are $V'V'V'$, $H'H'V'$,

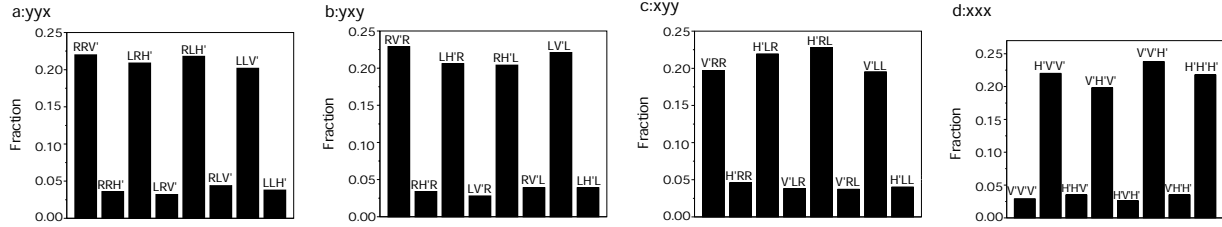


Figure 1.18: Outcomes of the joint polarization measurements carried out in [Bouwmeester et al., 1999]. a: yyx ; b: yxy ; c: xyy and d: xxx observed in the experiment. The experimental data show that the observed GHZ terms are in agreement with the predictions of quantum physics (tall bars) in a fraction of 0.85 ± 0.04 .

$H'V'H'$, and $V'H'H'$. As already demonstrated in Sec. 1.3.4 the prediction of quantum mechanics are the exact opposite: The GHZ-state, expressed in the xxx -basis reads

$$|\psi_{\text{GHZ}}^{ABC}\rangle = \frac{1}{2} \left(|H^A, H^B, H^C\rangle + |V^A, V^B, H^C\rangle + |H^A, V^B, V^C\rangle + |V^A, H^B, V^C\rangle \right), \quad (1.104)$$

with $x^A x^B x^C = +1$, unlike as calculated in the local realistic hypotheses.

A schematic sketch of the setup is given in Fig. 1.17. For each experiment there exist eight possible outcomes of which ideally four should never occur. However no experiment can be realized perfectly, hence these outcomes appear with some small probability (see Fig. 1.18). The fraction of correct events in the xxx -experiment can at most be equal to the sum of the fractions of all spurious events in the yyx , yxy , and xyy experiments (0.45 ± 0.03). However experimentally observed are such terms with a fraction of 0.87 ± 0.04 (Fig. 1.18(d)), which violates the local realistic expectation and accord with the predictions of quantum mechanics.

2

Neutron - Magnetic Field Interaction

2.1 Semiclassical Theory - Manipulating a Neutron Spin with a Classical Field

The motion of a free propagating neutron, interacting with magnetic $\vec{B}(\vec{r}, t)$ is described by a nonrelativistic Schrödinger equation, also referred to as *Pauli equation*, given by

$$\hat{H}\Psi(\vec{r}, t) = \left(-\frac{\hbar^2}{2m}\vec{\nabla}^2 - \mu\vec{\sigma}\vec{B}(\vec{r}, t) \right)\Psi(\vec{r}, t) = i\hbar\frac{\partial}{\partial t}\Psi(\vec{r}, t), \quad (2.1)$$

where m and μ are the mass ($1.6749 \cdot 10^{-27}$ kg) and the magnetic moment ($-1.913\mu_N$, with $\mu_N = 5.051 \cdot 10^{-27}$ J/T) of the neutron, respectively. $\vec{\sigma}$ is the Pauli vector operator. A solution is found by the two dimensional spinor wave function of the neutron, which is denoted as

$$\Psi(\vec{r}, t) = \begin{pmatrix} \Psi_+(\vec{r}, t) \\ \Psi_-(\vec{r}, t) \end{pmatrix} = \phi(\vec{r}, t)|S\rangle, \quad (2.2)$$

with spatial wave function $\phi(\vec{r}, t)$. The state vector for the spin eigenstates denoted as $|\uparrow\rangle$ and $|\downarrow\rangle$ is given by

$$|S\rangle = \cos\frac{\vartheta}{2}|\uparrow\rangle + e^{i\varphi}\sin\frac{\vartheta}{2}|\downarrow\rangle, \quad (2.3)$$

introducing polar angle ϑ and azimuthal angle φ , which can be represented on a *Bloch sphere* or *Poincaré sphere*, as shown in Fig 2.1. *Poincaré sphere* is usually used for the

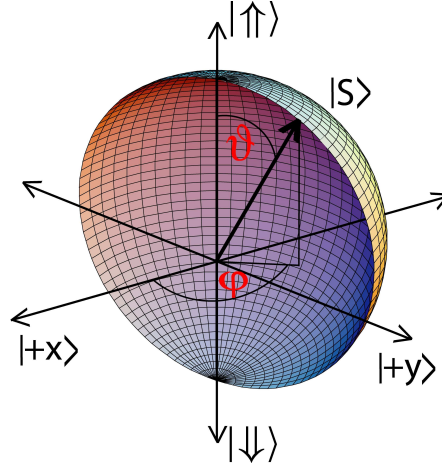


Figure 2.1: Bloch sphere description of arbitrary spin- $\frac{1}{2}$ state defined by polar angle ϑ and azimuthal angle φ .

representation of light polarization. In the field of general two-level systems the term *Bloch sphere* is conventionally used.

2.1.1 Larmor precession

The time evolution of the mean value of an operator \hat{A} is given by

$$\frac{d}{dt}\langle\hat{A}\rangle = \frac{d}{dt}\left(\langle\psi|\hat{A}|\psi\rangle\right) = \left(\frac{d}{dt}\langle\psi|\right)\hat{A}|\psi\rangle + \langle\psi|\left(\frac{d}{dt}\hat{A}\right)|\psi\rangle + \langle\psi|\hat{A}\left(\frac{d}{dt}|\psi\rangle\right). \quad (2.4)$$

With the derivative of $|\psi\rangle$ given by the *Schrödinger equation*

$$\hat{H}|\psi\rangle = i\hbar\frac{d}{dt}|\psi\rangle \rightarrow \frac{d}{dt}|\psi\rangle = \frac{1}{i\hbar}\hat{H}|\psi\rangle, \quad (2.5)$$

Eq.(2.4) now can be written in form of

$$\frac{d}{dt}\langle\hat{A}\rangle = \left\langle\frac{\partial\hat{A}}{\partial t}\right\rangle + \frac{1}{i\hbar}\langle[\hat{A}, \hat{H}]\rangle. \quad (2.6)$$

Eq.(2.6) is called *Heisenberg equation* and describes the time dependent evolution of an operator's expectation value. Obviously the operator corresponding to a conserved quantity must commute with the Hamiltonian \hat{H} :

$$\frac{d}{dt}\langle\hat{A}\rangle = \left\langle\frac{\partial}{\partial t}\hat{A}\right\rangle = 0 \rightarrow [\hat{A}, \hat{H}] = 0 \quad (2.7)$$

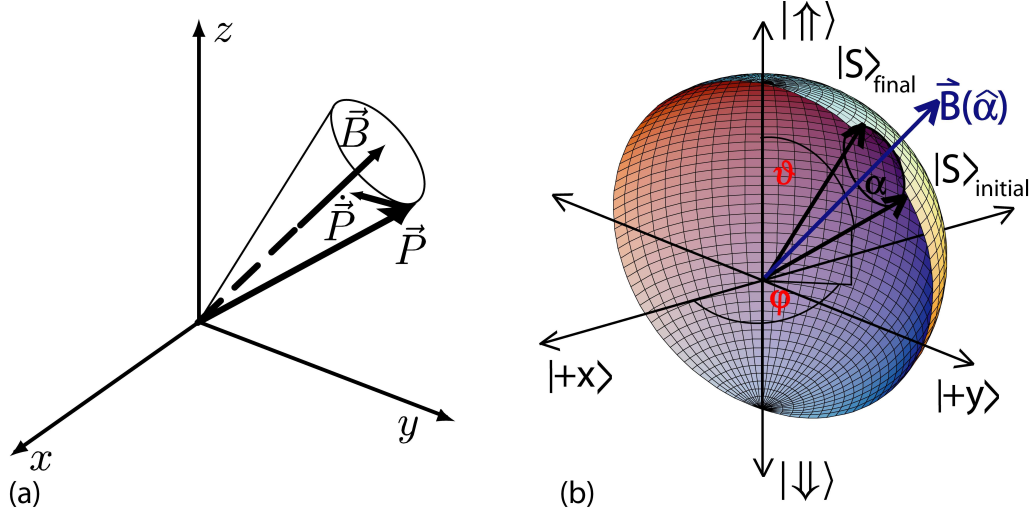


Figure 2.2: (a) Motion of polarization vector in real space: The polarization precesses about the direction of the external magnetic field, conserving the angle it embraces with the latter. (b) Bloch sphere description of precession of an arbitrary spin state defined by polar angle ϑ and azimuthal angle φ being transformed.

The trajectory of a free neutron in a magnetic field is described by the *Pauli equation*, given by Eq.(2.1), with statevector $|\Psi(t)\rangle$ corresponding to the two component spinor wavefunction defined in Eq.(2.46). In the static case the equation that has to be calculated is given by

$$\frac{d}{dt}\langle\vec{\sigma}\rangle = \frac{1}{i\hbar}\langle[\vec{\sigma}, \hat{H}]\rangle = \frac{\mu}{i\hbar}\langle[\vec{B} \cdot \vec{\sigma}, \vec{\sigma}]\rangle, \quad (2.8)$$

with

$$\frac{d}{dt}\langle\mu\vec{B}(t)\rangle = \mu\langle\frac{\partial}{\partial t}\vec{\sigma}\vec{B}\rangle + \frac{1}{i\hbar}\langle[\mu\vec{B}, \hat{H}(t)]\rangle \neq 0, \quad (2.9)$$

using

$$[\sigma_k, \sigma_l] = 2i \sum_{m=x,y,z} \epsilon_{klm} \sigma_m. \quad (2.10)$$

$[\vec{B} \cdot \vec{\sigma}, \sigma_j]$ can be expanded in a power series

$$[\vec{B} \cdot \vec{\sigma}, \sigma_j] = \sum_l [B_l \sigma_l, \sigma_j] = 2i \sum_k \sum_l \epsilon_{ljk} B_l \sigma_k = -2i(\vec{B} \times \vec{\sigma})_j, \quad (2.11)$$

this yields

$$\frac{d}{dt}\langle\vec{\sigma}\rangle = -\frac{2\mu}{\hbar}\langle\vec{B} \times \vec{\sigma}\rangle = -\gamma\langle\vec{B} \times \vec{\sigma}\rangle = -\gamma\vec{B} \times \langle\vec{\sigma}\rangle. \quad (2.12)$$

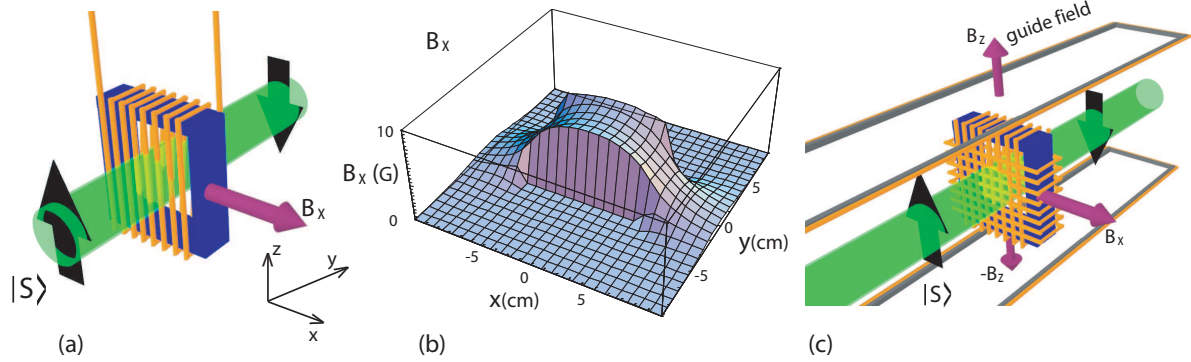


Figure 2.3: Direct Current (DC) spin-flipper (a) functional principle (b) Field configuration for highly non-adiabatic transition, required for Larmor precession (c) In practice a second coils ($-z$ direction), perpendicular to the original coil (x direction) is necessary to compensate the field component of the guide field ($+z$ direction) .

With the definition of the polarization vector, given by the expectation value of the Pauli spin operators

$$\langle \boldsymbol{\sigma} \rangle = \langle \Psi | \vec{\sigma} | \Psi \rangle = \vec{P}, \quad (2.13)$$

Eq.(2.12) can now be written in form of

$$\frac{d}{dt} \vec{P} = \vec{P} \times \gamma \vec{B}. \quad (2.14)$$

Eq.(2.14) is called *Bloch equation*. It describes so called *Larmor rotation*, which is the motion of the polarization vector \vec{P} in a homogeneous magnetic field \vec{B} , shown in Fig. (2.2) (a). Larmor precession within a coil, with a static magnetic field pointing in \hat{x} -direction, is utilized in Direct Current (DC) spin-rotators, as illustrated in Fig.2.3.

The spin rotation formalism in Hilbert space

An arbitrary rotation in three-dimensional space R^3 can be described by three *Euler rotations* by angles α, β, γ about the \hat{x}, \hat{y} and \hat{z} -axis. Each rotation is thereby represented a rotation matrix R . The sequential rotations are equivalent to a single rotation about an appropriate axis $\vec{\phi} = \phi \hat{\phi}$ by an angle ϕ . The transformation rotates the physical system according to

$$\vec{r}' = \hat{R}_z(\varphi) \vec{r}. \quad (2.15)$$

What is the transformation of the quantum-mechanical states that corresponds to the three-dimensional spatial rotation of the physical system performed in real space? A transformation that accounts for the vector property of a state vector in the two-dimensional Hilbert space \mathcal{H}^2 of spin is required.

A general rotation $R(\theta, \vartheta, \varphi)$ is given by

$$\hat{R}(\theta, \vartheta, \varphi) = \hat{R}_x(\theta)\hat{R}_y(\vartheta)\hat{R}_z(\varphi). \quad (2.16)$$

The transformation of a scalar $\phi(\vec{r})$ can be written in form of

$$\phi'(\vec{r}') = \phi(\vec{r}) \quad \text{or} \quad \phi'(\vec{r}) = \phi(R^{-1}\vec{r}), \quad (2.17)$$

with

$$\vec{r}' = R\vec{r}. \quad (2.18)$$

Due to the state vector representation of a quantum-mechanical system, such as neutron spin, the transformation properties of vectors have to be considered. For a rotation of a state vector in Hilbert space \mathcal{H}^2 an operator $\hat{\mathcal{R}}$ is introduced as follows:

$$|\vec{r}'\rangle = \hat{\mathcal{R}}|\vec{r}\rangle \quad (2.19)$$

Since the rotation is a reversible procedure $\hat{\mathcal{R}}$ has to be unitary.

$$\hat{\mathcal{R}}\hat{\mathcal{R}}^\dagger = \hat{\mathcal{R}}^\dagger\hat{\mathcal{R}} = \mathbb{1} \quad \text{and} \quad \hat{\mathcal{R}}^\dagger = \hat{\mathcal{R}}^{-1}. \quad (2.20)$$

In order to find a transformation for a wavefunction ψ in the form

$$\psi'(\vec{r}) = \hat{\mathcal{R}}\psi(\vec{r}) = \psi(\hat{R}^{-1}\vec{r}), \quad (2.21)$$

an infinitesimal rotation about \hat{z} axis is performed. Using $\hat{R}_z^{-1}(\varphi) = \hat{R}_z(-\varphi)$, and since for a small φ the trigonometric function can be approximated as $\cos(\varphi) = 1$ and $\sin(\varphi) = \varphi$, one obtains for the coordinates in three-dimensional space

$$\hat{R}_z^{-1}(\varphi) = \begin{pmatrix} 1 & \varphi & 0 \\ -\varphi & 1 & 0 \\ 0 & 0 & 1 \end{pmatrix} \begin{pmatrix} x \\ y \\ z \end{pmatrix} = \begin{pmatrix} x + \varphi y \\ -\varphi x + y \\ z \end{pmatrix}. \quad (2.22)$$

Consequently the wavefunction is denoted as

$$\psi'(x, y, z) = \psi(x + \varphi y, y - \varphi x, z) = \psi(x, y, z) + \frac{\partial \psi}{\partial x}(\varphi y) + \frac{\partial \psi}{\partial y}(-\varphi x)$$

$$= \psi(x, y, z) + \varphi \left(y \frac{\partial}{\partial x} - x \frac{\partial}{\partial y} \right) \psi(x, y, z). \quad (2.23)$$

Since $(y \frac{\partial}{\partial x} - x \frac{\partial}{\partial y})$ can be identified with $-\frac{i}{\hbar} \mathcal{L}_z$, since

$$\vec{\mathcal{L}} = \vec{r} \times \vec{p} = i\hbar \begin{pmatrix} z \frac{\partial}{\partial y} - y \frac{\partial}{\partial z} \\ x \frac{\partial}{\partial z} - z \frac{\partial}{\partial x} \\ y \frac{\partial}{\partial x} - x \frac{\partial}{\partial y} \end{pmatrix}, \quad (2.24)$$

$\psi'(\vec{r})$ can be written as

$$\psi'(\vec{r}) = \left(1 - \frac{i}{\hbar} \varphi \mathcal{L}_z \right) \psi(\vec{r}). \quad (2.25)$$

Or for an arbitrary orientation of the rotation axis given by $\vec{\varphi} = \varphi \hat{\varphi}$:

$$\psi'(\vec{r}) = \left(1 - \frac{i}{\hbar} \mathcal{L} \vec{\varphi} \right) \psi(\vec{r}) \quad (2.26)$$

For a finite rotation performed by the operator $\mathcal{U}(\alpha)$, with $\alpha = n \cdot \varphi$, the operator defined in Eq.(2.22) has to be applied n times, which because of

$$\lim_{n \rightarrow \infty} \left(1 + \frac{1}{n} \right)^n = e$$

$$\lim_{n \rightarrow \infty} \left(1 + \frac{a}{n} \right)^{\frac{n}{a}} = \left(\lim_{n \rightarrow \infty} \left(1 + \frac{a}{n} \right)^n \right)^{\frac{1}{a}} = e, \quad (2.27)$$

leads to

$$\hat{\mathcal{U}}(\alpha) = \lim_{n \rightarrow \infty} \left(\mathbb{1} - \frac{i}{\hbar} \vec{\mathcal{L}} \hat{\alpha} \frac{\alpha}{n} \right)^n = \exp \left(- \frac{i}{\hbar} \vec{\mathcal{L}} \vec{\alpha} \right). \quad (2.28)$$

Using $\vec{\mathcal{L}} \equiv \vec{S} = \frac{\hbar}{2} \vec{\sigma} \hat{\mathcal{U}}(\vec{\alpha})$ can finally be written in the form

$$\hat{\mathcal{U}}(\vec{\alpha}) = \exp \left(- i \frac{\vec{\sigma} \vec{\alpha}}{2} \right), \quad (2.29)$$

where $\vec{\sigma}$ is the Pauli spin operator, $\hat{\alpha}$ is the unit vector and α is the angel of rotation given by the Larmor precession defining the rotation axis $\vec{\alpha} = \alpha \hat{\alpha}$. Another representation of the unitary operator $\hat{\mathcal{U}}(\vec{\alpha})$ is given by

$$\hat{\mathcal{U}}(\vec{\alpha}) = \mathbb{1} \cos \left(\frac{\alpha}{2} \right) - i \vec{\sigma} \hat{\alpha} \sin \left(\frac{\alpha}{2} \right). \quad (2.30)$$

Since

$$e^{-\frac{1}{2}\vec{\sigma}\vec{\alpha}} = \sum_{k=0}^{\infty} \frac{1}{k!} \left(-i \frac{\vec{\sigma}\vec{\alpha}}{2} \right)^k = \sum_{k=0}^{\infty} \frac{1}{k!} \left(\frac{-i\alpha}{2} \right)^k (\vec{\sigma}\hat{\alpha})^k, \quad (2.31)$$

the sum can be split in a part with even and one with odd indices

$$e^{-\frac{1}{2}\vec{\sigma}\vec{\alpha}} = \sum_{k=0}^{\infty} \frac{1}{(2k)!} \left(\frac{-i\alpha}{2} \right)^{2k} (\vec{\sigma}\hat{\alpha})^{2k} + \sum_{k=0}^{\infty} \frac{1}{(2k+1)!} \left(\frac{-i\alpha}{2} \right)^{2k+1} (\vec{\sigma}\hat{\alpha})^{2k+1}, \quad (2.32)$$

using

$$(\vec{\sigma}\hat{\alpha})^2 = \sigma_i \alpha_i \sigma_j \alpha_j = \sigma_i \sigma_j \alpha_i \alpha_j = (\delta_{ij} \mathbb{1} + i \epsilon_{ijk} \sigma_k) \alpha_i \alpha_j = \delta_{ij} \alpha_i \alpha_j \mathbb{1} = \hat{\alpha}^2 \mathbb{1} = \mathbb{1} \quad (2.33)$$

this leads to

$$(\vec{\sigma}\hat{\alpha})^{2k} = \mathbb{1}, \quad (2.34)$$

and

$$(\vec{\sigma}\hat{\alpha})^{2k+1} = (\vec{\sigma}\hat{\alpha}). \quad (2.35)$$

Combined with Eq.(2.33) one obtains

$$\begin{aligned} e^{-\frac{1}{2}\vec{\sigma}\vec{\alpha}} &= \mathbb{1} \sum_{k=0}^{\infty} \frac{1}{(2k)!} \left(\frac{-i\alpha}{2} \right)^{2k} + (\vec{\sigma}\hat{\alpha}) \sum_{k=0}^{\infty} \frac{1}{(2k+1)!} \left(\frac{-i\alpha}{2} \right)^{2k+1} \\ &= \mathbb{1} \sum_{k=0}^{\infty} \frac{1}{(2k)!} \left(\frac{i\alpha}{2} \right)^{2k} - i(\vec{\sigma}\hat{\alpha}) \sum_{k=0}^{\infty} \frac{1}{(2k+1)!} i^{2k} \left(\frac{\alpha}{2} \right)^{2k+1} \\ &= \mathbb{1} \cos \left(\frac{\alpha}{2} \right) - i \vec{\sigma}\hat{\alpha} \sin \left(\frac{\alpha}{2} \right). \end{aligned} \quad (2.36)$$

To sum up: Neutron spin rotations by virtue of a magnetic field are described by the unitary operator $\hat{U}(\vec{\alpha})$ where $\vec{\sigma}$ is the Pauli spin operator and $\vec{\alpha} = \alpha \hat{\alpha}$ is the rotation vector. The angle of rotation α is given by the Larmor precession angle around the magnetic field (see Fig. (2.2) (b)).

2.1.2 The time-dependence of magnetic fields

In a purely **time dependent** magnetic field ($\vec{B} = \vec{B}(t)$) the total energy of a neutron is not a conserved quantity

$$\frac{d}{dt} \langle \hat{H}(t) \rangle = \left\langle \frac{\partial \hat{H}(t)}{\partial t} \right\rangle \neq 0. \quad (2.37)$$

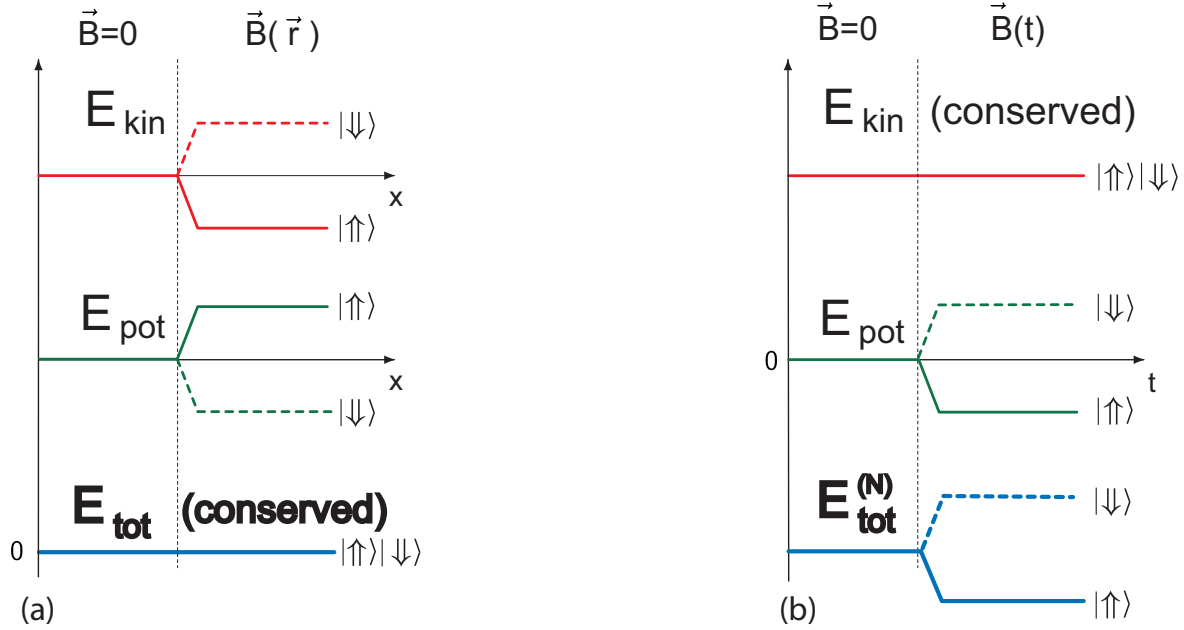


Figure 2.4: Potential, kinetic and total neutron energies upon application of magnetic fields of different types. (a): stationary (time-independent) magnetic field. Here the total energy remains unchanged, potential and kinetic energy are altered oppositely. (b): purely time-dependent magnetic field. Total and potential energy are changed, the kinetic energy remains constant.

Energy can be exchanged with the magnetic field via photon interaction. However the momentum is conserved

$$[\vec{p}, \hat{H}] = [i\hbar\vec{\nabla}, -\frac{\hbar^2}{2m}\vec{\nabla}^2 - \mu\vec{\sigma} \cdot \vec{B}] = i\hbar\mu\vec{\sigma}[\vec{\nabla}, \vec{B}] = 0, \quad (2.38)$$

since $\vec{\nabla}\vec{B}(t) = 0$ due to the fact that $B(t)$ is purely time dependent. Therefore the change in the total energy must originate from the potential energy

$$[-\vec{\mu} \cdot \vec{B}, \hat{H}] = [-\mu\vec{\sigma} \cdot \vec{B}, -\frac{\hbar^2}{2m}\vec{\nabla}^2 - \mu\vec{\sigma} \cdot \vec{B}] = \frac{\hbar\mu\vec{\sigma}}{2m}[\vec{B}, \vec{\nabla}^2] \neq 0. \quad (2.39)$$

A diagram of the kinetic, potential and total energy is shown in Fig. 2.4 (a). For a magnetic field $\vec{B} = B_z$, pointing in z -direction a solution of the Schrödinger equation, defined in Eq.(2.1), where according to Eq.(2.38) the spatial part of the wavefunction remains

unchanged, is given by

$$\Psi(y, t) = \phi(\vec{r}, t) (e^{i\mu\vec{B}_z t/\hbar} | \uparrow \rangle + e^{-i\mu\vec{B}_z t/\hbar} | \downarrow \rangle), \quad (2.40)$$

with $E_0 = \hbar\omega_0$ and

$$\phi(\vec{r}, t) = \frac{1}{(2\hbar)^{3/2}} \int a(\vec{k}) e^{i(\vec{k}\vec{r} - \omega_0(\vec{k})t)}, \quad (2.41)$$

where the amplitude $a(\vec{k})$ contains the coefficients of the linear superposition of the plane wave solutions of Eq.(2.1). The expectation value of x -component of the spin $\langle \vec{\sigma}_x \rangle$ yields

$$\langle \vec{\sigma}_x \rangle = P_x = \cos\left(\frac{2\mu B}{\hbar}t\right), \quad (2.42)$$

which is exactly the equation of the motion of the polarization with the Larmor frequency as defined in Eq.(2.14).

On the other hand in a **stationary** magnetic field ($\vec{B} = \vec{B}(\vec{r})$) the total energy of a neutron is indeed a conserved quantity since

$$\frac{\partial \hat{H}}{\partial t} = 0 \rightarrow \frac{d}{dt} \langle \hat{H} \rangle \equiv \frac{dE}{dt} = 0. \quad (2.43)$$

But one has to keep in mind that now neither the momentum nor the potential (*Zeeman magnetic energy*), written as $-\vec{\mu} \cdot \vec{B} = -\mu\vec{\sigma} \cdot \vec{B}$ is a conserved quantity due to

$$[\vec{p}, \hat{H}] = [i\hbar\vec{\nabla}, -\frac{\hbar^2}{2m}\vec{\nabla}^2 - \mu\vec{\sigma} \cdot \vec{B}] = i\hbar\mu\vec{\sigma}[\vec{\nabla}, \vec{B}] \neq 0 \quad (2.44)$$

$$[-\vec{\mu} \cdot \vec{B}, \hat{H}] = [-\mu\vec{\sigma} \cdot \vec{B}, -\frac{\hbar^2}{2m}\vec{\nabla}^2 - \mu\vec{\sigma} \cdot \vec{B}] = \frac{\hbar\mu\vec{\sigma}}{2m}[\vec{B}, \vec{\nabla}^2] \neq 0, \quad (2.45)$$

which is depicted in Fig. 2.4 (b).

In case of a neutron propagating in $+y$ -direction, with a polarization in arbitrary direction, and a static magnetic field with a field gradient parallel to its propagation direction (with $\vec{B}(y) = 0, \forall y > 0$ and $\vec{B}(y) = B_0 \cdot \vec{e}_z = B_z(y), \forall y > 0$) the usual *Zeeman splitting* within $\vec{B}(y)$ leads to following solutions of the Pauli equation:

$$\Psi(y, t) = \phi_+(y, t) e^{i\mu\vec{B}_z(y)t/\hbar} | \uparrow \rangle + \phi_-(y, t) e^{-i\mu\vec{B}_z(y)t/\hbar} | \downarrow \rangle, \quad (2.46)$$

where $| \uparrow \rangle$ and $| \downarrow \rangle$ denote the spin-up and spin-down eigenstates referring to a quantization axis along the static magnetic field (i.e. \vec{e}_z), with a linear superposition of plane waves with amplitudes $a_{\pm}(k \mp \Delta k)$

$$\phi(y, t)_{\pm} = \int a_{\pm}(k \mp \Delta k) e^{i((k \mp \Delta k) \cdot y - \omega(k)t)}, \quad (2.47)$$

where k is the momentum of the free particle and

$$k_{\pm} \simeq k \mp \frac{m|\mu|\vec{B}_z(y)}{(\hbar^2 k)} = k \mp \Delta k, \quad (2.48)$$

where Δk is the field-induced momentum shift. Again the expectation value of the spin $\langle \vec{\sigma} \rangle$ is calculated which yields

$$\begin{aligned} \langle \vec{\sigma}_x \rangle &= P_x = \int (a_+^*(k - \Delta k)a_-(k + \Delta k)e^{-2i\Delta ky} + a_+(k - \Delta k)a_-^*(k + \Delta k)e^{-2i\Delta ky}) dk \\ \langle \vec{\sigma}_y \rangle &= P_y = \int (a_+^*(k - \Delta k)a_-(k + \Delta k)e^{-2i\Delta ky} - a_+(k - \Delta k)a_-^*(k + \Delta k)e^{-2i\Delta ky}) dk \\ \langle \vec{\sigma}_z \rangle &= P_z = \int (|a_+(k)|^2 - |a_-(k)|^2) dk, \end{aligned} \quad (2.49)$$

which can be rewritten as

$$\begin{aligned} \langle \vec{\sigma}_x \rangle &= P_x = \int f(k) \sin \theta(k) \cos \phi(k, y) dk \\ \langle \vec{\sigma}_y \rangle &= P_y = \int f(k) \sin \theta(k) \sin \phi(k, y) dk \\ \langle \vec{\sigma}_z \rangle &= P_z = \int f(k) \cos \theta(k), \end{aligned} \quad (2.50)$$

with

$$\begin{aligned} f(k) &= |a_+(k)|^2 + |a_-(k)|^2, & \text{where } |a_{\pm}(k \mp \Delta k)| &\simeq |a_{\pm}(k)| \\ \sin \theta(k) &= \frac{2|a_+(k)||a_-(k)|}{f(k)} \\ \phi(k, y) &= 2y\Delta k + \phi_0 \frac{a_+^* a_-}{|a_+(k)||a_-(k)|}. \end{aligned} \quad (2.51)$$

As seen from this representation the polarization precesses about the x -axis

$$\phi(y) = \frac{2|\mu|B_z(y)}{\hbar} \frac{m}{\hbar k_0} y + \phi_0, \quad (2.52)$$

since v_0 is given by $v_0 = m/(\hbar k_0)$, it becomes evident, that the frequency of the rotation, within the rest frame of the neutron, equals the Larmor frequency. The divergency of the wavepacket, caused by the acceleration of the spin-down component (and the deceleration of the spin-up component), is referred to as *longitudinal Stern-Gerlach effect*.

At this point it should be mentioned that Eq.(2.47) describes an entangled state (when introducing state vectors for the momentum space) which reads

$$|\Psi\rangle = \cos \frac{\vartheta}{2} |k_+\rangle | \uparrow \rangle + e^{i\varphi} \sin \frac{\vartheta}{2} |k_-\rangle | \downarrow \rangle, \quad (2.53)$$

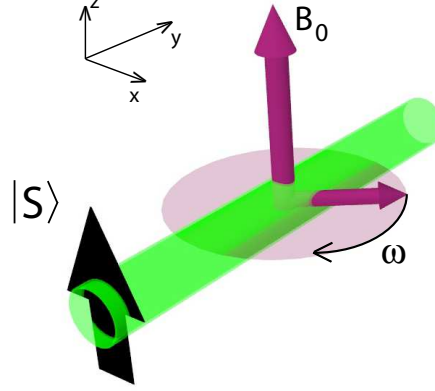


Figure 2.5: Combination of rotating and static magnetic field in spin flip configuration.

where $|k_{\pm}\rangle$ are the momentum eigenstates within the field $B_z(y)$, this topic will be discussed in more detail in Section 4.3.

Next a combination of a **rotating** (radio-frequency (RF)) and a **static** magnetic field, in a configuration known from nuclear magnetic resonance (NMR), is analyzed, which is illustrated in Fig. 2.5. For magnetic field in form of

$$\vec{B}(t) = \begin{pmatrix} B_1 \cos(\omega t) \\ B_1 \sin(\omega t) \\ B_0 \end{pmatrix}, \quad (2.54)$$

the *Pauli equation* for the spinor wavefunction is given by

$$i\hbar \frac{\partial}{\partial t} \Psi(x, t) = \left(-\frac{\hbar^2}{2m} \frac{\partial}{\partial x^2} - \mu \sigma_x B_1 \cos(\omega t) - \mu \sigma_y B_1 \sin(\omega t) - \mu \sigma_z B_0 \right) \Psi(x, t), \quad (2.55)$$

which is solved with a separation ansatz denoted as

$$\Psi(x, t) = \phi(x) \chi(t) \equiv \phi(x) \begin{pmatrix} \chi_1(t) \\ \chi_2(t) \end{pmatrix}. \quad (2.56)$$

This yields

$$i\hbar \frac{1}{\chi(t)} \frac{\partial}{\partial t} \chi(t) + \left(\mu B_1 (\sigma_x \cos(\omega t) + \sigma_y \sin(\omega t)) + \mu B_0 \sigma_z \right) = -\frac{\hbar^2}{2m} \frac{1}{\phi(x)} \frac{\partial^2}{\partial x^2} \phi(x) \equiv C. \quad (2.57)$$

Again both sides must be equal to a constant given by C , since the left side is only time depending and the right side only space dependent.

The right side (only depending on the coordinate x), given by

$$\left(\frac{\partial^2}{\partial x^2} + \frac{2m}{\hbar^2}C\right)\phi(x) = 0, \quad (2.58)$$

can easily be solved by the following solution:

$$\phi(x) = A \exp\left(i\sqrt{\frac{2m}{\hbar^2}Cx}\right) + B \exp\left(-i\sqrt{\frac{2m}{\hbar^2}Cx}\right) \quad (2.59)$$

with

$$A = \frac{1}{\sqrt{2\pi}}, B = 0, C = \frac{\hbar^2 k^2}{2m} \rightarrow \phi(x) = \frac{1}{\sqrt{2\pi}} e^{ikx}. \quad (2.60)$$

However the spinor part remains more complex:

$$i\hbar \frac{1}{\chi(t)} \frac{\partial}{\partial t} \chi(t) + \left(\mu B_1(\sigma_x \cos(\omega t) + \sigma_y \sin(\omega t)) + \mu B_0 \sigma_z\right) = \frac{\hbar^2 k^2}{2m} \quad (2.61)$$

With the substitution

$$\chi(t) = \zeta(t) \exp\left(-i\frac{\hbar k^2}{2m}t\right) \quad (2.62)$$

Eq.(2.61) can be transformed to

$$i\hbar \frac{\partial}{\partial t} \zeta(t) + \left(\mu B_1(\sigma_x \cos(\omega t) + \sigma_y \sin(\omega t)) + \mu B_0 \sigma_z\right) \zeta(t) = 0. \quad (2.63)$$

Now $\hat{\sigma}_+$ and $\hat{\sigma}_-$ are defined as follows

$$\begin{aligned} \hat{\sigma}_+ &\equiv \sigma_x + i\sigma_y \\ \hat{\sigma}_- &\equiv \sigma_x - i\sigma_y, \end{aligned} \quad (2.64)$$

which leads to

$$i\hbar \frac{\partial}{\partial t} \zeta(t) + \left(\frac{\mu B_1}{2}(\sigma_+ \exp(-i\omega t) + \sigma_- \exp(i\omega t)) + \mu B_0 \sigma_z\right) \zeta(t) = 0. \quad (2.65)$$

At this point a unitary transformation $\hat{U}(t)$ is introduced which transforms the equation in a system rotating around the z -axis with a frequency of the magnetic field

$$\zeta(t) = \hat{U}(t) \zeta_r(t) = \exp\left(-i\frac{\omega t}{2}\sigma_z\right) \zeta_r(t) \rightarrow \quad (2.66)$$

$$\begin{aligned} &\frac{\hbar\omega}{2}\sigma_z \exp\left(-i\frac{\omega t}{2}\sigma_z\right) \zeta_r(t) + i\hbar \exp\left(-i\frac{\omega t}{2}\sigma_z\right) \frac{\partial}{\partial t} \zeta_r(t) \\ &+ \left\{ \frac{\mu B_1}{2} \left(\hat{\sigma}_+ \exp(-i\omega t) \exp\left(-i\frac{\omega t}{2}\sigma_z\right) + \hat{\sigma}_- \exp(i\omega t) \exp\left(-i\frac{\omega t}{2}\sigma_z\right) \right) + \right. \\ &\left. \mu B_0 \exp\left(-i\frac{\omega t}{2}\sigma_z\right) \right\} \zeta_r(t) = 0 \end{aligned} \quad (2.67)$$

When the equation is multiplied with $\exp\left(i\frac{\omega t}{2}\sigma_z\right)$ and the exponential function is expanded in a power series with $\frac{\omega t}{2} = \alpha$

$$e^{i\alpha\sigma_z} = \mathbb{1} + i\alpha\sigma_z + \frac{(i\alpha)^2}{2!}\sigma_z^2 + \frac{(i\alpha)^3}{3!}\sigma_z^3 + \dots \quad (2.68)$$

with $\sigma_i^2 = \mathbb{1}$

$$e^{i\alpha\sigma_z} = \mathbb{1} + i\alpha\sigma_z + \frac{(i\alpha)^2}{2!}\mathbb{1} + \frac{(i\alpha)^3}{3!}\sigma_z + \dots = \begin{pmatrix} e^{i\alpha} & 0 \\ 0 & e^{-i\alpha} \end{pmatrix}. \quad (2.69)$$

When Eq.(2.67) is multiplied with $\exp\left(i\frac{\omega t}{2}\sigma_z\right)$ the following term appears

$$\begin{aligned} & \exp\left(i\frac{\omega t}{2}\sigma_z\right)\sigma_z \exp\left(-i\frac{\omega t}{2}\sigma_z\right) \\ &= \begin{pmatrix} e^{i\alpha} & 0 \\ 0 & e^{-i\alpha} \end{pmatrix} \begin{pmatrix} 1 & 0 \\ 0 & -1 \end{pmatrix} \begin{pmatrix} e^{-i\alpha} & 0 \\ 0 & e^{i\alpha} \end{pmatrix} = \begin{pmatrix} 1 & 0 \\ 0 & -1 \end{pmatrix} = \sigma_z \end{aligned} \quad (2.70)$$

and in the same manner

$$\exp\left(i\frac{\omega t}{2}\sigma_z\right)\hat{\sigma}_\pm \exp\left(-i\frac{\omega t}{2}\sigma_z\right) = \exp\left(\pm i\omega t\right)\hat{\sigma}_\pm. \quad (2.71)$$

This leads to the following simpler equation

$$i\hbar\frac{\partial}{\partial t}\zeta_r(t) = \left(-\frac{\hbar\omega}{2}\sigma_z - \frac{\mu B_1}{2}\underbrace{(\hat{\sigma}_+ + \hat{\sigma}_-)}_{2\sigma_x} - \mu B_0\sigma_z\right)\zeta_r(t). \quad (2.72)$$

Introducing the definitions $\omega_0 = -\frac{2\mu}{\hbar} = -\gamma B_0$ and $\omega_1 = -\gamma B_1$ the equation is given by

$$\frac{1}{\zeta_r(t)}\frac{\partial}{\partial t}\zeta_r(t) = -\frac{i}{2}\left((\omega_0 - \omega)\sigma_z + \omega_1\sigma_x\right). \quad (2.73)$$

Integration of Eq.(2.73) leads to the following equation

$$\ln \zeta_r(t) - \ln \zeta_r(0) = -\frac{i}{2}\left((\omega_0 - \omega)\sigma_z + \omega_1\sigma_x\right)t. \quad (2.74)$$

Since $\zeta_r(0) = \zeta(0)$ a solution is calculated as

$$\zeta_r(t) = \zeta(0)\left(-\frac{i}{2}\left((\omega_0 - \omega)\sigma_z + \omega_1\sigma_x\right)t\right), \quad (2.75)$$

which, in the non rotating system becomes

$$\zeta(t) = \zeta(0)\exp\left(-\frac{i\omega t}{2}\sigma_z - \frac{i}{2}\left((\omega_0 - \omega)\sigma_z + \omega_1\sigma_x\right)t\right). \quad (2.76)$$

A vector $\vec{\alpha}(t)$ is defined as

$$\vec{\alpha}(t) \equiv \begin{pmatrix} \omega_1 t \\ 0 \\ (\omega_0 - \omega)t \end{pmatrix}. \quad (2.77)$$

With $\vec{\alpha}(t)$ the Eq.(2.76) can be written as

$$\zeta_r(t) = \zeta(0) \exp\left(-i\frac{\omega t}{2}\sigma_z\right) \exp\left(-i\vec{\sigma}\frac{\vec{\alpha}(t)}{2}\right). \quad (2.78)$$

The result when the term $\exp\left(-i\vec{\sigma}\frac{\alpha(t)}{2}\right)$ is expanded in a power series is already known from Section 2.1.1, Eq.(2.30)

$$\exp\left(-i\vec{\sigma}\frac{\alpha(t)}{2}\right) = \mathbb{1} \cos\left(\frac{\alpha(t)}{2}\right) - i\vec{\sigma}\hat{\alpha} \sin\left(\frac{\alpha(t)}{2}\right). \quad (2.79)$$

This leads to the final result for $\zeta(t)$

$$\zeta(t) = \zeta(0) \exp\left(-i\frac{\omega t}{2}\sigma_z\right) \left\{ \mathbb{1} \cos\left(\frac{\alpha(t)}{2}\right) - i\vec{\sigma}\hat{\alpha} \sin\left(\frac{\alpha(t)}{2}\right) \right\}, \quad (2.80)$$

with the unit vector

$$\hat{\alpha} = \frac{\vec{\alpha}(t)}{\alpha(t)}, \quad (2.81)$$

which yields

$$\alpha(t) = t\sqrt{(\omega_0 - \omega)^2 + \omega_1^2} = \gamma t \sqrt{\left(B_0 + \frac{\omega}{\gamma}\right)^2 + B_1^2} = \gamma t B_{\text{eff}}, \quad (2.82)$$

and

$$\hat{\alpha} = \frac{\vec{\alpha}}{\alpha} = -\frac{1}{B_{\text{eff}}} \begin{pmatrix} B_1 \\ 0 \\ B_0 + \frac{\omega}{\gamma} \end{pmatrix} = -\hat{B}_{\text{eff}} = -\frac{\vec{B}_{\text{eff}}}{B_{\text{eff}}}. \quad (2.83)$$

The time independent effective magnetic field $B_{\text{eff}} = \sqrt{\left(B_0 + \frac{\omega}{\gamma}\right)^2 + B_1^2}$ is the field which the neutron is exposed in the rotating system. For

$$\omega = \omega_{\text{res}} = \omega_0 = -\gamma B_0 \quad (2.84)$$

the static field B_0 is fully suppressed. This case is called **frequency resonance**.

The complete wavefunction is given by

$$\Psi(x, t) = \frac{1}{\sqrt{2\pi}} \exp\left(ikx - i\frac{\omega t}{2}\sigma_z - i\frac{\hbar k^2}{2m}t\right) \left\{ \mathbb{1} \cos\left(\frac{\alpha(t)}{2}\right) - i\vec{\sigma}\hat{\alpha} \sin\left(\frac{\alpha(t)}{2}\right) \right\} \zeta(o). \quad (2.85)$$

If the incoming neutron beam is polarized in the +z direction, which means $\zeta(o) = \begin{pmatrix} 1 \\ 0 \end{pmatrix}$, the probability to find a neutron at the time τ polarized in the -z direction is given by

$$W_{\text{flip}} = \frac{1}{1 + \left(\frac{B_0 + \frac{\omega}{\gamma}}{B_1}\right)^2} \sin^2\left(\frac{\gamma B_1 \tau}{2} \sqrt{1 + \left(\frac{B_0 + \frac{\omega}{\gamma}}{B_1}\right)^2}\right), \quad (2.86)$$

and the wavefunction can be written as

$$\Psi(x, t) = \frac{1}{\sqrt{2\pi}} \exp\left(i\left(kx - \frac{\hbar k^2}{2m}t\right)\right) \begin{pmatrix} \exp\left(\frac{-i\omega t}{2}\right) \left(\cos\left(\frac{\alpha(t)}{2}\right) + i\frac{B_0 + \frac{\omega}{\gamma}}{B_{\text{eff}}} \sin\left(\frac{\alpha(t)}{2}\right) \right) \\ i \exp\left(\frac{i\omega t}{2}\right) \frac{B_1}{B_{\text{eff}}} \sin\left(\frac{\alpha(t)}{2}\right) \end{pmatrix} \quad (2.87)$$

using $\alpha(t) = \gamma t B_{\text{eff}}$, $B_{\text{eff}} = \sqrt{(B_0 + \frac{\omega}{\gamma})^2 + B_1^2}$ and $\gamma = \frac{2\mu}{\hbar}$. If in addition the **amplitude resonance**, determine the amplitude of the rotating field B_1 , is fulfilled

$$\omega_L \tau = \pi = -\gamma B_1 \tau \quad \rightarrow \quad B_1 = \frac{\pi \hbar}{2\tau |\mu|}, \quad (2.88)$$

where τ is the time the neutron requires to traverse the RF field region, a spin flip occurs with a probability of unity. An initial wave function (omitting all time-independent phase factors)

$$\Psi(0) \propto e^{-\frac{i}{\hbar}Et} \begin{pmatrix} 1 \\ 0 \end{pmatrix}, \quad (2.89)$$

yields after a π -flip

$$\Psi(\tau) \propto e^{-\frac{i}{\hbar}(E - \hbar\omega)t} \begin{pmatrix} 0 \\ 1 \end{pmatrix} \quad (2.90)$$

As seen from above the total energy is no longer conserved due to the exchange of photons of energy $\hbar\omega$ between the neutron and the RF field. The interaction has a resonance when the photon energy equals the Zeeman energy difference of the two spin eigenstates in the static field: $\hbar\omega = 2|\mu|B_0$. After the flip, neutron which had energy $\hbar^2 k_+^2 / (2m) + |\mu|B_0$ lost an amount $\Delta E = 2|\mu|E$, whereas they maintain their momentum \vec{k}_+ .

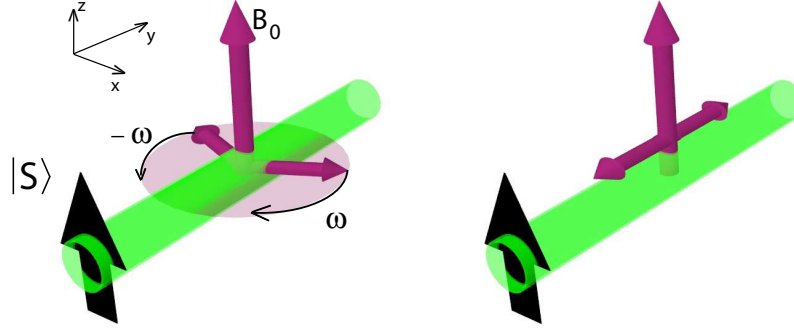


Figure 2.6: Graphical representation of an oscillating magnetic field decomposed in two counterrotating fields. Each of the rotating fields has half amplitude compared to the oscillating field.

For an oscillating field with phase of form $\vec{B}(t) = \begin{pmatrix} B_1 \sin(\omega t + \phi) \\ B_1 \cos(\omega t + \phi) \\ B_0 \end{pmatrix}$ the effective field in frequency resonance reads $\vec{B}_{\text{eff}} = \begin{pmatrix} B_1 \sin(\phi) \\ B_1 \cos(\phi) \\ 0 \end{pmatrix}$. For a real flip process an oscillating field is used instead of a rotating one:

$$\begin{aligned} \vec{B}_{\text{osz}} &= \begin{pmatrix} 0 \\ B_y \cos(\omega t) \\ B_0 \end{pmatrix} = \vec{B}_{\text{osz}} = \vec{B}_{1\text{rot}} + \vec{B}_{2\text{rot}} \\ &= \begin{pmatrix} \frac{B_y}{2} \sin(\omega t + \phi) \\ \frac{B_y}{2} \cos(\omega t + \phi) \\ \frac{B_0}{2} \end{pmatrix} + \begin{pmatrix} \frac{B_y}{2} \sin(-\omega t + \phi) \\ \frac{B_y}{2} \cos(\omega t + \phi) \\ \frac{B_0}{2} \end{pmatrix}, \quad (2.91) \end{aligned}$$

as seen the oscillating field can be decomposed as the sum of two rotating fields in opposite directions with frequencies ω , which is illustrated in Fig 2.6. The interaction representation used above describes the physics in a rotating frame with the field component ω with the Larmor precession of the spin in the static field. The other component is seen in this frame as a fast rotating field (2ω), whose effect can be neglected, which is referred to as *rotating wave approximation (RWA)*.

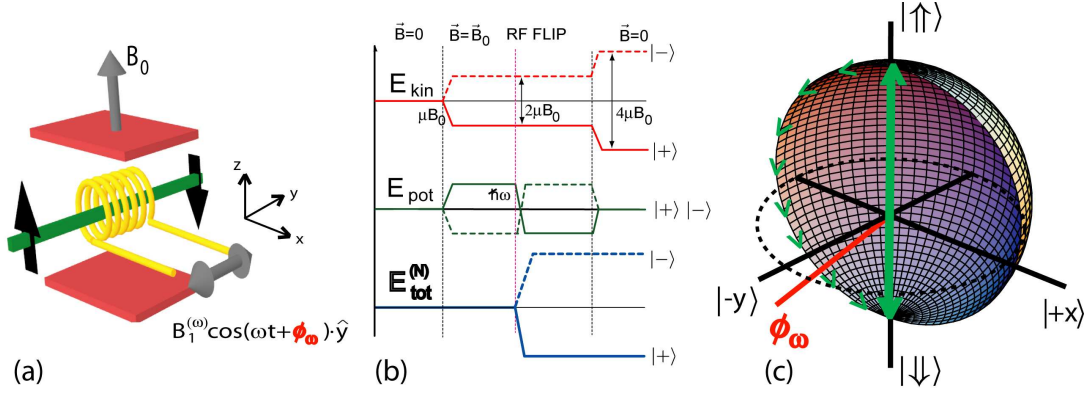


Figure 2.7: (a) A spin flip, due to the interaction with of an oscillating and stationary magnetic field. (b) Energy diagrams i.e., of kinetic, potential, and total energies. The spatially distributed potential induces changes of only kinetic and potential energies. In contrast, the time-dependent interaction leads to no change of kinetic and changes of potential energy, which results in changes of total energy. (c) Evolution on the Bloch sphere, viewed in the rotating frame.

A consequence of the rotating wave approximation is the so called *Bloch Siegert shift*, which originates from the second term in Eq.(2.91). In 1940 Bloch and Siegert proved [Bloch and Siegert, 1940] that the dropped part, oscillating rapidly, can give rise to a shift in the true resonance frequency such that $\omega_{res} \neq \omega_L$. Now the frequency resonance is given by

$$\omega_{res} = \frac{2|\mu|B_0}{\hbar} \left(1 + \frac{B_1^2}{16B_0^2} \right), \quad (2.92)$$

and the amplitude becomes

$$B_{rf}^{(\omega)} = \frac{\pi\hbar}{\tau|\mu|}. \quad (2.93)$$

A precession of this type, observed in the frame rotating at angular frequency ω around z -axis is referred to as the *Rabi oscillation*, in atomic and NMR physics. A typical RF-flipper, consisting of an arrangement of an oscillating field and a static field, including energy diagram is depicted in Fig 2.7.

2.2 Coupling a Spin 1/2 to Quantized Field

2.2.1 Quantum theory of radiation

In this Section a quantized model of radiation is presented, where essentially each mode of the radiation field is associated with a quantized simple harmonic oscillator. The electric field, linearly polarized in the x -direction, has to fulfill the boundary conditions of vanishing E-field at $z = 0$ and $z = L$ of the cavity. The field can be expanded in the normal modes denoted as

$$\vec{E}_x(z, t) = \sum_j \vec{e}_x A_j q_j(t) \sin(k_j z), \quad (2.94)$$

with q_j as the normal mode amplitude having the dimension of a length, $k_j = j\pi/L$ with $j=1,2,3$ and

$$A_j = \left(\frac{2\nu_j^2 m_j}{V\epsilon_0} \right)^2, \quad (2.95)$$

where $\nu_j = c \cdot k_j = j\pi c/L$ is the frequency of the mode and $V = LA$, and m_j is a constant with dimension of a mass. This constant is introduced in order to establish an analogy between the dynamical problem of a single mode of the electrical field and that of a harmonic oscillator. The nonvanishing component of the magnetic field, according to Eq.(2.94) reads

$$\vec{B}_y(z, t) = \sum_j \vec{e}_y A_j \frac{\dot{q}_j(t) \epsilon_0}{k_j} \cos(k_j z). \quad (2.96)$$

The energy contained in the field is

$$E = \frac{1}{2} \epsilon_0 (E_x^2 + c^2 B_y^2) = \frac{1}{2} \left(\epsilon_0 E_x^2 + \frac{B_y^2}{\mu_0} \right). \quad (2.97)$$

Thus the classical Hamiltonian function for the field is given by

$$\mathcal{H} = \frac{1}{2} \int_V d\tau (\epsilon_0 E_x^2 + \mu_0 B_y^2), \quad (2.98)$$

using Eq.(2.94) and Eq.(2.96)

$$\mathcal{H} = \frac{1}{2} \sum_j (m_j \nu_j^2 q_j^2 + m_j \dot{q}_j^2) = \frac{1}{2} \sum_j \left(m_j \nu_j^2 q_j^2 + \frac{p_j^2}{m_j^2} \right), \quad (2.99)$$

with $p_j = m_j \dot{q}_j$ being the canonical momentum of the j^{th} mode. Eq.(2.99) expresses the Hamiltonian of the radiation field, which is formally identical to a quantum-mechanical harmonic oscillator. Hence the radiation field is described as a sum of independent oscillator energies. Each mode of the field is equivalent to a mechanical harmonic oscillator.

Quantization

Now Eq.(2.99) can be quantized by identifying (in each term of the sum) q_j and p_j as operators \hat{X}_j and \hat{P}_j (for the j^{th} mode) of the quantum-mechanical oscillator with quadratic potential $V(x) = m\omega^2 x^2/2$. In quantum physics position and momentum become operators obeying the commutation relations $[\hat{X}, \hat{P}] = i\hbar$, with oscillators Hamiltonian given by

$$\hat{H} = \frac{\hat{P}^2}{2m} + \frac{m\omega^2 \hat{X}^2}{2}. \quad (2.100)$$

Introducing dimensionless position and momentum operators

$$\hat{X}_0 = \frac{\hat{X}}{2x_0} \quad \text{and} \quad \hat{P}_0 = \frac{\hat{P}}{p_0}, \quad (2.101)$$

the Hamiltonian reads

$$\hat{H} = \hbar\omega(\hat{P}_0^2 + \hat{X}_0^2), \quad (2.102)$$

with

$$\begin{aligned} [\hat{X}, \hat{P}] &= i\hbar\mathbb{1} \\ [\hat{X}, \hat{X}] &= [\hat{P}, \hat{P}] = 0. \end{aligned} \quad (2.103)$$

The electric field of the single mode becomes now an operator

$$\hat{E}_x(z, t) = \vec{e}_x \sqrt{\frac{2\nu_j^2 m_j}{V\epsilon_0}} q_j(t) \sin(k_j z), \quad (2.104)$$

as well as the magnetic field

$$\hat{B}_y(z, t) = \vec{e}_y \frac{\epsilon_j}{k_j} \sqrt{\frac{2\nu_j^2 m_j}{V\epsilon_0}} \dot{q}_j(t) \cos(k_j z). \quad (2.105)$$

Introducing the operators \hat{a}_j and \hat{a}_j^\dagger

$$\hat{a}_j = \frac{1}{2\hbar\nu_j}(\nu_j q + i\dot{q}) \quad \text{and} \quad \hat{a}_j^\dagger = \frac{1}{2\hbar\nu_j}(\nu_j q - i\dot{q}) \quad (2.106)$$

\dot{q}_j and q_j can be expressed in term of \hat{a}_j and \hat{a}_j^\dagger

$$q_j = \frac{\hbar}{2\nu_j}(\hat{a}_j + \hat{a}_j^\dagger) \quad \text{and} \quad \dot{q}_j = \frac{\hbar}{2\nu_j}(\hat{a}_j - \hat{a}_j^\dagger). \quad (2.107)$$

Therefore the Hamiltonian of the field can be rewritten in terms of \hat{a}_j and \hat{a}_j^\dagger

$$\hat{H} = \hbar \sum_j \nu_j \left(\hat{a}_j^\dagger \hat{a}_j + \frac{1}{2} \right). \quad (2.108)$$

The commutation relations between \hat{a}_j and \hat{a}_j^\dagger follow from those of q_j and p_j :

$$\begin{aligned} [\hat{a}_j, \hat{a}_{j'}^\dagger] &= i\hbar\delta_{jj'} \\ [\hat{a}_j, \hat{a}_{j'}] &= [\hat{a}_j^\dagger, \hat{a}_{j'}^\dagger] = 0 \end{aligned} \quad (2.109)$$

The operators \hat{a}_j and \hat{a}_j^\dagger are referred to as *annihilation* and *creation* operators. Finally the electric (and magnetic) field operators are denoted as

$$\begin{aligned} \hat{E}_x(z, t) &= \mathcal{E}_0(\hat{a}_j + \hat{a}_j^\dagger) \sin(k_j z) \\ \hat{B}_y(z, t) &= \mathcal{B}_0(\hat{a}_j - \hat{a}_j^\dagger) \cos(k_j z). \end{aligned} \quad (2.110)$$

The free electric and magnetic field can also be written in terms of \hat{a}_j and \hat{a}_j^\dagger

$$\begin{aligned} \hat{E}_x(z, t) &= \sum_j \mathcal{E}_j (\hat{a}_j e^{-i\nu_j t} + \hat{a}_j^\dagger e^{i\nu_j t}) \sin(k_j z) \\ \hat{B}_y(z, t) &= -i\epsilon_0 c \sum_j \mathcal{E}_j (\hat{a}_j e^{-i\nu_j t} - \hat{a}_j^\dagger e^{i\nu_j t}) \cos(k_j z) \\ &= \sum_j \mathcal{B}_j (\hat{a}_j e^{-i\nu_j t} - \hat{a}_j^\dagger e^{i\nu_j t}) \cos(k_j z), \end{aligned} \quad (2.111)$$

where

$$\mathcal{E}_j = \left(\frac{\hbar\nu_j}{\epsilon_0 V} \right)^{1/2} \quad \text{and} \quad \mathcal{B}_j = \left(\frac{\hbar\nu_j \mu_0}{V} \right)^{1/2}. \quad (2.112)$$

2.2.2 Fock and coherent states

Fock or number states

Suppose a single mode of the field of frequency ν having annihilation and creation operators \hat{a} and \hat{a}^\dagger , where $|n\rangle$ is the energy eigenstate corresponding to the energy eigenvalue E_n with

$$\hat{H}|n\rangle = \hbar\nu \left(\hat{a}^\dagger \hat{a} + \frac{1}{2} \right) |n\rangle = E_n |n\rangle. \quad (2.113)$$

Applying the operator \hat{a} from the left side, together with the commutation relation $[\hat{a}, \hat{a}^\dagger] = 1$

$$\hat{H}\hat{a}|n\rangle = (E_n - \hbar\nu)\hat{a}|n\rangle, \quad (2.114)$$

which indicates that the state

$$|n-1\rangle = \frac{a}{c_n}|n\rangle \quad (2.115)$$

is also an energy eigenstate, but with the reduced eigenvalue

$$E_{n-1} = E_n - \hbar\nu, \quad (2.116)$$

where c_n is a constant, determined from the normalization condition

$$\langle n-1|n-1\rangle = 1. \quad (2.117)$$

Applying this procedure n times one can move down the energy ladder in steps of $\hbar\nu$ until

$$\hat{H}\hat{a}|0\rangle = (E_0 - \hbar\nu)\hat{a}|0\rangle, \quad (2.118)$$

here E_0 is the ground state. Since energies smaller E_0 have no physical meaning the energy ladder is restricted to

$$\hat{a}|0\rangle = 0. \quad (2.119)$$

That state $|0\rangle$ is referred to as *vacuum state*, with

$$\hat{H}|0\rangle = \frac{1}{2}\hbar\nu|0\rangle = E_0|0\rangle, \quad (2.120)$$

which yields

$$E_0 = \frac{1}{2}\hbar\nu. \quad (2.121)$$

Hence, according to Eq.(2.116)

$$E_n = \left(n + \frac{1}{2}\right)\hbar\nu \quad (2.122)$$

and from Eq.(2.113)

$$\hat{a}^\dagger\hat{a}|n\rangle = n|n\rangle. \quad (2.123)$$

Therefore the energy eigenstate $|n\rangle$ is also an eigenstate of the *number operator* n defined as $n = \hat{a}^\dagger\hat{a}$. Now the normalization constant c_n from Eq.(2.117) can be calculated

$$\langle n-1|n-1\rangle = \frac{1}{|c_n|^2}\langle n|\hat{a}^\dagger\hat{a}|n\rangle = \frac{n}{|c_n|^2}\langle n|n\rangle = \frac{n}{|c_n|^2} = 1. \quad (2.124)$$

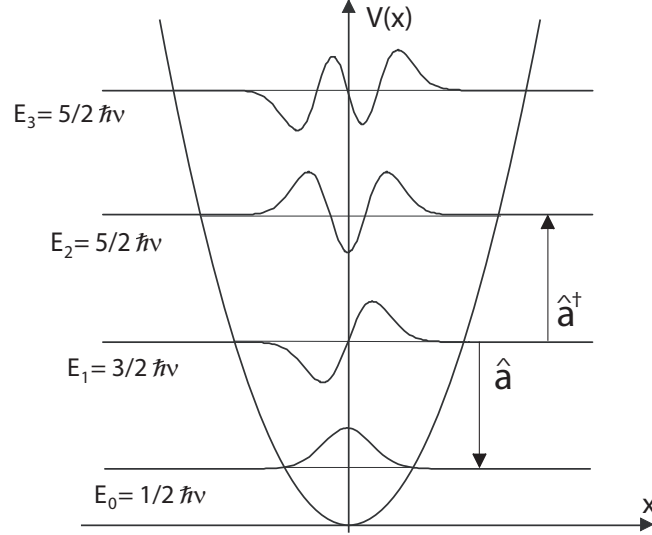


Figure 2.8: Energy level diagram for the quantum-mechanical oscillator associated with the electromagnetic field. The creation operator \hat{a}^\dagger adds a radiation field of energy $\hbar\nu$, whereas the annihilation operator \hat{a} subtracts the same amount of energy. The parabola represents the confining potential, the horizontal lines the Fock states ladder. Four eigen (wave) functions are also plotted.

For zero phase of the normalization constant becomes $\alpha_n = \sqrt{n}$ and Eq.(2.115) reads

$$\hat{a}|n\rangle = \sqrt{n}|n-1\rangle. \quad (2.125)$$

The same for \hat{a}^\dagger yields

$$\hat{a}^\dagger|n\rangle = \sqrt{n+1}|n+1\rangle. \quad (2.126)$$

A repeated use of this equation finally gives

$$|n\rangle = \frac{(\hat{a}^\dagger)^n}{\sqrt{n!}}|0\rangle. \quad (2.127)$$

The energy eigenvalues, as defined in Eq.(2.122) are interpreted as the presence of n *quanta* or *photons* of energy $\hbar\nu$, which is depicted in Fig.2.8. The eigenstates $|n\rangle$ are therefore called (eigen) number (or Fock) states. In contrast to the classical electromagnetic theory the eigenvalues E_n are discrete.

Fock state wavefunction:

The coordinate representation of the oscillator ground state $|0\rangle$, a Gaussian centred at the origin, is given by:

$$\Psi_{n=0}(x) = \langle x|0\rangle = (\nu/\pi\hbar)^{1/4} e^{-\nu x^2/(2\hbar)} \quad (2.128)$$

More generally, the wave functions of the $|n\rangle$ state is denoted

$$\Psi_n(x) = \langle x|n\rangle = \frac{2}{\sqrt{2^n n!}} H_n\left(\sqrt{\frac{\nu x}{\hbar}}\right) \Psi_0(x), \quad (2.129)$$

where

$$H_n(u) = (-1)^n e^{u^2} \frac{d^n}{du^n} e^{-u^2} \quad (2.130)$$

is the Hermite polynomial of order n . The wave function of the n^{th} excited state is therefore a Gaussian of x modulated by a polynomial function, which is plotted in Fig. 2.8. According to the definition of $\Psi_n(x)$ one finds

$$\langle x \rangle = \int_{-\infty}^{\infty} \Psi_n(x)^* \Psi_n(x) dx = 0 \quad \text{and} \quad \langle x^2 \rangle = \frac{\hbar}{\nu} \left(n + \frac{1}{2}\right). \quad (2.131)$$

Similarly

$$\langle p \rangle = 0 \quad \text{and} \quad \langle p^2 \rangle = \hbar\nu \left(n + \frac{1}{2}\right). \quad (2.132)$$

The uncertainty in generalized coordinates of momentum and coordinate is therefore given by

$$\begin{aligned} (\Delta p)^2 &= \langle p^2 \rangle - \langle p \rangle^2 = \hbar\nu \left(n + \frac{1}{2}\right) \\ (\Delta x)^2 &= \frac{\hbar}{\nu} \left(n + \frac{1}{2}\right). \end{aligned} \quad (2.133)$$

Thus the uncertainty product is

$$\Delta x \Delta p = \hbar \left(n + \frac{1}{2}\right), \quad (2.134)$$

which has minimum possible value of $\hbar/2$ for the ground state wavefunction Ψ_0 .

At this point an important property of the number states $|n\rangle$ should be mentioned: The average electric field of a number state, given by the corresponding expectation value of the single mode linearly polarized field operator yields

$$\langle n | \hat{E}_x(z, t) | n \rangle = \mathcal{E}_0 \sin(kz) \langle n | (\hat{a} + \hat{a}^\dagger) | n \rangle = 0, \quad (2.135)$$

and similarly for the magnetic field. Hence number states are only a good physical description for the vacuum state. However, the expectation value of the intensity operator E^2 yields

$$\langle n | \hat{E}_x(z, t)^2 | n \rangle = 2|\mathcal{E}_0|^2 \left(n + \frac{1}{2} \right) \quad (2.136)$$

There are nonzero fluctuations even for the vacuum state $|0\rangle$.

Fock state field quadratures:

The electric field operator, as introduced before in Eq.(2.135) is a function of \vec{r} , therefore it is convenient to introduce simpler position-independent field operators. In analogy with the mechanical oscillator case, dimensionless *field quadratures operators* \hat{X}_ϕ are introduced by

$$\hat{X}_\phi = \frac{\hat{a}e^{-i\phi}\hat{a}^\dagger e^{i\phi}}{2}, \quad (2.137)$$

with eigenstates $|x_\phi\rangle$. The operator \hat{X}_0 corresponds, in the case of a mechanical oscillator, to the dimensionless position operator, whereas $\hat{X}_{\pi/2}$ is associated to \hat{P}_0 . A two-dimensional phase space is spanned by the $\{\hat{X}_0, \hat{X}_{\pi/2}\}$, or, more generally, by $\{\hat{X}_\phi, \hat{X}_{\phi+\pi/2}\}$, which can be seen in Fig.2.9 for the vacuum state wave function and a three-photon Fock state. Any two orthogonal field quadratures $\{\hat{X}_\phi, \hat{X}_{\phi+\pi/2}\}$ satisfy the commutation rule

$$[\hat{X}_\phi, \hat{X}_{\phi+\pi/2}] = i/2, \quad (2.138)$$

and Heisenberg uncertainty relation in dimensionless units:

$$\Delta \hat{X}_\phi \Delta \hat{X}_{\phi+\pi/2} \leq 1/4. \quad (2.139)$$

Any field state can be expanded on the X_0 eigenstates. The expansions of Fock states are independent of the angle parameter ϕ . In each direction ϕ a density of shade proportional to the square modulus $|\langle x_\phi | x \rangle|^2$ of the wave function at distance r from the origin is plotted. For the vacuum state $|0\rangle$ this results in circular shape centred at the origin (see Fig.2.9 (a)). The Fock states carry no phase information and have zero quadrature (and zero electric field) averages.

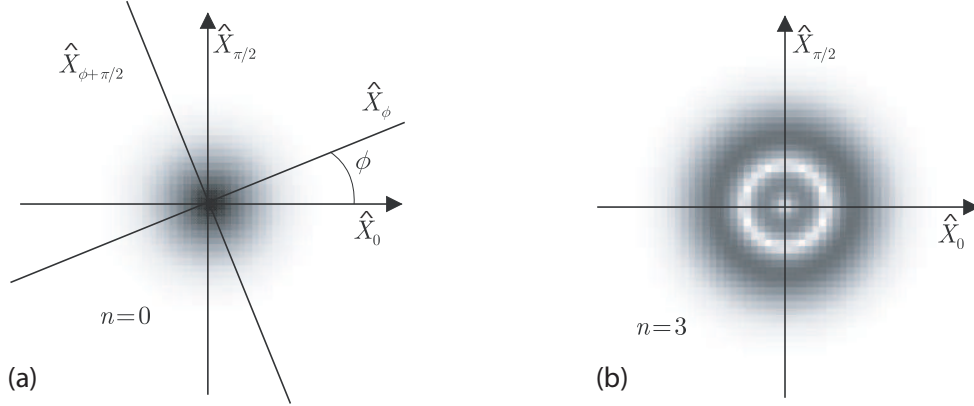


Figure 2.9: The phase space for the field in terms of quadratures. (a) The vacuum state ($n = 0$) wave functions in terms of \hat{X}_0 , $\hat{X}_{\pi/2}$, \hat{X}_ϕ and $\hat{X}_{\phi+\pi/2}$. (b) Graphical illustration of a three-photon ($n = 3$) Fock state in the quadrature phase space.

Coherent states

Classically an electromagnetic field consists of waves having well defined amplitude and phase. This is not the case if the electromagnetic field is treated as a Fock states, as described above. Fock states have well defined amplitude but completely uncertain phase (and zero average electric field), obviously do not correspond to the classical picture of an electromagnetic field. One would expect it having a well-defined amplitude and phase, described by a complex number (i.e. $\alpha = \alpha' + i\alpha''$). However, there exists such a quantum mechanical treatment of the electromagnetic field, where a field in *coherent states* has an equal amount of uncertainty in amplitude and phase.

For a mechanical oscillator, such classical states can be obtained by displacing the oscillator from its zero position, shifting its position by x while imparting to it a momentum kick p . The resulting states $|\alpha\rangle$ are the coherent states.

The displacement from $|0\rangle$ to $|\alpha\rangle$ is achieved by the translation operators in phase space

$$\mathcal{T}_x = e^{-2ix_0\hat{P}/\hbar} = e^{-2i\alpha'\hat{X}_{\pi/2}} \quad \text{and} \quad \mathcal{T}_p = e^{-2ip_0\hat{X}/\hbar} = e^{2i\alpha''\hat{X}_0}, \quad (2.140)$$

where $\hat{X}_{\pi/2}$ is identified with \hat{P}_0 . Using the Glauber identity

$$e^{\hat{A}+\hat{B}} = e^{-[\hat{A},\hat{B}]/2}e^{\hat{A}}e^{\hat{B}} \quad (2.141)$$

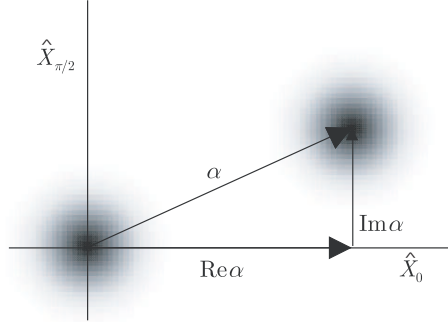


Figure 2.10: Graphical illustration of the action of the displacement operator on the vacuum state. The displacement by $\text{Re } \alpha$ along the X_0 quadrature axis, is followed by a displacement by $\text{Im } \alpha$ along the $X_{\pi/2}$ quadrature.

which is valid when both \hat{A} and \hat{B} commute with $[\hat{A}, \hat{B}]$. Signing them to $\hat{A} = 2i\alpha' \hat{X}_0$ and $\hat{B} = -2i\alpha' \hat{X}_{\pi/2}$ yields

$$\hat{\mathcal{T}}_x \hat{\mathcal{T}}_p = e^{i\alpha' \alpha''} e^{\alpha \hat{a}^\dagger - \alpha^* \hat{a}}. \quad (2.142)$$

The product $\hat{\mathcal{T}}_p \hat{\mathcal{T}}_q$ is equal (up to a phase factor) to the unitary displacement operator:

$$\hat{D}(\alpha) = e^{\alpha \hat{a}^\dagger - \alpha^* \hat{a}}, \quad (2.143)$$

having the following properties

$$\begin{aligned} \hat{D}^\dagger(\alpha) &= \hat{D}(-\alpha) = [\hat{D}(\alpha)]^{-1}; \hat{D}(0) = \mathbb{1} \\ \hat{D}^{-1}(\alpha) \hat{a} \hat{D}(\alpha) &= \hat{a} + \alpha \\ \hat{D}^{-1}(\alpha) \hat{a}^\dagger \hat{D}(\alpha) &= \hat{a}^\dagger + \alpha^*. \end{aligned} \quad (2.144)$$

A pictorial representation of the action of the displacement operator on the vacuum state $|0\rangle$ is depicted in Fig. 2.10. Choosing the simplest phase convention the coherent state $|\alpha\rangle$ is defined as:

$$|\alpha\rangle = \hat{D}(\alpha)|0\rangle \quad (2.145)$$

with $|0\rangle$ being the coherent state corresponding to a zero displacement amplitude.

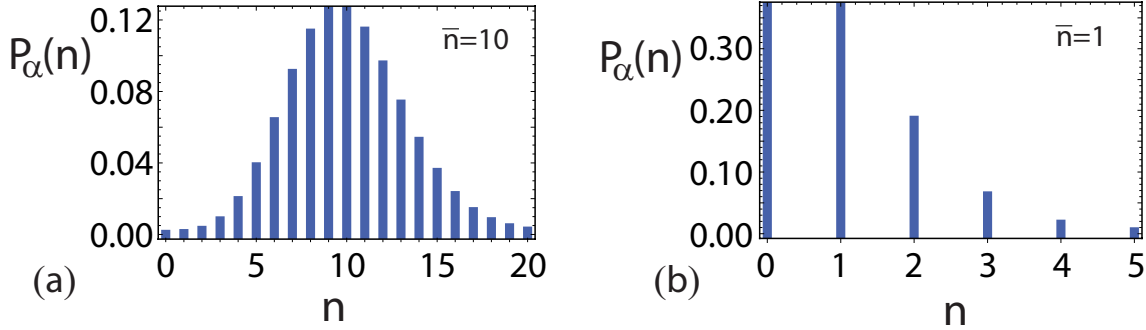


Figure 2.11: Photon number statistical distributions of coherent states for $\bar{n} = 10$ and $\bar{n} = 1$.

The coherent states are defined as the eigenstates of the annihilation operator \hat{a} with the eigenvalue α :

$$\hat{a}|\alpha\rangle = \alpha|\alpha\rangle \quad (2.146)$$

Similarly, the adjoint equation

$$\langle\alpha|\hat{a}^\dagger = \alpha^*\langle\alpha|, \quad (2.147)$$

expresses that $\langle\alpha|$ is a left eigenvector of \hat{a}^\dagger with the eigenvalue α^* . The expectation value of the photon number operator $\hat{N} = \hat{a}^\dagger\hat{a}$ of $|\alpha\rangle$ is

$$\bar{n} = \langle\alpha|\hat{a}^\dagger\hat{a}|\alpha\rangle = |\alpha|^2. \quad (2.148)$$

Using the definition of the displacement operator $\hat{D}(\alpha)$ expressed in Eq.(2.143) an expression of the coherent state α in terms of number states is found

$$|\alpha\rangle = \sum_{n=0}^{\infty} n c_n |n\rangle = e^{-|\alpha|^2/2} \sum_{n=0}^{\infty} \frac{\alpha^n}{\sqrt{n!}} |n\rangle, \quad (2.149)$$

with

$$|n\rangle = \frac{(a^\dagger)^n}{\sqrt{n!}} |0\rangle, \quad (2.150)$$

which is referred to as the Fock state representation of coherent states. The photon number probability distribution $p_\alpha(n) = |c_n|^2$ is of Poisson type

$$p_\alpha(n) = e^{-|\alpha|^2} \frac{|\alpha|^{2n}}{n!}, \quad (2.151)$$

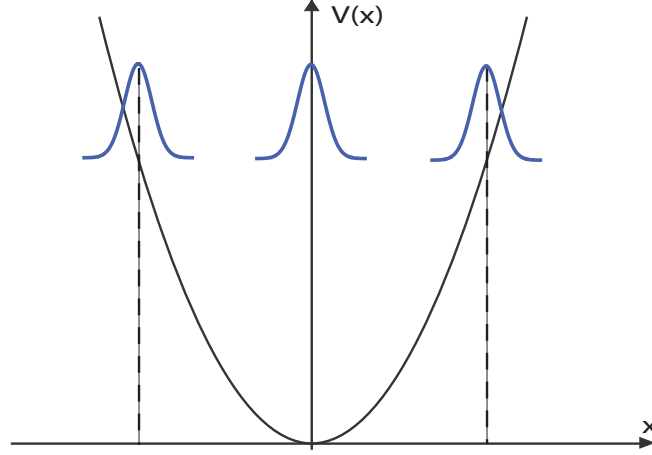


Figure 2.12: Evolution of a minimum uncertainty wave packet (of a coherent state) in a harmonic oscillator potential.

with an average photon number $\bar{n} = \langle \alpha | \hat{a}^\dagger \hat{a} | \alpha \rangle = |\alpha|^2$ and a photon number mean square-root deviation given by

$$\Delta N = \sqrt{\langle \alpha | N^2 | \alpha \rangle - \langle \alpha | N | \alpha \rangle^2} = |\alpha| = \sqrt{\bar{n}}. \quad (2.152)$$

Figure 2.11 shows $p_\alpha(n)$ for 10 and 1 photons on the average.

Coherent state wavefunction:

As shown in Eq.(2.134) the ground state wavefunction of the number state $|n\rangle$ has minimal uncertainty. So concerning the coherent states $|\alpha\rangle$ a wave packet with same variance Δx is desired, while it is undergoing a simple harmonic motion. If one can find such a wave packet it would indeed correspond most closely to a classical field. Assuming the wavefunction $\Psi_\alpha(x, t)$ at time $t = 0$ is of form Eq.(2.128), but displaced by an amount x_0

$$\Psi_\alpha(x, 0) = \langle x|0\rangle = (\nu/\pi\hbar)^{1/4} e^{-\nu(x-x_0)^2/(2\hbar)}, \quad (2.153)$$

which implies the following probability density in time

$$|\Psi_\alpha(x, t)|^2 = (\nu/\pi\hbar)^{1/2} e^{-\nu(x-x_0 \cos(\nu t))^2/(2\hbar)}. \quad (2.154)$$

Thus the wave packet in Eq.(2.154) oscillates back and forth in a simple harmonic potential, without changing its shape. To phrase it differently: the wave packet *coheres*, having

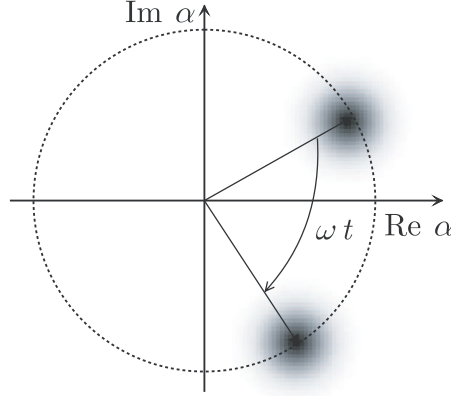


Figure 2.13: Graphical illustration of time evolution of a coherent state.

minimum uncertainty, namely $\Delta x \Delta p = \hbar/2$. This particular behaviour is illustrated in Fig. 2.12. It is the closest quantum-mechanical analog to a free classical single mode field.

Time evolution of the coherent states

The time evolution of a coherent state can be derived from its expansion over the Fock stationary states basis. The time evolution of an individual Fock state reads

$$|n(t)\rangle = e^{-i(n+1/2)\omega t}|n\rangle. \quad (2.155)$$

The evolution of $|\alpha(t)\rangle$ is therefore given by

$$|\alpha(t)\rangle = e^{-|\alpha|^2/2} \sum_{n=0}^{\infty} \frac{\alpha^n}{\sqrt{n!}} e^{-i(n+1/2)\omega t} |n\rangle = e^{-i\omega t/2} |\alpha e^{-i\omega t}\rangle = |\alpha(0)e^{-i\omega t}\rangle. \quad (2.156)$$

The complex amplitude rotates at frequency ω and phase ϕ_ω around the origin. It has the same dynamics as the classical amplitude. The average electric field evolves exactly as the classical field. A pictorial representation can be seen in Fig. 2.13. With the time evolution of the coherent states it is possible to evaluate the average electric field

$$\begin{aligned} \langle \alpha(t) | \hat{E}_x(z, t) | \alpha(t) \rangle &= \mathcal{E}_0 \sin(kz) \langle \alpha(t) | (\hat{a} + \hat{a}^\dagger) | \alpha(t) \rangle \\ &= \mathcal{E}_0 \sin(kz) (\alpha(0)e^{-i\omega t} + \alpha(0)^* e^{i\omega t}) \\ &= \mathcal{E}_0 \sin(kz) |\alpha(0)| \cos(\phi_0 - \omega t), \end{aligned} \quad (2.157)$$

where $\alpha_0 = |\alpha_0|e^{i\phi_0}$, which corresponds to a classical field with amplitude $|\alpha_0|$ and phase ϕ_0 .

2.2.3 Mach-Zehnder and Ramsey interferometer

The Mach-Zehnder interferometer

A Mach-Zehnder interferometer is realized by combining two beam-splitter and two mirrors, as depicted in Fig. 2.14. It has two input modes referred to as a and b , one of them is initially vacuum. The modes are first mixed by the beam-splitter B1, being the key element in most optical interferometers. The coherent input state, containing $\bar{n} = |\alpha|^2$ photons, $|\Psi_i\rangle = |\alpha, 0\rangle$ is transformed by beam-splitter B1 into

$$|\Psi_i\rangle \xrightarrow{\text{BS}} |\Psi'\rangle = |\alpha/\sqrt{2}, i\alpha/\sqrt{2}\rangle. \quad (2.158)$$

The phase-shifter, acting on mode (b), changes the state in

$$|\Psi'\rangle \xrightarrow{\text{PS}} |\Psi''\rangle = |\alpha/\sqrt{2}, ie^{i\phi}\alpha/\sqrt{2}\rangle. \quad (2.159)$$

Finally the modes are mixed again, by B2, resulting in the final state

$$|\Psi''\rangle \xrightarrow{\text{BS}} |\Psi_f\rangle = \left| \frac{\alpha}{2}(1 - e^{i\phi}), \frac{i\alpha}{2}(1 + e^{i\phi}) \right\rangle. \quad (2.160)$$

The mean photon numbers n_a and n_b recorded by the two detectors D_a and D_b are given by

$$n_{a,b} = \frac{1}{2}\bar{n}(1 \mp \cos \phi). \quad (2.161)$$

When ϕ is varied, these signals exhibit complementary (phase-opposite) oscillations. All photons are detected in D_b for $\phi = 0$, and in D_a for $\phi = \pi$ respectively, which is obviously the classical result.

In the case of photons, as described up to this point, many particles cross the interferometer at the same time. However this is irrelevant to the operation of the interferometer itself. The photon partition probabilities between modes (a) and (b) is *n-independent*. Consequently, if only one photon at a time would impinge on the interferometer, the average signals would be the same. This feature will become of special interest, when in Section 3.1 the neutron interferometer of Mach-Zehnder type [Rauch et al., 1974] is introduced. Here it is indeed that case that, due to the low neutron density, really only one neutron is in the interferometer at a time, resulting in single-neutron interference (self interference of massive single-particles).

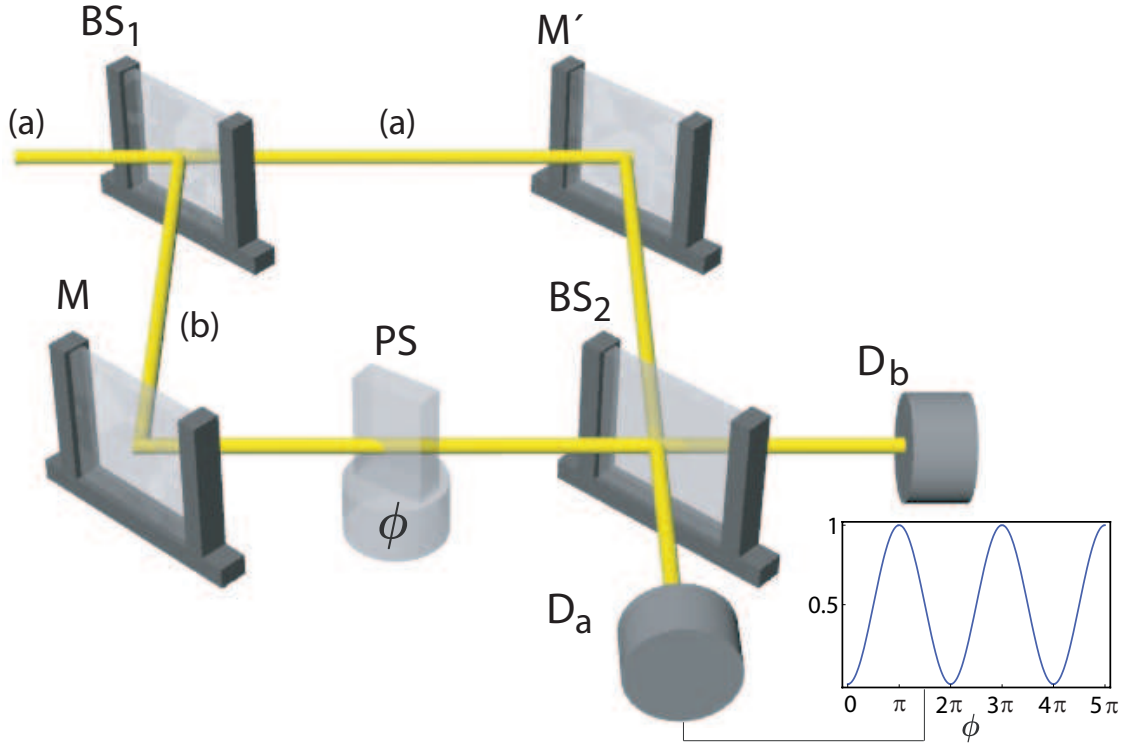


Figure 2.14: Graphical illustration of a MachZehnder interferometer, consisting of two beam-splitters (BS_1 and BS_2), two mirrors (M and M') and an adjustable phase shift (PS) ϕ .

The Ramsey interferometer

A combination of two $\pi/2$ -pulses, also exhibits sinusoidal (population) oscillations, as introduced in Section 2.1.2: this is generally referred to as *Ramsey interferometer* in NMR and atomic physics. For neutrons the similar scheme is seen in a polarimeter. The first pulse $R1$ creates a coherent superposition of orthogonal eigenstates, by transforming the initial state $|\Psi_i\rangle = |\uparrow\rangle$ according to

$$|\Psi_i\rangle \xrightarrow{R1} |\Psi'\rangle = \frac{1}{\sqrt{2}} (|\uparrow\rangle + |\downarrow\rangle). \quad (2.162)$$

Before the second pulse $R2$ probes it, a tunable phase shift (for example a static magnetic field) is applied:

$$|\Psi'\rangle \xrightarrow{PS} |\Psi''\rangle = \frac{1}{\sqrt{2}} (|\uparrow\rangle + e^{i\phi} |\downarrow\rangle). \quad (2.163)$$

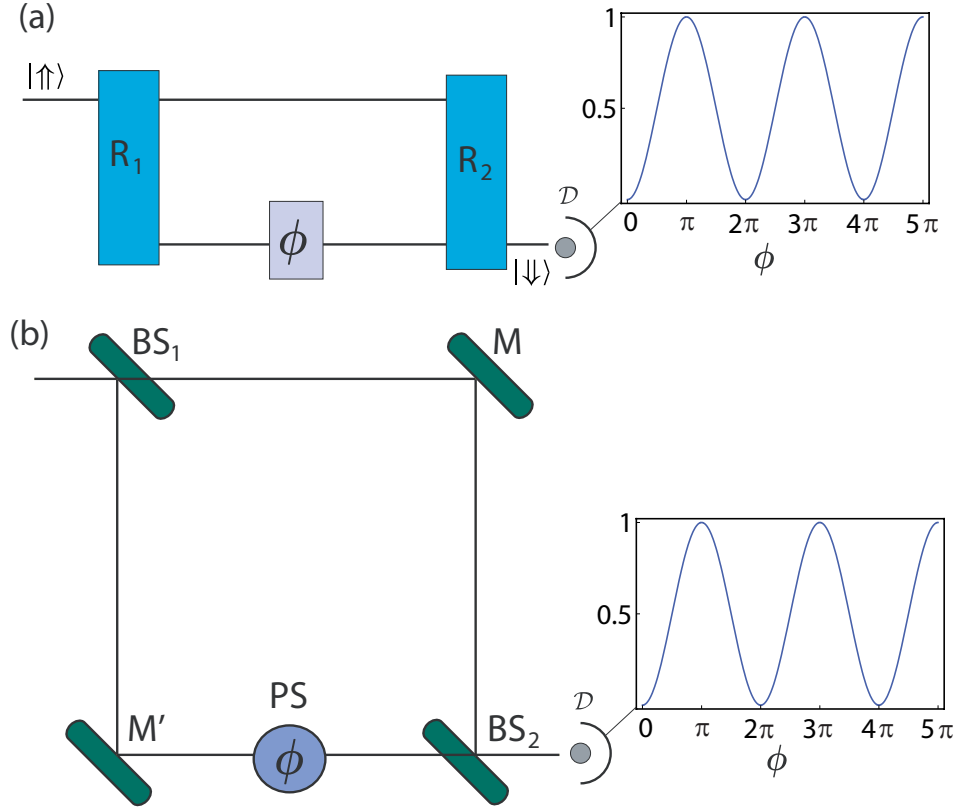


Figure 2.15: (a) Ramsey interferometer set-up, consisting of two indistinguishable paths. (b) Scheme of a Mach-Zehnder interferometer. The conceptual analogy with the Ramsey interferometer is obvious.

After the second pulse R_2 the system is found in the final state

$$|\Psi''\rangle \xrightarrow{R_2} |\Psi_f\rangle = \frac{1}{2} \left((1 - e^{i\phi}) |\uparrow\rangle + (1 + e^{i\phi}) |\downarrow\rangle \right). \quad (2.164)$$

The probability of finding finally the system in $|\uparrow\rangle$ ($|\downarrow\rangle$) is given by

$$P_{\uparrow,\downarrow} = \frac{1}{2} (1 \mp \cos \phi), \quad (2.165)$$

a result formally identical to the Mach-Zehnder counting signal defined in Eq.(2.161), where the interfering beams have well-identified trajectories. A comparison between these two types of interferometers is given in Fig 2.15.

2.2.4 The Jaynes-Cummings model and the dressed states

General concept

Considering the coupling of any two-level system, for instance an atom, having an upper level $|e\rangle$ connected to level $|g\rangle$ by transition at angular frequency ω_{eg} , with a quantum harmonic oscillator of frequency ω_{rf} . This model is applied in various physical situations such as in cavity quantum electrodynamics (single atom is coupled to a cavity mode - here the ω_{eg} is given by the electric dipole transition), as well as a single ion in a trap (when two internal ionic states are coupled by laser beams to the harmonic oscillator motional states in the trap). As will be described in Section 3.2, with minor modifications one can apply this scheme, for neutrons in oscillating magnetic fields in the framework of an interferometric experiment (in this particular case ω_{eg} corresponds to ω_L the Larmor frequency defined by the static magnetic field for the RF spin-flip). Historically, this model was introduced by Jaynes and Cummings [Jaynes and Cummings, 1963] as an idealization of the matter-field coupling in free space.

In the most general form the total Hamiltonian is denoted as

$$\begin{aligned}\hat{H}_{\text{J-C}} &= \hat{H}_{s=1/2} + \hat{H}_{\text{rf}} + \hat{H}_{\text{int}} \\ &= \hat{H}_{s=1/2} + \hbar\omega_{\text{rf}}\hat{a}^\dagger\hat{a} + \hbar\frac{\Omega_0}{2}(\hat{a}^\dagger\hat{\sigma}_+ + \hat{a}\hat{\sigma}_-)\end{aligned}\quad (2.166)$$

The term \hat{H}_{rf} accounts for the energy of (n) RF photons of frequency ω . $\hat{H}_{s=1/2}$ is the Hamiltonian of the spin 1/2 system (an atom for instance), and \hat{H}_{int} is the interaction Hamiltonian, in a general representation, with coupling strength Ω_0 , again dependent on the spin system (in case of atom and cavity the coupling Hamiltonian, \hat{H}_{int} is given by $-\hat{D}\hat{E}_c$, where \hat{D} is the atomic dipole operator introduced and \hat{E}_c the cavity electric field operator at the atomic location).

The *uncoupled* eigenstates of $\hat{H}_{s=1/2}$ and \hat{H}_{rf} are given by the tensor products $|e, n\rangle$ and $|g, n\rangle$ of the spin 1/2 system and the RF field with energies

$$E_{e,n} = \hbar(\omega_{eg}/2 + n\omega_{\text{rf}}) \quad \text{and} \quad E_{g,n} = \hbar(-\omega_{eg}/2 + n\omega_{\text{rf}}).\quad (2.167)$$

However, the eigenstates of the total Jaynes-Cummings Hamiltonian $\hat{H}_{\text{J-C}}$ are given by

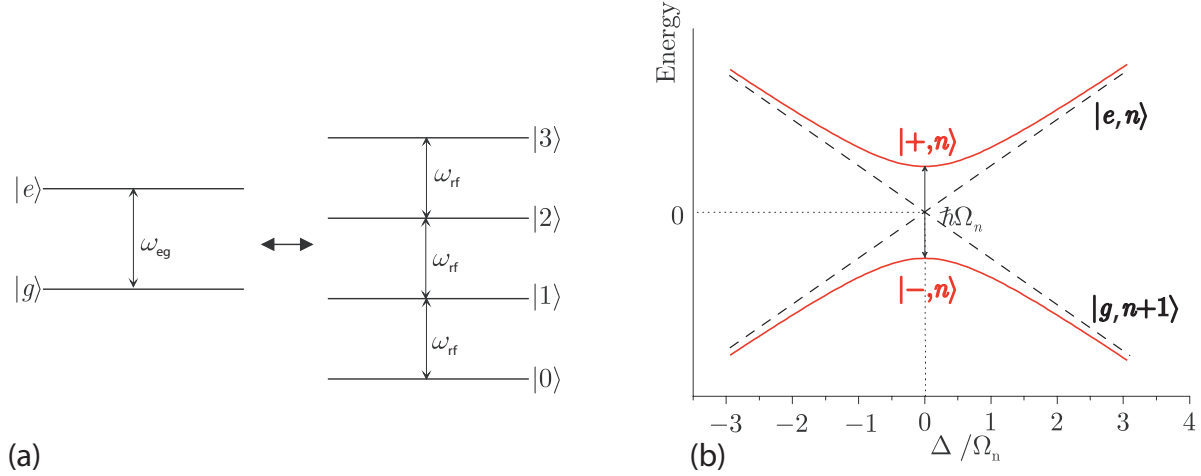


Figure 2.16: (a) Coupling a two-level system to a single field mode treated as an harmonic oscillator. (b) Dressed state (red) energies as a function of the detuning Δ . The uncoupled state energies are represented as dotted lines.

$$E_n^\pm = (n + \frac{1}{2})\hbar\omega_{rf} \pm \frac{\hbar}{2}\sqrt{\Delta^2 + \Omega_n^2}, \quad (2.168)$$

where Δ is the *detuning* given by

$$\Delta = \omega_{eg} - \omega_{rf}, \quad (2.169)$$

and $\Omega_n = \Omega_0\sqrt{n+1}$. The corresponding eigenvectors are denoted as $|+, n\rangle$ and $|-, n\rangle$, which is illustrated in Fig. 2.16. They are given by

$$\begin{aligned} |+, n\rangle &= \cos\frac{\theta_n}{2}|e, n\rangle + i\sin\frac{\theta_n}{2}|g, n+1\rangle \\ |-, n\rangle &= \sin\frac{\theta_n}{2}|e, n\rangle - i\cos\frac{\theta_n}{2}|g, n+1\rangle, \end{aligned} \quad (2.170)$$

where θ_n is the *mixing angle*, varying between 0 and π , is calculated as

$$\tan\theta_n = \frac{\Omega_n}{\Delta}. \quad (2.171)$$

These states denoted as $|+, n\rangle$ and $|-, n\rangle$ defined in Eq.(2.170), are called the *dressed states* of the atom-field system, whereas the states $|e, n\rangle$ and $|g, n+1\rangle$ are called *bare states* of the uncoupled system. The dressed states are also nonseparable entangled states, i.e., states that cannot be factorized into a product of an atom state and a field state.

Neutron spin coupling to field quanta

The neutrons energy in the magnetic field, due to the neutrons magnetic moment, is denoted as $E_{\text{mag}} = \vec{\mu}\vec{B} = \gamma\vec{S}\vec{B}$. The corresponding Hamiltonian \hat{H}_{mag} is

$$\hat{H}_{\text{mag}} = \gamma\vec{S}\vec{B} \quad \text{with} \quad B_{osz} = \begin{pmatrix} B(t) \\ 0 \\ B_0 \end{pmatrix} \quad \text{and} \quad \vec{S} = \frac{\hbar}{2} \begin{pmatrix} \sigma_x \\ \sigma_y \\ \sigma_z \end{pmatrix}. \quad (2.172)$$

First operators $\hat{\sigma}_+$ and $\hat{\sigma}_-$ are defined as

$$\hat{\sigma}_+ = \begin{pmatrix} 0 & 1 \\ 0 & 0 \end{pmatrix} \quad \text{and} \quad \hat{\sigma}_- = \begin{pmatrix} 0 & 0 \\ 1 & 0 \end{pmatrix}, \quad (2.173)$$

with the following action on the spin eigenstates $|\uparrow\rangle$ and $|\downarrow\rangle$

$$\begin{aligned} \hat{\sigma}_-|\uparrow\rangle &= |\downarrow\rangle & \hat{\sigma}_+|\uparrow\rangle &= 0 \\ \hat{\sigma}_-|\downarrow\rangle &= 0 & \hat{\sigma}_+|\downarrow\rangle &= |\uparrow\rangle, \end{aligned} \quad (2.174)$$

and $\sigma_x = \hat{\sigma}_+ + \hat{\sigma}_-$. The quantized magnetic field, at the position of its maximal intensity, according to Eq.(2.110), for a single mode is given by

$$\hat{B}_x(t) = \left(\frac{\hbar\omega_{\text{rf}}\mu_0}{V} \right)^{1/2} (\hat{a} + \hat{a}^\dagger). \quad (2.175)$$

Plugging in Eq.(2.175) into Eq.(2.172) yields

$$\begin{aligned} \hat{H}_{\text{mag}} &= \frac{\hbar}{2} \underbrace{\gamma B_0}_{\omega_L} \sigma_z + \frac{\hbar}{2} \gamma \underbrace{\left(\frac{\hbar\omega_{\text{rf}}\mu_0}{V} \right)^{1/2}}_{B_1^{(\omega)}} (\hat{a} + \hat{a}^\dagger) (\hat{\sigma}_+ + \hat{\sigma}_-) \\ &= \hbar \frac{\omega_L}{2} \sigma_z + \hbar \frac{\Omega_0}{2} (\hat{a}_j + \hat{a}_j^\dagger) (\hat{\sigma}_+ + \hat{\sigma}_-) \\ &= \mu B_0 \sigma_z + \mu B_1^{(\omega)} (\hat{a}_j + \hat{a}_j^\dagger) (\hat{\sigma}_+ + \hat{\sigma}_-), \end{aligned} \quad (2.176)$$

with the coupling strength $\Omega_0 = \gamma B_1^{(\omega)} = (2\mu/\hbar)B_1^{(\omega)}$. Thus the total Hamiltonian, consisting of the magnetic energy and the energy of the radiation field, is given by

$$\begin{aligned} \hat{H}_{\text{J-C}} &= \hat{H}_{\text{field}} + \hat{H}_{\text{mag}} = \\ &= \underbrace{\hbar\omega_{\text{rf}} \left(\hat{a}^\dagger \hat{a} + \frac{1}{2} \right)}_{\hat{H}_{\text{rf-field}}} + \underbrace{\frac{\hbar}{2} \omega_L \sigma_z}_{\hat{H}_{\text{stat.field-spin}}} + \underbrace{\hbar \frac{\Omega_0}{2} (\hat{a} + \hat{a}^\dagger) (\hat{\sigma}_+ + \hat{\sigma}_-)}_{\hat{H}_{\text{int}}}, \end{aligned} \quad (2.177)$$

$\underbrace{\hspace{15em}}_{\hat{H}_0}$

where the interaction Hamiltonian \hat{H}_{int} accounts for the coupling of the neutron with the radiation field, i.e. the energy exchange between the neutron and the quantized magnetic field. For the Hamiltonian \hat{H}_{int} it is not possible to find analytical solutions.

This yields the following approach: For the uncoupled Hamiltonian ($\omega_0 = 0$) the analytical solutions are found in the product space of the eigenstates of the quantized field $|n\rangle$ and the spin eigenstates $|\uparrow\rangle$ and $|\downarrow\rangle$. In order to find a suitable approximation for the interaction Hamiltonian \hat{H}_{int} the time-dependence \hat{H}_{int} is analyzed. The time evolution of \hat{a} and \hat{a}^\dagger is derived from the commutator with the Hamiltonian of the quantized field ($\hat{H}_{\text{field}} = \hbar\omega(\hat{a}^\dagger\hat{a} + \frac{1}{2})$):

$$\begin{aligned}\frac{d\hat{a}}{dt} &= \frac{i}{\hbar}[\hat{H}_{\text{field}}, \hat{a}] = -i\omega_{\text{rf}}\hat{a} \quad \rightarrow \quad \hat{a}(t) = \hat{a}(0)e^{-i\omega_{\text{rf}}t} \\ \frac{d\hat{a}^\dagger}{dt} &= \frac{i}{\hbar}[\hat{H}_{\text{field}}, \hat{a}^\dagger] = i\omega_{\text{rf}}\hat{a}^\dagger \quad \rightarrow \quad \hat{a}^\dagger(t) = \hat{a}^\dagger(0)e^{i\omega_{\text{rf}}t}\end{aligned}\quad (2.178)$$

Now the same procedure is applied to the operators σ_- and σ_+ with the corresponding Hamiltonian $H_{\text{stat.field-spin}} = \frac{\hbar}{2}\omega_L\sigma_z$:

$$\begin{aligned}\frac{d\sigma_-}{dt} &= \frac{i}{\hbar}[\hat{H}_{\text{stat.field-spin}}, \sigma_-] = -i\omega_L\sigma_- \quad \rightarrow \quad \sigma_-(t) = \sigma_-(0)e^{-i\omega_L t} \\ \frac{d\sigma_+}{dt} &= \frac{i}{\hbar}[\hat{H}_{\text{stat.field-spin}}, \sigma_+] = i\omega_L\sigma_+ \quad \rightarrow \quad \sigma_+(t) = \sigma_+(0)e^{-i\omega_L t}\end{aligned}\quad (2.179)$$

Thus the four combinations of the operators are given by

$$\hat{a}(t)\hat{\sigma}_-(t) = \hat{a}(0)\hat{\sigma}_-(0)e^{-i(\omega_{\text{rf}}+\omega_L)t}, \quad \hat{a}^\dagger(t)\hat{\sigma}_+(t) = \hat{a}^\dagger(0)\hat{\sigma}_+(0)e^{i(\omega_{\text{rf}}+\omega_L)t}\quad (2.180)$$

and

$$\hat{a}(t)\hat{\sigma}_+(t) = \hat{a}(0)\hat{\sigma}_+(0)e^{i(\omega_L-\omega_{\text{rf}})t}, \quad \hat{a}^\dagger(t)\hat{\sigma}_-(t) = \hat{a}^\dagger(0)\hat{\sigma}_-(0)e^{i(\omega_{\text{rf}}-\omega_L)t}.\quad (2.181)$$

The two combinations in Eq.(2.180) ($\hat{a}(t)\hat{\sigma}_-(t)$ and $\hat{a}^\dagger(t)\hat{\sigma}_+(t)$) change very fast in time, due to the sum of the frequencies. However, for a long observation time (several periods of ω_{rf}) they average to zero.

Another argument is the following: The operator $\hat{a}(t)\sigma_-(t)$ decreases the energy of the total system by an amount of $-\hbar(\omega_{\text{rf}} + \omega_L)$. The spin is flipped from $|\uparrow\rangle$ to $|\downarrow\rangle$ and a photon is annihilated. the second operator ($\hat{a}^\dagger(t)\hat{\sigma}_+(t)$) increases the energy by $\hbar(\omega_{\text{rf}} + \omega_L)$, here the spin is flipped from $|\downarrow\rangle$ to $|\uparrow\rangle$ and a photon is created. Both

operators violate the energy conservation law. Thus they can only act within a very short time, within the time-energy uncertainty.

On the other hand the two combinations in Eq.(2.181) ($\hat{a}(t)\hat{\sigma}_+(t)$ and $\hat{a}^\dagger(t)\hat{\sigma}_-(t)$) preserve the energy in the resonance case ($\omega_{\text{rf}} = \omega_{\text{L}}$). The first operator ($\hat{a}(t)\hat{\sigma}_+(t)$) describes a scenario where the energy gained from the annihilation is absorbed by the neutron for the transition from $|\downarrow\rangle$ to $|\uparrow\rangle$. In the other case ($\hat{a}^\dagger(t)\hat{\sigma}_-(t)$) the energy released by the flip from $|\uparrow\rangle$ to $|\downarrow\rangle$ is exploited for the creation of a photon. Therefore both operators have only a weak time-dependency close to the resonance and their time evolution can be neglected. This together with the neglect of the two operators in Eq.(2.180) yields the following approximation for the total Hamiltonian:

$$\hat{H}_{\text{J-C}} = \underbrace{\hbar\omega_{\text{rf}}\left(\hat{a}^\dagger\hat{a} + \frac{1}{2}\right)}_{\hat{H}_{\text{rf-field}}} + \underbrace{\frac{\hbar}{2}\omega_{\text{L}}\sigma_z}_{\hat{H}_{\text{stat.field-spin}}} + \underbrace{\hbar\Omega_0(\hat{a}\hat{\sigma}_+ + \hat{a}^\dagger\hat{\sigma}_-)}_{\hat{H}'_{\text{int}}}. \quad (2.182)$$

$\underbrace{\hspace{15em}}_{\hat{H}_0}$

This approximation is the quantized version of the rotating wave approximation. Now the time evolution of the total Hamiltonian \hat{H} can be derived analytically. The eigenvectors of \hat{H}_0 are elements of the product space of the eigenvectors of $\hat{H}_{\text{rf-field}}$ and $\hat{H}_{\text{stat.field-spin}}$ denoted as $|\uparrow, n\rangle$ and $|\downarrow, n\rangle$. Concerning the energy eigenvalues the following equations are found:

$$\begin{aligned} \hat{H}_0|\uparrow, n\rangle &= \hbar\left(\frac{\omega_{\text{L}}}{2}\left(n + \frac{1}{2}\right)\omega_{\text{rf}}\right)|\uparrow, n\rangle \\ \hat{H}_0|\downarrow, n\rangle &= \hbar\left(-\frac{\omega_{\text{L}}}{2}\left(n + \frac{1}{2}\right)\omega_{\text{rf}}\right)|\downarrow, n\rangle \end{aligned} \quad (2.183)$$

In order to sort this infinite number of eigenstates one should take a look at the action of the interaction Hamiltonian H'_{int} , which connects the vectors $|\uparrow, n\rangle$ and $|\downarrow, n+1\rangle$. Thus it is useful to decompose the eigenvector system of H_0 into n two-dimensional, orthogonal subspaces R_{E_n} , where each contains two and only two eigenstates states denoted as $|\uparrow, n\rangle$ and $|\downarrow, n+1\rangle$. To analyze the action of the total Hamiltonian H also H is decomposed with components H_n acting on one subspace:

$$\hat{H}_{\text{J-C}} = \sum_{n=0}^{\infty} \hat{H}_n^{\text{J-C}} \quad (2.184)$$

The operators H_n can now be rewritten in a $\{|\uparrow, n\rangle, |\downarrow, n+1\rangle\}$ -basis, which yields

$$\hat{H}_n^{\text{J-C}} = \frac{\omega_L}{2} \begin{pmatrix} 1 & 0 \\ 0 & -1 \end{pmatrix} + \hbar\omega_{\text{rf}} \begin{pmatrix} n + \frac{1}{2} & 0 \\ 0 & n + \frac{3}{2} \end{pmatrix} + \hbar\frac{\Omega_0}{2} \begin{pmatrix} 0 & \sqrt{n+1} \\ \sqrt{n+1} & 0 \end{pmatrix} \quad (2.185)$$

introducing the detuning Δ (resonance is found for $\Delta = 0$)

$$\Delta = \omega_L - \omega_{\text{rf}}, \quad (2.186)$$

Eq.(2.185) can be rearranged as

$$\hat{H}_n^{\text{J-C}} = \hbar(n+1)\omega_{\text{rf}} \begin{pmatrix} 1 & 0 \\ 0 & 1 \end{pmatrix} + \frac{\hbar}{2} \begin{pmatrix} \Delta & \Omega_n \\ \Omega_n & \Delta \end{pmatrix}, \quad (2.187)$$

with $\Omega_n = \Omega_0\sqrt{n+1}$. The eigenvalues are given by

$$\begin{aligned} E_{+n} &= \hbar(n+1)\omega_{\text{rf}} + \frac{\hbar}{2}\sqrt{\Delta^2 + \Omega_n^2} \\ E_{-n} &= \hbar(n+1)\omega_{\text{rf}} - \frac{\hbar}{2}\sqrt{\Delta^2 + \Omega_n^2} \end{aligned} \quad (2.188)$$

The term $\sqrt{\Delta^2 + \Omega_n^2} := R_n$ is referred to as *quantized Rabi frequency*. Using the transformation matrix T_n a new eigensystem is defined denoted as

$$\begin{pmatrix} |+, n\rangle \\ |-, n\rangle \end{pmatrix} = T_n \begin{pmatrix} |\uparrow, n\rangle \\ |\downarrow, n+1\rangle \end{pmatrix}, \quad (2.189)$$

where

$$T_n = \begin{pmatrix} \cos \Theta_n & \sin \Theta_n \\ -\sin \Theta_n & \cos \Theta_n \end{pmatrix}, \quad (2.190)$$

with

$$\begin{aligned} \cos \Theta_n &= \frac{R_n - \Delta}{\sqrt{(R_n - \Delta)^2 + \Omega_n^2}} \\ \sin \Theta_n &= \frac{\Omega_n}{\sqrt{(R_n - \Delta)^2 + \Omega_n^2}}. \end{aligned} \quad (2.191)$$

The state $|\Psi(0)\rangle = |\uparrow, 0\rangle$ will then evolve in time as

$$|\Psi(t)\rangle = e^{-i(\omega_{\text{rf}} - \Delta)t} \left(-\cos \frac{\Theta_n}{2} e^{-i\Omega_n t/2} |+, n\rangle + \sin \frac{\Theta_n}{2} e^{i\Omega_n t/2} |-, n\rangle \right). \quad (2.192)$$

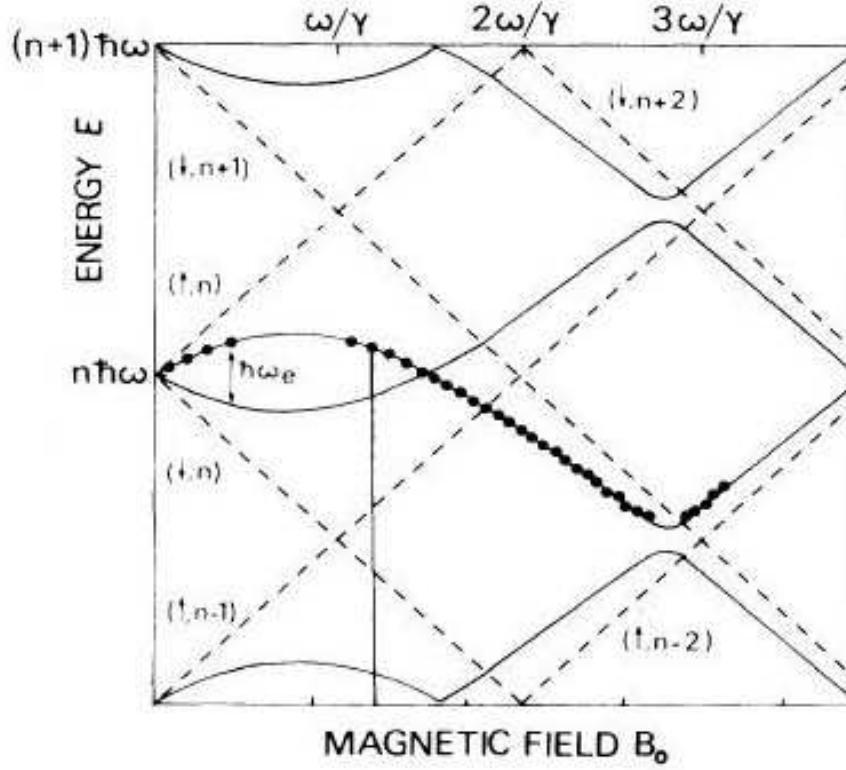


Figure 2.17: Energy level diagram for dressed neutron states as depicted in [Muskat et al., 1987]. The dashed lines represent the Zeeman splitting. The energy levels repeal each other due to the coupling ($+H_{\text{int}}$) between neutron and photon field.

The states $|+, n\rangle$ and $|-, n\rangle$ are the *dressed-neutron states*, whereas $|\uparrow, n\rangle$ and $|\downarrow, n+1\rangle$ are the uncoupled (*bare*) states.

The Hamiltonian for the dressed states can be written in form of

$$H_n^{\text{dr.st.}} = \hbar(n+1)\omega_{\text{rf}} \begin{pmatrix} 1 & 0 \\ 0 & 1 \end{pmatrix} + \frac{\hbar}{2} \begin{pmatrix} -R_n & 0 \\ 0 & R_n \end{pmatrix}, \quad (2.193)$$

with the corresponding eigenstates

$$\begin{aligned} |+, n\rangle &= \cos \frac{\Theta_n}{2} |\uparrow, n\rangle + i \sin \frac{\Theta_n}{2} |\downarrow, n+1\rangle \\ |-, n\rangle &= \sin \frac{\Theta_n}{2} |\uparrow, n\rangle - i \cos \frac{\Theta_n}{2} |\downarrow, n+1\rangle, \end{aligned} \quad (2.194)$$

A graphical representation of the measured energy of the dressed states for neutrons in an oscillating magnetic field [Muskat et al., 1987] is given in Fig. 2.17. It can easily be seen

shown, that an initial state $|\Psi_0\rangle = |\uparrow, 0\rangle$ is not stationary for the description of the coupled system. Therefore one has to find the inverse relations of Eq.(2.194) given by

$$\begin{aligned} |\uparrow, n\rangle &= -\cos\frac{\Theta_n}{2}|+, n\rangle + \sin\frac{\Theta_n}{2}|-, n\rangle \\ |\downarrow, n+1\rangle &= \sin\frac{\Theta_n}{2}|+, n\rangle + \cos\frac{\Theta_n}{2}|-, n\rangle, \end{aligned} \quad (2.195)$$

Thus the probability that the system flips from $|\uparrow, 0\rangle$ to $|\downarrow, 1\rangle$ is

$$p = |\langle\downarrow| \langle 1|\Psi(t)\rangle|^2 = \frac{Q_1^2}{\Omega_1^2} \sin^2 \frac{\Omega_1^2 t}{2}. \quad (2.196)$$

Finally the situation is discussed where the field is initially in a coherent state $|\alpha\rangle$. Here the initial state is given by $|\Psi(0)\rangle = |\uparrow\rangle \otimes |\alpha\rangle$, which can be written in terms of the dressed states:

$$\begin{aligned} |\Psi(t)\rangle &= |\uparrow\rangle \otimes |\alpha\rangle = e^{-|\alpha|^2/2} \sum_{n=0}^{\infty} \frac{\alpha^n}{\sqrt{n!}} |\uparrow, n\rangle \\ &= e^{-|\alpha|^2/2} \sum_{n=0}^{\infty} \frac{\alpha^n}{\sqrt{n!}} \left(-\cos\frac{\Theta_n}{2}|+, n\rangle(t) + \sin\frac{\Theta_n}{2}|-, n\rangle(t) \right), \end{aligned} \quad (2.197)$$

where the time dependences of the dressed states is given by

$$|\pm, n\rangle(t) = e^{-iE_{\pm n}\hbar/t} |\pm, n\rangle. \quad (2.198)$$

This is exactly used in the in the description of the experiments presented in this thesis.

2.3 Geometric Phase for Two-Level Systems

In the language of quantum mechanics a pure physical state is represented by a state vector in Hilbert space. From this state one can calculate the probability of finding the particle at a specific place with a certain spin. Furthermore, the state vector carries phase information, a non-physical property that cannot be measured in an intensity measurement. However, a *phase difference* between states vectors is a physical quantity, giving rise to the phenomenon of *interference*. Phase accumulation is, at first sight, a consequence of dynamics of the state evolutions. In addition to and independent of this dynamical phase M. V. Berry discovered in the beginning of the eighties of the last century a phase due to the geometrical origin of the state evolution [Berry, 1984].

The total phase acquired during an evolution of a quantal system generally consists of two components: the usual dynamical phase $-1/\hbar \int H(t)dt$, which depends on the dynamical properties, like energy or time, and a geometric phase γ , which is, considering a spin- $\frac{1}{2}$ system, minus half the solid angle ($\Omega/2$) of the curve traced out in ray space. The peculiarity of *Berry's phase* lies in the fact that it does not depend on the dynamics of the system, but purely on the evolution path of the state in parameter space.

Since its discovery by Berry the topological concept has been widely expanded and has undergone several generalizations. The first experimental evidence of an adiabatic and cyclic geometric phase, commonly called Berry phase, was achieved with photons in 1986 [Tomita and Chiao, 1986] and later with neutrons [Bitter and Dubbers, 1987]. Generalizations such as non-adiabatic [Aharonov and Anandan, 1987], non-cyclic [Samuel and Bhandari, 1988], and off-diagonal evolutions, where initial and final states are mutually orthogonal [Manini and Pistoiesi, 2000], have been considered. Corresponding experimental verification using neutrons for a cyclic geometric phase [Hasegawa et al., 1996], as well as non-cyclic evolutions [Wagh et al., 1998, Weinfurter and Badurek, 1990, Filipp et al., 2005], and off-diagonal evolutions have been demonstrated [Hasegawa et al., 2001, Hasegawa et al., 2002]. In addition to an early approach by Uhlmann [Uhlmann, 1991], an alternative concept of the geometric phase for mixed input states based on interferometry was developed by Sjöqvist *et al* [Sjöqvist et al., 2000]. Theoretical predictions have been tested using NMR [Du et al., 2003], single-photon interferometry [Du et al., 2003, Ericsson et al., 2005] and

neutron polarimetry [Klepp et al., 2008]. The idea has also been extended to the off-diagonal case [Filipp and Sjöqvist, 2003b, Filipp and Sjöqvist, 2003a].

2.3.1 Classic analogue of Berry's phase

For understanding the concept of *geometric phases* it is instructive to study an analogue from elementary geometry first. A vector pointing to an arbitrary direction is placed on the surface of a sphere. Now this vector is transported along a *geodesic* to the equator, along the equator and finally back to the starting point. During this transport the vector has to stay tangential to the surface. It does not change its magnitude and the angle between the vector and the geodesic path is kept constant at any time. If all these conditions are fulfilled during the whole process the transport is called *parallel transport*, which is depicted in Fig.2.18. After finishing the excursion the vector has changed its direction by an angle α . This angle α equals the solid angle Ω enclosed by the loop,

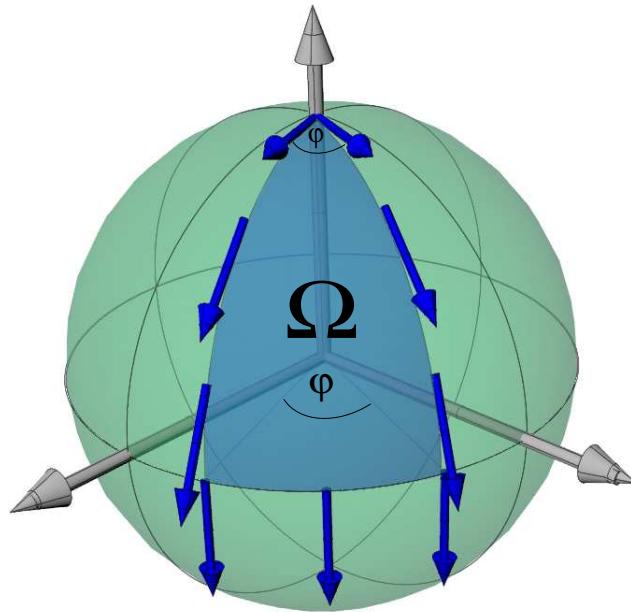


Figure 2.18: Parallel transport of a vector on a sphere.

$\Omega = \frac{1}{2}4\pi\frac{\alpha}{2\pi}$, since $\frac{1}{2}4\pi$ is the solid angle of a half-sphere and $\frac{\alpha}{2\pi}$ is the portion surrounded by the loop shown in Fig. 2.18.

2.3.2 Derivation of Berry's phase

Adiabatic, cyclic evolution

The concept introduced in Sec. 2.3.1 can be generalized to any surface using a proper definition of parallel transport. However, for the discussion of geometric phase, tied to the evolution within the spin subspace, a sphere is sufficient, since for a two-level system the state can be represented on a Bloch sphere.

In 1984 a paper was published in which by M.V. Berry described the geometric phase acquired by transporting a quantal system governed by the Hamiltonian $\hat{H}(\vec{R}(t))$ depending on the parameters \vec{R} . The parameters change slowly, which means that *adiabatic* transformation is assumed. Consequently the system will remain in eigenstates of $\hat{H}(\vec{R}(t))$ at any time t . For a cyclic evolution $\vec{R}(\tau) = \vec{R}(0)$ the Hamiltonian takes on its original form at the final time τ and the system returns to its initial state. Thereby the state has been transported around a loop $\hat{C} : t \in [0, \tau] \rightarrow |\psi(t)\rangle$ in *parameter space*. Here $|\psi(t)\rangle$ is denoting the instantaneous state of the system, which is equivalent to the eigenstate $|n(\vec{R}(t))\rangle$.

The time evolution of the system is given by the *Schrödinger equation*

$$\hat{H}(\vec{R}(t))|\psi(t)\rangle = i\hbar\frac{d}{dt}|\psi(t)\rangle. \quad (2.199)$$

An eigenstate of $\hat{H}(\vec{R}(t))$ at time $t = 0$ is given by

$$|\psi(0)\rangle = |n(\vec{R}(0))\rangle. \quad (2.200)$$

A solution at time t therefore is denoted as

$$|\psi(t)\rangle = e^{i\Phi_n(t)}|n(\vec{R}(t))\rangle, \quad (2.201)$$

with $|n(\vec{R}(t))\rangle$ as an eigenstate of $\hat{H}(\vec{R}(t))$ with energy $E_n(\vec{R}(t))$. To calculate $\Phi_n(t)$ Eq.(2.201) has to be inserted in Eq.(2.199) which results in

$$-i\hbar\left(i\frac{d\Phi_n(t)}{dt}e^{i\Phi_n(t)}|n(\vec{R}(t))\rangle + e^{i\Phi_n(t)}\frac{d}{dt}|n(\vec{R}(t))\rangle\right) = e^{i\Phi_n(t)}E_n(\vec{R}(t))|n(\vec{R}(t))\rangle, \quad (2.202)$$

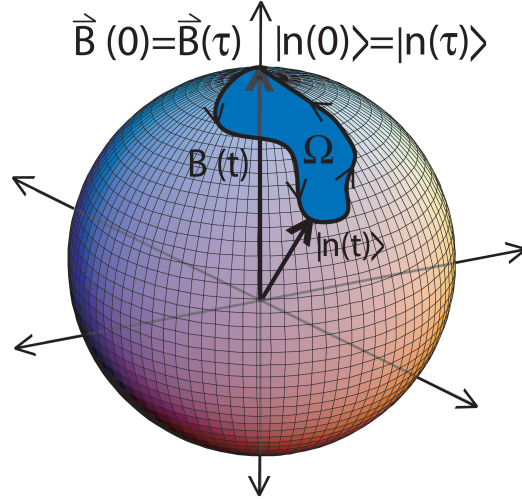


Figure 2.19: Curve \mathcal{C} traced out on the Bloch sphere encloses the solid angle Ω which is proportional to the geometric phase. The parameter space of the magnetic field can be identified with the state space of a spin-1/2 particle, as long as the magnitude of the magnetic field is kept constant.

multiplied by $\langle n(\vec{R}(t)) | e^{-i\phi_n(t)}$ from the left side one gets

$$\begin{aligned} -\hbar \frac{d\Phi_n(t)}{dt} + i\hbar \langle n(\vec{R}(t)) | \frac{d}{dt} | n(\vec{R}(t)) \rangle &= E_n(\vec{R}(t)) \\ \frac{d\Phi_n(t)}{dt} &= -\frac{1}{\hbar} E_n(\vec{R}(t)) + i \langle n(\vec{R}(t)) | \frac{d}{dt} | n(\vec{R}(t)) \rangle. \end{aligned} \quad (2.203)$$

A solution can be found by integrating Eq.(2.203)

$$\Phi_n(\tau) = -\frac{1}{\hbar} \int_0^\tau E_n(\vec{R}(t)) dt + i \int_0^\tau \langle n(\vec{R}(t)) | \frac{d}{dt} | n(\vec{R}(t)) \rangle, \quad (2.204)$$

and applying the chain rule

$$\langle n(\vec{R}(t)) | \frac{d}{dt} | n(\vec{R}(t)) \rangle = \frac{d\vec{R}(t)}{dt} \langle n(\vec{R}) | \vec{\nabla}_{\vec{R}} | n(\vec{R}) \rangle, \quad (2.205)$$

which finally leads to

$$\Phi_n(\tau) = -\frac{1}{\hbar} \int_0^\tau E_n(\vec{R}(t)) dt + i \oint_0^\tau \langle n(\vec{R}) | \vec{\nabla}_{\vec{R}} | n(\vec{R}) \rangle, \quad (2.206)$$

for a closed path \mathcal{C} in the *parameter space* with $|n(\vec{R}(T))\rangle = |n(\vec{R}(0))\rangle$, which is depicted in Fig.2.19. The first term corresponds to the usual expression of the phase accumulated

by a system in a state with energy $E(t)$ for a time τ , and is referred to as the *dynamical phase*.

$$\delta_n = -\frac{1}{\hbar} \int_0^\tau E_n(\vec{R}(t)) dt. \quad (2.207)$$

The *geometric phase* is defined by the second term given by

$$\gamma_n(\mathcal{C}) = i \oint_0^\tau \langle n(\vec{R}) | \vec{\nabla}_{\vec{R}} | n(\vec{R}) \rangle. \quad (2.208)$$

As long as the magnetic field changes slowly, the system will remain in an eigenstate for all times t and the geometric and dynamical phase components are given by δ_n and $\gamma_n(\mathcal{C})$.

Example - Neutron in a magnetic field

Considering a system consisting of a neutron in a magnetic field with a Hamiltonian for the interaction between the spin and magnetic field is denoted as

$$\hat{H}_{\text{mag}}(\vec{B}(t)) = \gamma \hat{S} \vec{B}(t) = \vec{\mu} \vec{B}(t), \quad (2.209)$$

where $\hat{S} = \hbar/2(\sigma_x, \sigma_y, \sigma_z)$ is the spin operator with the components of $\vec{B}(t)$ identified with the parameter $\vec{R}(t)$. As already discussed in Section 2.1 an arbitrary spin state can be parameterized in terms of the polar and azimuthal angle φ and ϑ , respectively:

$$|\psi\rangle = \cos \frac{\vartheta}{2} |\uparrow\rangle + e^{i\varphi} \sin \frac{\vartheta}{2} |\downarrow\rangle \quad (2.210)$$

In the simplest case \vec{B} is static and direction of the magnetic field defines the quantisation axis, thus the Hamiltonian is given by

$$\hat{H}_{\text{mag}} = -\mu \vec{B} \sigma_z. \quad (2.211)$$

The time evolution of a neutron, initially in the eigenstate $|\psi(0)\rangle = |\uparrow\rangle$, according to the Schrödinger equation is denoted as

$$|\psi(t)\rangle = e^{i\hat{H}_{\text{mag}}t/\hbar} |\psi(0)\rangle. \quad (2.212)$$

The phase factor

$$e^{i\hat{H}_{\text{mag}}t/\hbar} = e^{i-\mu\vec{B}\sigma_z t/\hbar} = \cos\left(\frac{\omega_L t}{2}\sigma_z\right) + i \sin\left(\frac{\omega_L t}{2}\sigma_z\right), \quad (2.213)$$

where the Larmor frequency is

$$\omega_L = \frac{2\mu\vec{B}}{\hbar} = \gamma\vec{B}, \quad (2.214)$$

and series expansion yields

$$e^{i\hat{H}_{\text{mag}}t/\hbar} = \cos\left(\frac{\omega_L t}{2}\right) + i\sigma_z \sin\left(\frac{\omega_L t}{2}\right). \quad (2.215)$$

Thus the final state at $t = \tau$ is

$$|\psi(\tau)\rangle = e^{i\omega_L\tau/\hbar}|\psi(0)\rangle, \quad (2.216)$$

where the phase factor $e^{i\omega_L\tau/\hbar}$ denotes the dynamical phase proportional to the Zeeman energy. Since there is no evolution path in parameter space, caused by the Hamiltonian, there is no geometric phase.

A completely different situation arises for a slowly changing of the Hamiltonian, assuming an adiabatic evolution. Here the neutron spin direction will be pinned to the direction of the magnetic field $\vec{B}(t)$ at any time, thereby remaining in an eigenstate of the Hamiltonian. Thus the state will acquire in addition a geometric (*Berry*) phase $\gamma_n(\mathcal{C})$, which is independent of the Larmor frequency ω_L . The magnetic field $\vec{B}(t)$ is parameterized by the direction spherical coordinates $\theta_B(t)$ and $\phi_B(t)$, respectively:

$$\vec{B}(t) = B\vec{n}(t) \quad \text{with} \quad \vec{n}(t) = \begin{pmatrix} \cos\phi_B(t) \sin\theta_B(t) \\ \sin\phi_B(t) \sin\theta_B(t) \\ \cos\theta_B(t). \end{pmatrix} \quad (2.217)$$

The corresponding eigenstates of the Hamiltonian $\hat{H} = -\mu B\vec{n}(t) \cdot \vec{\sigma}$ are given by

$$\begin{aligned} |\psi_\uparrow\rangle &= \cos\frac{\theta_B(t)}{2}|\uparrow\rangle + e^{i\phi_B(t)}\sin\frac{\theta_B(t)}{2}|\downarrow\rangle \\ |\psi_\downarrow\rangle &= \sin\frac{\theta_B(t)}{2}|\uparrow\rangle - e^{i\phi_B(t)}\cos\frac{\theta_B(t)}{2}|\downarrow\rangle. \end{aligned} \quad (2.218)$$

In order to derive the geometric phase associated to the spin-up state, as defined in Eq.(2.208), one has to calculate $\gamma_n(\mathcal{C}) = i\oint_0^\tau \langle n(\vec{R})|\vec{\nabla}_{\vec{R}}|n(\vec{R})\rangle$, where $|n(\vec{R})\rangle$ is given by $|\psi_\uparrow\rangle$ with

$$\begin{aligned} \langle\psi_\uparrow|\frac{\partial}{\partial\theta_B}|\psi_\uparrow\rangle &= 0 \\ \langle\psi_\uparrow|\frac{\partial}{\partial\phi_B}|\psi_\uparrow\rangle &= i\sin^2\frac{\theta_B}{2} = \frac{i}{2}(1 - \cos\theta_B). \end{aligned} \quad (2.219)$$

When an evolution along a circle of latitude was chosen, which yields a constant θ_B . Finally Berry's phase is obtained by integration

$$\gamma_n^\uparrow(\mathcal{C}) = i \int_0^{2\pi} \frac{i}{2} (1 - \cos \theta_B) d\phi_B = -\pi(1 - \cos \theta_B) = -\frac{\Omega}{2}. \quad (2.220)$$

For example if $\theta_B = \pi/2$, a walk along the equatorial line, Berry's phase is obtained as $\gamma_n^\uparrow(\mathcal{C}) = -\pi$, which is minus half of the solid angle (2π) as seen from the origin.

For a longitude (geodesic) evolution along θ_B one always finds

$$\gamma_n^\uparrow(\mathcal{C}) = i \int_0^{2\pi} \frac{i}{2} (1 - \cos \theta_B) d\theta_B = -\pi = -\frac{\Omega}{2}. \quad (2.221)$$

2.3.3 The geometric phase of Aharonov and Anandan

Non-adiabatic, cyclic evolution

In 1987, Berry's phase was generalized by Aharonov and Anandan [Aharonov and Anandan, 1987]. They extended Berry's result for a special case in the adiabatic approximation, to non-adiabatic and any cyclic evolution of a quantum system (for example a spinning particle in a static magnetic field).

The key idea of this new concept is to associate the geometric phase with the closed curve in the *projective Hilbert space* instead of the parameter space of the Hamiltonian. Therefore the projective Hilbert or *ray space* has to be introduced: It is a general property of quantum-mechanical states that they are only defined modulo a $U(1)$ phase factor, having no physical relevance. All states that differ merely by a phase factor give rise to the same physics. One might think at the first moment that discussions about the geometric phase are insignificant from this point of view, but a relative phase difference between two states in superposition, such as $|\Psi\rangle = |\psi\rangle + e^{i\Phi}|\psi'\rangle$ results in a different state. Only global phases can be neglected, for example $|\Psi\rangle$ and $e^{i\Phi'}|\Psi\rangle$ are indistinguishable.

Assume a system evolves in a cyclic evolution, after one cycle the system is described as

$$|\psi(\tau)\rangle = e^{i\Phi}|\psi(0)\rangle \quad \text{with } \Phi \text{ real.} \quad (2.222)$$

The curve traced out in Hilbert space \mathcal{H} has an image in the projective Hilbert space \mathcal{P} as depicted in Fig. 2.20. Mathematically the projective space is defined over a projective

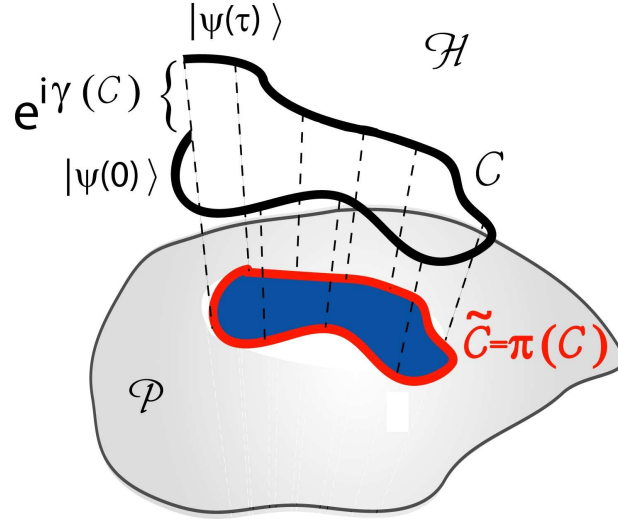


Figure 2.20: Projective Hilbert space (ray space) with an open curve \mathcal{C} in Hilbert space \mathcal{H} and projection (closed curve) $\tilde{\mathcal{C}} = \pi(\mathcal{C})$ in projective Hilbert space \mathcal{P} . The rays denote states differing only by a $U(1)$ phase factor.

map $\pi : \mathcal{H} \rightarrow \mathcal{P}$, where

$$\pi(|\psi\rangle) = \{|\psi^c\rangle : |\psi^c\rangle = c|\psi\rangle, c \text{ is a nonvanishing complex number}\}. \quad (2.223)$$

So the projective Hilbert space is a space in which an element is an equivalence class of state vectors that differ by multiplication by a nonvanishing complex number. Hence, now one can add additional phases at any point along the curve without changing the curve in projective Hilbert space. Suppose a state $|\phi(t)\rangle$ is given by

$$|\phi(t)\rangle = e^{-if(t)}|\psi(t)\rangle \quad \text{with} \quad f(t) - f(\tau) = \Phi \quad (2.224)$$

Then, according to Eq.(2.222) $|\phi(\tau)\rangle = |\phi(0)\rangle$ and the Schrödinger equation Eq.(2.199) one finds

$$\frac{df}{dt} = -\frac{1}{\hbar}\langle\psi(t)|\hat{H}|\psi(t)\rangle + i\langle\phi(t)|\frac{d}{dt}|\phi(t)\rangle. \quad (2.225)$$

The projections in \mathcal{P} of the curves traced out by $|\psi(t)\rangle$ and $|\phi(t)\rangle$ are the same (such as an infinite number of other curves). However, the particular choice for $f(t)$, according to Eq.(2.224), has the advantage that the final phase difference Φ can be split into a

dynamical and a geometrical part as before. Integration of Eq.(2.225) results in

$$f(\tau) - f(0) = -\frac{1}{\hbar} \int_0^\tau \langle \psi(t) | \hat{H} | \psi(t) \rangle dt + i \int_0^\tau \langle \phi(t) | \frac{d}{dt} | \phi(t) \rangle dt = \Phi, \quad (2.226)$$

where the dynamical part is given by the first term

$$\delta = -\frac{1}{\hbar} \int_0^\tau \langle \psi(t) | \hat{H} | \psi(t) \rangle dt, \quad (2.227)$$

and the geometric phase arises from the second term and can be written as

$$\gamma(\mathcal{C}) = \Phi + \frac{1}{\hbar} \int_0^\tau \langle \psi(t) | \hat{H} | \psi(t) \rangle dt = i \int_0^\tau \langle \phi(t) | \frac{d}{dt} | \phi(t) \rangle dt. \quad (2.228)$$

Since there are many curves $\mathcal{C} \in \mathcal{H}$ projecting on to the same $\tilde{\mathcal{C}} \in \mathcal{P}$ and one can find the same $|\phi(t)\rangle$ for all these Hamiltonians (due to an appropriate choice of $f(t)$) the phase factor $e^{i\gamma_n(\mathcal{C})}$ is independent of \hat{H} . So it does not depend on the choice of Hilbert space representation. Furthermore is $\gamma(\mathcal{C})$ independent of the choice of the parameter t (reparametrisation invariance) and is uniquely defined up to $2\pi n$, where n is an integer: Considering two curves \mathcal{C}' and \mathcal{C}'' with the same $\tilde{\mathcal{C}} \in \mathcal{P}$ traced out by the state vectors $|\psi(t)'\rangle$ and $|\psi(t)''\rangle$ respectively with $|\psi(t)''\rangle = e^{i\alpha(t)} |\psi(t)'\rangle$, where $\alpha(\tau) - \alpha(0) = 2n\pi$. They have the same geometric phase factor due to

$$\begin{aligned} \gamma(\mathcal{C}) &= i \int_0^\tau \langle \psi(t)'' | \frac{d}{dt} | \psi(t)'' \rangle dt = i \int_0^\tau (i\dot{\alpha}(t) + \langle \psi(t)' | \frac{d}{dt} | \psi(t)' \rangle) dt \\ &= 2\pi n + i \int_0^\tau \langle \psi(t)' | \frac{d}{dt} | \psi(t)' \rangle dt. \end{aligned} \quad (2.229)$$

Therefore all curves in \mathcal{H} that project to the same closed curve in \mathcal{P} have the same geometric phase modulo 2π .

2.3.4 Related experiments

First experimental demonstrations of Berry's phase by use of optical fiber

In 1986 the first experimental verification of Berry's topological phase was reported by A. Tomita and R. Y. Chiao in Berkeley, at the university of California [Tomita and Chiao, 1986]. The key element in this pioneering experiment was a single mode, helically wounded optical fiber. Within this fiber a photon of given helicity could be adiabatically transported around a closed loop in momentum space. The experiment clearly confirmed the topological nature of Berry's phase, by applying several deformations to the fiber path. The final angle of rotation of linearly polarized light was found to be independent of these deformations as long as the solid angle of the path in momentum space remained constant.

A schematic representation of the setup is depicted in Fig. 2.21 (a). Using a He-Ne laser and a pair of linear polarizers (one at each end of the fiber) the rotation angle of the plane of polarization could be measured in a 180 cm long single mode fiber. The fiber was

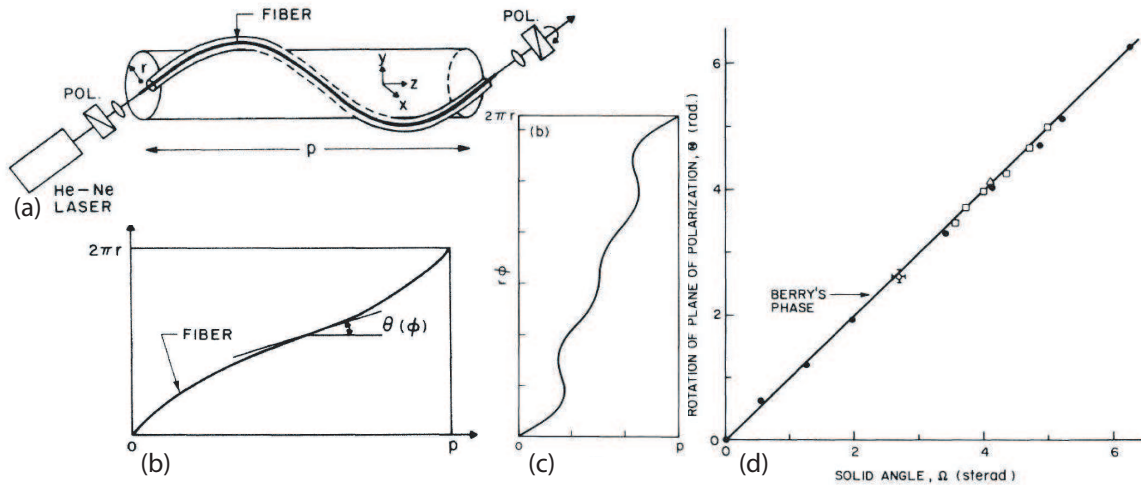


Figure 2.21: (a) Experimental setup from [Tomita and Chiao, 1986] to obtain Berry's phase. (b) Geometry used to calculate the solid angle in momentum space of twisted fiber. (c) Path of nonuniform helix due to deformations. (d) Measured angle of rotation vs. calculated solid angle in momentum space. The solid line represents the theoretical predictions based on Berry's phase.

wounded helically around a tube, with the output end of the fiber free to rotate. In order to form a closed circuit \mathcal{C} in momentum space the propagation directions of the input and output of the fiber were kept identical.

In a first run the fiber was wound into a uniform helix, with a variable pitch angle θ , thereby changing the pitch length p as well as the radius r (but the fiber length remained constant). With this geometry $\cos \theta = p/s$ a solid angle in momentum space, in this particular case surrounded by a circle, and given by

$$\Omega(\mathcal{C}) = 2\pi(1 - \cos \theta), \quad (2.230)$$

was obtained (see Fig. 2.21 (b)). Thus yielding a Berry's phase of $\gamma(\mathcal{C}) = \sigma\Omega(\mathcal{C})$, with $\sigma = \pm 1$ being the helicity quantum number of the photon.

The experiment was repeated using different deformations i.e variations of the path \mathcal{C} of the fiber, having the same solid angle Ω , subtended by \mathcal{C} , which is illustrated in Fig. 2.21 (c). Here the solid angle is given by

$$\Omega(\mathcal{C}) = \int_0^{2\pi} (1 - \cos \theta(\phi)) d\phi. \quad (2.231)$$

Figure 2.21 (d) shows the measured rotation Θ angle versus the calculated solid angle Ω . Open circles represent data from uniform helices and squares or triangles from non uniform helices. One can clearly see that in all cases the measured rotation angles Θ agree with the calculated magnitude of Berry's phase $\gamma(\mathcal{C})$.

Experimental verification of Berry's phase using slow neutrons

Only one year later T. Bitter and D. Dubbers reported the first demonstration of Berry's phase with a fermion system [Bitter and Dubbers, 1987]. Phase was acquired by spinor rotations due to an adiabatic transport of the magnetic field vector around a closed loop \mathcal{C} , using a twisted magnetic field.

The experiment was carried out at the high-flux reactor at the ILL, Grenoble, using a slow (500 m/s), monochromatic beam. The setup is arranged in such way that the direction of the polarization vector of the neutrons entering the cylinder can be chosen arbitrarily, as can the component of polarization analyzed afterwards. Within the cylinder the neutrons enter and leave a static helical magnetic field, which is perpendicular to the

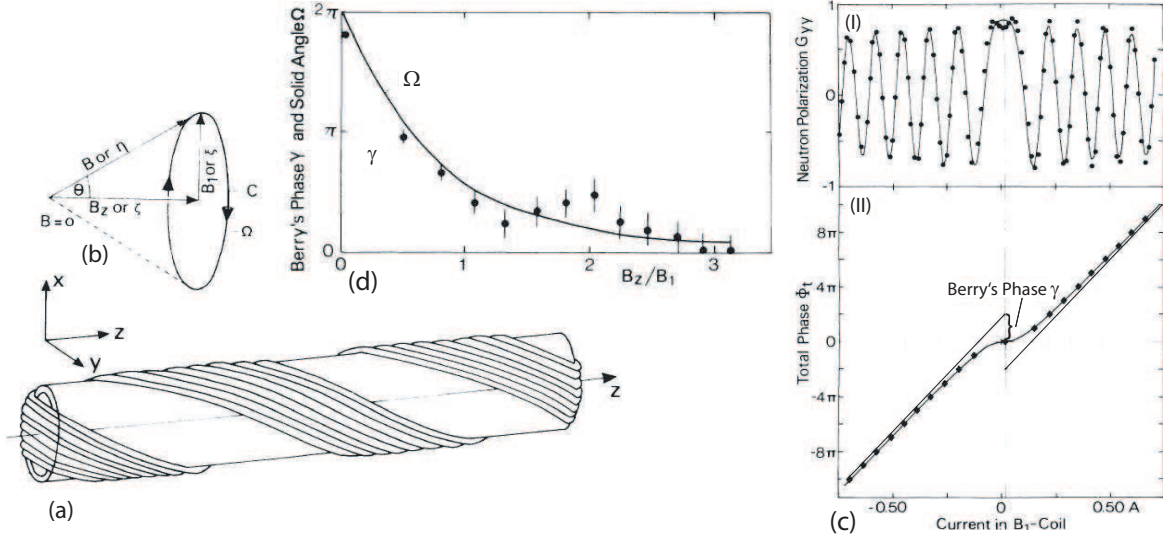


Figure 2.22: (a) Arrangement of the helical coil for right handed B_1 , with beam along the z -direction from [Bitter and Dubbers, 1987]. (b) Solid angle Ω according to the magnetic field components B_1 and B_z . (cI) neutron spin rotation patterns. (cII) Observed and calculated phase shifts Φ_t . (d) Berry's phase γ at different solid angles Ω , due to variations of the fraction B_z/B_1 .

propagation direction of the neutrons within the beam. The field accounts for a complete right turn about the beam axis. The coil, producing the magnetic field is wound along the surface of a hollow cylinder, which is 40 cm long and 8 cm in diameter, as seen in Fig.2.22 (a). A second coil is wound onto the first but in opposite direction. The resulting combination can be applied to produce an elliptically polarized rotating field. The purpose of this arrangement is to prove that independence of Berry's phase from the contour \mathcal{C} in parameter space, as long as the solid angle Ω traced out is kept fixed.

The opening angle of the path \mathcal{C} is $\omega = \pm 2\pi$ if only B_1 is applied. Other values of Ω can be achieved by imposing an additional axial static field, denoted as B_z (see Fig.2.22 (b)). Figure 2.22 (cI) shows a measurement of the polarization G_{yy} , with $B_z = 0$ and $P_\beta(T) = G_{\alpha\beta}(T)P_\alpha(0)$, with $P_\alpha(0)$ being the initial polarization and $P_\beta(T)$ the polarization component after leaving the field region. Without Berry's phase the patterns in Fig. 2.22 (cI) would be of simple cosine type. Figure. 2.22 (cII) shows the B_1 dependence of the measured phase angle Φ_t . Finally in Fig. 2.22 (d) Berry's phase γ is

depicted as a function B_1/B_z . The solid curve denotes the calculated values for the solid angle $\Omega = 2\pi(1 - B_1/B_z)$.

With this measurements Berry's law has been verified for fermions using a straightforward realization of a topological phase experiment. As seen in Fig. 2.22 (c I) the total phase Φ_t is dominated by the dynamical phase δ_n , being much larger compared to the geometric phase γ . Thus the separation of the geometric phase γ from the total phase Φ_t was an impressive experimental achievement here.

Geometric phase experiments in nuclear magnetic resonance (NMR)

Berrys phase in NMR

At the same time NMR experiments, in the rotating frame, have confirmed the predictions of Berry for simple conical circuits, with a slowly in time varying Hamiltonian. For the simplest case of a cone, with opening angle θ constant the solid angle is given by $\Omega = 2\pi(1 - \cos \theta)$. In case that such a conical circuit is traversed adiabatically, that is with small δ , where $\delta = 2\pi/\tau$ and τ is the period of the circuit. A spin eigenstate with magnetic quantum number m should accumulate a geometrical phase $\gamma(\mathcal{C}) = 2\pi m(1 - \cos \theta)$ in addition to the dynamical phase. In the experiment performed by Suter and his co-workers [Suter et al., 1987] in Berkeley, at the university of California, they measured the Berry phase acquired by a spin-1/2 in a magnetic field of constant magnitude and varying direction in the rotating frame. The Experiment was performed on the proton spins of a water/acetone sample in a superconducting magnet. The experimental outline is the following: An ensemble of spin-1/2 nuclei I is exposed to a high static magnetic field B_0 along the z -axis so that their Larmor frequency is given by $\omega_0 = \gamma_I B_0$ where γ_I is the magnetogyric ratio. Hence the spins develop an equilibrium magnetic polarization. In the next step the spins are irradiated at a frequency ω_{rf} near ω_0 with a circularly polarized radio-frequency (RF) field with magnitude $B_1 = \omega_1/\gamma_I$. The evolving magnetization is detected with a phase sensitive detector operating at frequency ω_{det} , introducing

$$\begin{aligned}\Delta &= \omega_0 - \omega_{\text{det}} \\ \delta &= \omega_{\text{rf}} - \omega_{\text{det}}.\end{aligned}\tag{2.232}$$

In Fig. 2.23 (a) ω_{rf} has been set equal to ω_{det} , yielding $\delta = 0$, whereas Fig. 2.23 (b) reflects the general situation in which $\delta \neq 0$. This is equivalent to a magnetic field of magni-

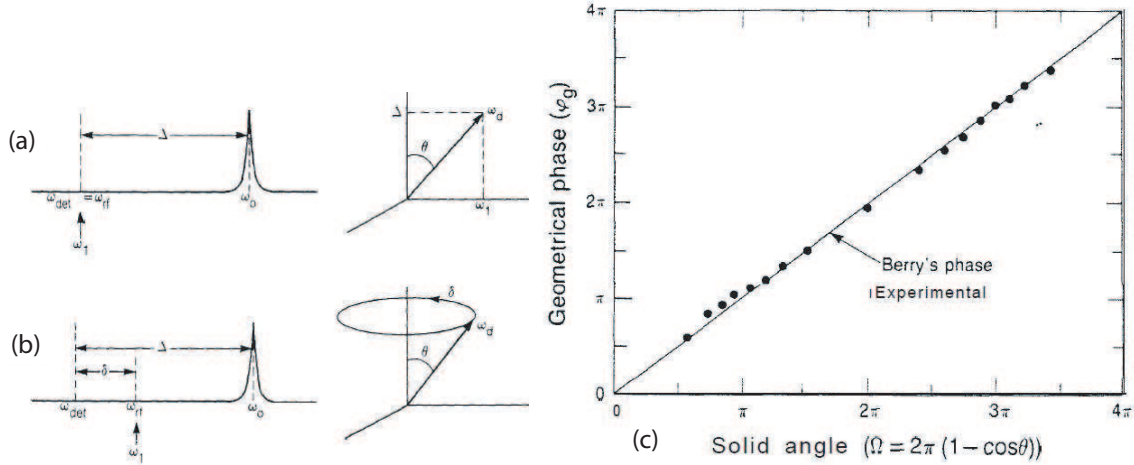


Figure 2.23: Rotating (detector) frame pictures of spins irradiated at frequency ω_{rf} near resonance ω_0 with a circularly polarized radio-frequency field of magnitude $B_1 = \omega_1/\gamma$ for (a) $\omega_{rf} = \omega_{det}$ and (b) $\omega_{rf} \neq \omega_{det}$, taken from [Suter et al., 1987]. (c) Plot of experimentally measured geometrical phase γ .

tude $B = \omega_d/\gamma_I$ moving in a cone of angle 2θ around the z axis at frequency δ . Thus Fig. 2.23 (b) is the high field detector frame equivalent of conical circuits in the laboratory. To implement a general circuits in the rotating frame ω_d and polar angle θ can be varied by modulating ω_0 , ω_{rf} and ω_1 according to

$$\begin{aligned}\omega_d &= \sqrt{\Delta^2 + \omega_1^2} \\ \theta &= \frac{1}{\tan \frac{\omega_1}{\Delta}}\end{aligned}\quad (2.233)$$

The geometrical phase is present as a small factor in the presence of the large dynamical phase. The effects of the dynamical phase may be removed by reversing the direction of B . Then the dynamical phase is refocused as an echo at the end of the circuit leaving only the pure geometrical phase γ , which is depicted in Fig. 2.23 (c).

Aharonov and Anandan quantum phase in NMR interferometry

Only one year later Suter and his co-workers reported on the first observation of the geometric phase of Aharonov and Anandan [Suter et al., 1988], a reformulated and gen-

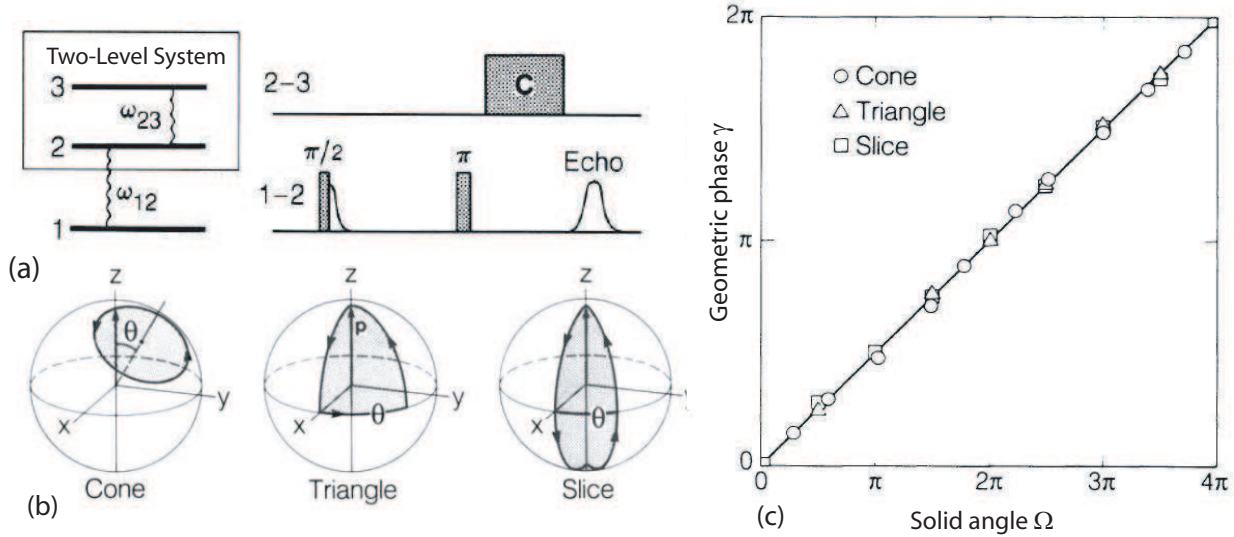


Figure 2.24: (a) Fictitious spin 1/2 system in [Suter et al., 1988] consisting of states 2 and 3. (b) Circuits traced out, using different magnetic field configurations. (c) Observed geometric phase γ versus the solid angle Ω for the three circuit types.

eralized version for non-adiabatic evolutions of Berry's phase (see Section 2.3.3). They presented a NMR interferometer experiment, where a quantum system evolves through a circuit \mathcal{C} in projective Hilbert space, thereby acquiring a geometric phase γ , related to the topology of the circuit.

For demonstration of a geometric phase in the sense of Aharonov and Anandan a NMR interferometry related to neutron interferometry was utilized. The two-level system consisting of states 2 and 3 (see Fig. 2.24 (a)) is treated as a fictitious spin 1/2 system. Time-dependent magnetic fields are applied to take the two-level system through a circuit. A $\pi/2$ pulse of the 1-2 transition creates a coherent superposition of the two states, whose phase is used as a reference signal for the actual geometric phase measurement. The two-level system polarization vector, z in the beginning, is made to undergo a circuit by applying appropriate perturbations to the 2-3 transition.

The experiment was performed on the spin 1 manifold of two proton spin 1/2 in in CH_2CL_2 and the static field was 8.4 T and the rotating magnetic fields at frequencies $\omega_{23}=362.024$ MHz and $\omega_{23}=362.029$ MHz had amplitudes of 1.7 and $1.3 \mu\text{T}$ respectively, which is illustrated in Fig. 2.24 (a).

The cone circuits (see Fig. 2.24 (b, left)) were induced by a tilted magnetic field with an angle θ in respect to the z -axis, in the rotating frame. For the spherical triangle and slices (see Fig. 2.24 (b, center) and Fig. 2.24 (b, right), respectively) pulses were applied perpendicular to the polarization vector. For instance for the spherical triangle a $\pi/2$ pulse along $(0,1,0)$, followed by a θ pulse along $(0,0,1)$, and finally a $\pi/2$ half pulse along $(\sin\theta, -\cos\theta, 0)$, and so on. For the spherical triangle and the slice circuits the dynamical phase vanishes, since the applied field was always orthogonal to the state, generating parallel transport. For the cone the dynamical phase was observed in a reference experiment. Figure 2.24 (c) depicts the observed geometric phase γ versus the solid angle Ω for the three circuit types introduced in Fig. 2.24 (b).

Geometric phase in neutron polarimetry

In 1990 Badurek and Weinfurter presented a experiment, in which a geometric phase, due to the interaction with a rotating magnetic field, was observed [Weinfurter and Badurek, 1990]. The time-evolution for the neutrons for this particular field configuration given by $\vec{B}(t) = B(\cos(\omega t), \sin(\omega t), 0)$ is described by the Pauli equation:

$$i\hbar\frac{\partial}{\partial t}|\Psi(t)\rangle = -\mu B \begin{pmatrix} 0 & e^{-i\omega t} \\ e^{i\omega t} & 0 \end{pmatrix} |\Psi(t)\rangle. \quad (2.234)$$

As already discussed for a in Section 2.1.2 a solution of the Pauli equation can be derived by transforming into a rotating coordinate system: $|\Psi(t)\rangle = \hat{U}(t)|\Phi(t)\rangle$, with $\hat{U}(t) = \exp(-i\omega t\sigma_z/2)$, which also describes the evolution of the eigenvectors $|n(t)\rangle = \hat{U}(t)|n(0)\rangle$, which are orientated along $\pm x$. Then Eq.(2.234) becomes

$$\begin{aligned} i\hbar\frac{\partial}{\partial t}|\Phi(t)\rangle &= \left(\hat{U}^\dagger(t)\hat{H}\hat{U}(t) - i\hbar\hat{U}^\dagger(t)\frac{\partial}{\partial t}\hat{U}(t)\right)|\Phi(t)\rangle \\ &= \frac{1}{2}\left(\hbar\omega_L\sigma_x - \hbar\omega\sigma_z\right)|\Phi(t)\rangle, \end{aligned} \quad (2.235)$$

with Larmor frequency $\omega_L = \gamma B$. In the adiabatic approximation, $\langle n(0)|\hat{U}^\dagger(t)\hat{U}|n(0)\rangle = 0$ (which also fulfills the parallel transportation law) or $\omega_L \gg \omega$ a solution is given by

$$|\Psi(\tau)\rangle_{\text{ad}} = \hat{U}(\tau)e^{-i\omega_L\tau\sigma_x/2}|\Psi(0)\rangle. \quad (2.236)$$

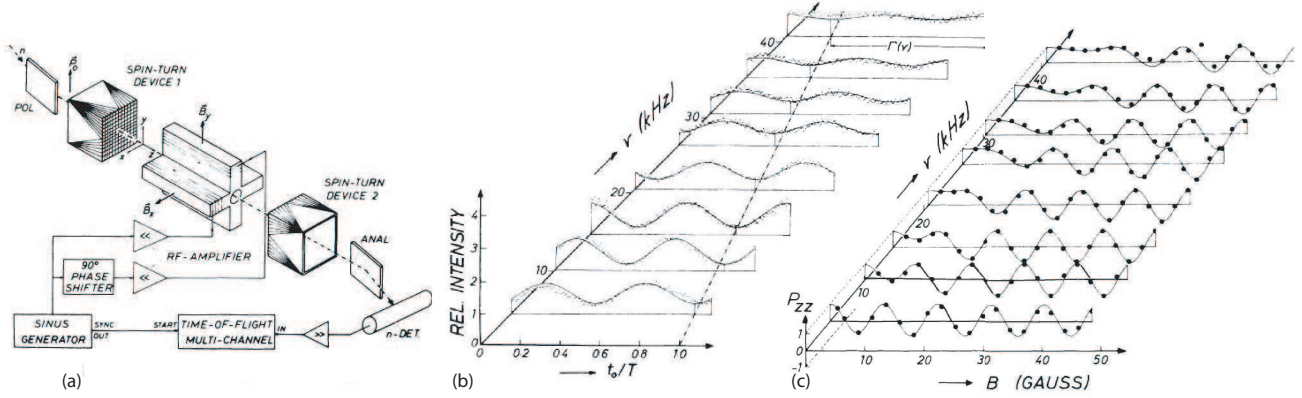


Figure 2.25: (a) Experimental setup from [Weinfurter and Badurek, 1990] for geometric phase observation in neutron polarimetry. (b) Relative intensity P_{yy} , (c) polarization change along the z -axis as a function of the rotation frequencies for different amplitudes.

However the exact solution of Eq.(2.235) is given by

$$|\Psi(\tau)\rangle = \hat{U}(\tau) \exp\left(-i/2(\omega_L\tau(\sigma_x \cos(\omega t_0) + \sigma_y \sin(\omega t_0)) - \omega\tau\sigma_z)\right)|\Psi(0)\rangle, \quad (2.237)$$

where t_0 is denoting the moment when each neutron enters the field region. The term $\delta = \omega_L\tau$ in Eq.(2.237) represents the usual dynamical phase, dependent on the strength of the magnetic field and the time the neutron is exposed to it. Whereas the term $\exp(-i/2\omega\tau\sigma_z) = \exp(-i/2\gamma\sigma_z)$ accounts for the geometric phase, purely depending on the solid angle $\Omega = \omega\tau$ subtended by the varying field direction.

Figure 2.25 (a) depicts a schematic illustration of the experimental setup, consisting of two Heusler crystals the first one used to monochromatize and polarize the initial beam, adiabatic spin turners to select the appropriate polarization direction to be analyzed, and the two mutually orthogonal split pair coils. A time-of-flight multichannel detector, triggered by the periodic signal of the field, allows to correlate the time the neutron enters the field region, denoted as t_0 , with the respective field direction.

So to observe a purely geometric phase effect, one has to analyze the change of the polarization along the z and y -direction, as seen in Eq.(2.237). In Fig 2.25 (b) the relative intensity P_{yy} (initial and analyzed direction is y) is plotted for different rotation frequencies of the magnetic field at constant amplitude of 38 G. The dashed line indicates the increase of the geometric phase shift for higher frequencies. Finally Fig 2.25 (c) illustrates

the polarization change along the z -axis as a function of the rotation frequencies and for different amplitudes. It can be seen that the geometric phase influences the polarization not only in the adiabatic, but also in the non-adiabatic regime.

It should be mentioned that in this experiment time-dependent rotating fields allowed to reveal geometric phase effects also for non-cyclic evolutions. Varying the direction, as well as the frequency of the rotating field, but keeping the amplitude constant, offers the possibility to reach the same final state in parameter space via different paths. The observed phase change thus solidly reflects the geometric evolution of the system.

3

Interferometric Experiments

3.1 Neutron Interferometry

Neutron interferometry [Rauch et al., 1974, Rauch and Werner, 2000] has become a unique tool for studies on the quantum-mechanical nature of matter waves. A beam of massive particles is split by amplitude division (Mach-Zehnder type see Section 2.2.2), and superposed coherently after passing through different regions of space. During these space-like separation, typically a few centimeter, the neutron's wavefunction is modified in phases (and amplitude), due to various interactions. Since the neutron interacts with the environment via all four forces, this interaction may be of nuclear, magnetic, electric or gravitational type, depending on which neutron optical devices are inserted. The topic of neutron interferometry belongs to the field of *self-interference*, since at a given instant at most one neutron propagates through the interferometer - if at all.

History

In 1964, when advances in semiconductor technology had allowed the production of large monolithic perfect crystal silicon ingots, U. Bonse and M. Hart invented a single-crystal interferometer for X-rays based on the effects of dynamical diffraction in perfect crystals [Bonse and Hart, 1965]. This type of interferometer was then applied to neutrons

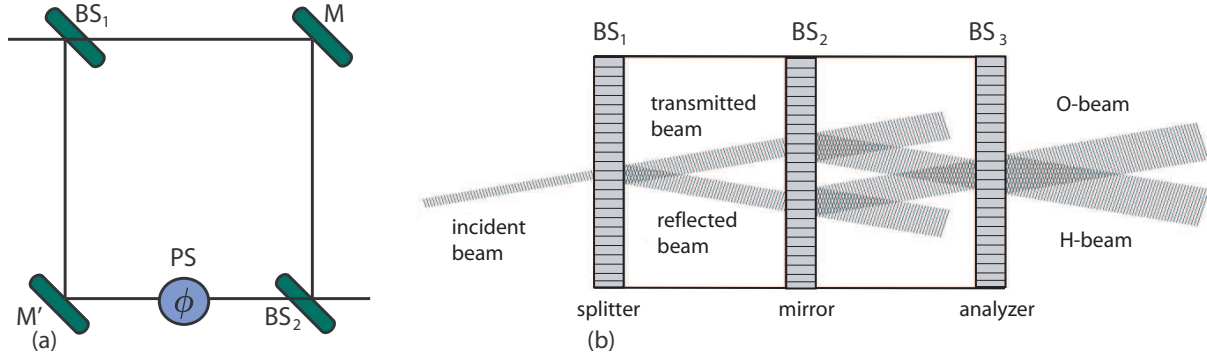


Figure 3.1: (a) Optical Mach-Zehnder interferometer. (b) Perfect crystal neutron interferometer of type Mach-Zehnder.

resulting in the first interference fringes sighted in 1974 by Rauch, Treimer and Bonse [Rauch et al., 1974] at the rather small (250kW) TRIGA reactor in Vienna. The obtained interference demonstrates in impressive manner the wave-like nature of neutrons.

Over the years numerous remarkable experiments on the fundamentals of quantum mechanics, have been carried out using neutron interferometry. Just to mention a few, there is the verification of the $4\text{-}\pi$ -spinor symmetry [Rauch et al., 1975], followed by investigations of the influence of gravitation of the earth on the neutron's wavefunction, and experiments on spin superposition [Summhammer et al., 1983, Badurek et al., 1983, Badurek et al., 1986]. More recently single-particle entanglement between the spinor and the spatial part of the neutron wave function [Hasegawa et al., 2003] and full tomographic state analysis [Hasegawa et al., 2007] have been accomplished, as well as demonstration of quantum contextuality [Hasegawa et al., 2006, Bartosik et al., 2009].

3.1.1 Functional principle

A neutron interferometer consists of a single silicon perfect-crystal, as depicted in Fig. 3.1 (b), cut in such a way that the incoming neutron beam is split at the first plate, acting as a beam splitter (silicon has practically no absorption for thermal neutrons). The sub beams are reflected by the second plate, which is virtually also a beam splitter. However, in analogy to the Mach Zehnder interferometer for light the second plate is often referred to as a mirror (the Skew-symmetric interferometer in Fig. 3.2 has a split

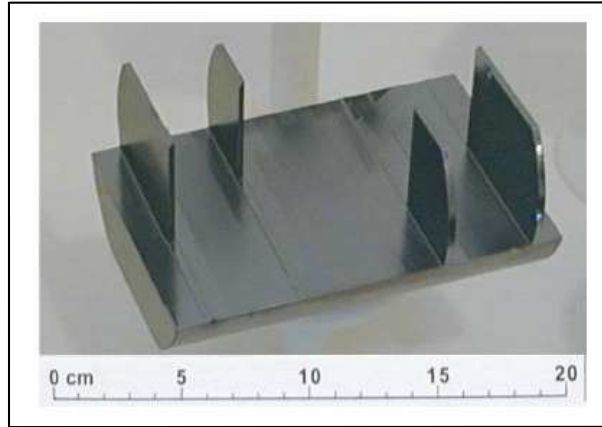


Figure 3.2: Skew-symmetric single-crystal neutron interferometer.

second plate to provide more space for neutron optical devices to be inserted). Finally before the beams are recombined at the last plate (analyzer), an adjustable relative phase is applied, yielding the well known intensity oscillations of the two beams emerging behind the interferometer (see Fig 3.3 (b)), usually denoted as O- and H-beam, respectively. The neutron's interferometer's operation is based on the division of amplitudes by dynamic Bragg reflection from perfect crystals at Bragg angle θ_B , as it was implemented for X-rays. In the standard configuration, a monolithic triple-plate (or split triple-plate) interferometer in Laue (L) geometry (surface of the plates is perpendicular to the reflecting net planes) is used. This arrangement provides a macroscopic beam separation (~ 5 cm) and a non-dispersive response to the incident beam. Operating in the triple-Laue (LLL) configuration, together with an auxiliary phase shifter, the interferometer is geometrically analogous to a common Mach-Zehnder interferometer in light optics, which is schematically illustrated in Fig. 3.1 (a).

An intrinsic feature of diffraction at perfect crystals is the extremely narrow width of their reflection curves, of a few arc seconds only. This accounts for a particular challenge for the alignment of splitter, mirror and analyzer crystal, since arc second tolerance corresponds to positional accuracy in the order of the lattice parameter (\AA). The only way to assure an alignment in the order of the lattice parameter is to cut the whole interferometer out of a single a monocrystalline silicon ingot.

Behind the first plate (beam splitter) the neutron's wave function is found in a super-

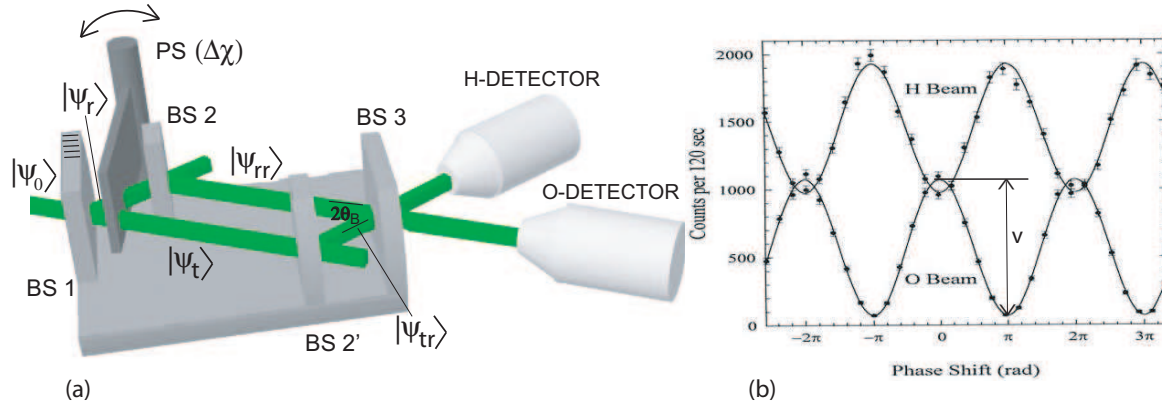


Figure 3.3: (a) (Skew-symmetric) neutron interferometer with the incident beam $|\Psi_0\rangle$ being split at beam splitter 1 (BS 1) and recombined at BS 3. The phase shifter PS induces a relative phase difference ($\Delta\chi$) between the two sub-beams yielding in interference fringes. (b) Interference fringes due to rotation of the phase shifter, observed in the O- , and H-beam.

position of the transmitted and a reflected sub-beams, which is depicted in Fig 3.3 (a). In terms of state vectors the initial state $|\Psi_i\rangle$ is given by

$$|\Psi_0\rangle \xrightarrow{\text{BS1}} |\Psi_i\rangle = t|\Psi_t\rangle + r|\Psi_r\rangle, \quad (3.1)$$

where $|\Psi_t\rangle$ and $|\Psi_r\rangle$ denote the transmitted and reflected beam, respectively. The factors t and r (with $|t|^2 + |r|^2 = 1$, for a non-absorptive beam-splitter) account for the ratio of transmission (t) and reflection (r), which is for a 50:50 beam splitter given by $t \propto r \propto 1/\sqrt{2}$. Now an additional slab that produces an adjustable phase shift is inserted, which yields

$$|\Psi_i\rangle \xrightarrow{\text{PS}} |\Psi'\rangle = te^{i\chi_1}|\Psi_t\rangle + re^{i\chi_2}|\Psi_r\rangle, \quad (3.2)$$

where $\chi_i = -N_{\text{ps}}b_c\lambda D_i$, with the thickness of the phase shifter plate D_i , the neutron wavelength λ , the coherent scattering length b_c and the particle density N_{ps} in the phase shifter plate. By rotating the plate, χ_i can be varied systematically. Introducing a relative phased difference $\Delta\chi = \chi_2 - \chi_1$ (this will be explained in more detail in the course of this Section), the state leaving the interferometer at the third plate, where the sub-beams are

recombined, is denoted as

$$|\Psi'\rangle \xrightarrow{\text{BS3}} |\Psi_f\rangle = (trr|\Psi_{\text{trr}}\rangle + e^{i\Delta\chi}rrt|\Psi_{\text{rrt}}\rangle). \quad (3.3)$$

This yields the well known intensity oscillations, which can be seen in Fig 3.3 (b), with interference fringes of the intensity

$$I_{\text{O}} = \langle\Psi_f|\Psi_f\rangle = A(1 + \cos(\Delta\chi)), \quad (3.4)$$

with $A = 2|r|^4|t|^2$. Similar the intensity found in the H-beam is

$$I_{\text{H}} = \langle\Psi_{f'}|\Psi_{f'}\rangle = B - A(1 + \cos(\Delta\chi)), \quad (3.5)$$

with

$$\begin{aligned} |\Psi_{f'}\rangle &= (trt|\Psi_{\text{trt}}\rangle + e^{i\Delta\chi}rrr|\Psi_{\text{rrr}}\rangle) \\ \text{and } B &= |t|^4|r|^2 + |r|^6. \end{aligned} \quad (3.6)$$

Equation (3.4) is only valid for $\langle\Psi_{\text{trr}}|\Psi_{\text{rrt}}\rangle = 1$, indicating that $|\Psi_{\text{trr}}\rangle$ and $|\Psi_{\text{rrt}}\rangle$ are fully overlapping and coherent. If not (in practice) an additional fringe visibility or *contrast* ($\nu \in [0, 1]$) has to be introduced. The reduced intensity then reads

$$I_{\text{H}} \propto 1 + \nu \cos(\Delta\chi). \quad (3.7)$$

The wave functions corresponding to the state vectors described here are calculated using dynamical theory of diffraction, which is discussed in detail in [Rauch and Petrascheck, 1976a, Rauch and Petrascheck, 1976b], and briefly summarized on the next pages.

Dynamical theory of diffraction

The neutron wave function $\psi(\vec{r})$ inside the crystal is deduced by solving the stationary Schrödinger equation for the time-independent crystal potential $V(\vec{r})$

$$\left(-\frac{\hbar^2}{2m}\vec{\nabla}^2 + V(\vec{r})\right)\psi(\vec{r}) = E\psi(\vec{r}), \quad (3.8)$$

where the potential $V(\vec{r})$ is given by the sum over all nuclear scattering centres located at \vec{r}_i

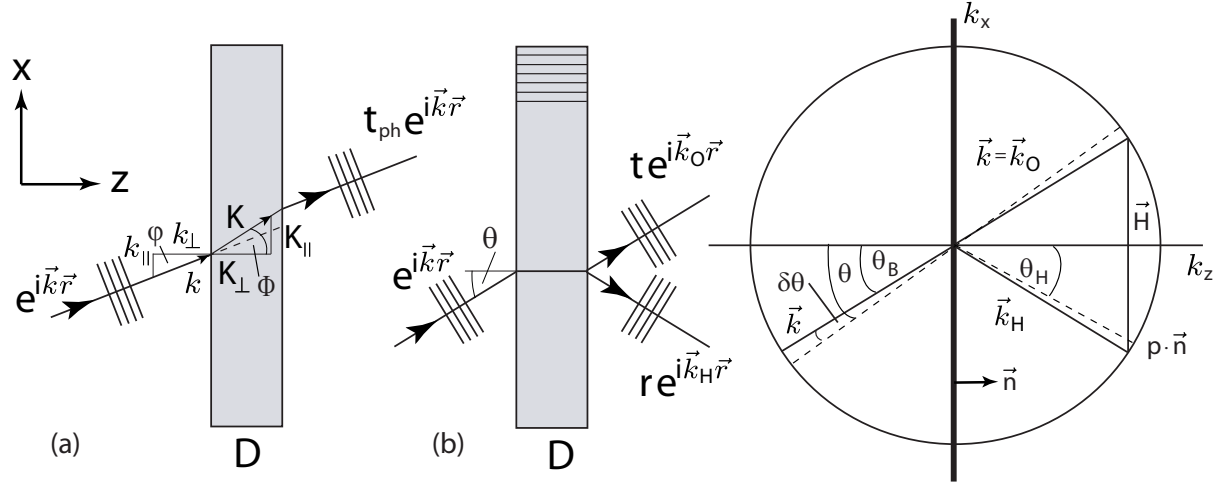


Figure 3.4: Two cases for a neutron beam incident on a medium: (a) far off a Bragg condition (or homogeneous non-crystalline media) only the phase of the wavefunction is affected, whereas when the Bragg condition is fulfilled (b) a transmitted and refracted beam appears.

$$V(\vec{r}) = \frac{2\pi\hbar^2 b_c}{m_n} \sum_i \delta(\vec{r} - \vec{r}_i), \quad (3.9)$$

with m_n being the mass of the neutron. Since the potential is periodic, this equation can be transformed into reciprocal space using the ansatz

$$\psi(\vec{r}) = e^{i\vec{K}\vec{r}} \sum_{\vec{H}} u(\vec{H}) e^{i\vec{H}\vec{r}}, \quad (3.10)$$

where \vec{K} is the wave vector inside the crystal and \vec{H} is a reciprocal lattice vectors (with $\vec{H} = h\vec{g}_1 + k\vec{g}_2 + l\vec{g}_3$, where h, k, l are the *Miller indices*). Hence one obtains an infinite set of coupled equations for the amplitudes $u(\vec{H})$.

$$\left(\frac{\hbar^2}{2m} |\vec{K} + \vec{H}|^2 - E \right) u(\vec{H}) = - \sum_{\vec{H}'} V(\vec{H} - \vec{H}') u(\vec{H}'), \quad (3.11)$$

where $V(\vec{H} - \vec{H}')$ is the Fourier transform of $V(\vec{r})$ given by

$$\begin{aligned} V(\vec{H}) &= \frac{1}{V} \int V(\vec{r}) e^{-i\vec{H}\vec{r}} d\vec{r} \\ &= \frac{2\pi\hbar^2 b_c}{Vm} \sum_j e^{-i\vec{H}\vec{r}_j} \end{aligned}$$

$$= \frac{2\pi\hbar^2 b_c}{Vm} \sum_{\vec{R}_j} e^{-\vec{H}\vec{R}_j} \sum_{\vec{a}_i} e^{-\vec{H}\vec{a}_i}, \quad (3.12)$$

where \vec{r}_j is the position of a nuclear scattering center in the lattice, given by $\vec{r}_j = \vec{R}_j + \vec{a}_i$, with \vec{R}_j being the position of origin of the crystal elementary cell, and \vec{a}_i is the position within the crystal elementary cell. The volume of the crystal is given by $V = N_c V_c$, where N_c is the number of elementary cells, and V_c is the volume of crystal elementary cell.

The first part of sum in Eq.(3.12) yields

$$\begin{aligned} \frac{1}{N_c} \sum_{\vec{R}_j} e^{i\vec{K}\vec{R}_j} &= 1 \quad \text{for } \vec{K} = \vec{H} \\ &= 0 \quad \text{for } \vec{K} \neq \vec{H}. \end{aligned} \quad (3.13)$$

The second part of the sum in Eq.(3.12) is called *structure factor*, it is defined by the atomic structure within the elementary cell.

$$F = \sum_{\vec{a}_i} e^{-\vec{H}\vec{a}_i} = \begin{cases} 8, & \text{for } h+k+l = 4n \text{ (e.g. silicon in } h,k,l = 220 \text{ direction)} \\ 4(1 \pm i), & \text{all } hkl \text{ odd/even (e.g. silicon in } h,k,l = 111 \text{ direction)} \end{cases} \quad (3.14)$$

Thus Eq.(3.12) can be written as

$$V(\vec{K}) = V(\vec{H}) = V(h, k, l) = \frac{2\pi\hbar^2 b_c}{V_c m} F. \quad (3.15)$$

A detailed discussion of the techniques to solve Eq.(3.11) can be found for example in [Rauch and Petrascheck, 1976a, Rauch and Petrascheck, 1976b].

One-beam approximation

Here only the $\vec{H} = 0$ contribution is considered, where it is assumed that the neutron-nucleus interaction is small and that consequently the difference between the wave vector within the crystal and the vacuum wave vector is negligible. The reflected beam can safely be neglected if the optical potential $V(0)$ is small compared to the kinetic energy of the incident neutron. In the case of $V(\vec{H}) := V(0)$ F is given by the number of scattering centers in the elementary cell (no periodic structures are taken into account). Since $1/V_c$ is the number of elementary cells per volume unit, $V(0)$ is given by

$$V(0) = \frac{2\pi\hbar^2 b_c}{m} N. \quad (3.16)$$

For a thermal beam with a wavelength of $\sim 2\text{\AA}$ the kinetic energy is ~ 0.02 eV, which is orders of magnitude larger than typical values of $V(0)$, for example for silicon $V_{\text{Si}}(0) = 53,9751$ neV. Thus the corresponding equation is given by

$$\left(\frac{\hbar^2 K_0^2}{2m} - E\right)u(0) = -V(0)u(0), \quad (3.17)$$

with

$$V(0) = \frac{2\pi\hbar^2 b_c}{m}N, \quad (3.18)$$

and

$$K_0^2 = \frac{2m}{\hbar^2}(E - V(0)) = \frac{2Em}{\hbar^2}\left(1 - \frac{V(0)}{E}\right). \quad (3.19)$$

According to the energy conservation, for the free neutron with momentum \vec{k} , of magnitude $k := |\vec{k}|$, the kinetic energy is given by $E = \hbar^2 k^2 / (2m)$. Hence

$$K_0^2 = \frac{2m}{\hbar^2}(E - V(0)) = k^2\left(1 - \frac{V(0)}{E}\right), \quad (3.20)$$

since $V(0)/E \ll 1$ one can write

$$K_0 = k\left(1 - \frac{V(0)}{2E}\right). \quad (3.21)$$

Plugging Eq.(3.18) in Eq.(3.21) yields

$$\frac{V(0)}{2E} = \frac{2\pi\hbar^2 b_c N}{m} \frac{2m}{2\hbar^2 k^2} = \lambda^2 \frac{N b_c}{2\pi}, \quad (3.22)$$

in analogy to light optics the refractive index n is defined as

$$n := \frac{K}{k} \sim 1 - \frac{V(0)}{2E} = 1 - \lambda^2 \frac{N b_c}{2\pi}. \quad (3.23)$$

In general the wave vector changes both direction and magnitude - the neutron wave is refracted, which is depicted in Fig. 3.4 (a). Note, that for most materials $V(0) > 0$ ($b_c > 0$) this leads to a refractive index slightly smaller than one ($n < 1$). However, the neutron index of refraction is typically very close to one, e.g. for silicon $(n_{\text{Si}} - 1) = -0.97 \cdot 10^{-6}$. Despite the additional potential energy the kinetic energy is lowered. The one-beam approximation is valid for a perfect crystal far off any Bragg condition, as well as for homogeneous non-crystalline media.

The direction of the beam \vec{K} is calculated according to the continuity of the tangential component $\vec{k}_{\parallel} = \vec{K}_{\parallel}$.

$$K^2 = K_{\perp}^2 + K_{\parallel}^2 = K_{\perp}^2 + k_{\parallel}^2 = k^2 \left(1 - \frac{V(0)}{E}\right) = k_{\parallel}^2 + k_{\perp}^2 - k^2 \frac{V(0)}{E}, \quad (3.24)$$

for the perpendicular component K_{\perp}

$$K_{\perp} = \sqrt{k_{\perp}^2 - k^2 \frac{V(0)}{E}} \sim k_{\perp} \left(1 - \frac{1}{2} \frac{k^2 V(0)}{k_{\perp}^2 E}\right) = k_{\perp} \left(1 - \frac{1}{2} \frac{V(0)}{\cos^2 \varphi E}\right). \quad (3.25)$$

Using $k_{\perp} = \vec{k} \cdot \vec{n}_s = k \cos \alpha$, where \vec{n}_s is the surface normal, Eq.(3.25) can be written as

$$\vec{K} = \vec{k} - \frac{k}{\cos \alpha} \frac{V(0)}{2E} \vec{n}_s. \quad (3.26)$$

Now one can calculate the phase shift χ induced by a phase shifter of thickness D .

$$\chi := (\vec{K} - \vec{k}) \cdot \vec{r} = -\lambda^2 \frac{N b_c k D}{2\pi \cos \alpha} = -\lambda N b_c \underbrace{\frac{D}{\cos \alpha}}_{D_0}, \quad (3.27)$$

with $D = \vec{n}_s \cdot \vec{r}$.

Two-beam approximation

A Bragg reflection is obtained when the Bragg condition is fulfilled:

$$n\lambda = 2d_{hkl} \sin \theta_B \quad \text{with} \quad d_{hkl} = \frac{a}{\sqrt{h^2 + k^2 + l^2}}, \quad (3.28)$$

being the lattice plane distance defined the miller indices (h, k, l) and the lattice constant a . The thermal neutron wave length is typically in the range of 1.9 to 2.7 Å, which corresponds to energies of 22 to 11 meV and Bragg angles of 30 to 45 degrees for silicon (220)-net plane reflection ($a_{\text{Si}} = 5.43101993 \cdot 10^{-10}$ m). Close to a Bragg condition two reciprocal lattice points lie near the Ewald sphere and therefore two amplitudes of the system of coupled equations, defined in Eq.(3.11), have to be taken into account. The amplitudes $u(\vec{O})$ and $u(\vec{H})$ belong to the forward and reflected direction, and are obtained as solutions of the following system of coupled equations:

$$\begin{aligned} \left(-\frac{\hbar^2}{2m} |\vec{K}|^2\right) u(\vec{O}) &= -V(\vec{O})u(\vec{O}) - V(-\vec{H})u(\vec{H}) \\ \left(-\frac{\hbar^2}{2m} |\vec{K} + \vec{H}|^2\right) u(\vec{H}) &= -V(\vec{H})u(\vec{O}) - V(\vec{O})u(\vec{H}), \end{aligned} \quad (3.29)$$

with $V(\vec{O}) = V(0) = (2\pi\hbar^2 b_c N)/m$ and $V(\vec{H}) = (2\pi\hbar^2 b_c F)/(V_c m)$. The structure factor F is given by $F = 8$ if the sum of the Miller indices h, k, l can be divided by 4, for example (220) and $F = 4(1 \pm i)$ for h, k, l all odd e.g. (111).

Assuming the Laue case, where the crystal planes are oriented perpendicular to the crystal surface, the coupled equations Eq.(3.29) lead to the standard formulas for the transmission and reflection amplitudes of the neutron wave behind a crystal of thickness D . As illustrated in Fig. 3.4 (b) an incident plane wave $\psi_{\text{in}} = \exp(i\vec{k}\vec{r})$ with a small deviation from the exact Bragg angle, $\theta = \theta_B + \delta\theta$, has the following amplitudes and directions of the transmitted and reflected wave, ψ_O and ψ_H respectively:

$$\begin{aligned}\psi_O &= t(y)\psi_{\text{in}} = t(y)e^{i\vec{k}_O\vec{r}} & t(y) &= e^{-iPD} \left(\cos \left(A\sqrt{1+y^2} \right) + iy \frac{1}{\sqrt{1+y^2}} \sin \left(A\sqrt{1+y^2} \right) \right) \\ \psi_H &= r(y)e^{i\vec{k}_H\vec{r}} = r(y)e^{ipz_0} e^{i\vec{k}_O\vec{r}} & r(y) &= -e^{-iPD} \sqrt{b} \frac{|V(\vec{H})|}{V(-\vec{H})} \left(i \frac{1}{\sqrt{1+y^2}} \sin \left(A\sqrt{1+y^2} \right) \right) \\ & & \psi_H &= r(y)e^{i(\vec{H}\vec{r} - p(\vec{n}\vec{r} - z_0))} \psi_{\text{in}},\end{aligned}\tag{3.30}$$

where

$$b = \frac{\cos \theta}{\cos \theta_B}, \quad A = \frac{\pi D}{\Delta_0} \quad \text{and} \quad \Delta_0 = \frac{\pi V_c \cos \theta_B}{b_c |F| \lambda},\tag{3.31}$$

Δ_0 is referred to as *Pendellösung length*, z_0 is the position of the crystal plate, and y is a dimensionless parameterization of the Bragg deviation $\delta\theta$

$$y = \frac{-\delta\theta \sin(2\theta_B)}{V(\vec{O})E},\tag{3.32}$$

Table 3.1: Fundamental and material constants for silicon.

| | | |
|------------|--|--|
| b_c | coherent neutron scattering length | $b_{c\text{Si}} = 4.1507 \cdot 10^{-15} \text{ m}$ |
| a | lattice constant | $a_{\text{Si}} = 5.43101993 \cdot 10^{-10} \text{ m}$ |
| V_c | volume of crystal elementary cell | $V_{c\text{Si}} = a_{\text{Si}}^3$ |
| N | density of crystal atoms | $N_{\text{Si}} = 8/V_{c\text{Si}}$ |
| d | distance of Bragg planes | $d_{hkl\text{Si}} = a_{\text{Si}}/\sqrt{h^2 + k^2 + l^2}$ |
| F | structure factor | $F_{\text{Si}220} = 8 \quad F_{\text{Si}111} = 4(1 \pm i)$ |
| $V(0)$ | $= Nb_c 2\pi\hbar^2/m$ optical potential | $V_{\text{Si}}(0) = 53.9751 \text{ neV}$ |
| Δ_0 | Pendellösung length | $68 \mu\text{m}(\text{Si}_{220}, \lambda = 1.9 \text{ \AA})$ |

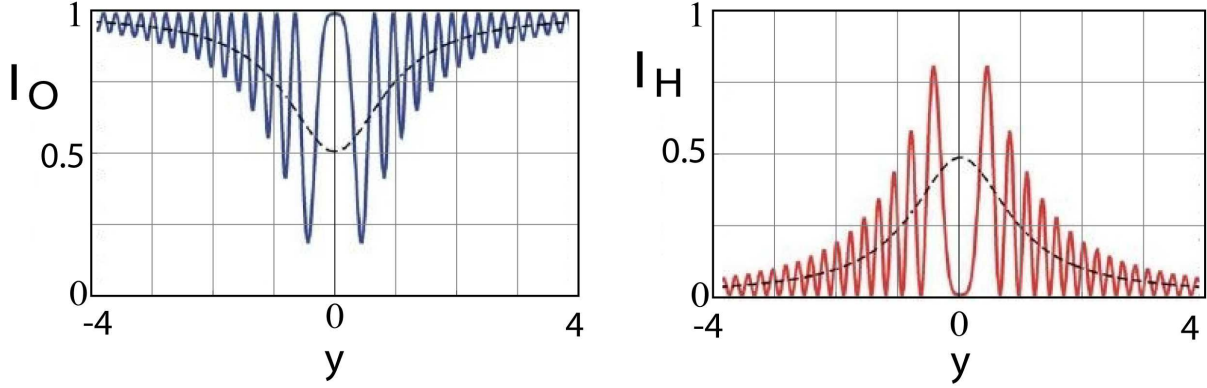


Figure 3.5: Intensity of the forward ($I_O(y) = |t(y)|^2$) and reflected ($I_H(y) = |r(y)|^2$) beam behind a perfect crystal slab, The dashed lines show the average over the Pendellösungs oscillations.

and P and p are given by

$$P = -\frac{\pi y}{\Delta_0} - \frac{k}{2 \cos \theta} \frac{V(0)}{E}, \quad p = \frac{2\pi y}{\Delta_0} + \frac{k(1-b)}{2 \cos \theta} \frac{V(0)}{E}. \quad (3.33)$$

In a non-absorbing medium forward and reflected direction fulfill the relation

$$|t(y)|^2 + |r(y)|^2 = 1. \quad (3.34)$$

In Tab. 3.1 the relevant material constants for silicon are summarized. Intensity of the forward and reflected direction, including average over the Pendellösungs oscillations, are plotted in Fig 3.5.

If Eq.(3.30) is applied to the second and third interferometer blade, the incident wave may also be in \vec{k}_H direction, which is depicted in Fig. 3.6:

$$\begin{aligned} \text{a: } t(y) &= e^{-iPD} \left(\cos \left(A\sqrt{1+y^2} \right) + iy \frac{1}{\sqrt{1+y^2}} \sin \left(A\sqrt{1+y^2} \right) \right) \\ \text{b: } r(y) &= -e^{-iPD} \sqrt{b} \frac{|V(\vec{H})|}{V(-\vec{H})} \left(i \frac{1}{\sqrt{1+y^2}} \sin \left(A\sqrt{1+y^2} \right) \right) \\ \text{c: } t'(y) &= t(-y) \\ \text{d: } r'(y) &= r(-y) \end{aligned} \quad (3.35)$$

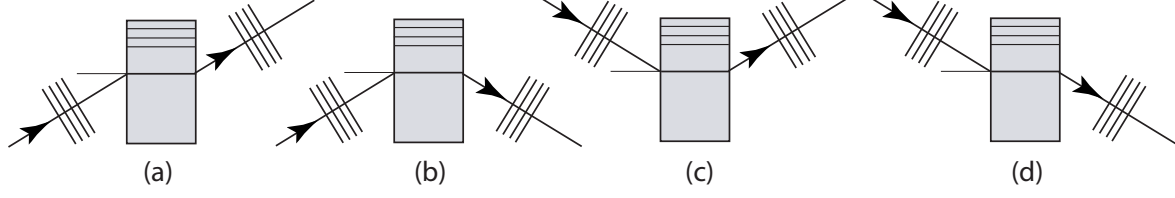


Figure 3.6: Different initial directions for reflection and transmission.(a): $t(y)$, (b): $r(y)$, (c): $r(-y)$, and (d): $t(-y)$.

By applying the formulas in Eq.(3.35) to the second and third interferometer plate all wave functions depicted in Fig. 3.7 can be calculated.

Path *I*:

$$\begin{aligned}
 \text{behind the beam splitter: } \psi_t &= t(y)\psi_{\text{in}} \\
 \text{behind the mirror: } \psi_{tr} &= r(y)e^{i(\vec{H}\vec{r}-p(\vec{n}\vec{r}-z_0^M))}\psi_t \\
 \text{behind the analyzer O-direction: } \psi_{IO} &= t(-y)e^{i(-\vec{H}\vec{r}+p(\vec{n}\vec{r}-z_0^A))}\psi_{tr} \\
 \text{behind the analyzer H-direction: } \psi_{IH} &= r(-y)\psi_{tr}, \tag{3.36}
 \end{aligned}$$

which results in

$$\begin{aligned}
 \psi_{IO} &= t(y)r(y)t(-y)e^{-ip(z_0^A-z_0^M)}\psi_{\text{in}} \\
 \psi_{IH} &= t(y)r(y)r(-y)e^{ipz_0^M}e^{i(\vec{H}\vec{r}-p\vec{n}\vec{r})}\psi_{\text{in}}. \tag{3.37}
 \end{aligned}$$

Path *II*:

$$\begin{aligned}
 \text{behind the beam splitter: } \psi_r &= r(y)e^{i(\vec{H}\vec{r}-p\vec{n}\vec{r}-z_0^{\text{BS}})}\psi_{\text{in}} \\
 \text{behind the mirror: } \psi_{rr} &= t(-y)e^{i(-\vec{H}\vec{r}+p\vec{n}\vec{r}-z_0^M)}\psi_r \\
 \text{behind the analyzer O-direction: } \psi_{IIO} &= t(y)\psi_{rr} \\
 \text{behind the analyzer H-direction: } \psi_{IIH} &= r(y)e^{i(\vec{H}\vec{r}-p\vec{n}\vec{r}-z_0^A)}\psi_{rr}, \tag{3.38}
 \end{aligned}$$

which yields

$$\begin{aligned}
 \psi_{IIO} &= r(y)t(-y)t(y)e^{-ip(z_0^M-z_0^{\text{BS}})}\psi_{\text{in}} \\
 \psi_{IIH} &= r(y)t(-y)r(y)e^{i(\vec{H}\vec{r}-p\vec{n}\vec{r}-p(-z_0^A+z_0^M-z_0^{\text{BS}}))}\psi_{\text{in}}. \tag{3.39}
 \end{aligned}$$

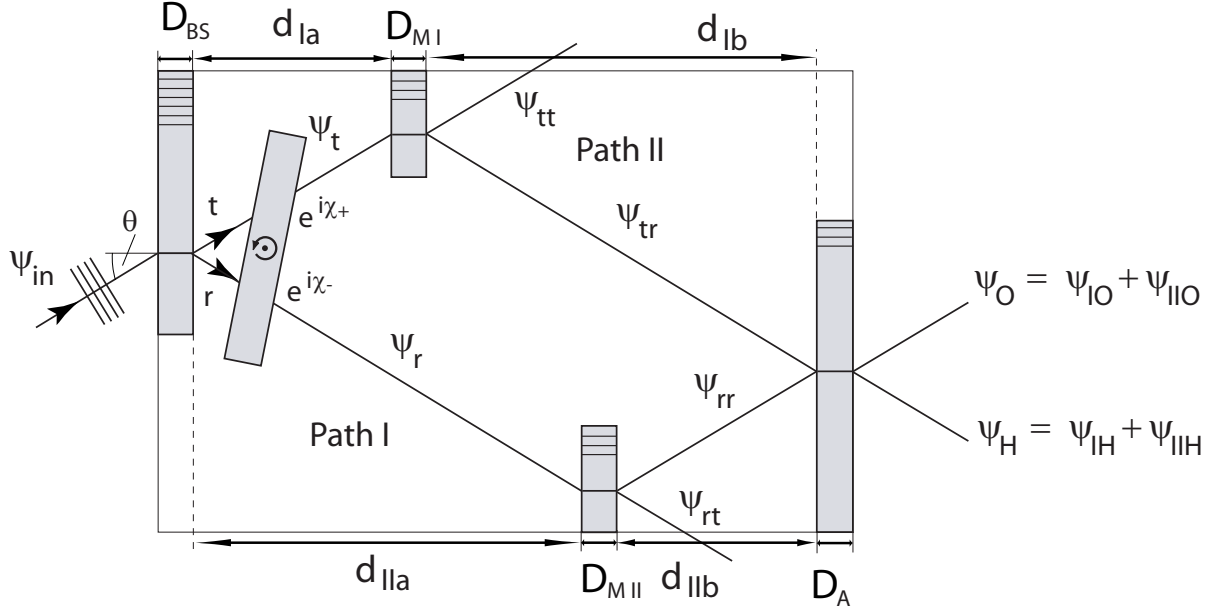


Figure 3.7: Wave functions in the interferometer.

Thus the focus conditions for fully constructive interference in the O beam:

$$D_{BS} = D_A, \quad D_{MI} = D_{MII}, \quad d_{Ib} = d_{IIa}, \quad \text{and} \quad d_{Ia} = d_{IIb} \quad (3.40)$$

yields

$$\psi_{IO} = \psi_{IIO} \quad \psi_O = \psi_{IO} + \psi_{IIO} = 2t(y)r(y)t(-y)e^{-ip(z_0^M - z_0^{BS})}. \quad (3.41)$$

Finally, the intensity measured in the O-beam is given by

$$|\psi_O|^2 = 4 \left(\frac{\sin^2(A\sqrt{1+y^2})}{1+y^2} \right)^2 \left(1 - \frac{\sin^2(A\sqrt{1+y^2})}{1+y^2} \right), \quad (3.42)$$

and for the H-beam

$$|\psi_H|^2 = b \frac{\sin^2(A\sqrt{1+y^2})}{1+y^2} \left(1 - 2 \frac{\sin^2(A\sqrt{1+y^2})}{1+y^2} \right)^2. \quad (3.43)$$

Phase shift χ

In order to obtain an interferogram it is necessary to tune a relative phase shift between the partial beams. This is achieved by the scalar phase shift due to the coherent nuclear

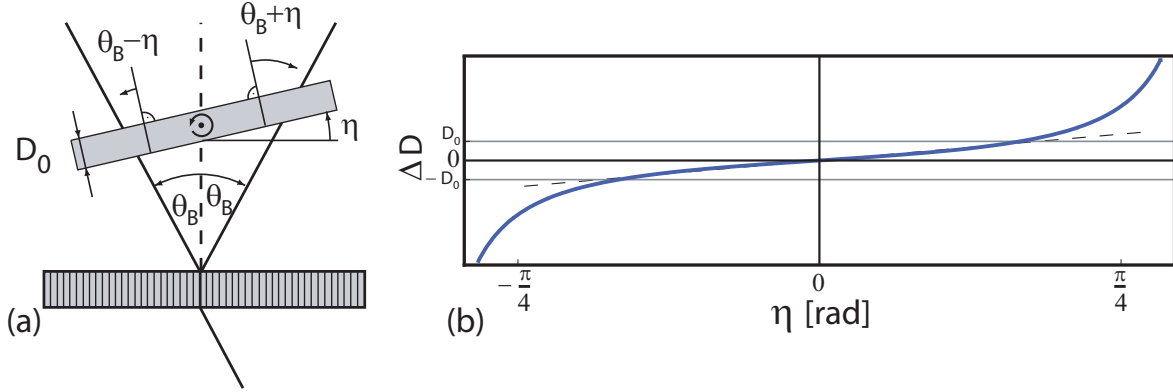


Figure 3.8: Geometry of the phase shifter slab in the interferometer and thickness variation ΔD when rotating the phase shifter slab by an angle η .

scattering in the material. As derived in Eq.(3.27) a material piece of thickness D_0 coherent scattering amplitude b_c and particle density N causes a phase shift denoted as

$$\chi = -\lambda N b_c D_0. \quad (3.44)$$

For instance, 0.15 mm of aluminium at 2 \AA wavelength cause a phase shift of 2π rad.

As it is only the relative phase shift of the partial beams that counts for interferometry, it has become a widely used method to rotate a slab of matter that extends across both sub beams about an axis perpendicular to the interferometer. The thickness of the slab is therefore changed differently for the two partial beams, depending on the angle η , as depicted in Fig 3.8(a). Thus the phase difference is determined by the path difference, which yields

$$\Delta D = \left(\frac{1}{\cos(\theta_B + \eta)} - \frac{1}{\cos(\theta_B - \eta)} \right) D_0, \quad (3.45)$$

where θ_B is the Bragg angle and η the rotation angle of the phase shifter slab. As seen in Fig. 3.8(b) the function ΔD is almost linear for small η . Thus an interferogram recorded versus η remains sinusoid essentially.

Paths on Bloch sphere - The neutron interferometer as a two-level system

The state of a neutron in an interferometer can be treated formally as a two-level system, where the two dimensional Hilbert space is spanned by the orthogonal states for paths

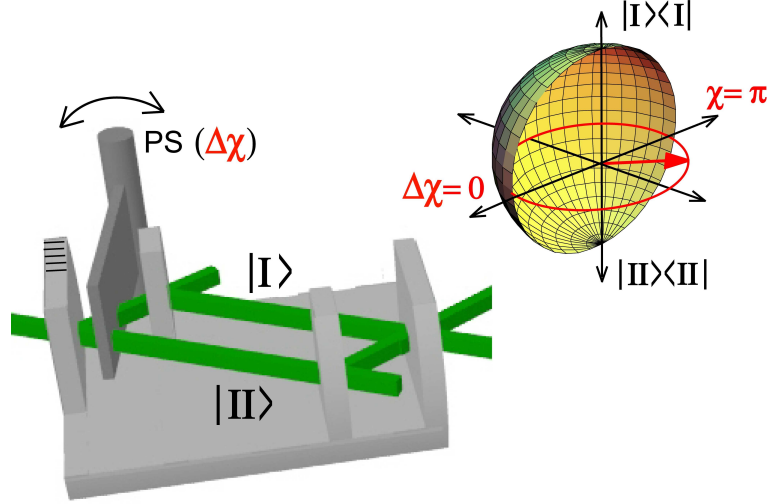


Figure 3.9: Bloch sphere representation of the neutron interferometer system. A equal superposition of $|I\rangle$ and $|II\rangle$ is found on the equator of the Bloch sphere.

$|I\rangle$ and $|II\rangle$, just like the spin eigenstates $|\uparrow\rangle$ and $|\downarrow\rangle$. The north and south pole of the sphere are consequently identified with states having a well-defined path. Thus $|I\rangle$ and $|II\rangle$ are eigenstates of the observables $|I\rangle\langle I|$ and $|II\rangle\langle II|$. An equally weighted superposition of path eigenstates is therefore found on the equator of a Bloch sphere. The phase shifter induces a relative phase shift $\Delta\chi$ between the superposing states denoted as

$$\frac{1}{\sqrt{2}}(|I\rangle + |II\rangle) \xrightarrow{\text{PS}} \frac{1}{\sqrt{2}}(|I\rangle + e^{i\Delta\chi}|II\rangle), \quad (3.46)$$

determining the azimuthal angle, which is illustrated in Fig 3.9.

3.1.2 Spin path entanglement preparation

The neutrons spin state is represented as a vector element of a complex two dimensional Hilbert space and is transformed from one state to another via a two dimensional unitary matrix \hat{U} element of $SU(2)$ as seen in Sec.2.1.1. Thus the interference patterns are sensitive to changes of the spin state if they are different for the particular interferometer paths. Behind the first plate of the interferometer the following state occurs for an

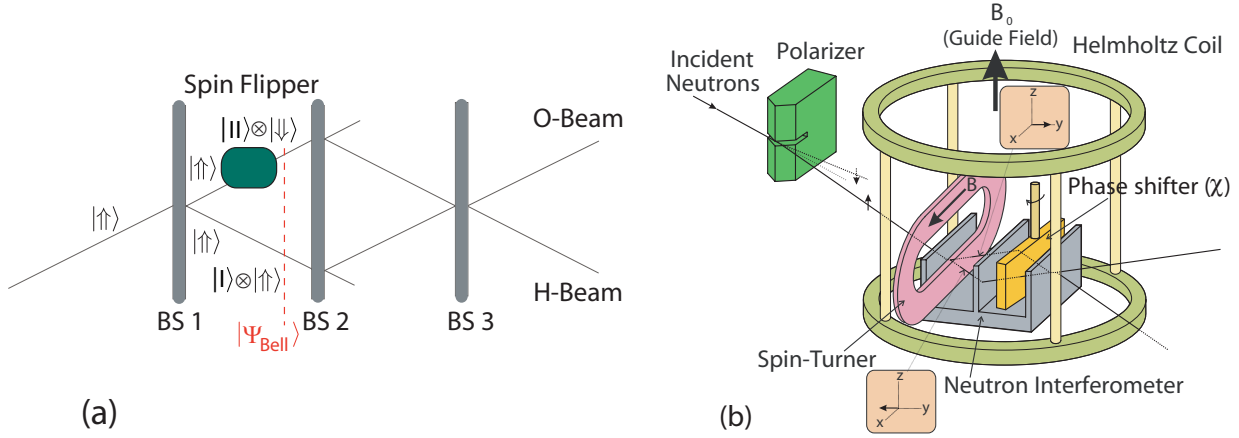


Figure 3.10: (a) Principal of spin path entanglement preparation in neutron interferometry. The spin in one arm is flipped, thereby creating a Bell state. (b) Actual neutron interferometric setup from [Hasegawa et al., 2003] using a Mu-metal spin-turner.

arbitrary initial spin state $|\psi^{\text{spin}}\rangle$

$$|\Psi_0\rangle \xrightarrow{\text{BS}} |\Psi_i\rangle = \frac{1}{\sqrt{2}} \left(|I\rangle + |II\rangle \right) \otimes |\psi^{\text{spin}}\rangle. \quad (3.47)$$

If now a magnetic field \vec{B} , for example in path $|II\rangle$, is switched on the spin part is changed according to

$$|\Psi_i\rangle \xrightarrow{II:\vec{B}} |\Psi'\rangle = \frac{1}{\sqrt{2}} \left(|I\rangle \otimes |\psi^{\text{spin}}\rangle + |II\rangle \otimes \hat{U}|\psi^{\text{spin}}\rangle \right), \quad (3.48)$$

where \hat{U} denotes the interaction between spin and magnetic field. This state is generally called an entangled state simply because it cannot be written in a product form. Thus a spin path entangled state in neutron interferometry is created. The principal of preparing a particular entangled state, i. e. a maximally entangled Bell state illustrated in Fig. 3.10. An incident neutron beam, which is spin up polarized $|\psi_{\text{in}}^{\text{spin}}\rangle = |\uparrow\rangle$, is coherently split into two sub beams at the first plate of the interferometer. In one of the two path (for example $|II\rangle$) a spin flipper is inserted, flipping the spin from $|\uparrow\rangle$ to $|\downarrow\rangle$ in this particular arm of the interferometer. Behind the spin flipper the neutrons wavefunction exhibits entanglement between the spinor and the spatial part, and the corresponding state vector is denoted as

$$|\Psi_{\text{Bell}}\rangle = \frac{1}{\sqrt{2}} \left(|I\rangle \otimes |\uparrow\rangle + |II\rangle \otimes |\downarrow\rangle \right). \quad (3.49)$$

In the first experiments, a violation of a Bell-like inequality [Hasegawa et al., 2003] as well as full tomographic state analysis [Hasegawa et al., 2007], of the Bell state have been realized using a Mu-metal spin-turner. For this procedure a soft-magnetic Mu-metal sheet, which gives considerably high permeability induced by a weak magnetic field, was utilized. A sheet of 0.5mm thick in an oval ring form was used and two DC-coils were applied to magnetize this soft-magnetic sheet. Here both subbeams were exposed to the soft-magnetic Mu-metal sheet. In one arm the initial spin was turned from $|\uparrow\rangle$ to $|\Leftarrow\rangle$, whereas in the other arm, due to a different relative path lengths within the soft-magnetic Mu-metal, the spin was turned from $|\uparrow\rangle$ to $|\Rightarrow\rangle$. The produced Bell state was

$$|\Psi_{\text{Bell}}^{\mu}\rangle = \frac{1}{\sqrt{2}}\left(|\Rightarrow\rangle \otimes |\text{I}\rangle + |\Leftarrow\rangle \otimes |\text{II}\rangle\right). \quad (3.50)$$

However the main problem of this procedure lies in the fact that the a Mu-metal sheet, used to manipulate spin in interferometer, caused an unwanted loss of contrast (roughly 20 per cent), due to inhomogeneous phase shift. Thus a solution for this particular issue was requested.

3.2 Coherent Energy Manipulation

In this Section a spin-path entanglement preparation scheme is introduced, where the unwanted decrease of contrast, due to Mu-metal sheet of the spin-flipper as seen in Sec. 3.1.2, is circumvented. In order avoid such a loss, **radio-frequency (RF)** spin-flippers, as already introduced in Section 2.1.2, have been developed to replace the Mu-metal spin-flipper in the interferometer. Here the neutrons do not touch any material, hence the loss in contrast is expected to be marginal. To eliminate an undesired thermal impact, which would lead instantaneous loss of contrast of the interferometer, the RF-flipper has to be equipped with a water-cooling system.

3.2.1 Theoretical Background

When operating an RF-flipper inside the interferometer, there is a fundamental insufficiency, due to the interaction with a time-dependent magnetic field. As shown in Section 2.1.2 the total energy is no longer a conserved quantity in RF-flip process. The corresponding wave function is given by

$$|\Psi\rangle = \frac{1}{\sqrt{2}} \left(e^{(-i/\hbar)Et} |\text{I}\rangle \otimes |\uparrow\rangle + e^{(-i/\hbar)(E-\Delta E)t} e^{i\chi} |\text{II}\rangle \otimes |\downarrow\rangle \right), \quad (3.51)$$

with

$$\omega_{\text{rf}} = \Delta E/\hbar. \quad (3.52)$$

After passing the RF-flipper neutrons which were initially polarized parallel to the guide field B_0 (z -direction), and had the energy $E = \hbar^2 k^2/(2m) + |\mu|B_0$, have been flipped and lost an amount of energy $\Delta E = 2|\mu|B_0$. The polarization of this state is not stationary, due to a energy difference of $\Delta E = \hbar\omega$ between the spin components:

$$\langle \Psi | \vec{\sigma} | \Psi \rangle = (\cos(\chi - \omega t), \sin(\chi - \omega t), 0), \quad (3.53)$$

as demonstrated in [Badurek et al., 1983], where a stroboscopic neutron detection, triggered by the oscillating field, was applied to observe the nonstationary interference patterns defined in Eq.(3.53).

However, the energy difference between the orthogonal spin states can be compensated by inserting a second RF-flipper, behind the third plate if the interferometer, operating

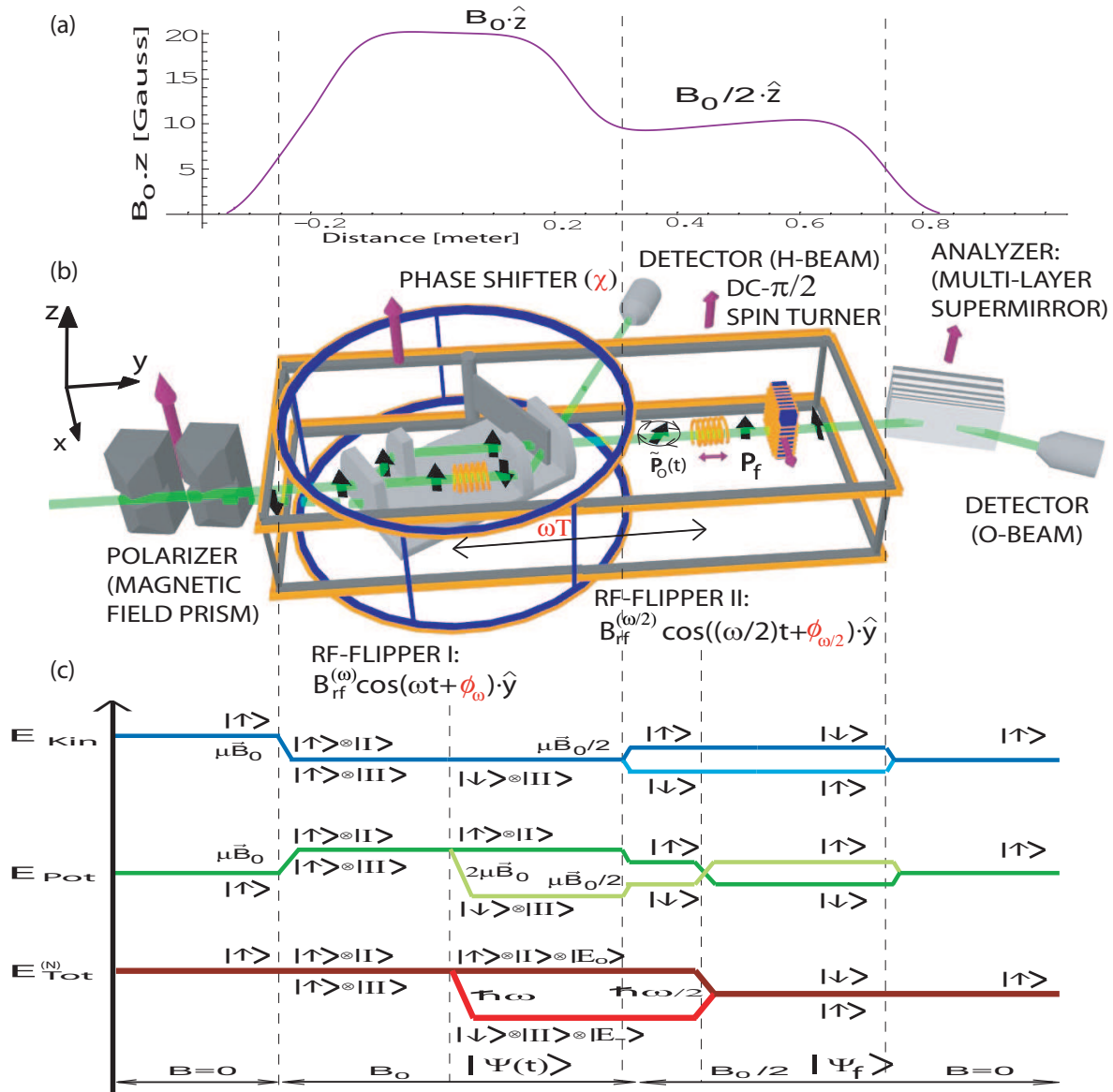


Figure 3.11: (b) Schematic representation of the arrangement of two radio-frequency flip coils the first within one path of the skew-symmetric Mach-Zehnder-type neutron interferometer and the other driven by the half frequency behind the interferometer, accelerator coil, $\pi/2$ spin turner. (c) Energy level diagram of the two interfering sub-beams. (a) Calculated static magnetic guide field gradient.

at a frequency of $\omega/2$. This flipper evens the energy difference between the two spin components, by absorption (in state |I>) and emission (in state |II>) of photons of energy $E = \hbar\omega/2$. Hence a combination of two different guide fields, providing the requested static magnetic fields to fulfill the frequency resonance Eq.(2.1.2) for ω and $\omega/2$, is required. A schematic representation of the setup is depicted in Fig. 3.11 (b). In Fig. 3.11 (c), the corresponding energy diagram is illustrated. Finally Fig. 3.11 (a) shows a plot of the associated guide field configuration, required for the two guide field regions B_0 and $B_0/2$.

The corresponding Jaynes-Cummings Hamiltonian

Concerning a theoretical treatment of the induced RF spin flip the time evolution of the system is described by a photon-neutron state vector, which is an eigenvector of the corresponding modified Jaynes-Cummings (J-C) Hamiltonian [Jaynes and Cummings, 1963, Shore and Knight, 1993]. The J-C Hamiltonian can be adopted for a system consisting of a neutron coupled to a quantized RF-field [Muskat et al., 1987].

Since two RF-fields, operating at frequencies ω and $\omega/2$, are involved in the actual experiment, the modified corresponding J-C Hamiltonian is denoted as

$$\begin{aligned} \mathcal{H}_{\text{J-C}} = & -\frac{\hbar^2}{2m}\nabla^2 - \mu B_0(\vec{r})\sigma_z + \hbar(\omega\hat{a}_\omega^\dagger\hat{a}_\omega + \frac{\omega}{2}\hat{a}_{\omega/2}^\dagger\hat{a}_{\omega/2}) \\ & + \mu\left(\frac{B_1^{(\omega)}(\vec{r})}{\sqrt{N_\omega}}(\hat{a}_\omega^\dagger\sigma_+ + \hat{a}_\omega\sigma_+) + \frac{B_1^{(\omega/2)}(\vec{r})}{\sqrt{N_{\omega/2}}}(\hat{a}_{\omega/2}^\dagger\sigma_+ + \hat{a}_{\omega/2}\sigma_+)\right). \end{aligned} \quad (3.54)$$

with $\sigma_\pm = \frac{1}{2}(\sigma_x \pm i\sigma_y)$. The first term accounts for the kinetic energy of the neutron. The second term leads to the usual Zeeman splitting of $2|\mu|B_0$. The third term adds the photon energy of the oscillating fields of frequencies ω and $\omega/2$, by use of the creation and annihilation operators a^\dagger and a . Finally, the last term represents the coupling between photons and the neutron, where $N_{\omega_j} = \langle \hat{a}_{\omega_j}^\dagger \hat{a}_{\omega_j} \rangle$ represents the mean number of photons with frequencies ω_j in the RF-field. Note that the first two and the last terms concern the spatial $|\psi(\vec{r})\rangle$ and the (time-dependent) energy $|E(t)\rangle$ subspaces of neutrons, respectively.

The state vectors of the oscillating fields are represented by coherent states $|\alpha\rangle$, which are eigenstates of a^\dagger and a . The eigenvalues of coherent states are complex numbers, so one can write

$$\hat{a}|\alpha\rangle = \alpha|\alpha\rangle = |\alpha|e^{i\phi}|\alpha\rangle \text{ with } |\alpha| = \sqrt{N}. \quad (3.55)$$

The action of σ_{\pm} on $|\uparrow\rangle$ and $|\downarrow\rangle$ is given by

$$\begin{aligned}\sigma_-|\uparrow\rangle &= |\downarrow\rangle & \sigma_+|\uparrow\rangle &= 0 \\ \sigma_-|\downarrow\rangle &= 0 & \sigma_+|\downarrow\rangle &= |\uparrow\rangle.\end{aligned}\quad (3.56)$$

Using Eq. (3.54) one can define a total state vector including not only the neutron system $|\Psi_N\rangle$, but also the two quantized oscillating magnetic fields:

$$|\Psi_{\text{tot}}\rangle = |\alpha_\omega\rangle \otimes |\alpha_{\omega/2}\rangle \otimes |\Psi_N\rangle, \quad (3.57)$$

where for simplicity a single-plane-wave representation for the neutron's wavefunction is chosen:

$$|\Psi_N\rangle = e^{-(i/\hbar)E_0t} \left(\cos\frac{\theta}{2}|\uparrow\rangle + e^{i\varphi}\sin\frac{\theta}{2}|\downarrow\rangle \right) \quad (3.58)$$

At this point one can take a look at the action of the interaction Hamiltonian (of one RF-field at frequency ω) on a spin-up state:

$$\begin{aligned}& \left(\frac{\mu B_1^{(\omega)}(\mathbf{r})}{\sqrt{N_\omega}} (\hat{a}_\omega^\dagger \sigma_+ + \hat{a}_\omega \sigma_+) \right) (|\alpha_\omega\rangle \otimes e^{-(i/\hbar)E_0t} |\uparrow\rangle) \\ &= \left(\frac{\mu B_1^{(\omega)}(\mathbf{r})}{\sqrt{N_\omega}} \underbrace{|\alpha_\omega\rangle}_{\alpha} e^{i\phi(t)_\omega} \right) (|\alpha_\omega\rangle \otimes e^{-(i/\hbar)E_0t} |\downarrow\rangle),\end{aligned}\quad (3.59)$$

where $\mu B_1^{(\omega)}$ represents the usual coupling strength of the neutron field interaction, as discussed in Section 2.2.4, which yields after the interaction with RF-field

$$|\Psi_N^{\text{Fin}}\rangle = e^{i\phi_\omega} (|\alpha_\omega\rangle \otimes e^{-(i/\hbar)E_0t} |\downarrow\rangle). \quad (3.60)$$

A spin flip due to emission of a photon of energy $\hbar\omega$ and a phase factor $e^{i\phi_\omega(t)}$ from the coherent state of the oscillating field.

Now the time evolution of a dressed state, as defined in Eq.(2.198), is taken into account, to see the effect after passing the RF-field region:

$$\begin{aligned}& \left(\frac{2\mu B_1^{(\omega)}(\mathbf{r})}{\sqrt{N_\omega}} (a_\omega^\dagger \sigma_+ + a_\omega \sigma_+) \right) (|\alpha_\omega\rangle \otimes e^{-(i/\hbar)E_0t} |\uparrow\rangle) = e^{i\omega t} e^{i\phi_\omega} (|\alpha_\omega\rangle \otimes e^{-(i/\hbar)E_0t} |\downarrow\rangle) \\ &= e^{i\phi_\omega} (|\alpha_\omega\rangle \otimes e^{-(i/\hbar)(E_0 - \hbar\omega)t} |\downarrow\rangle)\end{aligned}\quad (3.61)$$

Here $e^{-(i/\hbar)E_0t}$ is associated with a corresponding state vector $|E_0\rangle$, just like in an atomic two-level system (see Section 2.2.4), where a certain energy level is associated with a

ground state $|g\rangle$. Hence $e^{-(i/\hbar)(E_0 - \hbar\omega)t}$ can be identified with $|E_0 - \hbar\omega\rangle$ (in analogy to the excited state $|e\rangle$). Thus Eq.(3.61) yields

$$\begin{aligned} & \left(\frac{2\mu B_1^{(\omega)}(\mathbf{r})}{\sqrt{N_\omega}} (a_\omega^\dagger \sigma_+ + a_\omega \sigma_-) \right) (|\alpha_\omega\rangle \otimes |\uparrow\rangle \otimes |E_0\rangle) \\ & = e^{i\phi_\omega} (|\alpha_\omega\rangle \otimes |\downarrow\rangle \otimes |E_0 - \hbar\omega\rangle). \end{aligned} \quad (3.62)$$

Thus, a third degree of freedom in neutron interferometric has become experimental accessible. Due to its experimental accessibility within a magnetic resonance field [Badurek et al., 1983] the neutron's energy degree of freedom seems to be an almost ideal for *multi entanglement* preparation.

3.2.2 Radio frequency (RF) coil construction

For the experiments described in [Sponar et al., 2008b] and [Sponar et al., 2010a] the RF-flipper coil depicted in Fig.3.12 was utilized inside the interferometer. The body of the flip coils was cut of s a single bloc of copper, which was chosen due to its thermal conductivity. The fabrication was done at the facility at the atomic institute in Vienna. The coil is equipped with a water-cooling system to minimize the thermal exposure of

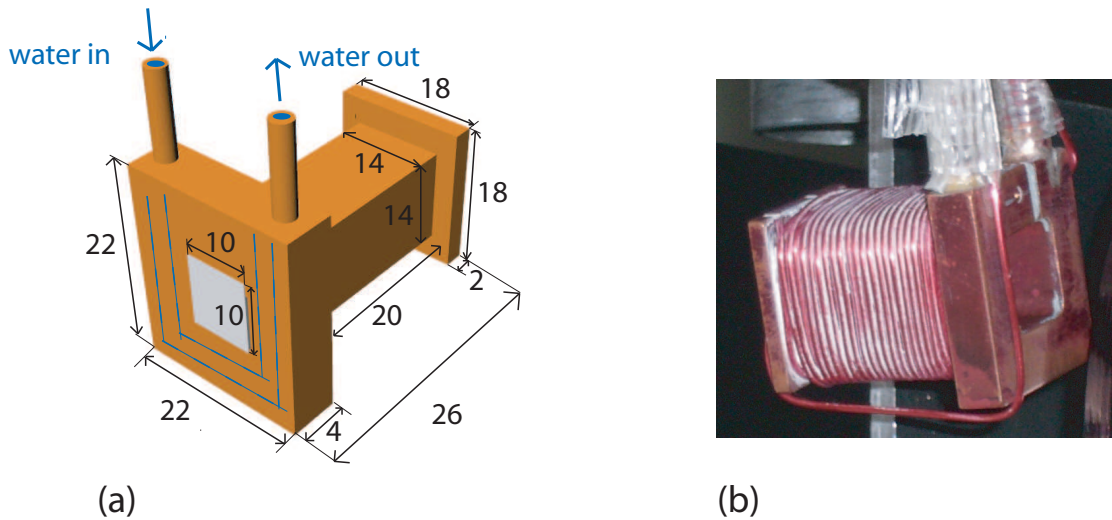


Figure 3.12: (a) Construction plan RF-coil (dimensions in mm). (b) Photograph of the RF-coil with wire thickness 0.7mm, wound in two layers.

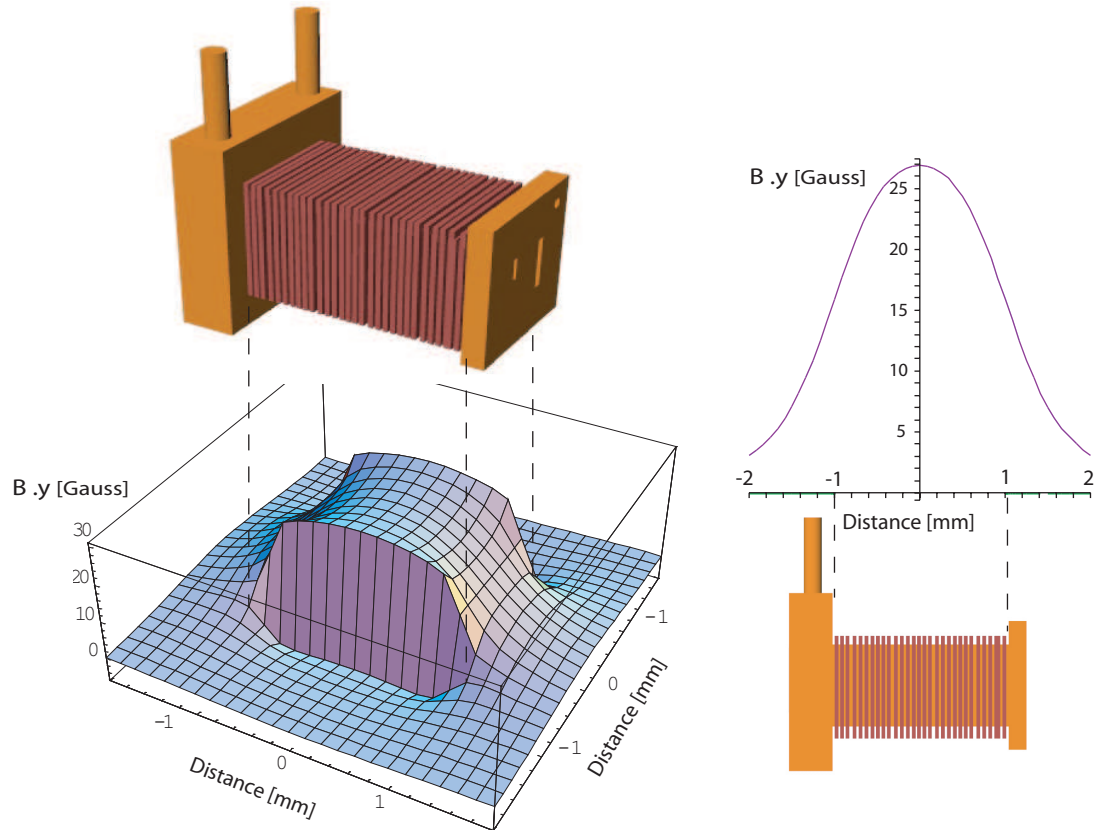


Figure 3.13: (left) Calculated magnetic field field B_y of the RF-flipper coil. A maximal field of $B_{\text{rot}} = 26.9$ Gauss is required for a spin flip. (right) Magnetic field along the propagation direction $(0, y, 0)$ of the rectangular coil.

Table 3.2: Characteristics of the LC-circuit with 58 kHz

| value | calculated | measured |
|-------------|-----------------------|--------------------|
| Windings | 42(2x21) | 42(2x21) |
| Inductivity | 21.2 μH | 21.7 μH |
| Capacity | 0.35495 μF | 0.4 μF |



Figure 3.14: Photograph of the setup with circular and rectangular Helmholtz coil arrangement. top: Rectangular Helmholtz coil before setup is put together. One can see the water cooling system and the thermal isolation. bottom: (red frame) Configuration of a circular and rectangular Helmholtz coils for magnetic guide fields $B_0 \sim 20$ G and $B_0/2 \sim 10$ G. (Green) RF-flipper in the interferometer with thermal isolation and (blue) before operating without thermal isolation. (Yellow) Rectangular guide field with cooling water supply for the guide field, and supermirror analyzer.

the interferometer, causing loss in contrast. The dimensions can be seen in the construction plan depicted in Fig.3.12 (a). Before the windings were added a slit along the entire coil was cut through the top surface, to prevent Foucault currents (can only be seen in Fig.3.12 (b)). The main limitation towards the coil length stems from the skew-symmetric neutron interferometer, (see for instance Fig.3.11), which was used for the experiments. A wire of a thickness of 0.7 mm was chosen for the winding of the coil. The characteristics of the parallel LC circuit, designed to produce the oscillating magnetic field, are summarized in Tab. 3.2.

In respect to the time of flight of the neutrons through the RF-flipper and according to its dimensions a mean magnetic field amplitude B_{osz} of 34.3 Gauss (which corresponds to $B_{rot} = 17.15$ Gauss for one rotating part of the field) was calculated for a spin flip. According to the associated longitudinal field dependence, as illustrated in Fig. 3.13, this corresponds to a maximal field amplitude of 26.9 Gauss, induced by a current of 1.3 A. In respect to a frequency of 58 kHz of the LC-circuit a guide field of 19.9 Gauss had to be applied. This field originates partly from the circular Helmholtz coil and partly from the rectangular, both depicted in Fig 3.14.

The second RF-flipper, placed outside of the interferometer, was driven accordingly with a frequency of 29 kHz. The coil was wired on a PVC-pipe with diameter of 35 mm and a length of 75 mm having 50 windings. Since this flipper is outside of the interferometer no water cooling system was required.

3.2.3 Interferometric setup

The polarizer-analyzer system

The polarizer: Magnetic Field Prism

As seen from Eq.(3.49) the incident beam is supposed to be in a $|\uparrow\rangle$ eigenstate. This is achieved by a spin-dependent birefringence of the incoming neutrons upon passage through the air gap of a prismatic permanent magnet yoke. Thereby the neutron beam is split in two polarized sub-beams with slightly different directions, which is depicted in Fig. 3.15. When entering a magnetic field \vec{B} neutrons of wavenumber \vec{k}_0

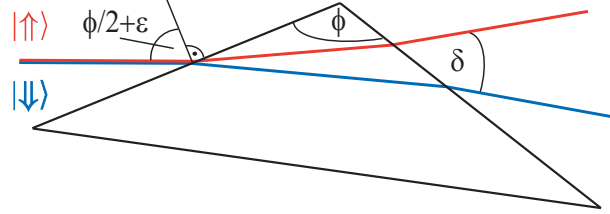


Figure 3.15: Schematic representation of the magnetic field prism, and trajectory of the spin eigenstates.

exhibit a spin-dependent change of momentum

$$\frac{\Delta k}{k_0} \sim \pm \frac{m\mu B}{\hbar^2 k_0^2}, \quad (3.63)$$

due to the different Zeeman energies $\pm\mu B$ of the eigenstates $|\uparrow\rangle$ and $|\downarrow\rangle$. Thus the field acts as a birefringent medium with a spin-dependent refractive index

$$n_{\uparrow,\downarrow} = \frac{k}{k_0} \sim 1 \pm \frac{m\mu B}{\hbar^2 k_0^2}. \quad (3.64)$$

When an unpolarized neutron beam crosses the boundary between a field-free region and the magnetic field the $|\downarrow\rangle$ spin state is refracted *towards* a direction perpendicular to the boundary, whereas the $|\uparrow\rangle$ state undergoes refraction *from* this direction. If two successive boundaries are traversed which are inclined to each other by an angle ϕ , thereby forming a so-called *field prism*, the two spin states propagate in different directions separated by an angle

$$\delta(\phi, \epsilon, B, E_0) = \frac{2\mu B}{E_0} \frac{\sin \phi}{\cos \phi + \cos(2\epsilon)}, \quad (3.65)$$

where the kinetic energy of the incident neutrons is given by $E_0 = \hbar^2 k_0^2 / (2m)$, and the asymmetry angle ϵ describes the deviation of the prism orientation from symmetric neutron passage. For thermal neutrons a field of about 1 T causes an angular splitting of the order of a few arcseconds. With this arrangement [Badurek et al., 2000], using a prismatically shaped permanent magnet yoke (apex angle $\phi = 116$ degree), at a neutron wavelength of 1.895 Å the two peaks, corresponding to the $|\uparrow\rangle$ and the $|\downarrow\rangle$ state, are separated by an angle of 5.2 ± 0.2 arc seconds, which is depicted in Fig 3.16. This value corresponds to the extremely narrow width of perfect crystal Bragg reflections. Therefore

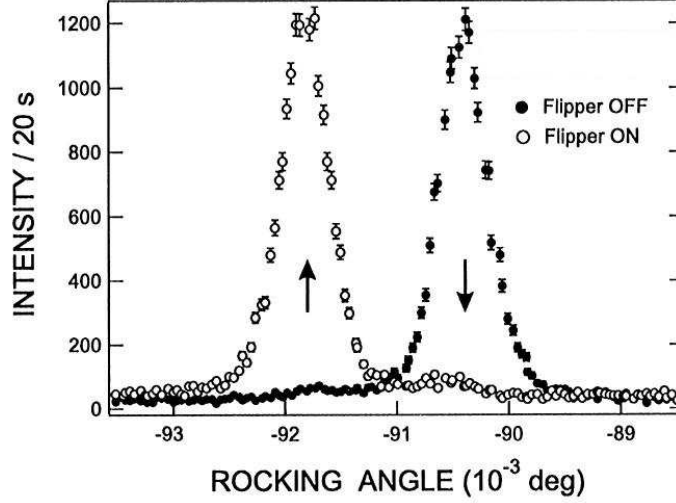


Figure 3.16: Peak separation due to spin dependent reflection on a magnetic field prism from [Badurek et al., 2000].

only one spin component fulfills the Bragg condition at the first plate of the interferometer. This method is capable of polarizing neutrons within perfect crystal interferometers.

The analyzer: Multilayer supermirror array

For a neutron beam incident on a medium, perpendicular to its surface, the reflectivity is calculated as

$$R = \left| \frac{n - 1}{n + 1} \right|^2, \quad (3.66)$$

where n is the refractive index as defined in Eq.(3.23). For $n = 0$ total refraction is observed, yield a critical wave length

$$\lambda_{\text{cr}} = \sqrt{\frac{2\pi}{Nb_c}}. \quad (3.67)$$

For an arbitrary incident angle φ the normal component k_{\perp} has to be analyzed for calculating a critical angle φ_{cr}

$$k_{\perp} = k \sin \varphi \rightarrow \lambda_{\perp} \sim \frac{\lambda}{\sin \varphi}. \quad (3.68)$$

Hence the critical angle is given by

$$\varphi_{\text{cr}} = \lambda \sqrt{\frac{Nb_c}{2\pi}}, \quad (3.69)$$

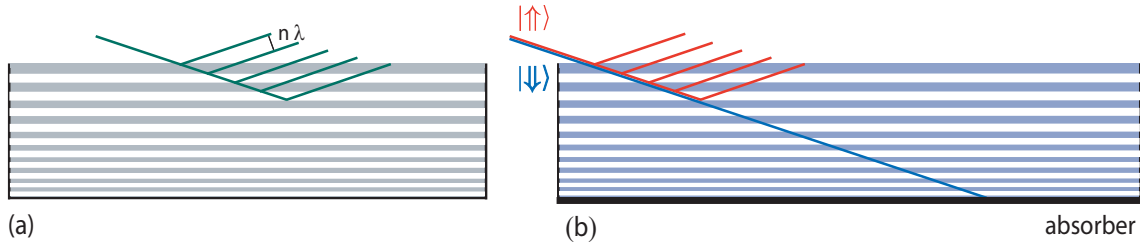


Figure 3.17: (a) Non-magnetic multilayer structure (neutron guide), (b) Multilayer supermirror with absorber to filter one spin component (polarizer).

which is for example ~ 0.2 degree for Ni and neutrons of 2 \AA wave length.

Suppose a *multilayer* structure of two media A and B having different coherent scattering length $b_{c(A,B)}$. For an incident angle $\varphi > \varphi_{cr}$ at every single boundary layer there will occur a transmitted and a reflected sub beam. If the thickness of the layers is chosen in such way that the partial waves of the reflected sub beams have a optical path difference of $n\lambda$ constructive interference will be observed, which is illustrated in Fig. 3.17 (a). The multilayer structure can be interpreted as a one dimensional crystal, with the layer thickness as its lattice constant. If the thickness of the layers varies only slightly, from layer to layer, there will be an appropriate lattice constant for a diversity of wavelengths. The entire structure behaves like a medium with higher critical angle φ_{cr} , (or with smaller critical wavelength λ_{cr}), typically by a factor three. A suitable combination of materials is found by Ni ($b_c = 10.3 \text{ fm}$) and Ti ($b_c = -3.3 \text{ fm}$), which are utilized in neutron guides.

If alternating a magnetic and a non-magnetic medium is utilized not only the nuclear scattering length, but also the magnetic scattering length has to be considered. This can be used for beam polarization, since the sign of the magnetic scattering length depends of the orientation of the spin towards the magnetization of the medium. If a combination is chosen such that the sum of the nuclear scattering length and the magnetic scattering length for one spin component (for instance $|\downarrow\rangle$) equals the scattering length of the non-magnetic substance, then this spin component will not be reflected, since there is no difference in the refractive index of the two layers for this spin component. However, the other spin component ($|\uparrow\rangle$) will be (partly) reflected. The transmitted spin component ($|\downarrow\rangle$) is absorbed after the last layer, which is illustrated in Fig. 3.17 (b). An arrangement as discussed here is referred to as *supermirror*, often used as polarizer or analyzer.

Coil adjustment

The two RF-flippers, one inside and one outside of the interferometer are driven by a Yokogawa FG-120 signal generator with a frequency of 58 kHz and accordingly 29 kHz. In order to fulfill the frequency resonance condition guide field scans (with RF-flipper operating at 58 kHz on) were performed to obtain a minimal count rate, which is depicted in Fig. 3.18 (left). The spinor rotation angle induced by the RF-spin flipper is determined by the amplitude $B_1^{(\omega)}$ of the oscillating magnetic field. The resulting intensity modulation when varying the amplitude $B_1^{(\omega)}$ is shown in Fig. 3.18 (right). The obtained flip ratios for both RF-flippers and the DC spin-rotator are summarized in Tab. 3.3.

As seen from Tab. 3.3 the measurements have been performed with $|\uparrow\rangle$ and $|\downarrow\rangle$ as

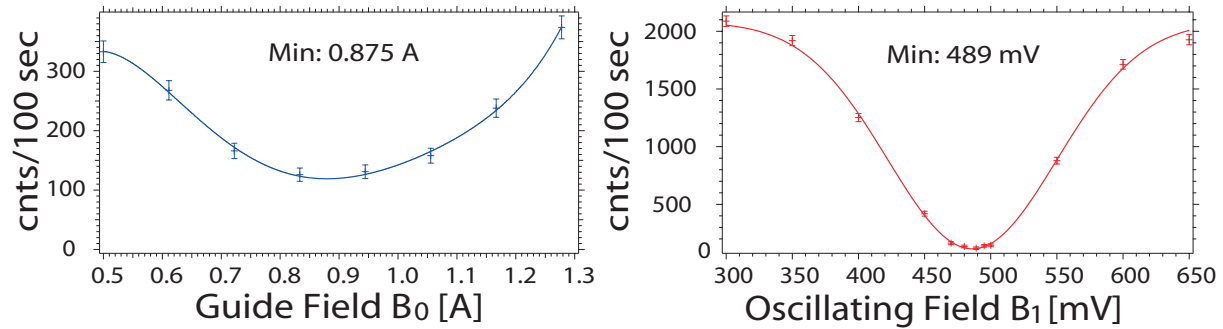


Figure 3.18: B_0 and B_1^ω scans of the RF-flipper inside the interferometer ($\omega = 58 \text{ kHz}$).

Table 3.3: Typical flip ratios for the two RF-flipper and the DC spin-rotator.

| Flipper type | Flipp Ratio | Error |
|---|-------------|-------|
| initial polarization $ \downarrow\rangle$: | | |
| RF(ϕ_ω) | 61 | 8 |
| RF($\phi_{\omega/2}$) | 63 | 9 |
| DC | 50 | 6 |
| initial polarization $ \uparrow\rangle$: | | |
| RF(ϕ_ω) | 24 | 2 |
| RF($\phi_{\omega/2}$) | 37 | 4 |
| DC | 30 | 4 |

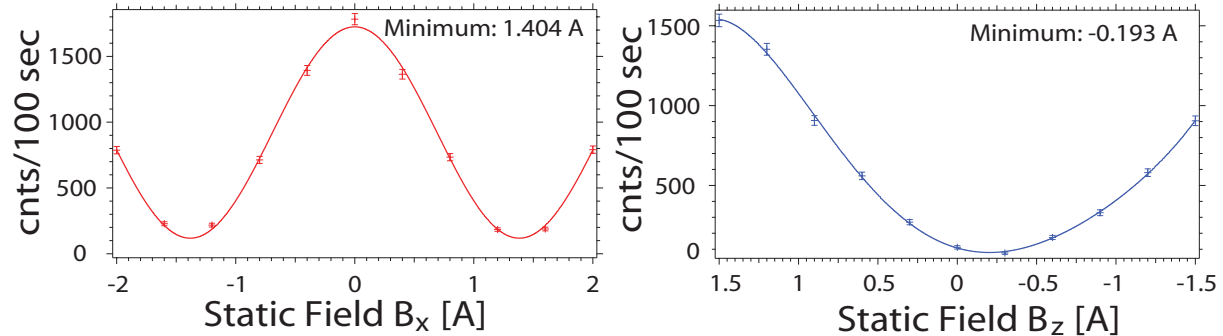


Figure 3.19: B_x and B_z scans of the DC spin-rotator. The B_x scan plotted here was performed, in a first run, without compensation of the guide field (B_z).

initial polarization. The motivation for this will be explained in more detail in the course of this Section. Intensity modulations of the DC spin-rotator, due to adjustments of the fields B_x and B_z , which is required to compensate the effect of the guide field, are depicted in Fig. 3.19.

Measurement procedure

In a perfect Si-crystal neutron interferometer the wavefunction behind the first plate, acting as a beam splitter, is a linear superposition of the sub-beams belonging to the right ($|I\rangle$) and the left path ($|II\rangle$).

In present experiment, only the beam in path II is exposed to the RF-field of frequency ω , resulting in a spin flip. The spin flip configuration of the first RF-field ensures an entanglement of spin and spatial degree of freedom of the neutron state [Hasegawa et al., 2003]. Interacting with a time-dependent magnetic field, the total energy of the neutron is no longer conserved after the spin-flip [Alefeld et al., 1981, Gähler and Golub, 1987, Golub et al., 1994, Grigoriev et al., 2004]. Photons of energy $\hbar\omega$ are exchanged with the RF-field, this particular behavior of the neutron is described by the 'dressed-particle' formalism [Muskat et al., 1987, Summhammer, 1993]. Consequently the two sub-beams $|I\rangle$ and $|II\rangle$ now differ in total energy (see Fig. 4.12(b)). Therefore the neutron state can be considered to consist of the three subsystems, namely the total energy, path and spin degree of freedom. A coherent superposition of $|I\rangle$ and $|II\rangle$ results in

the multiply entangled dressed state vector, expressed as

$$|\Psi(t)\rangle \propto |\alpha_\omega\rangle \otimes |\alpha_{\omega/2}\rangle \otimes \frac{1}{\sqrt{2}} \left(|I\rangle \otimes |\uparrow\rangle + e^{i\omega t} e^{i\chi} |II\rangle \otimes e^{i\phi_\omega} |\downarrow\rangle \right). \quad (3.70)$$

According to the notation introduced in Sec. 2.2.4 Eq.(3.70) can be rewritten as

$$|\Psi(t)\rangle \propto |\alpha_\omega\rangle \otimes |\alpha_{\omega/2}\rangle \otimes \frac{1}{\sqrt{2}} \left(|I\rangle \otimes |E_0\rangle \otimes |\uparrow\rangle + e^{i\chi} |II\rangle \otimes |E_0 - \hbar\omega\rangle \otimes e^{i\phi_\omega} |\downarrow\rangle \right) \quad (3.71)$$

The spin in path $|II\rangle$ is flipped by a RF-flipper, which requires two magnetic fields: A static field $B_0 \cdot \hat{\mathbf{z}}$ and a perpendicular oscillating field $B^{(1)} = B_{\text{if}}^{(\omega)} \cos(\omega t + \phi_\omega) \cdot \hat{\mathbf{y}}$ satisfying the amplitude and frequency resonance condition

$$B_1^{(\omega)} = \frac{\pi \hbar}{\tau |\mu|} \text{ and } \omega = \frac{2|\mu|B_0}{\hbar} \left(1 + \frac{B_1^2}{16B_0^2} \right), \quad (3.72)$$

where μ is the magnetic moment of the neutron and τ denotes the time the neutron is exposed to the RF-field. The second term in ω is due to the Bloch-Siegert shift [Bloch and Siegert, 1940]. The oscillating field is produced by the water-cooled RF-coil, introduced in the last Section, operating at a frequency of $\omega/2\pi = 58$ kHz. The static field is provided by a uniform magnetic guide field $B_0^{(\omega)} \sim 2$ mT, produced by a pair of water-cooled Helmholtz coils.

The sub beams differ by an adjustable phase factor $e^{i\chi}$ ($\chi = -N_{\text{ps}} b_c \lambda D$, with the thickness of the phase shifter plate D , the neutron wavelength λ , the coherent scattering length b_c and the particle density N_{ps} in the phase shifter plate). By rotating the plate, χ can be varied systematically. The state vector of the neutron acquires a phase $\pm\phi_\omega$ during the interaction with the oscillating field, given by $B(t) = B_1 \cos(\omega t + \phi_\omega)$, induced by the action of the operators \hat{a}_ω and \hat{a}_ω^\dagger in the last term of Eq. (3.54). The neutron part of the total state vector is represented by a path-energy-spin entanglement within a single-neutron system.

The two sub-beams are recombined at the third plate, which is described by the projection operator $\hat{O}^{(P)} = \frac{1}{2}(|I\rangle + |II\rangle)(\langle I| + \langle II|)$, resulting in a time-dependent state vector due to the different energies of the two partial wavefunctions. Due to the orthogonality of the energy and spin eigenstates the measured polarization is zero and no intensity modulations are observed in the H-beam, have the following polarization

$$\vec{P}_H(t) = \left(\cos(\chi + \pi - \omega t - \phi_\omega), \sin(\chi + \pi - \omega t - \phi_\omega), 0 \right), \quad (3.73)$$

which can be seen in Fig. 3.21 (top). The polarization in the O-beam is expressed as

$$\vec{P}_O(t) = \left(\cos(\chi - \omega t - \phi_\omega), \sin(\chi - \omega t - \phi_\omega), 0 \right). \quad (3.74)$$

This phenomenon has been measured separately [Badurek et al., 1983], and is related to the spinor precession known from zero-field spin-echo experiments [Gähler and Golub, 1987, Grigoriev et al., 2004].

The beam recombination is followed by an interaction with the second RF-field, with half frequency $\omega/2$. The total state vector is given by

$$\begin{aligned} |\Psi'\rangle &= |\alpha_\omega\rangle \otimes |\alpha_{\omega/2}\rangle \otimes (|I\rangle + |II\rangle) \\ &\otimes \frac{1}{\sqrt{2}} \left(e^{i\phi_{\omega/2}} e^{i\frac{\omega}{2}(t+T)} |\Downarrow\rangle + e^{i\omega t} e^{-i\frac{\omega}{2}(t+T)} e^{i\chi} e^{i(\phi_\omega - \phi_{\omega/2})} |\Uparrow\rangle \right) \\ &\propto |\alpha_\omega\rangle \otimes |\alpha_{\omega/2}\rangle \otimes (|I\rangle + |II\rangle) \otimes \frac{1}{\sqrt{2}} \left(e^{i\phi_{\omega/2}} |\Downarrow\rangle + e^{-i\omega T} e^{i\chi} e^{i(\phi_\omega - \phi_{\omega/2})} |\Uparrow\rangle \right), \end{aligned} \quad (3.75)$$

where ϕ_ω and $\phi_{\omega/2}$ are the phases induced by the two RF-fields. The second RF-flipper is operating at $\omega/2\pi = 29$ kHz, which is half the frequency of the first RF-flipper. The oscillating field is denoted as $B_1^{(\omega/2)} \cos((\omega/2)t + \phi_{\omega/2}) \cdot \hat{\mathbf{y}}$, and the strength of the guide field was tuned to $B_0^{(\omega/2)} \sim 1$ mT in order to satisfy the frequency resonance condition. By choosing a frequency of $\omega/2$ for the second RF-flipper, the time-dependence of the state vector is eliminated since both components acquire a phase $e^{\pm i\omega/2(t+T)}$, depending on the spin orientation. Only a constant phase offset of $e^{-i\omega T}$, which is referred to as *zero-field phase*, with T being the neutron's propagation time between the centre of the first and second RF-flipper coil, remains in the stationary state vector. Hence the second RF-flipper compensates the energy difference between the two spin components, by absorption and emission of photons of energy $E = \hbar\omega/2$.

Alternatively this can be seen by applying the operator

$$\hat{O}^{(E)} = \frac{1}{\sqrt{2}} |E_0 - \hbar\omega/2\rangle (\langle E_0| + (\langle E_0 - \hbar\omega|)), \quad (3.76)$$

which represents mathematically the energy transfer, Eq.(3.71) is transformed to

$$\begin{aligned} |\Psi_f\rangle &\propto |\alpha_\omega\rangle \otimes |\alpha_{\omega/2}\rangle \otimes (|I\rangle + |II\rangle) \otimes |E_0 - \hbar\omega/2\rangle \\ &\otimes \frac{1}{\sqrt{2}} \left(e^{i\phi_{\omega/2}} |\Downarrow\rangle + e^{-i\omega T} e^{i\chi} e^{i(\phi_\omega - \phi_{\omega/2})} |\Uparrow\rangle \right). \end{aligned} \quad (3.77)$$

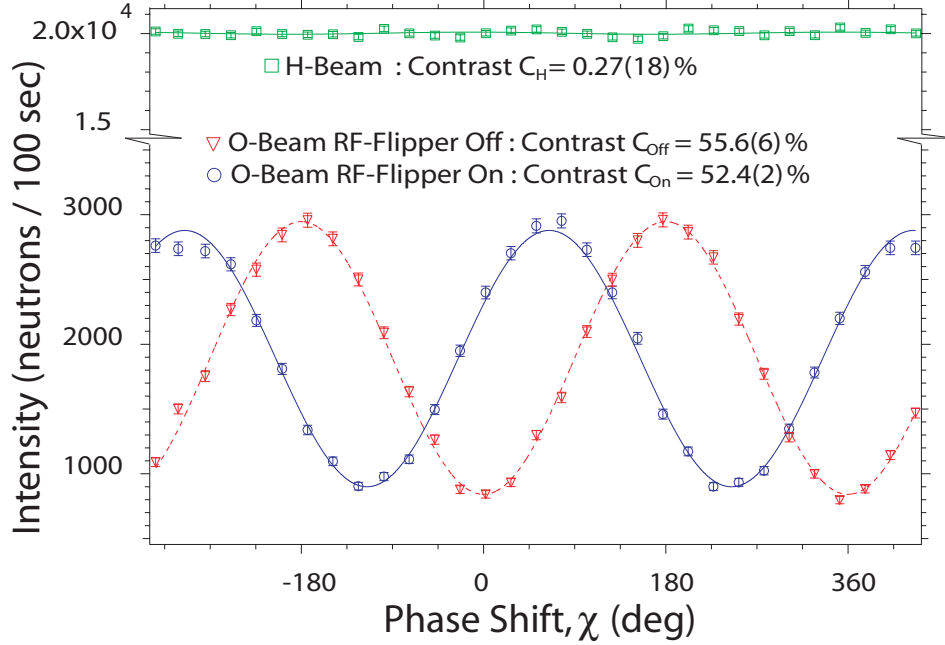


Figure 3.20: Typical interference patterns of H and O-detector (blue). A reference measurement is performed by turning off the RF-flipper inside the interferometer (dotted, red).

The energy difference between the orthogonal spin states is compensated by choosing a frequency of $\omega/2$ for the second RF-flipper, resulting in a stationary state vector. Hence the time dependence of the polarization vector is eliminated:

$$\vec{P}_O^{\text{fin}} = (\cos \Delta_{\text{tot}}, \sin \Delta_{\text{tot}}, 0), \quad (3.78)$$

with

$$\Delta_{\text{tot}} = (\chi - 2\phi_{\omega/2} + \phi_{\omega} - \omega T), \quad (3.79)$$

consisting of the phases induced the path (phase shifter χ), spin (phases of the two RF-fields $\phi_{\omega}, \phi_{\omega/2}$), and energy manipulation (zero-field phase ωT).

Finally, the spin is rotated back by an angle $\delta = \pi/2$ (in the $\hat{\mathbf{x}}, \hat{\mathbf{z}}$ plane) to the $\hat{\mathbf{z}}$ -direction by use of a $\pi/2$ static field spin-turner, and analyzed along the $\hat{\mathbf{z}}$ -direction due to the spin dependent reflection within a Co-Ti multi-layer supermirror, being a projection operator $\hat{O}^{(S)} = |\uparrow\rangle\langle\uparrow|$ to the spin.

A typical interference pattern is depicted in Fig. 3.20. In the O-beam a fringe contrast of $C_{On} = 52.4(2)\%$ is achieved, whereas no oscillation are observed in the H-detector,

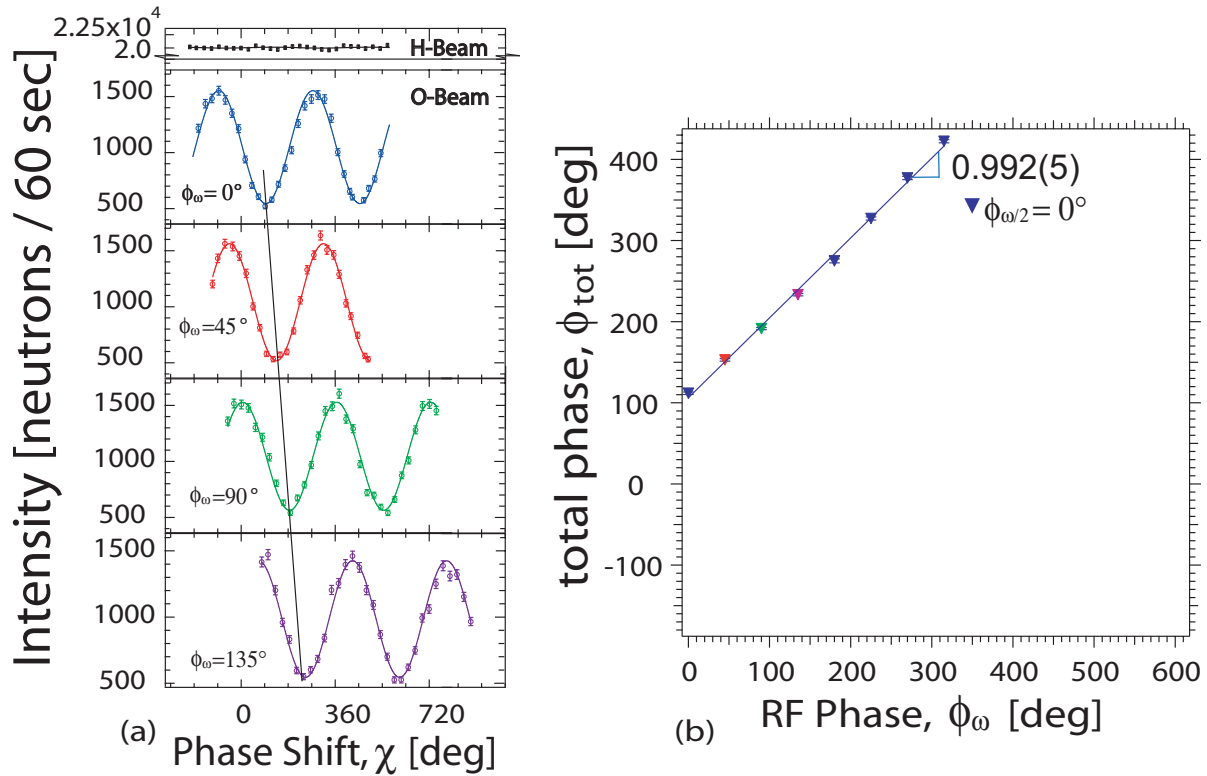


Figure 3.21: (a) Typical interference patterns of H and O-detector. In the H-beam no interference fringes are observed due to orthogonal energy states in the interfering sub-beams, whereas the O-beam exhibits time-independent sinusoidal intensity oscillations, when rotating the phase shifter plate (χ). A phase shift of the occurs by varying ϕ_ω (b) Total phase $\Delta\phi_{\text{tot}}$ vs. RF phase ϕ_ω (flipper in the interferometer), with RF phase $\phi_{\omega/2} = 0$ (flipper outside the interferometer).

where no further manipulations are applied. The principle of energy compensation is visualized in Fig. 3.11 (c). In order to observe a relative phase shift, in practice it is necessary to perform a reference measurement. This is achieved by turning off the RF-flipper inside the interferometer, thus yielding the relative phase difference. Typical interference patterns, when scanning χ , for different settings of ϕ_ω , are depicted in Fig. 3.21 (a). The total (relative) phase difference $\Delta\phi_{\text{tot}}$ is observed when varying ϕ_ω , which is plotted in Fig. 3.21 (b).

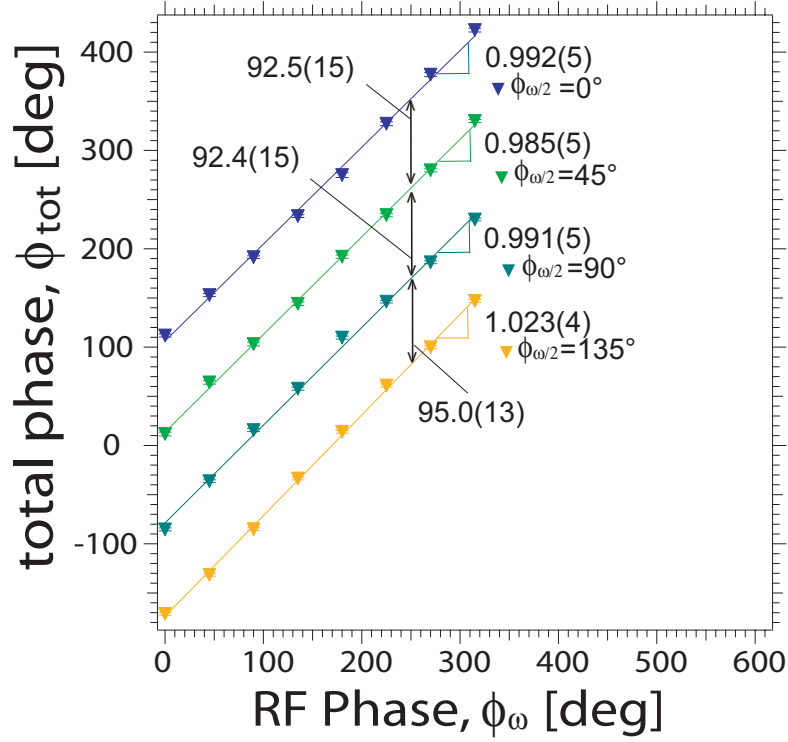


Figure 3.22: Total phase $\Delta\phi_{\text{tot}}$ vs. RF phase ϕ_{ω} (flipper in the interferometer), with $\phi_{\omega/2} = 0, 45, 90$ and 135 deg (flipper outside the interferometer). Varying $\phi_{\omega/2}$ yields a two times larger phase shift compared to ϕ_{ω} as predicted by Eq(3.79).

In Fig 3.22 the total phase difference $\Delta\phi_{\text{tot}}$ is plotted versus ϕ_{ω} for different values of $\phi_{\omega/2}$. According to Eq(3.79) the total phase difference $\Delta\phi_{\text{tot}}$ is shifted by $-2\phi_{\omega/2}$, which can be seen clearly in the plot for four selected values of $\phi_{\omega/2}$. The stationary interference oscillations can be written in form of

$$I_0 \propto 1 + \nu \cos(\chi + \Phi - \omega T), \quad (3.80)$$

introducing the fringe visibility ν and the relative (spin) phase $\Phi = \phi_{\omega} - 2\phi_{\omega/2}$, the phase from the coherent nuclear scattering χ (phase shifter), and the zero-field phase ωT (from energy manipulation).

However, even for $\phi_{\omega} = \phi_{\omega/2} = 0$ the total phase ϕ exhibits an offset, as seen in Fig. 3.21 (b) and Fig 3.22. This is due to the zero-field phase contribution ωT , but also

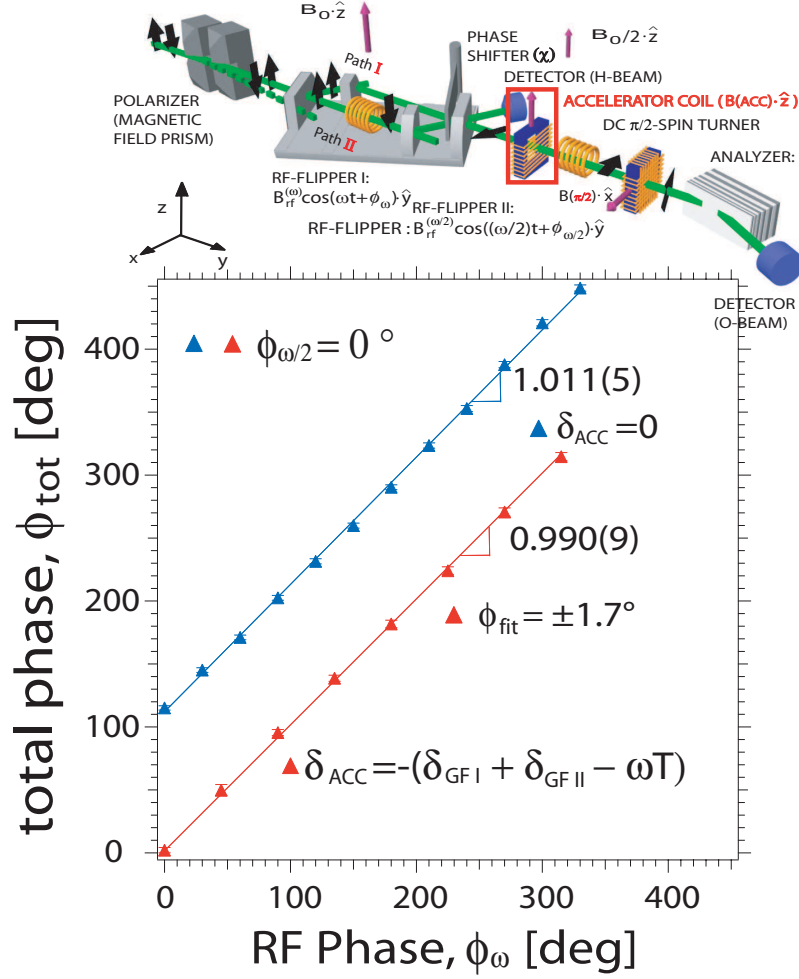


Figure 3.23: Total phase $\Delta\phi_{tot}$ vs. RF phase ϕ_ω . An additional tunable accelerator coil (with static magnetic field pointing in $+z$ -direction) compensates the phase contributions of the constant zero field phase ωT and the dynamical phase accumulated by Larmor precession within the static guide field regions $B_0^{(\omega)} \cdot \hat{z}$ and $B_0^{(\omega/2)} \cdot \hat{z}$, denoted as δ_{GFI} and δ_{GFII} .

due to dynamical phase contribution, resulting from Larmor precession within the guide field regions $B_0^{(\omega)} \cdot \hat{z}$ and $B_0^{(\omega/2)} \cdot \hat{z}$, denoted as δ_{GFI} and δ_{GFII} , which have not been mention yet. These contributions are compensated by an additional Larmor precession within a tunable accelerator coil with a static field, pointing in the \hat{z} -direction. Thus by choosing

$$\delta_{ACC} = -(\delta_{GFI} + \delta_{GFII} - \omega T) \quad (3.81)$$

no more offset is observed for $\phi_\omega = \phi_{\omega/2} = 0$, which is depicted in Fig. 3.23.

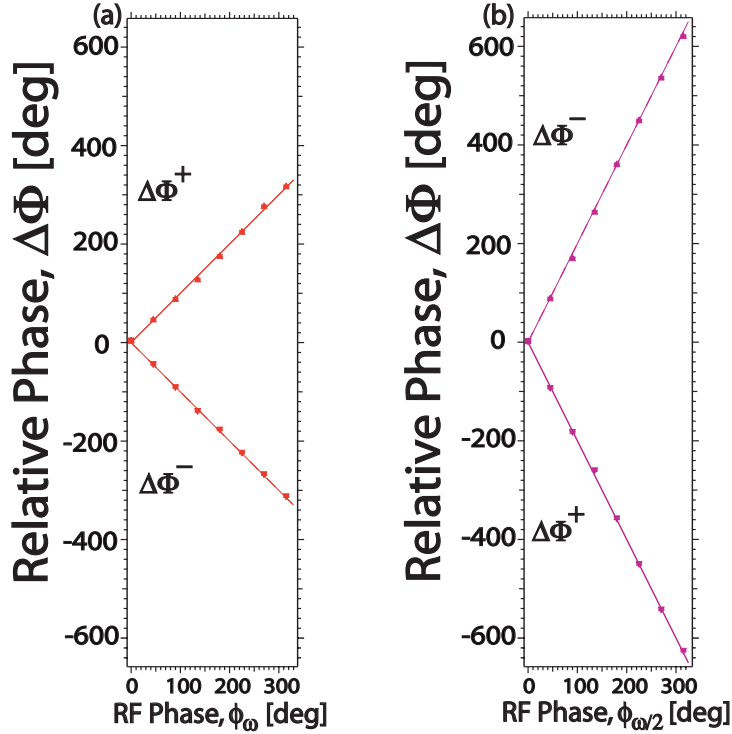


Figure 3.24: (a) Relative phase $\Delta\Phi^\pm$ vs. ϕ_ω , and (b) $\Delta\Phi^\pm$ vs. $\phi_{\omega/2}$. The sign of the phase depends on the chosen initial polarization.

As already explained in Sec 3.2.3 (polarizer-analyzer system), it is possible to invert the initial polarization simply by rotating the interferometer by a few seconds of arc. Thereby the spin-down component is selected to enter the interferometer, which is expected to lead to an inversion of the relative phase. Thus a relative phase difference $\Delta\Phi^\pm = \pm\phi_\omega \mp 2\phi_{\omega/2}$, where \pm denotes the respective initial spin orientation is observed. Figure 3.24 (a) shows a plot of the relative phase $\Delta\Phi^\pm$ versus ϕ_ω , with $\phi_{\omega/2} = 0$, and a phase shift $\Delta\Phi^\pm$ caused by a variation of ϕ_ω . As expected, the slope is positive for initial spin up orientation (1.007(8)), and negative for the spin down case (-0.997(5)). In Fig. 3.24 (b) $\phi_{\omega/2}$ is varied, while ϕ_ω is kept constant, yielding slopes of -1.995(8) and 1.985(7), depending again on the initial beam polarization.

The experiment was carried out at the neutron interferometer instrument S18 at the high-flux reactor of the Institute Laue-Langevin in Grenoble, France. Here a silicon perfect-crystal monochromator is installed permanently in the neutron guide to

monochromatize the incident neutron beam to a mean wave length of $\lambda_0 = 1.91 \text{ \AA}$ with the monochromaticity $\Delta\lambda/\lambda_0 \sim 0.02$. The cross section of the beam is roughly $5 \times 5 \text{ mm}^2$. Birefringent magnetic field prisms in \hat{z} -direction, are used to polarize the incident beam in \hat{z} -direction, before the beam enters the interferometric setup. In a non-dispersive arrangement of the monochromator and the interferometer crystal the angular separation can be used such that only the spin-up (or spin-down) component fulfills the Bragg-condition at the first interferometer plate (beam splitter).

The arrangement of two RF-flippers of frequencies ω and $\omega/2$ can be interpreted as an interferometer-scheme for the neutron's total energy. Due to energy splitting the first RF-flipper generates a superposition of two coherent energy states, similar to the action of the first beam-splitter of a Mach-Zehnder interferometer, where a single beam is split spatially into two coherent sub-beams. The second flipper compensates the energy difference and therefore acts as a beam analyzer equivalent to the last beam-splitter of the interferometer.

The results of the experiment discussed in this Section are summarized in [Sponar et al., 2008b]. This experiment can be seen within a framework related to tripartite entanglement. The neutron part of the multi entangled statevector given by

$$|\Psi_N\rangle \propto \frac{1}{\sqrt{2}} \left(|I\rangle \otimes |E_0\rangle \otimes |\uparrow\rangle + |II\rangle \otimes |E_0 - \hbar\omega\rangle \otimes |\downarrow\rangle \right), \quad (3.82)$$

denotes a Greenberger-Horne-Zeilinger (GHZ)-like state [Greenberger et al., 1989, Greenberger et al., 1990]. Classification of a GHZ-like state in a single-neutron system will be the subject of the next Section.

3.3 GHZ-States in Neutron Interferometry

In this Section the GHZ-like state, prepared by coherent manipulation of energy, spin and path degree of freedom, is analyzed with an inequality derived by Mermin. The obtained value $M = 2.558 \pm 0.004 \not\leq 2$ exhibits a clear violation of the classical boundary. The result confirms the quantum-mechanical predictions which contradict with classical assumptions.

3.3.1 State preparation

As already foreshadowed in Section 3.2.3, utilizing an RF-flipper in one arm of the interferometer yields a state of the incident neutron that can be represented as a triply entangled GHZ-like state. After the first plate of the interferometer (beam splitter) the state is transformed into a 50:50 superposition of path I ($|I\rangle$) and path II ($|II\rangle$). The RF flipper, operating at frequency ω (with $B^{(1)} = B_{\text{rf}}^{(\omega)} \cos(\omega t + \phi_\omega) \cdot \hat{\mathbf{y}}$, where $\phi_\omega = 0$) induces a spin flip process due to a time-dependent interaction, as discussed in detail in Sec.2.2.4. Along with the spin flip an energy transitions from the initial energy state $|E_0\rangle$ to the state $|E_0 - \hbar\omega\rangle$ is induced, due to an exchange of photons of energy $\hbar\omega$ i.e spin $|\uparrow\rangle$ (in path II) loses energy of $\hbar\omega$. Thus a triply entangled GHZ-like state denoted as

$$|\Psi_N\rangle \propto \frac{1}{\sqrt{2}} \left(|I\rangle \otimes |E_0\rangle \otimes |\uparrow\rangle + |II\rangle \otimes |E_0 - \hbar\omega\rangle \otimes |\downarrow\rangle \right), \quad (3.83)$$

is prepared. The entanglement is achieved between three degrees of freedom of the neutron, namely spin, path and total energy. Each of them is referred to as a two-level quantum system with associated Hilbert space spanned by the two orthogonal eigenstates: $|I\rangle, |II\rangle$ for the path subspace, $|\uparrow\rangle, |\downarrow\rangle$ for the total energy, and finally $|E_0\rangle, |E_0 - \hbar\omega\rangle$ for the spin subspace.

3.3.2 Mermin-like inequality

Since a contradiction between quantum mechanics and local hidden variable theories for the GHZ state is found only for perfect situations (which cannot be realized experimentally), an inequality is used to demonstrate the peculiarities of the GHZ state. Mermin

analyzed the GHZ argument in detail and derived an inequality pertinent for an experimental test of local hidden variable theories [Mermin, 1990]. Since our GHZ-like state consists of an entanglement between degrees of freedom in a single-neutron system we test noncontextual hidden variable theories using a sum of four expectation values defined as

$$M = E(\sigma_x^{(P)}\sigma_x^{(E)}\sigma_x^{(S)}) - E(\sigma_x^{(P)}\sigma_y^{(E)}\sigma_y^{(S)}) - E(\sigma_y^{(P)}\sigma_x^{(E)}\sigma_y^{(S)}) - E(\sigma_y^{(P)}\sigma_y^{(E)}\sigma_x^{(S)}), \quad (3.84)$$

where $\sigma_{x,y}^{(i)}$ are the Pauli operators in path, total energy and spin subspace. The value of M is bounded by 2 for any noncontextual hidden variable theorie, whereas quantum mechanics predicts an upper limit of 4 for the GHZ state. The Pauli operators used in Eq.(3.84) can be decomposed as

$$\begin{aligned} \sigma_x^{(i)} &= \hat{P}^{(i)}(0) - \hat{P}^{(i)}(\pi) \\ \sigma_y^{(i)} &= \hat{P}^{(i)}(\pi/2) - \hat{P}^{(i)}(3\pi/2), \end{aligned} \quad (3.85)$$

with $\hat{P}(\alpha)^{(S)}$, $\hat{P}(\beta)^{(k)}$ and $\hat{P}(\gamma)^{(E)}$ being the projection operators onto an up down superposition on the equatorial plane in path, total energy and spin subspace. The azimuthal angle is given by an angle parameter χ , γ and α , respectively. The operators are defined as

$$\begin{aligned} \hat{P}^{(P)}(\chi) &= \frac{1}{\sqrt{2}}(|\text{I}\rangle + e^{-i\chi}|\text{II}\rangle)(\langle\text{I}| + e^{i\chi}\langle\text{II}|) \\ \hat{P}^{(E)}(\gamma) &= \frac{1}{\sqrt{2}}(|E_0\rangle + e^{-i\gamma}|E_0 - \hbar\omega\rangle)(\langle E_0| + e^{i\gamma}\langle E_0 - \hbar\omega|) \\ \hat{P}^{(S)}(\alpha) &= \frac{1}{\sqrt{2}}(|\uparrow\rangle + e^{-i\alpha}|\downarrow\rangle)(\langle\uparrow| + e^{i\alpha}\langle\downarrow|), \end{aligned} \quad (3.86)$$

where χ , γ and α are the azimuthal angles on the Bloch spheres depicted, having only the values 0 and π or $\pi/2$ and $3\pi/2$, sine only σ_x and σ_y occur in Eq.(3.84) (see Fig. 3.25). Each expectation Value $E(\sigma_{x,y}^{(P)}\sigma_{x,y}^{(E)}\sigma_{x,y}^{(S)})$ is experimentally determined by a combination of normalized count rates, using appropriate setting of χ , γ and α : for instance

$$\begin{aligned} E(\sigma_x^{(P)}\sigma_y^{(E)}\sigma_y^{(S)}) &= E(\alpha : (0; \pi), \beta : (\frac{\pi}{2}; \frac{3\pi}{2}), \gamma : (\frac{\pi}{2}; \frac{3\pi}{2})) \\ &= \langle\Psi_{\text{GHZ}}|(\hat{P}(0)^{(P)} - \hat{P}(\pi)^{(P)}) \otimes (\hat{P}(\frac{\pi}{2})^{(E)} - \hat{P}(\frac{3\pi}{2})^{(E)}) \otimes (\hat{P}(\frac{\pi}{2})^{(S)} - \hat{P}(\frac{3\pi}{2})^{(S)})|\Psi_{\text{GHZ}}\rangle = \frac{A}{B} \end{aligned} \quad (3.87)$$

with

$$\begin{aligned}
A = & \left(N(0, \frac{\pi}{2}, \frac{\pi}{2}) - N(\pi, \frac{\pi}{2}, \frac{\pi}{2}) - N(0, \frac{\pi}{2}, \frac{3\pi}{2}) + N(\pi, \frac{\pi}{2}, \frac{3\pi}{2}) \right. \\
& \left. - (N(0, \frac{3\pi}{2}, \frac{\pi}{2}) - N(\pi, \frac{3\pi}{2}, \frac{\pi}{2}) + N(0, \frac{3\pi}{2}, \frac{3\pi}{2}) + N(\pi, \frac{3\pi}{2}, \frac{3\pi}{2})) \right) \quad (3.88)
\end{aligned}$$

and

$$\begin{aligned}
B = & \left(N(0, \frac{\pi}{2}, \frac{\pi}{2}) + N(\pi, \frac{\pi}{2}, \frac{\pi}{2}) + N(0, \frac{\pi}{2}, \frac{3\pi}{2}) + N(\pi, \frac{\pi}{2}, \frac{3\pi}{2}) \right. \\
& \left. + N(0, \frac{3\pi}{2}, \frac{\pi}{2}) - N(\pi, \frac{3\pi}{2}, \frac{\pi}{2}) + N(0, \frac{3\pi}{2}, \frac{3\pi}{2}) + N(\pi, \frac{3\pi}{2}, \frac{3\pi}{2}) \right), \quad (3.89)
\end{aligned}$$

where for example $N(0, \pi/2, \pi/2)$ is the count rate for $\chi = 0$, $\gamma = \pi/2$ and $\alpha = \pi/2$.

3.3.3 Measurement process and modification of the setup

As seen from Δ_{tot} in Eq.(3.78) of Section 3.2.3 each of the three degrees of freedom can be manipulated (in principal) independently and the associated observables are separately measurable. A schematic illustration of the setup, together with a Bloch sphere description of the associated measurement directions on path, spin and total energy are depicted in Fig. 3.25. The projective measurements of each degree of freedom are carried out due to phase manipulations between the eigenstates of the individual sub systems, resulting in the desired azimuthal angle on the Bloch sphere.

Path phase

The phase manipulation of the path subspace is accomplished with an auxiliary phase shifter made of a parallel-sided Si plate. Here the path phase χ is given by $\chi = -N_{\text{ps}}b_c\lambda D$, with the thickness of the phase shifter plate D , the neutron wavelength λ , the coherent scattering length b_c and the particle density N_{ps} in the phase shifter plate.

Spin phase

In this experiment the tunable accelerator coil was used to tune the spin phase α . In particular the spin phase is accumulated by Larmor precession within the static magnetic field of the accelerator coil ($B_{\text{ACC}} \cdot \hat{z}$) with $\alpha = \omega_L \tau_{\text{ACC}}$, where ω_L is the Larmor frequency depending on B_{ACC} and τ_{ACC} is the propagation time through the accelerator coil.

Energy phase

The manipulation of the energy phase is achieved by zero-field precession between the two RF-flippers. The first RF spin-flipper induces the energy difference $\hbar\omega$, which is balanced by the second RF flipper by choosing a frequency of $\omega/2$, resulting in the zero field phase difference $\gamma = \omega T$ (as described in Sec. 3.2.3). Here T is the propagation time between the two RF-flippers at distance d , which can be varied, since the second RF coil is

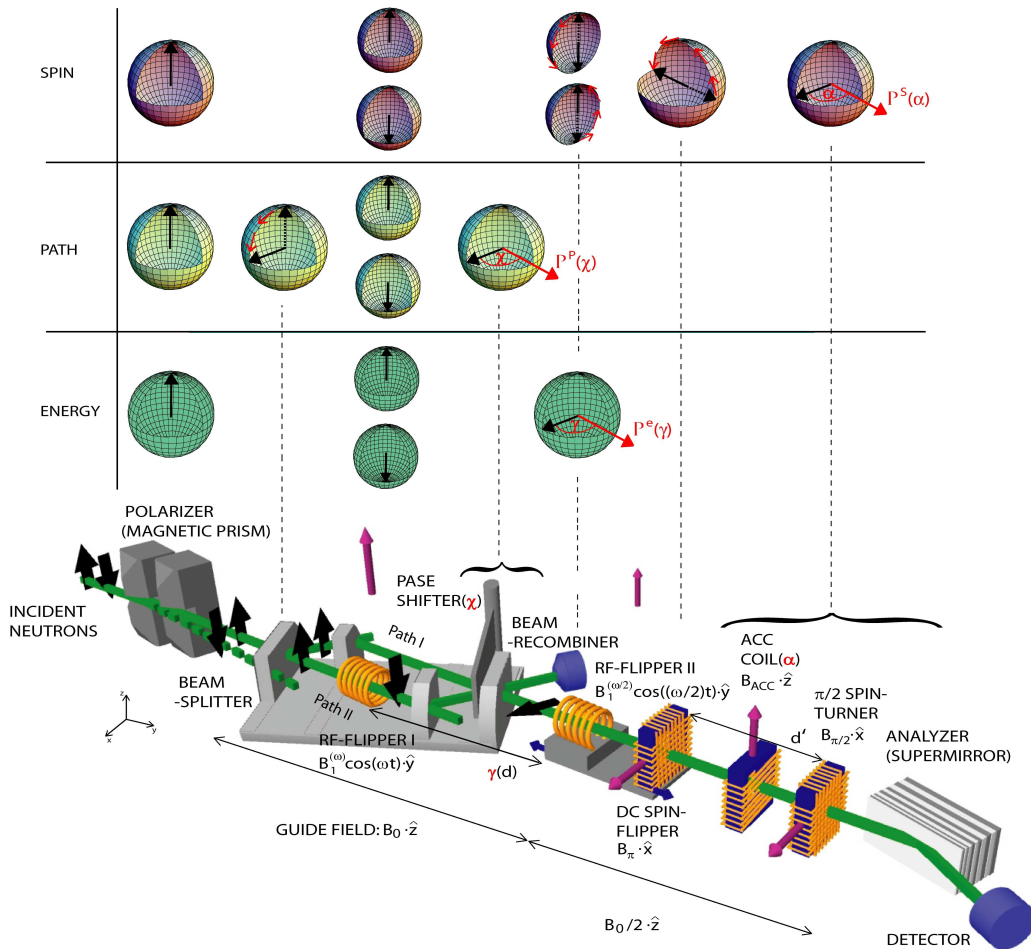


Figure 3.25: Schematic view of the experimental apparatus for classification of a GHZ-like state, together with Bloch-sphere descriptions to depict evolutions of each quantum state (i.e., spin, path and energy degrees of freedom). The directions of the projective measurements P^j are depicted by thick red arrows in Bloch spheres.

mounted on a translation stage. This displacement of the second RF-flipper is the crucial point in this experiment, since by increasing the distance between the RF-flippers not only the zero field phase $\gamma = \omega T$ is changed, but also the Larmor precession angle within the static guide field B_0 which induces an additional undesired spin phase contribution $\alpha' = \omega_{L(B_0)}$. However the aim is to address the zero field precession independently from Larmor precession.

This is achieved by an auxiliary DC-flipper, which is mounted on the same translation stage subsequently to the second RF-flipper. The modifications of the setup are illustrated in Fig. 3.25. Thus no additional phase shift, induced by Larmor precession, resulting from the change of Δd is observed. Phase contributions with the same sign occur in the regions between first and second RF-flippers ($d + \Delta d$) and between DC-flipper and the DC $\pi/2$ spin-rotator (denoted $d' - \Delta d$), compensating each other. Thus the total Larmor precession angle remains constant ($(d + d')\omega_{L(B_0)}$), though changing the position (Δd) of the second RF-flipper. The displacement only affects the zero field precession angle $\gamma = \omega T \propto \omega(d + \Delta d)$. To demonstrate this individual tuning of Larmor and zero field precession an independent polarimetric experiment was carried out. The results are given in detail in Section 4.1 and are summarized in [Sponar et al., 2008a]. Apart from this additional DC spin flipper the same setup was used as in Section 3.2.3 with $\phi_\omega = \phi_{\omega/2} = 0$.

3.3.4 Experimental results

Again the experiment was carried out at the neutron interferometer instrument S18 at the high-flux reactor of the Institute Laue-Langevin in Grenoble, France. A graphical representation of the main components of the experimental setup together with a Bloch-sphere description depicting evolutions of each degree of freedom and the directions for the projective measurements, is depicted in Fig. 3.25.

According to the required projective measurements spin phase α and energy phase γ each was tuned at $0, \pi/2$ and $3\pi/2$, while path phase scans χ (i.e., oscillation measurements) were performed. The resulting sixteen oscillations are depicted in Fig. 3.26, the dashed lines denote the values $\chi = 0, \pi/2$ and $3\pi/2$, which are required for the determination of M , as defined in Eq.(3.84). The average contrast of the oscillations were just

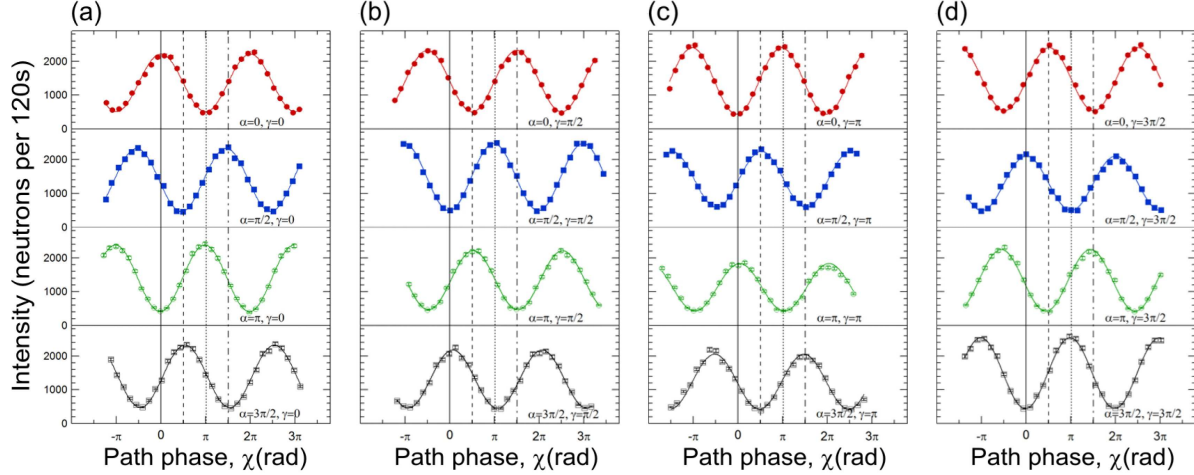


Figure 3.26: Typical interference patterns of the O-detector obtained by varying the path phase χ . The phases α and γ , for the spin and the energy, respectively, are tuned at $0, \pi/2, \pi$ and $3\pi/2$ in order to accomplish project measurements associated with $\hat{P}^j(0), \hat{P}^j(\pi/2), \hat{P}^j(\pi)$ and $\hat{P}^j(3\pi/2)$, with $j = \text{spin, path and energy}$.

below 70 per cent, which is clearly above the threshold visibility of 50 per cent, required for a violation of the Mermin like inequality.

Measured intensity oscillations were fitted to sinusoidal curves by applying a least squares method. The four expectation values, as defined in Eq.(3.84), were extracted from the fit curves. Statistical errors were estimated to 0.001, thereby taking all fit errors from single measurement curves into account. One set of measurements consists of thirty-

Table 3.4: The four experimentally determined expectation values and the final M value.

| Observable | Settings | | | Determined Values |
|--|-------------------|-------------------|-------------------|-------------------|
| | χ | γ | α | |
| $\sigma_x^{(P)} \sigma_x^{(E)} \sigma_x^{(S)}$ | $(0; \pi)$ | $(0; \pi)$ | $(0; \pi)$ | 0.659(2) |
| $\sigma_x^{(P)} \sigma_y^{(E)} \sigma_y^{(S)}$ | $(0; \pi)$ | $(\pi/2; 3\pi/2)$ | $(\pi/2; 3\pi/2)$ | -0.603(2) |
| $\sigma_y^{(P)} \sigma_x^{(E)} \sigma_y^{(S)}$ | $(\pi/2; 3\pi/2)$ | $(0; \pi)$ | $(\pi/2; 3\pi/2)$ | -0.664(2) |
| $\sigma_y^{(P)} \sigma_y^{(E)} \sigma_x^{(S)}$ | $(\pi/2; 3\pi/2)$ | $(\pi/2; 3\pi/2)$ | $(0; \pi)$ | 0.632(2) |

$$M = 2.558(4)$$

two oscillation measurements, since intensities with and without spin flipper (reference measurement) were recorded. This was done in order to observe a relative phase shift, allowing corrections of the path phase χ instability, afterward. Four sets of thirty-two oscillations to reduce statistical errors. A final result of $M = 2.558 \pm 0.004$, exhibiting a clear violation $M \not\leq 2$ of the noncontextual border. The individual results of the four expectation values, together with settings of variables and the final value of M , are listed in Tab. 3.4. The results of this measurement are summarized in [Hasegawa et al., 2010].

3.4 Geometric Phase in Entangled Systems

In this Section the influence of the geometric phase on a Bell measurement, as proposed by Bertlmann *et al.* in [Phys. Rev. A 69, 032112 (2004)], and expressed by the Clauser-Horne-Shimony-Holt (CHSH) inequality, is studied for a spin-path entangled neutron state in an interferometric setup. The Bell-like inequality, relying on correlations between the spin and path degrees of freedom of a single-neutron system, is analyzed in detail under the influence of the geometric phase. The geometric phase is generated in one of the complementary Hilbert spaces, in our case the spin subspace. It is experimentally demonstrated that the effect of geometric phase can be balanced by a change in Bell angles. The geometric phase is acquired during a time dependent interaction with a radio-frequency (RF) field. Two schemes, polar and azimuthal adjustment of the Bell angles, are realized and analyzed in detail. The former scheme yields a sinusoidal oscillation of the correlation function S , dependent on the geometric phase, such that it varies in the range between 2 and $2\sqrt{2}$ and, therefore, always exceeds the boundary value 2 between quantum mechanics and noncontextual theories. The latter scheme results in a constant, maximal violation of the Bell-like-CHSH inequality, where S remains $2\sqrt{2}$ for all settings of the geometric phase.

In Section 3.4.1 the theoretical framework, as developed in [Bertlmann et al., 2004], is briefly described first for two entangled spin $\frac{1}{2}$ -particles. Expectation values and Bell-like inequalities are defined and the concept of *polar* and *azimuthal angle adjustment* is introduced. Next the concept is applied to a spin-path entangled neutron state. Section 3.4.2 explains the actual measurement process. It focuses on experimental issues such as state preparation, manipulation of geometric phase, joint measurements, as well as the experimental strategy. In the principal part data analysis and experimental results are presented. This is followed by Section 3.4.3 consisting of discussion and conclusion.

3.4.1 Theory

Berry phase for an entangled state of two spin- $\frac{1}{2}$ particles

First a detailed summary of the theoretical framework as introduced by Bertlmann *et al.* in [Phys. Rev. A 69, 032112 (2004)] is presented at this point, before the actual neutron

interferometric experiment is explained.

Particle A , without loss of generality moving in y -direction (see Fig. 3.27), is interacting with a time-dependent magnetic field $\vec{B}(t)$ with unit vector $\vec{n}(t)$. The magnetic field $\vec{B}(t)$ rotates adiabatically with an angular velocity ω_0 around the z axis under an angle θ . The interaction is described by the Hamiltonian

$$\hat{H} = \frac{1}{2}\mu\vec{B}(t)\vec{\sigma}, \quad (3.90)$$

with the coupling constant given by $\mu = g\mu_B$, where g is the Landé factor and μ_B the Bohr magneton. Thus the eigenstates of the spin operator in direction $\vec{n}(t)$, expanded in the σ_z basis yield

$$\begin{aligned} |\uparrow_n(t)\rangle &= \cos\frac{\theta}{2}|\uparrow_z\rangle + \sin\frac{\theta}{2}e^{i\omega_0 t}|\downarrow_z\rangle \\ |\downarrow_n(t)\rangle &= -\sin\frac{\theta}{2}|\uparrow_z\rangle + \cos\frac{\theta}{2}e^{i\omega_0 t}|\downarrow_z\rangle. \end{aligned} \quad (3.91)$$

The corresponding time-independent energy levels are given by

$$E_{\pm} = \pm\frac{\mu}{2} = \pm\hbar\omega_1. \quad (3.92)$$

Here an adiabatic ($\omega_0/\omega_1 \ll 1$) and cyclic time evolution for the period $t = 2\pi/\omega_0$ of these eigenstates, is assumed. Consequently each eigenstate picks up a phase factor that can be split into a geometrical and a dynamical part of the following form

$$\begin{aligned} |\uparrow_n(0)\rangle \rightarrow |\uparrow_n(\tau)\rangle &= e^{i\gamma_+(\theta)}e^{i\delta_+}|\uparrow_n(0)\rangle \\ |\downarrow_n(0)\rangle \rightarrow |\downarrow_n(\tau)\rangle &= e^{i\gamma_-(\theta)}e^{i\delta_-}|\downarrow_n(0)\rangle, \end{aligned} \quad (3.93)$$

with

$$\gamma_+(\theta) = -\pi(1 - \cos\theta) \quad \text{and} \quad \gamma_-(\theta) = -\pi(1 + \cos\theta) = -\gamma_+(\theta) - 2\pi \quad (3.94)$$

and

$$\delta_+(\theta) = -\frac{1}{\hbar}E_+\tau = -2\pi\frac{\omega_1}{\omega_0} \quad \text{and} \quad \delta_-(\theta) = +\frac{1}{\hbar}E_-\tau = +2\pi\frac{\omega_1}{\omega_0} = -\delta_+(\theta). \quad (3.95)$$

Here γ_{\pm} denotes the Berry phase which is precisely half of the solid angle swept out by the magnetic field during the rotation and δ_{\pm} is the usual dynamical phase, both as introduced in Section 2.3.

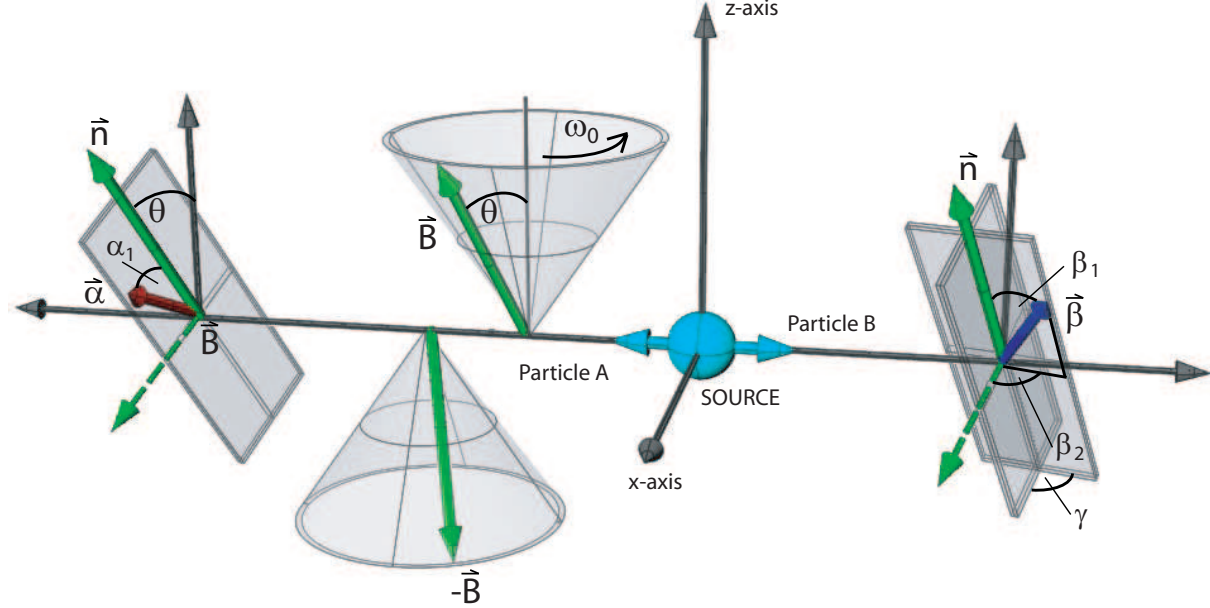


Figure 3.27: Graphical representation of the measurement scheme. The vector \vec{n} denotes the quantization direction, $\vec{\alpha}$ and $\vec{\beta}$ denote the measurement directions determining the measurement planes.

Next the dynamical effect which would dominate the geometrical one is eliminated, by using the so called *phase-echo* method. First the propagating particle *A* is subjected to the rotating magnetic field in the direction $\vec{n}(\theta)$ for one period and therefore picks up the phases defined in Eq.(3.93). Afterwards the particle passes another rotating field which points in direction $-\vec{n}(\theta)$ again for one period. Then the states change according to

$$\begin{aligned} |\uparrow_n\rangle &\equiv |\uparrow_{-n}\rangle \rightarrow e^{i\gamma-(\pi-\theta)} e^{i\delta_-} |\uparrow_{-n}\rangle \equiv e^{i\gamma+(\theta)} e^{i\delta_-} |\uparrow_n\rangle \\ |\downarrow_n\rangle &\equiv |\downarrow_{-n}\rangle \rightarrow e^{i\gamma+(\pi-\theta)} e^{i\delta_+} |\downarrow_{-n}\rangle \equiv e^{i\gamma-(\theta)} e^{i\delta_+} |\downarrow_n\rangle. \end{aligned} \quad (3.96)$$

Thus following net effect after two rotation periods is given by

$$|\uparrow_n\rangle \rightarrow e^{2i\gamma_+} |\uparrow_n\rangle \quad \text{and} \quad |\downarrow_n\rangle \rightarrow e^{2i\gamma_-} |\downarrow_n\rangle, \quad (3.97)$$

or for two half periods of rotation one obtains

$$|\uparrow_n\rangle \rightarrow e^{i\gamma_+} |\uparrow_n\rangle \quad \text{and} \quad |\downarrow_n\rangle \rightarrow e^{i\gamma_-} |\downarrow_n\rangle. \quad (3.98)$$

Considering an entangled state of two spin- $\frac{1}{2}$ particles, e.g., the antisymmetric Bell singlet state $|\Psi_-^{AB}\rangle$, where particle A couples twice to the adiabatically rotating magnetic fields as described before. Consequently only one subspace of the Hilbert space is influenced by the phases acquired due to the interaction with the rotating magnetic fields.

To identify the Berry phase the initial Bell singlet state is decomposed into the eigenstates of the interaction Hamiltonian

$$|\Psi_-^{AB}(\tau)\rangle = \frac{1}{\sqrt{2}} \left(|\uparrow_n^A\rangle \otimes |\downarrow_n^B\rangle - |\downarrow_n^A\rangle \otimes |\uparrow_n^B\rangle \right). \quad (3.99)$$

According to the *phase-echo* arrangement, after one cycle, the state picks up precisely the geometric phase defined in Eq.(3.98), which can be (apart from an overall phase factor) written as

$$|\Psi_-^{AB}(0)\rangle = \frac{1}{\sqrt{2}} \left(|\uparrow_n^A\rangle \otimes |\downarrow_n^B\rangle - e^{-2i\gamma} |\downarrow_n^A\rangle \otimes |\uparrow_n^B\rangle \right), \quad (3.100)$$

with $\gamma = \gamma_+ = \gamma_-$. As in common Bell experiments, simultaneous measurement of the spin components of the particles A and B is performed, which is depicted in Fig.3.27. Projection operator onto an up (+) and a down (-) spin state along an arbitrary direction $\vec{\alpha}$ are defined as

$$\hat{P}_{\pm}(\vec{\alpha}) = |\pm \vec{\alpha}\rangle \langle \pm \vec{\alpha}|, \quad (3.101)$$

with

$$\begin{aligned} |+\vec{\alpha}\rangle &= \cos \frac{\alpha_1}{2} |\uparrow_n\rangle + e^{i\alpha_2} \sin \frac{\alpha_1}{2} |\downarrow_n\rangle \\ |-\vec{\alpha}\rangle &= -\sin \frac{\alpha_1}{2} |\uparrow_n\rangle + e^{i\alpha_2} \cos \frac{\alpha_1}{2} |\downarrow_n\rangle, \end{aligned} \quad (3.102)$$

where α_1 denotes the polar angle measured from the \vec{n} direction and α_2 the azimuthal angle. The measurement of particle B is carried out along the direction $\vec{\beta}$ with polar and azimuthal angles β_1 and β_2 , respectively. Introducing the observables

$$\begin{aligned} \hat{A}(\vec{\alpha}) &= \hat{P}_+(\vec{\alpha}) - \hat{P}_-(\vec{\alpha}) \\ \hat{B}(\vec{\beta}) &= \hat{P}_+(\vec{\beta}) - \hat{P}_-(\vec{\beta}), \end{aligned} \quad (3.103)$$

one can define an expectation value for a joint measurement of spins along the directions $\vec{\alpha}$ and $\vec{\beta}$

$$\begin{aligned} E(\vec{\alpha}, \vec{\beta}) &= \langle \Psi_-^{AB}(\tau) | \hat{A}(\vec{\alpha}) \otimes \hat{B}(\vec{\beta}) | \Psi_-^{AB}(\tau) \rangle \\ &= -\cos \alpha_1 \cos \beta_1 - \cos(\alpha_2 - \beta_2 + 2\gamma) \sin \alpha_1 \sin \beta_1. \end{aligned} \quad (3.104)$$

Next, a Bell-like inequality in CHSH-formalism [Clauser et al., 1969] is introduced, consisting of four expectation values with the associated directions $\vec{\alpha}$, $\vec{\alpha}'$ and $\vec{\beta}$, $\vec{\beta}'$ for joint measurements of spin and path, respectively

$$\begin{aligned}
 S(\vec{\alpha}, \vec{\alpha}', \vec{\beta}, \vec{\beta}', \gamma) &= |E(\vec{\alpha}, \vec{\beta}) - E(\vec{\alpha}, \vec{\beta}') + E(\vec{\alpha}', \vec{\beta}) + E(\vec{\alpha}', \vec{\beta}')| \\
 &= \left| -\sin \alpha_1 (\cos(\alpha_2 - \beta_2 + 2\gamma) \sin \beta_1 - \cos(\alpha_2 - \beta_2' + 2\gamma) \sin \beta_1') - \cos \alpha_1 (\cos \beta_1 - \cos \beta_1') \right. \\
 &\quad \left. - \sin \alpha_1' (\cos(\alpha_2' - \beta_2 + 2\gamma) \sin \beta_1 + \cos(\alpha_2' - \beta_2' + 2\gamma) \sin \beta_1') - \cos \alpha_1' (\cos \beta_1 + \cos \beta_1') \right|.
 \end{aligned} \tag{3.105}$$

The boundary of Eq.(3.105) is given by the value 2 for any local hidden variable theory. Without loss of generality one angle can be eliminated by setting, e.g., $\vec{\alpha} = 0$ ($\alpha_1 = \alpha_2 = 0$), which gives

$$\begin{aligned}
 S(\vec{\alpha}', \vec{\beta}, \vec{\beta}', \gamma) &= \left| -\sin \alpha_1' (\cos(\alpha_2' - \beta_2 + 2\gamma) \sin \beta_1 + \cos(\alpha_2' - \beta_2' + 2\gamma) \sin \beta_1') \right. \\
 &\quad \left. - \cos \alpha_1' (\cos \beta_1 + \cos \beta_1') - \cos \beta_1 + \cos \beta_1' \right|.
 \end{aligned} \tag{3.106}$$

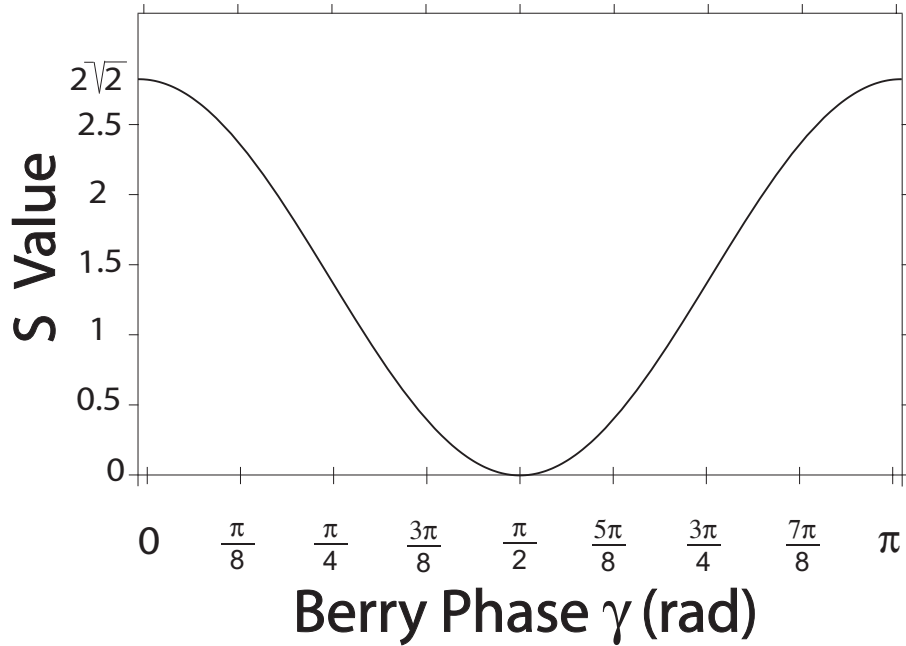


Figure 3.28: S value under variation of Berry phase γ for the common Bell angles $\alpha_1 = 0$, $\alpha_1' = \frac{\pi}{2}$, $\beta_1 = \frac{\pi}{4}$, $\beta_1' = \frac{3\pi}{4}$ (and azimuthal parts fixed at $\alpha_2' = \beta_2 = \beta_2' = 0$).

Keeping the polar angles α'_1 , β_1 and β'_1 constant at the usual Bell angles $\alpha'_1 = \frac{\pi}{2}$, $\beta_1 = \frac{\pi}{4}$, $\beta'_1 = \frac{3\pi}{4}$ (and azimuthal parts fixed at $\alpha'_2 = \beta_2 = \beta'_2 = 0$) S is reduced to

$$S(\gamma) = | -\sqrt{2} - \sqrt{2} \cos(2\gamma) |, \quad (3.107)$$

where the familiar maximum value of $2\sqrt{2}$ is reached for $\gamma = 0$. For $\gamma = \pi/2$ the value of S approaches zero, which is illustrated in Fig 3.28.

Polar Angle Adjustment

Here the case is considered when the azimuthal angles are kept constant, e.g., $\alpha'_2 = \beta_2 = \beta'_2 = 0$ ($\alpha_2 = 0$), denoted as

$$S(\alpha'_1, \beta_1, \beta'_1, \gamma) = \left| -\sin \alpha'_1 \left(\cos(2\gamma) \sin \beta_1 + \cos(2\gamma) \sin \beta'_1 \right) - \cos \alpha'_1 (\cos \beta_1 + \cos \beta'_1) - \cos \beta_1 + \cos \beta'_1 \right|. \quad (3.108)$$

The polar Bell angles β_1 , β'_1 and α'_1 ($\alpha_1 = 0$), yielding a maximum S -value, can be determined, with respect to the geometric phase γ , by calculating the partial derivatives (the extremum condition) of S in Eq.(3.108):

$$\begin{aligned} \frac{\partial S}{\partial \beta_1} &= \sin \beta_1 + \cos \alpha'_1 \sin \beta_1 - \cos(2\gamma) \sin \alpha'_1 \cos \beta_1 = 0 \\ \frac{\partial S}{\partial \beta'_1} &= -\sin \beta'_1 + \cos \alpha'_1 \sin \beta'_1 - \cos(2\gamma) \sin \alpha'_1 \cos \beta'_1 = 0 \end{aligned}$$

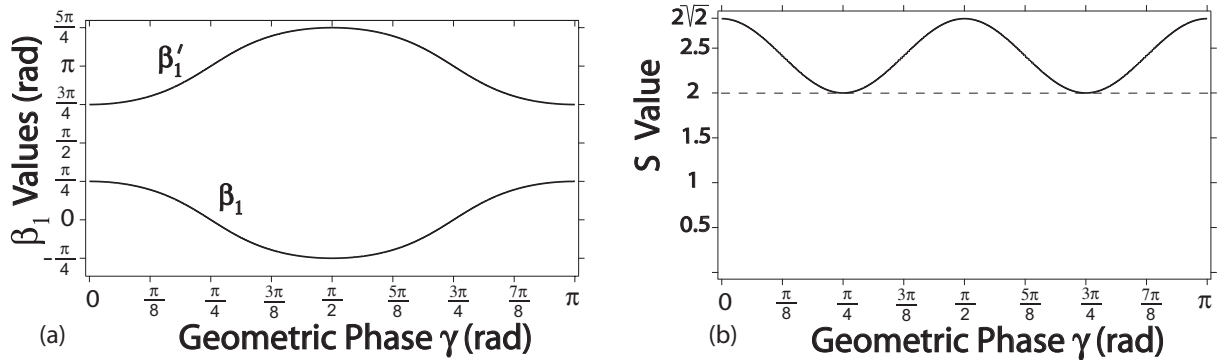


Figure 3.29: (a) Bell angles β_1 and β'_1 with respect to the Berry phase γ . (b) The maximum of the S function with respect to the Berry phase γ (for $\alpha'_2 = \beta_2 = \beta'_2 = 0$).

$$\frac{\partial S}{\partial \alpha'_1} = \sin \alpha'_1 (\cos \beta_1 + \cos \beta'_1) - \cos(2\gamma) \cos \alpha'_1 (\sin \beta_1 + \sin \beta'_1) = 0. \quad (3.109)$$

The solutions are given by

$$\begin{aligned} \beta_1 &= \arctan(\cos(2\gamma)) \\ \beta'_1 &= \pi - \beta_1 \\ \alpha'_1 &= \frac{\pi}{2}. \end{aligned} \quad (3.110)$$

With these angles the maximal S decreases for $\gamma : 0 \rightarrow \frac{\pi}{2}$ and touches at $\gamma = \frac{\pi}{2}$ even the limit of the CHSH inequality $S = 2$, which is depicted in Fig. 3.29 (b). The associated values for β_1 and β'_1 with respect to the Berry phase γ can be seen in Fig. 3.29 (a).

Azimuthal Angle Adjustment

Next the situation is discussed where the standard maximal value $S = 2\sqrt{2}$ can be achieved by keeping the polar angles α'_1 , β_1 and β'_1 constant at the Bell angles $\alpha'_1 = \frac{\pi}{2}$, $\beta_1 = \frac{\pi}{4}$, $\beta'_1 = \frac{3\pi}{4}$, ($\alpha_1 = 0$), while the azimuthal parts, α'_2 , β_2 and β'_2 ($\alpha_2 = 0$), are varied. The corresponding S function is denoted as

$$S(\alpha'_2, \beta_2, \beta'_2, \gamma) = \left| -\sqrt{2} - \frac{\sqrt{2}}{2} \left(\cos(\alpha'_2 - \beta_2 + 2\gamma) + \cos(\alpha'_2 - \beta'_2 + 2\gamma) \right) \right|. \quad (3.111)$$

The maximum value $2\sqrt{2}$ is reached for

$$\begin{aligned} \beta_2 &= \beta'_2, \text{ and} \\ \alpha'_2 - \beta'_2 &= -2\gamma \pmod{\pi}. \end{aligned} \quad (3.112)$$

3.4.2 Geometric phase in a single-neutron interferometer experiment

Following the notation given in [Bertlmann et al., 2004], the neutron's wavefunction in the experiment is defined in a tensor product of two Hilbert spaces: One Hilbert space is spanned by two possible paths in the interferometer given by $|I\rangle, |II\rangle$, and the other by spin-up and spin-down eigenstates, denoted as $|\uparrow\rangle$ and $|\downarrow\rangle$, referred to a quantization axis along a static magnetic field.

Before the actual experiment is explained a short summary of the applied notation is given, since numerous angles are due to appear in this Section. Angles denoted as $\vec{\alpha}$ are associated with path, and angles denoted as $\vec{\beta}$ with spin subspace. The ' symbol is used to distinguish different measurement directions of one subspace, required for a CHSH-Bell measurement [Clauser et al., 1969] (e.g. $\vec{\alpha}$ and $\vec{\alpha}'$ represent the measurement directions for the path subspace). Index 1 denotes polar angles, whereas index 2 is identified with azimuthal angles (e.g. β_1 and β_1' are polar angles of the spin subspace). Finally, the $^\perp$ symbol is used for adding π to an angle (e.g. $\alpha_1^\perp = \alpha_1 + \pi$).

Interacting with a time dependent magnetic field, the spin-path entangled Bell-like state acquires a geometric phase γ tied to the evolution within the spin subspace [Bertlmann et al., 2004]

$$|\Psi_{\text{Bell}}(\gamma)\rangle = \frac{1}{\sqrt{2}} \left(|\text{I}\rangle \otimes |\uparrow\rangle + |\text{II}\rangle \otimes e^{i\gamma} |\downarrow\rangle \right). \quad (3.113)$$

In contrast to the theoretical framework, here only a geometric phase factor of γ is acquired, since only one sub beam is interacting with the magnetic field. Unlike in the proposed scheme for two entangled spin $\frac{1}{2}$ -particles, in the experimental realization a geometric phase of Aharonov and Anandan type, i.e. non-adiabatic and cyclic, as introduced in Section 2.3.3, is accumulated, since the RF spin flip is a non-adiabatic process.

For a joint measurement of spin and path projection operators for the path

$$\hat{P}_\pm^{\text{P}}(\vec{\alpha}) = |\pm \vec{\alpha}\rangle \langle \pm \vec{\alpha}|, \quad (3.114)$$

with

$$\begin{aligned} |+\vec{\alpha}\rangle &= \cos \frac{\alpha_1}{2} |\text{I}\rangle + e^{i\alpha_2} \sin \frac{\alpha_1}{2} |\text{II}\rangle \\ |-\vec{\alpha}\rangle &= -\sin \frac{\alpha_1}{2} |\text{I}\rangle + e^{i\alpha_2} \cos \frac{\alpha_1}{2} |\text{II}\rangle, \end{aligned} \quad (3.115)$$

where α_1 denotes the polar angle and α_2 the azimuthal angle, and, for the spin subspace,

$$\hat{P}_\pm^{\text{S}}(\vec{\beta}) = |\pm \vec{\beta}\rangle \langle \pm \vec{\beta}|, \quad (3.116)$$

with

$$\begin{aligned} |+\vec{\beta}\rangle &= \cos \frac{\beta_1}{2} |\uparrow\rangle + e^{i\beta_2} \sin \frac{\beta_1}{2} |\downarrow\rangle \\ |-\vec{\beta}\rangle &= -\sin \frac{\beta_1}{2} |\uparrow\rangle + e^{i\beta_2} \cos \frac{\beta_1}{2} |\downarrow\rangle, \end{aligned} \quad (3.117)$$

are defined. Using these observables one can define an expectation value for a joint measurement of spin and path along the directions $\vec{\alpha}$ and $\vec{\beta}$

$$E(\vec{\alpha}, \vec{\beta}) = \langle \Psi | \hat{A}^P(\vec{\alpha}) \otimes \hat{B}^S(\vec{\beta}) | \Psi \rangle \quad (3.118)$$

$$= -\cos \alpha_1 \cos \beta_1 - \cos(\alpha_2 - \beta_2 - \gamma) \sin \alpha_1 \sin \beta_1, \quad (3.119)$$

which slightly differs from Eq.(3.104), since the state is of a different Bell type and the geometric phase has only half magnitude. Thus there occur some minor changes in the unbalanced S value and in the conditions for polar and azimuthal adjustment which are the following:

polar adjustment:

$$S(\alpha'_1, \beta_1, \beta'_1, \gamma) = \left| -\sin \alpha'_1 \left(\cos \gamma \sin \beta_1 + \cos \gamma \sin \beta'_1 \right) - \cos \alpha'_1 (\cos \beta_1 + \cos \beta'_1) - \cos \beta_1 + \cos \beta'_1 \right|, \quad (3.120)$$

$$\beta_1 = \arctan(\cos \gamma), \quad \beta'_1 = \pi - \beta_1 \quad \text{and} \quad \alpha'_1 = \frac{\pi}{2}. \quad (3.121)$$

azimuthal adjustment:

$$S(\alpha'_2, \beta_2, \beta'_2, \gamma) = \left| -\sqrt{2} - \frac{\sqrt{2}}{2} \left(\cos(\alpha'_2 - \beta_2 - \gamma) + \cos(\alpha'_2 - \beta'_2 - \gamma) \right) \right|, \quad (3.122)$$

$$\beta_2 = \beta'_2 \quad \text{and} \quad \alpha'_2 - \beta'_2 = \gamma \pmod{\pi}, \quad (3.123)$$

where for convenience $\beta_2 = 0$ is chosen, finally yielding $\alpha'_2 = \gamma$. A graphical illustration, together with a Bloch sphere description of these conditions, is given in Fig. 3.30.

Neutron interferometric setup and state preparation

The preparation of entanglement between spatial and the spinor degrees of freedom is achieved by a beam splitter and a subsequent spin flip process in one sub beam: Behind the beam splitter (first plate of the IFM) the neutron's wave function is found in a coherent superposition of $|I\rangle$ and $|II\rangle$, and only the spin in $|II\rangle$ is flipped by the first RF-flipper within the interferometer (see Fig. 3.31).

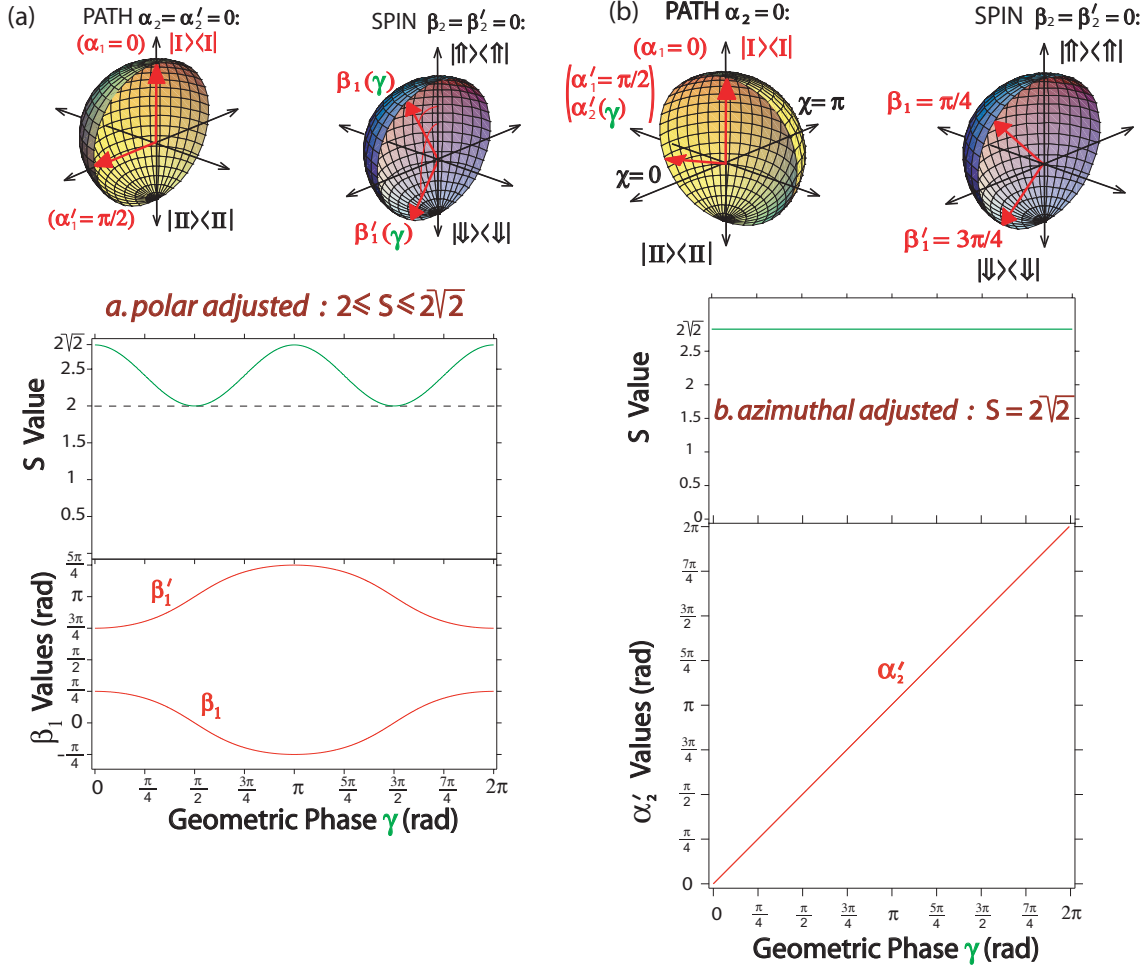


Figure 3.30: (a) Bell angles β_1 and β'_1 with respect to the Berry phase γ . (b) The maximum of the S function with respect to the Berry phase γ (for $\alpha'_2 = \beta_2 = \beta'_2 = 0$).

The entangled state which emerges from a coherent superposition of $|I\rangle$ and $|II\rangle$ is expressed as

$$|\Psi_{\text{Bell}}\rangle = \frac{1}{\sqrt{2}} \left(|I\rangle \otimes |\uparrow\rangle + |II\rangle \otimes e^{i\phi_\omega} |\downarrow\rangle \right), \quad (3.124)$$

after the interaction with the oscillating field, given by $B^{(1)} = B_{\text{rf}}^{(\omega)} \cos(\omega t + \phi_\omega) \cdot \hat{\mathbf{y}}$ (for the moment the time-dependent phase $e^{i\omega t}$ is omitted).

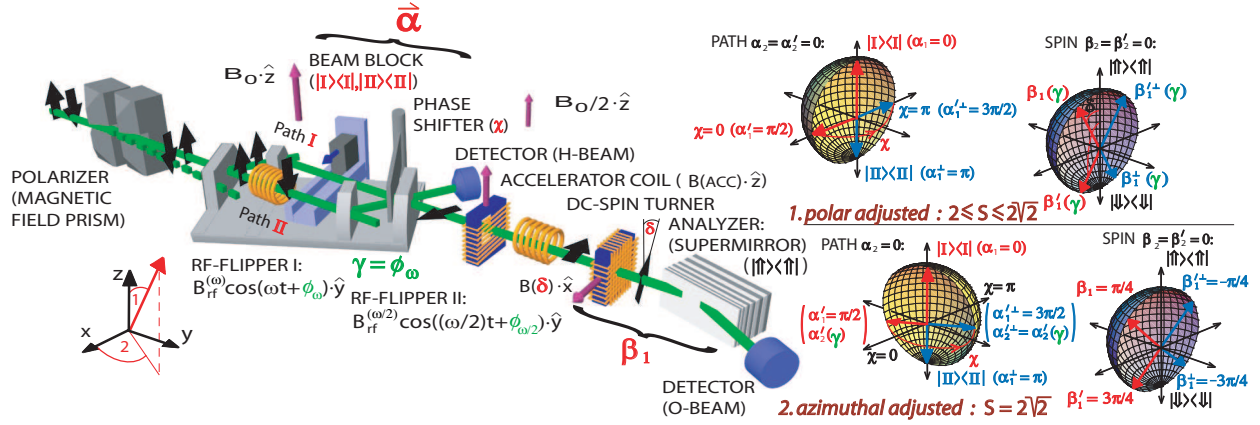


Figure 3.31: Experimental apparatus for joint measurement of spinor and path degrees of freedom with respect to the geometric phase. The incident neutron beam is polarized by a magnetic field prism. The spin state acquires a geometric phase γ during the interaction with the two RF-fields and is flipped twice. The beam block is required for measurements solely in one path ($\pm \hat{z}$ direction of the path measurement). Finally, the spin is rotated by an angle δ (in the \hat{x}, \hat{z} plane), by a dc-spin turner, for a polarization analysis and count rate detection. The Bloch-sphere description includes the measurement settings of $\vec{\alpha}$ and $\vec{\beta}(\delta)$, determining the projection operators, used for joint measurement of spin and path. $\vec{\alpha}$ is tuned by a combination of the phase shifter (χ) and the beam block, and $\vec{\beta}$ is adjusted by the angle δ .

Manipulation of geometric and dynamical phases

The effect of the first RF-flipper, placed inside the interferometer (path II), is described by the unitary operator $\hat{U}(\phi_\omega)$, which induces a spinor rotation from $|\uparrow\rangle$ to $|\downarrow\rangle$, denoted as $\hat{U}(\phi_\omega)|\uparrow\rangle = e^{i\phi_\omega}|\downarrow\rangle$. The rotation axis encloses an angle ϕ_ω with the \hat{y} -direction, and is determined by the oscillating magnetic field $B^{(1)} = B_{\text{rf}}^{(\omega)} \cos(\omega t + \phi_\omega) \cdot \hat{y}$. Without loss of generality one can insert a unity operator, given by $\mathbb{1} = \hat{U}^\dagger(\phi_0)\hat{U}(\phi_0)$, yielding

$$\begin{aligned} \hat{U}(\phi_\omega)|\uparrow\rangle &= \overbrace{\hat{U}(\phi_\omega)\hat{U}^\dagger(\phi_0)\hat{U}(\phi_0)}^{\mathbb{1}}|\uparrow\rangle \\ &= e^{i\gamma}|\downarrow\rangle, \end{aligned} \quad (3.125)$$

where $\hat{U}(\phi_0)$ can be interpreted as a rotation from $|\uparrow\rangle$ to $|\downarrow\rangle$, with the \hat{y} -direction being the rotation axis ($\phi_0 = 0$), and $\hat{U}^\dagger(\phi_0)$ describes a rotation about the same axis

back to the initial state $|\uparrow\rangle$. Consequently, $\hat{U}(\phi_\omega)\hat{U}^\dagger(\phi_0)$ can be identified to induce the geometric phase γ , along the reversed evolution path characterized by ϕ_0 ($|\downarrow\rangle$ to $|\uparrow\rangle$), followed by another path determined by ϕ_ω ($|\uparrow\rangle$ to $|\downarrow\rangle$). In the rotating frame of reference [Suter et al., 1988] the two semi-great circles enclose an angle ϕ_ω and the solid angle $\Omega = -2\phi_\omega$, yielding a pure geometric phase

$$\gamma = -\Omega/2 = \phi_\omega, \quad (3.126)$$

which is depicted in Fig.3.32. The entangled state, as described in [Bertlmann et al., 2004], is represented by

$$|\Psi_{\text{Exp}}(\gamma)\rangle = \frac{1}{\sqrt{2}}\left(|\text{I}\rangle \otimes |\uparrow\rangle + |\text{II}\rangle \otimes e^{i\omega t} e^{i\gamma} |\downarrow\rangle\right), \quad (3.127)$$

including the geometric phase $\gamma = \phi_\omega$ and a time-dependent dynamic phase ωt . In the next step an experimental strategy to cancel the dynamic phase component, by use of a

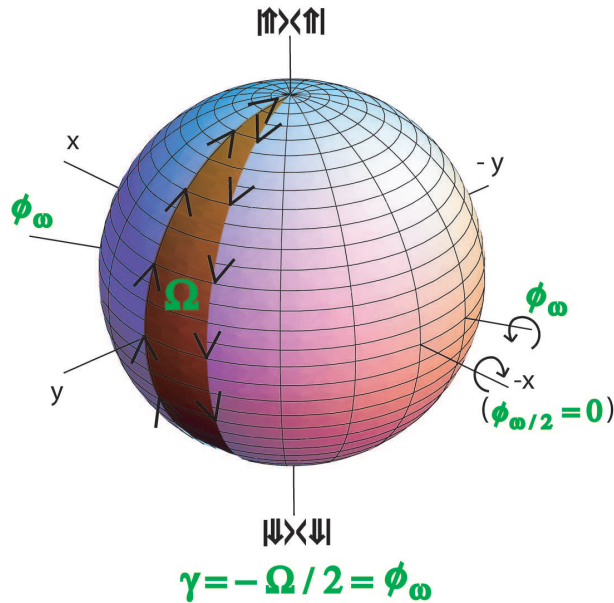


Figure 3.32: Bloch sphere representation of the spinor evolution within the first RF-flipper, placed inside the interferometer (path II), in the rotating frame of reference. The geometric phase γ is given by minus half of the solid angle Ω , traced out by the state vector, depending on the phase ϕ_ω of the oscillating magnetic field in the RF-flipper.

second RF-flipper [Sponar et al., 2008b], is utilized: At the last plate of the interferometer the two sub-beams are recombined, followed by an interaction with the second RF-field, with half frequency $\omega/2$ denoted as $B^{(1)} = B_{\text{rf}}^{(\omega/2)} \cos((\omega/2)t + \phi_{\omega/2}) \cdot \hat{\mathbf{y}}$. The value of $\phi_{\omega/2}$ was set to zero during the complete experiment. Therefore the spin down component (spin up from path I which is flipped at the second RF-flipper) acquires a phase $\omega/2(t+T)$ which is the same amount but opposite sign of the phase of the spin up component (path II). The final state is given by

$$\begin{aligned} |\Psi_{\text{Fin}}(\gamma)\rangle &= (|\text{I}\rangle + |\text{II}\rangle) \otimes \frac{1}{\sqrt{2}} \left(e^{i\omega/2(t+T)} e^{i\phi_{\omega/2}} |\downarrow\rangle + e^{i\chi} e^{i\omega t} e^{-i\omega/2(t+T)} e^{i(\gamma - \phi_{\omega/2})} |\uparrow\rangle \right) \\ &\propto (|\text{I}\rangle + |\text{II}\rangle) \otimes \frac{1}{\sqrt{2}} \left(e^{i\chi} e^{i(\gamma - \omega T)} |\uparrow\rangle + |\downarrow\rangle \right), \end{aligned} \quad (3.128)$$

where ωT is the zero-field phase, with T being the neutron's propagation time between the two RF flippers and the geometric phase $\gamma = \phi_{\omega}$. The instants when the neutron is at the centre of the first and second flipper coil are denoted as t and $t + T$, respectively. The energy difference between the orthogonal spin components is compensated by choosing a frequency of $\omega/2$ for the second RF-flipper, yielding a stationary state vector (see energy level diagram in Fig. 3.11 (c) in Section 3.2).

In our experiment the $|\uparrow\rangle$ eigenstate (in path I and II) also acquires dynamical phase as it precesses about the magnetic guide field in $+\hat{\mathbf{z}}$ -direction. After a spin-flip (only in path II) the $|\downarrow\rangle$ eigenstate still gains another dynamical phase but of opposite sign compared to the situation before the spin-flip. The phases of the two guide fields and the zero-field phase ωT are compensated by an additional Larmor precession within a tunable accelerator coil with a static field, pointing in the $+\hat{\mathbf{z}}$ -direction.

At this point an alternative approach towards the generation of geometric phase is explained, where unlike in the proposed setup in [Bertlmann et al., 2004], the geometric phase is not acquired solely in one arm of the interferometer. Here the two RF-flippers, one inside and one outside of the interferometer contribute to the geometric phase generation, while dynamic phases accumulated in the two curves are canceled [Zhu and Wang, 2003, Ota et al., 2009]. From the laboratory frame the spinor evolution within the RF-flipper placed inside the interferometer (path II) and the second RF-flipper is the following: The neutron spin traces out a curve from $|\uparrow\rangle$ to $|\downarrow\rangle$ on the Bloch sphere, whose polar and azimuthal angles increase linearly with time, at the rates ω . The spin returns to its initial state $|\uparrow\rangle$ when passing the second RF-flipper operating at a frequency of $\omega/2$. The $|\uparrow\rangle$ -

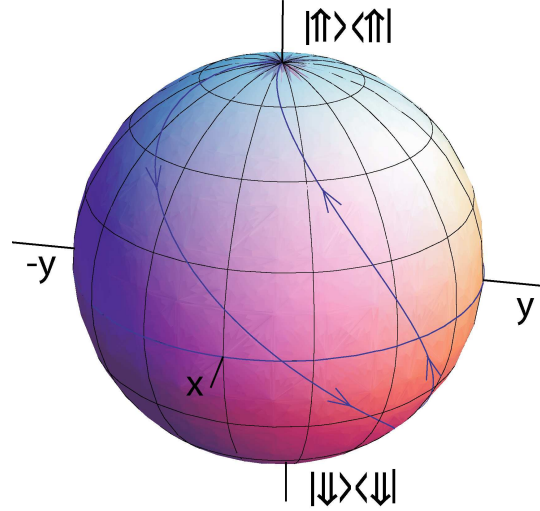


Figure 3.33: Bloch sphere representation of the spinor evolution within the first RF-flipper (frequency ω , $\phi_\omega = \pi/2$), placed inside the interferometer (path II) and second RF-flipper (frequency $\omega/2$, $\phi_{\omega/2} = 0$). The geometric phase γ is given by minus half of the solid angle Ω , traced out by the state vector.

to- $|\downarrow\rangle$ and $|\downarrow\rangle$ -to- $|\uparrow\rangle$ curves intersect the equator at the azimuthal angles $\omega t + \phi_\omega - \pi/2$ and $\omega(t+T)/2 + \phi_{\omega/2} + \pi/2$ respectively, which can be seen in Fig. 3.33. The solid angle Ω yields a pure geometric phase $\gamma = -\Omega/2$ as in [Wagh et al., 2000, Allman et al., 1997]. The geometric phase γ acquired on path II is given by

$$\begin{aligned} \gamma = -\Omega/2 &= \omega t - \omega/2(t+T) + \phi_\omega - \phi_{\omega/2} - \pi \\ &= \omega(t-T)/2 + \phi_\omega - \pi, \end{aligned} \quad (3.129)$$

since $\phi_{\omega/2} = 0$ with t and $t+T$ denoting the instants when the neutron is at the centre of the first and second flipper coil respectively. The term π arises from the second spin flip ($|\downarrow\rangle$ -to- $|\uparrow\rangle$), starting at an azimuthal angle further than the up-to-down curve by π .

Joint measurements

Experimentally, the probabilities of joint (projective) measurements are proportional to the following count rates, detected after path ($\vec{\alpha}$) and spin ($\vec{\beta}$) manipulation.

$$\begin{aligned}
N_{++}(\vec{\alpha}, \vec{\beta}) &= N_{++}(\vec{\alpha}, (\beta_1, 0)) \propto \langle \Psi_{\text{Exp}}(\gamma) | \hat{P}_+^{\text{P}}(\vec{\alpha}) \otimes \hat{P}_+^{\text{S}}(\beta_1, 0) | \Psi_{\text{Exp}}(\gamma) \rangle \\
N_{+-}(\vec{\alpha}, \vec{\beta}) &= N_{++}(\vec{\alpha}, (\beta_1 + \pi, 0)) \equiv N_{++}(\vec{\alpha}, (\beta_1^\perp, 0)) \\
&\propto \langle \Psi_{\text{Exp}}(\gamma) | \hat{P}_+^{\text{P}}(\vec{\alpha}) \otimes \hat{P}_+^{\text{S}}(\beta_1^\perp, 0) | \Psi_{\text{Exp}}(\gamma) \rangle \\
N_{-+}(\vec{\alpha}, \vec{\beta}) &= N_{++}((\alpha_1 + \pi, \alpha_2), (\beta_1, 0)) \equiv N_{++}((\alpha_1^\perp, \alpha_2), (\beta_1, 0)) \\
&\propto \langle \Psi_{\text{Exp}}(\gamma) | \hat{P}_+^{\text{P}}(\alpha_1^\perp, \alpha_2) \otimes \hat{P}_+^{\text{S}}(\beta_1, 0) | \Psi_{\text{Exp}}(\gamma) \rangle \\
N_{--}(\vec{\alpha}, \vec{\beta}) &= N_{++}((\alpha_1^\perp, \alpha_2), (\beta_1^\perp, 0)) \propto \langle \Psi_{\text{Exp}}(\gamma) | \hat{P}_+^{\text{P}}(\alpha_1^\perp, \alpha_2) \otimes \hat{P}_+^{\text{S}}(\beta_1^\perp, 0) | \Psi_{\text{Exp}}(\gamma) \rangle.
\end{aligned} \tag{3.130}$$

The expectation value of a joint measurement of $A^{\text{P}}(\vec{\alpha})$ and $B^{\text{S}}(\vec{\beta})$

$$E(\vec{\alpha}, \vec{\beta}) = \langle \Psi(\gamma) | A^{\text{P}}(\vec{\alpha}) \otimes B^{\text{S}}(\vec{\beta}) | \Psi(\gamma) \rangle \tag{3.131}$$

is experimentally determined from the count rates

$$E(\vec{\alpha}, \vec{\beta}) = \frac{N_{++}(\vec{\alpha}, \vec{\beta}) - N_{+-}(\vec{\alpha}, \vec{\beta}) - N_{-+}(\vec{\alpha}, \vec{\beta}) + N_{--}(\vec{\alpha}, \vec{\beta})}{N_{++}(\vec{\alpha}, \vec{\beta}) + N_{+-}(\vec{\alpha}, \vec{\beta}) + N_{-+}(\vec{\alpha}, \vec{\beta}) + N_{--}(\vec{\alpha}, \vec{\beta})}. \tag{3.132}$$

With these expectation values S is defined by

$$S = E(\vec{\alpha}, \vec{\beta}) - E(\vec{\alpha}, \vec{\beta}') + E(\vec{\alpha}', \vec{\beta}) + E(\vec{\alpha}', \vec{\beta}'). \tag{3.133}$$

Experimental setup

The experiment was carried out at the neutron interferometer instrument S18 at the high-flux reactor of the Institute Laue-Langevin (ILL) in Grenoble, France. A sketch of the setup is depicted in Fig. 3.31. A monochromatic beam, with mean wavelength $\lambda_0 = 1.91 \text{ \AA}$ ($\Delta\lambda/\lambda_0 \sim 0.02$) and $5 \times 5 \text{ mm}^2$ beam cross-section, is polarized by a birefringent magnetic field prism in $\hat{\mathbf{z}}$ -direction [Badurek et al., 2000]. Due to the angular separation at the deflection, the interferometer is adjusted so that only the spin-up component fulfills the Bragg condition at the first interferometer plate (beam splitter).

As in our previous experiment [Sponar et al., 2008b], the spin in path $|II\rangle$ is flipped by a RF-flipper, which requires two magnetic fields: A static field $B_0 \cdot \hat{\mathbf{z}}$ and a perpendicular oscillating field $B^{(1)} = B_{\text{rf}}^{(\omega)} \cos(\omega t + \phi_\omega) \cdot \hat{\mathbf{y}}$ with amplitude

$$B_1^{(\omega)} = \frac{\pi \hbar}{\tau |\mu|} \text{ and } \omega = \frac{2|\mu|B_0}{\hbar} \left(1 + \frac{B_1^2}{16B_0^2}\right), \tag{3.134}$$

where μ is the magnetic moment of the neutron and τ denotes the time the neutron is exposed to the RF-field. The second term in ω is due to the Bloch-Siegert shift [Bloch and Siegert, 1940]. The oscillating field is produced by a water-cooled RF-coil with a length of 2 cm, operating at a frequency of $\omega/2\pi = 58$ kHz. The static field is provided by a uniform magnetic guide field $B_0^{(\omega)} \sim 2$ mT, produced by a pair of water-cooled Helmholtz coils.

The two sub-beams are recombined at the third crystal plate where $|I\rangle$ and $|II\rangle$ only differ by an adjustable phase factor $e^{i\chi}$ (path phase χ is given by $\chi = -Nb_c\lambda D$, with the thickness of the phase shifter plate D , the neutron wavelength λ , the coherent scattering length b_c and the particle density N in the phase shifter plate). By rotating the plate, χ can be varied systematically. This yields the well known intensity oscillations of the two beams emerging behind the interferometer.

The O-beam passes the second RF-flipper, operating at $\omega/2\pi = 29$ kHz, which is half the frequency of the first RF-flipper. The oscillating field is denoted as $B_{\text{rf}}^{(\omega/2)} \cos((\omega/2)t + \phi_{\omega/2}) \cdot \hat{\mathbf{y}}$, and the strength of the guide field was tuned to $B_0^{(\omega/2)} \sim 1$ mT in order to satisfy the frequency resonance condition. This flipper compensates the energy difference between the two spin components, by absorption and emission of photons of energy $E = \hbar\omega/2$ (see [Sponar et al., 2008b]).

Finally, the spin is rotated by an angle δ (in the $\hat{\mathbf{x}}, \hat{\mathbf{z}}$ plane) with a static field spin-turner, and analyzed due to the spin dependent reflection within a Co-Ti multi-layer supermirror along the $\hat{\mathbf{z}}$ -direction. With this arrangement consisting of a dc-spin turner and a supermirror the spin can be analyzed along arbitrary directions in the $\hat{\mathbf{x}}, \hat{\mathbf{z}}$ plane, determined by δ , which is measured from the $\hat{\mathbf{z}}$ axis (see Fig. 3.31, and later front panel of Fig. 3.37 for intensity modulations due to χ -scans).

Experimental Strategy

Polar Angle Adjustment

Projective measurements are performed on parallel planes defined by $\alpha_2 = \alpha'_2 = \beta_2 = \beta'_2 = 0$ (see Fig. 3.31). For the path measurement the directions are given by $\vec{\alpha} : \alpha_1 = 0, \alpha_2 = 0$ (Fig. 3.34, Fig. 3.35), and $\vec{\alpha}' : \alpha'_1 = \pi/2, \alpha'_2 = 0$ (Fig. 3.37). The angle $\vec{\alpha}$, which corresponds to $+\hat{\mathbf{z}}$ (and $-\hat{\mathbf{z}}$ for $\alpha_1^\perp = \alpha_1 + \pi = \pi, \alpha_2 = 0$) is achieved by the use of a

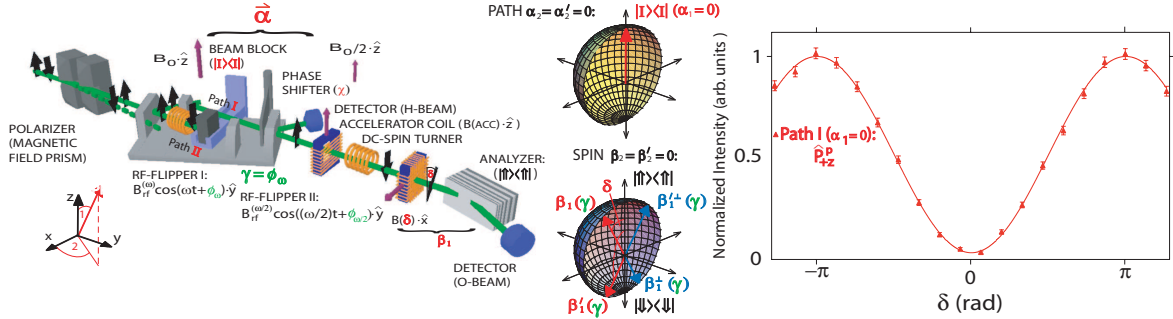


Figure 3.34: (right) Typical intensity modulations obtained by inserting a beam block in path II, being the projections on the $+\hat{z}$ direction of the path measurement, denoted as $\hat{P}_{+z}^p : (\alpha_1 = 0, \alpha_2 = 0)$. The oscillation remains the same when altering the geometric phase γ . (left) Setup configuration and Bloch sphere description of the associated measurement directions of path and spin.

beam block which is inserted to stop beam II (I) in order to measure along $+\hat{z}$ (and $-\hat{z}$). The corresponding operators are given by

$$\hat{P}_{+z}^p(\alpha_1 = 0, \alpha_2 = 0) = |I\rangle\langle I| \quad \text{and} \quad \hat{P}_{-z}^p(\alpha_1^\perp = \pi, \alpha_2 = 0) = |II\rangle\langle II|. \quad (3.135)$$

The results of the projective measurement are plotted versus different angles δ of the spin analysis, which is depicted in Fig. 3.34 and Fig. 3.35. Complementary oscillations were

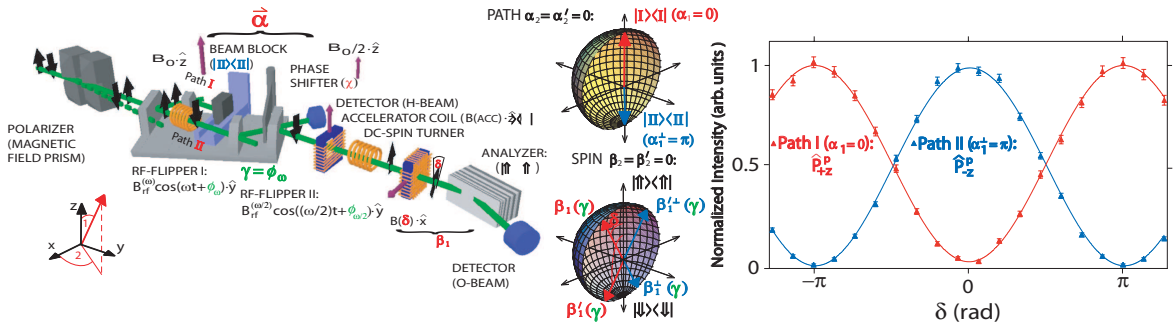


Figure 3.35: (right) Typical intensity modulations obtained by inserting a beam block, being the projections on the $\pm\hat{z}$ direction of the path measurement, denoted as $\hat{P}_{+z}^p : (\alpha_1 = 0, \alpha_2 = 0)$ and $\hat{P}_{-z}^p : (\alpha_1^\perp = \pi, \alpha_2 = 0)$. The oscillations are independent of geometric phase γ . (left) Setup configuration and Bloch sphere description.

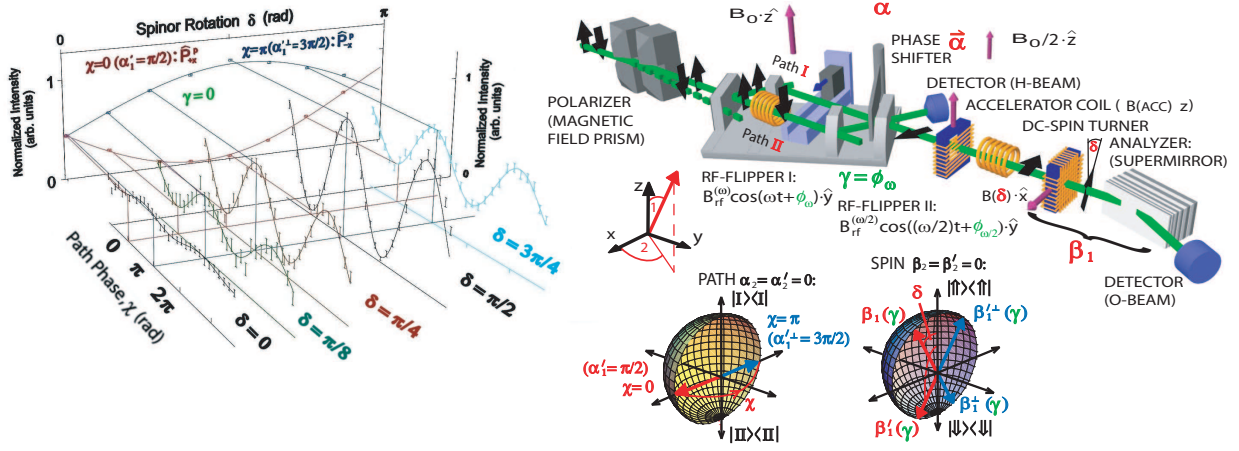


Figure 3.36: Typical interference patterns of the O-beam ($\alpha'_1 = \pi/2$) for $\delta = 0, \pi/8, \pi/4, \pi/2, 3\pi/4$, being the direction of the spin analysis, and geometric phase $\gamma = 0$. Intensities at the path phase $\chi = 0$ and $\chi = \pi$ are extracted from least square fits of the oscillations (beam block removed). The resulting curves (rear panel) represent the projections to the $\pm \hat{x}$ direction of the path subspace, denoted as $\hat{P}_{+x}^p : (\alpha'_1 = \pi/2, \alpha'_2 = 0)$ and $\hat{P}_{-x}^p : (\alpha'_1 = 3\pi/2, \alpha'_2 = 0)$. Bloch sphere description indicates the corresponding measurement direction for spin and path subspace.

obtained due to the spin flip in path $|\text{II}\rangle$. These curves are insensitive to the geometric phase γ , due to the lack of superposition with a referential sub-beam.

The angle α' is set by a superposition of equal portions of $|\text{I}\rangle$ and $|\text{II}\rangle$, represented on the equator of the Bloch sphere (here the beam block is removed). The interferograms are achieved by a rotation of the phase shifter plate, associated with a variation of the path phase χ , repeated at different values of the spin analysis direction δ . The projective measurement for $\alpha'_1 = \pi/2, \alpha'_2 = 0$ corresponds to a phase shifter position of $\chi = 0$ (and $\alpha'_1 = \alpha'_1 + \pi = 3\pi/2, \alpha'_2 = 0$ to $\chi = \pi$). Projection operators read as

$$\hat{P}_{+x}^p(\alpha'_1 = \frac{\pi}{2}, \alpha'_2 = 0) = \frac{1}{2} \left((|\text{I}\rangle + |\text{II}\rangle) (\langle\text{I}| + \langle\text{II}|) \right) \quad (3.136)$$

$$\hat{P}_{-x}^p(\alpha'_1 = \frac{3\pi}{2}, \alpha'_2 = 0) = \frac{1}{2} \left((|\text{I}\rangle - |\text{II}\rangle) (\langle\text{I}| - \langle\text{II}|) \right). \quad (3.137)$$

The interferogram obtained for $\gamma = 0$ and $\delta = \pi/2$, in Fig. 3.36, is utilized to determine the zero point of the path phase χ , which defines the $+\hat{x}$ -direction ($\alpha'_1 = \pi/2, \alpha'_2 = 0$) for the path measurement.

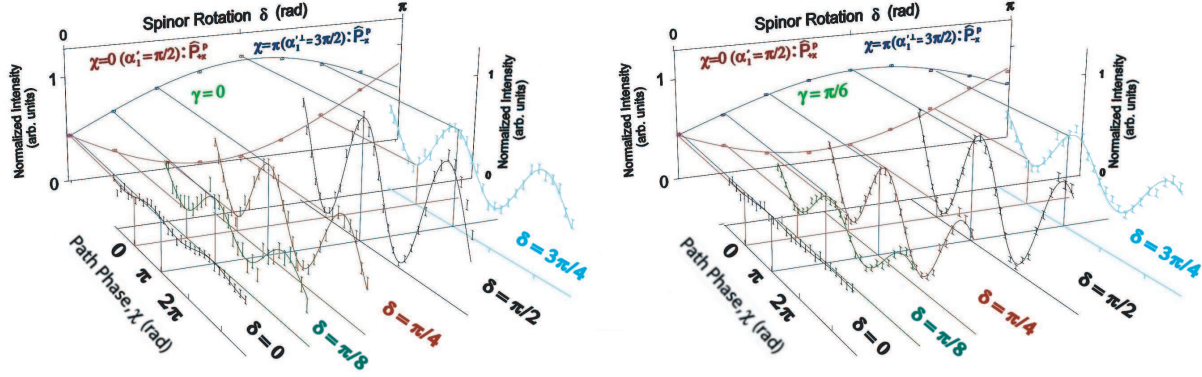


Figure 3.37: Typical interference patterns of the O-beam ($\alpha_1^\perp = \pi/2$) for $\delta = 0, \pi/8, \pi/4, \pi/2, 3\pi/4$, being the direction of the spin analysis, and geometric phase $\gamma = 0$ (left) and $\gamma = \pi/6$ (right side). Intensities at the path phase $\chi = 0$ and $\chi = \pi$ are extracted from least square fits of the oscillations. The resulting curves (rear panel) represent the projections to the $\pm \hat{x}$ direction of the path subspace, denoted as $\hat{P}_{+x}^P : (\alpha_1^\perp = \pi/2, \alpha_2^\perp = 0)$ and $\hat{P}_{-x}^P : (\alpha_1^\perp = 3\pi/2, \alpha_2^\perp = 0)$. The shift of the oscillations (see for instance $\delta = \pi/2$), due to the geometric phase γ , yields a lower contrast of the curves \hat{P}_{+x}^P and \hat{P}_{-x}^P .

In order to obtain phase shifter scans of higher accuracy, scans over two periods were recorded (see Fig. 3.36) and the values for $\chi = 0$ and π are extracted from the data by least square fits. These extracted points, marking the $\pm \hat{x}$ -direction of the path measurement, are plotted versus different angles of δ , as shown in Fig. 3.36, rear diagram. All phase shifter scans were repeated for different angles δ for the spin analysis from $\delta=0$ to $\delta = \pi$ in steps of $\pi/8$, and for several geometric phases γ (steps of $\pi/6$, and beginning from $\gamma = \pi$ steps of $\pi/4$), depicted in the rear panel of Fig. 3.37 for five selected settings of δ ($\delta = 0, \pi/8, \pi/4, \pi/2, 3\pi/4$) and two geometric phases ($\gamma = 0, \pi/6$). Note that the contrast of the curves \hat{P}_{+x}^P and \hat{P}_{-x}^P is decreasing when altering the geometric phase γ . This is due to the shift in the individual interferograms caused by the geometric phase γ .

Azimuthal Angle Adjustment

Here the Bell angles (polar angles) remain fixed at the usual values and are set at δ for the projective spin measurement, and by the beam block (and fixed phase shifter positions) for the path measurement. The angle between the measurement planes is adjusted by one

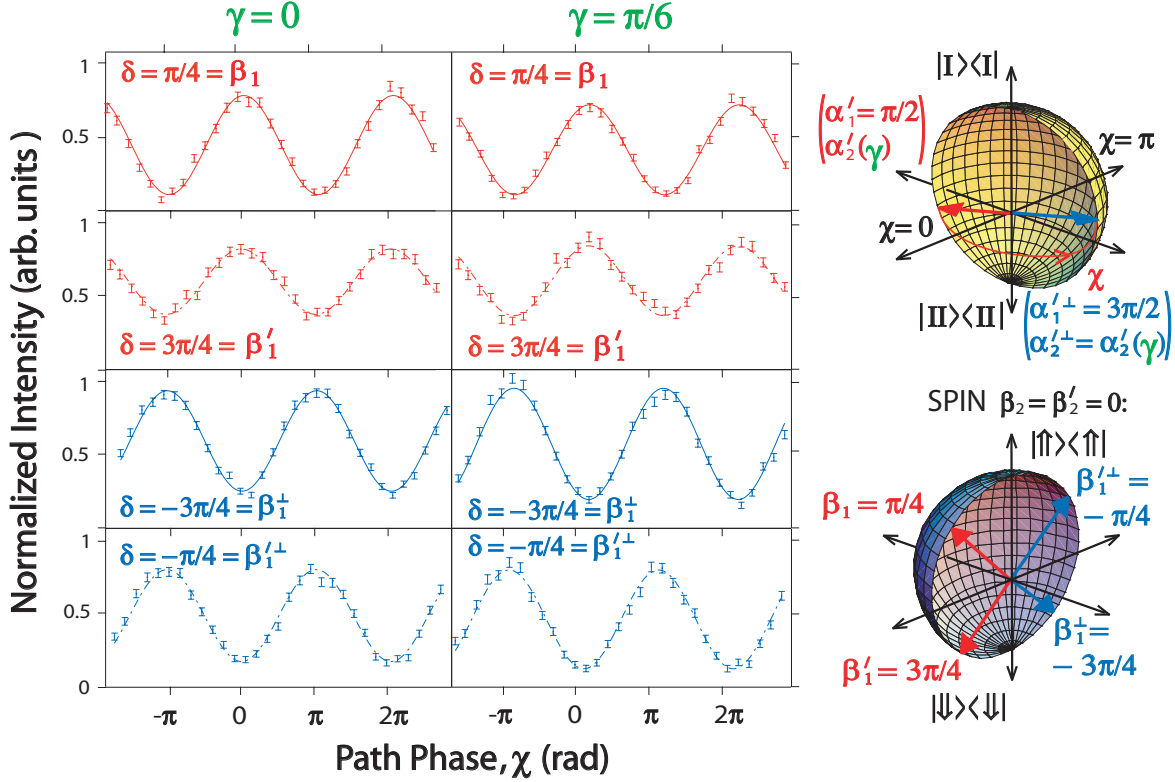


Figure 3.38: (left) Typical interference patterns of the O-beam ($\alpha'_1 = \pi/2$) for $\delta = \pi/4 = \beta_1$, $\delta = 3\pi/4 = \beta'_1$, $\delta = -3\pi/4 = \beta_1^\perp$ and $\delta = -\pi/4 = \beta_1^{\perp'}$ ($\beta_2 = \beta_2' = 0$) and geometric phase $\gamma = 0$ (left graph) and $\gamma = \pi/6$ (right graph). Phase shifter scans χ are performed for a forthcoming determination of α'_2 . (right panel) Bloch sphere description associated with the corresponding measurement direction for spin and path sub space.

azimuthal angle (α'_2), which is deduced by phase shifter (χ) scans.

For the spin measurement the directions are fixed and given by $\vec{\beta}$: $\beta_1 = \pi/4$, $\beta_2 = 0$ and $\vec{\beta}'$: $\beta'_1 = 3\pi/4$, $\beta'_2 = 0$ (together with $\beta_1^\perp = -3\pi/4$, $\beta_1^{\perp'} = -\pi/4$), see Fig. 3.38 left for Bloch description of the spin measurement directions. For the projective path measurement the fixed directions read as $\alpha_1 = 0$ ($\alpha_1^\perp = \pi$, see Fig. 3.35 for measurements with beam block), and $\alpha'_1 = \pi/2$ ($\alpha_1^{\perp'} = 3\pi/2$). Phase shifter (χ) scans are performed in order to determine α'_2 , which is depicted in Fig. 3.38 for two values of the geometric phase: $\gamma = 0$ and $\gamma = \pi/6$. One can see a shift of the oscillations due to the geometric phase γ .

3.4.3 Data analysis and experimental results

Polar Angle Adjustment

Using least square fits from the *polar angle adjustment* measurement curves in Fig. 3.35 and Fig. 3.37, together with Eq.(3.133) the S -value is calculated as a function of the parameters β_1 and β'_1 which is plotted in Fig.3.39 for $\gamma = 0$, together with a schematic illustration of the calculation of the function $S(\beta_1, \beta'_1, \gamma = 0)$. The local maximum of the surface is determined numerically. As seen from Fig.3.39 the predictions from Eq.(3.121) are reproduced evidently. In Fig. 3.40 the S -value is calculated for three selected values of γ : $\gamma = 0$, $\gamma = \pi/2$ and $\gamma = \pi$ ($\gamma = 0$ and $\gamma = \pi$ are chosen since the fringe displacement is maximal for these two settings and $\gamma = \pi/2$ illustrates the increase of S to a value of 2). Numerical determination of a maximal S -value, yields the settings for β_1 and β'_1 , which

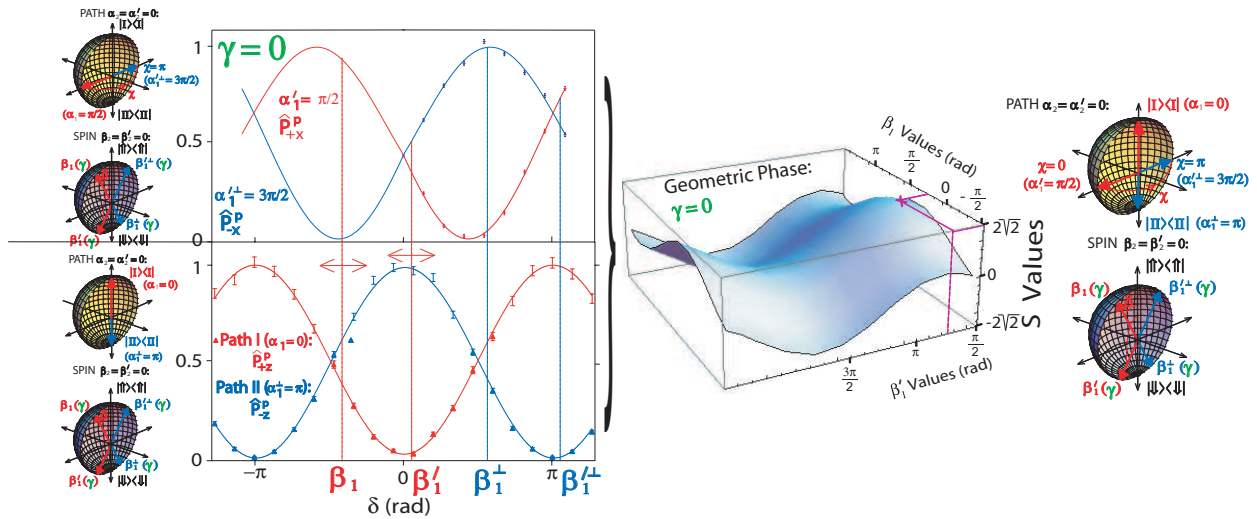


Figure 3.39: S -values for geometric phases $\gamma = 0$, derived from the least square fits of the projective measurements along $\pm \hat{z}$ (beam block Fig. 3.35 or left, bottom) and $\pm \hat{x}$ (varying χ Fig. 3.37 or left, top) direction for the path measurement ($\alpha_1 = 0$, $\alpha'_1 = \pi/2$ and $\alpha_2 = \alpha'_2 = 0$) using Eq.(3.108). β_1 and β'_1 represent the direction of the spin analysis, which are changed systematically by a variation of δ while β_2 and β'_2 remain constant at the value zero (*polar adjustment*). The position of the maximum is determined numerically. Here measurements for $\gamma = 0$ are utilized, where $S_{MAX} = 2\sqrt{2}$. The β_1 and β'_1 values result as predicted in Eqs.(3.121) for S_{MAX} .

are compared with the predicted values for β_1 and β'_1 from Eq.(3.121), summarized as:

$$\begin{aligned}\beta_1 &= \arctan(\cos \gamma) \\ \beta'_1 &= \pi - \beta_1 \\ \alpha'_1 &= \frac{\pi}{2}\end{aligned}\quad (3.138)$$

The resulting S values, derived by using the adjusted Bell angles β_1 and β'_1 , are plotted

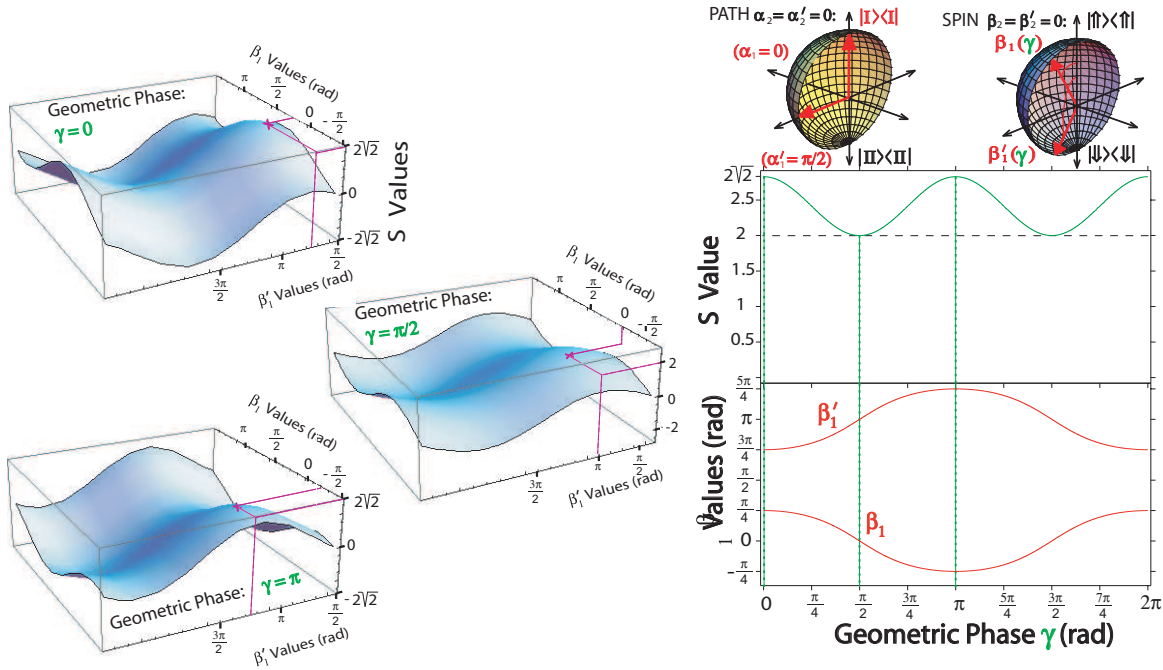


Figure 3.40: (left) S -values for different settings of geometric phases $\gamma = 0, \pi/2, \pi$, derived from the least square fits of the projective measurements along $\pm \hat{z}$ (beam block Fig. 3.35) and $\pm \hat{x}$ (varying χ Fig. 3.37) direction for the path measurement ($\alpha_1 = 0$, $\alpha'_1 = \pi/2$ and $\alpha_2 = \alpha'_2 = 0$) using Eq.(3.108). β_1 and β'_1 represent the direction of the spin analysis, which are changed systematically by a variation of δ while β_2 and β'_2 remain constant at the value zero (*polar adjustment*). The position of the maximum is determined numerically for different settings the geometric phases γ (here for example $\gamma = 0$ where $S_{MAX} = 2\sqrt{2}$, $\gamma = \pi/2$ with $S_{MAX} = 2$, and $\gamma = \pi$, with $S_{MAX} = 2\sqrt{2}$). The β_1 and β'_1 values result as predicted in Eqs.(3.121) (right) Predicted values for β_1 and β'_1 , with respect to the geometric phase γ and associated Bloch description for corresponding measurement directions of spin and path sub space.

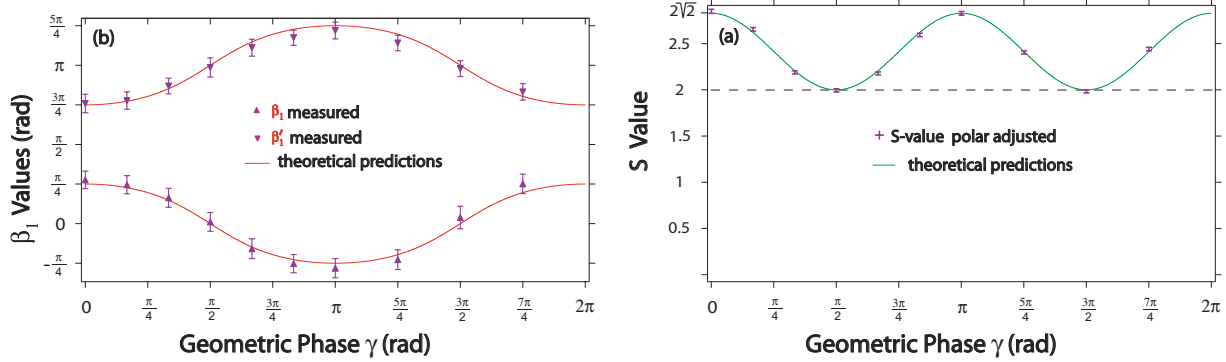


Figure 3.41: (a) *Polar adjusted* S -values versus geometric phase γ with adapted Bell angles (β_1 and β'_1) according to the geometric phase γ . (b) the corresponding modified Bell angles are plotted versus the geometric phase γ .

in Fig. 3.41 (a) versus the geometric phase γ . The theoretical predictions from Eq.(3.120) depicted as green line are evidently reproduced. The maximal S decreases from $\gamma=0$ to $\gamma = \pi/2$ where the boundary of the CHSH inequality $S = 2$ is reached, followed by an increase to the familiar value $S = 2\sqrt{2}$.

In Fig. 3.41 (b) the deduced β_1 and β'_1 values are plotted versus the geometric phase γ . β_1 and β'_1 follow the theoretical behavior, red line, predicted by Eq.(3.121). One can see a peak for β_1 (and a dip for β'_1) at $\gamma = \pi$.

Azimuthal Angle Adjustment

In Fig. 3.42 selected S values calculated from least square fits of the *azimuthal angle adjustment* measurements are depicted, where $\beta_1 = \pi/4$, $\beta'_1 = 3\pi/4$, $\beta_1^\perp = 5\pi/4$, $\beta_1^{\perp\perp} = -\pi/4$ and $\alpha'_1 = \pi/2$ (see Fig. 3.38) and $\alpha_1 = 0$, $\alpha_1^\perp = \pi$ (Fig. 3.35) versus geometric phase γ . A simple shift of the oscillation of the S -value is observed due to the geometric phase (see Fig. 3.42 front panel). The maximum S -value of $2\sqrt{2}$ is always found for $\alpha'_2 = \gamma$, as predicted in Eq.(3.123), which is indicated in the rear panel of Fig. 3.42. The complete measurement set of S -values versus the geometric phase γ is plotted in Fig. 3.43 (a)-*S-value azimuthal adjusted*. As predicted in Eq.(3.122) a constant value of $2\sqrt{2}$ is obtained for all values of the geometric phase γ .

Figure 3.43 (b) shows adjusted α'_2 versus the geometric phase γ : It is clearly seen,

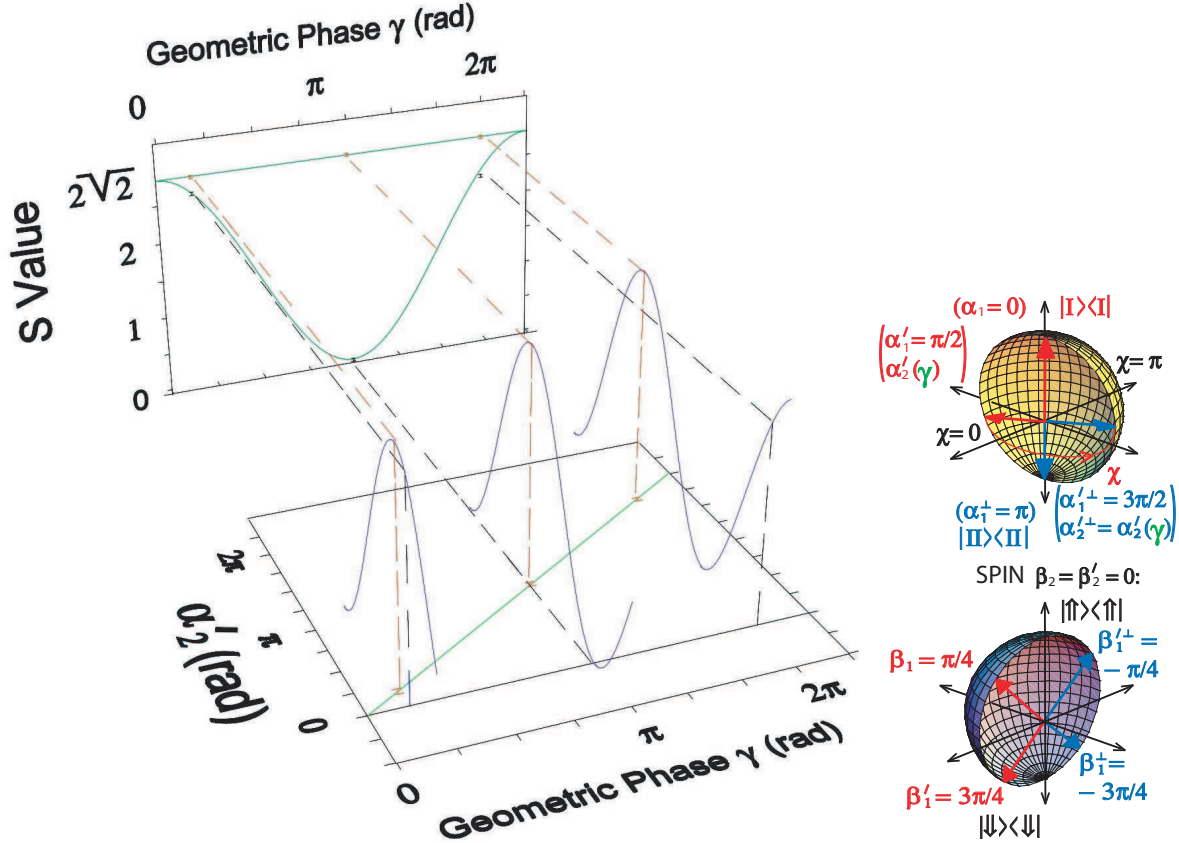


Figure 3.42: (left) S -values derived from least square fits of the projective spin and path measurements for $\beta_1 = \pi/4$, $\beta'_1 = 3\pi/4$, $\beta_1^\perp = -3\pi/4$, $\beta'_1{}^\perp = -\pi/4$ and $\alpha'_1 = \pi/2$, $\alpha'_1{}^\perp = 3\pi/2$ (see Fig. 3.38), and $\alpha_1 = 0$, $\alpha_1^\perp = \pi$ (see Fig. 3.35), versus geometric phase γ . The maximum S -value of $2\sqrt{2}$ is always found for $\alpha'_2 = \gamma$ as predicted in Eq.(3.123) (*azimuthal adjustment*). If no corrections are applied to the Bell angles ($\alpha'_2 = 0$) S approaches zero at $\gamma = \pi$.(right) Bloch sphere description for corresponding measurement direction of spin and path.

that adjusted α'_2 fulfills the theory condition (red line) namely a linear dependency as expressed in Eq.(3.123) :

$$\alpha'_2 - \beta'_2 = \gamma \pmod{\pi} = \alpha'_2, \quad (3.139)$$

since $\beta'_2 = 0$ has been chosen.

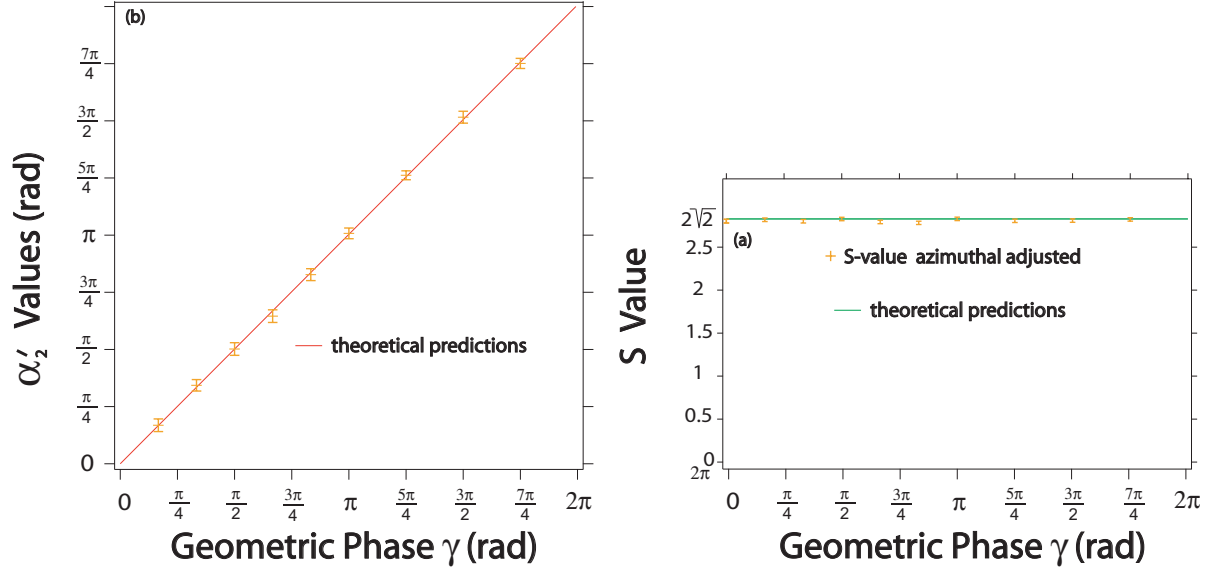


Figure 3.43: (a) *Azimuthal adjusted* S -values versus geometric phase γ with balanced Bell angle (α'_2) according to the geometric phase γ , and without corrections. (b) the corresponding modified Bell angle is plotted versus the geometric phase γ .

Absence of adjustment

Finally the case is investigated where no corrections at all are applied to the Bell angles. Keeping the polar angles α_1 , α'_1 , β_1 and β'_1 constant at the usual Bell angles $\alpha_1 = 0$, $\alpha'_1 = \frac{\pi}{2}$, $\beta_1 = \frac{\pi}{4}$, $\beta'_1 = \frac{3\pi}{4}$ (and azimuthal parts fixed at $\alpha_2 = \alpha'_2 = \beta_2 = \beta'_2 = 0$) the theoretical prediction for the S function given by

$$S(\vec{\alpha}', \vec{\beta}, \vec{\beta}', \gamma) = \left| -\sin \alpha'_1 \left(\cos(\alpha'_2 - \beta_2 + \gamma) \sin \beta_1 + \cos(\alpha'_2 - \beta'_2 + \gamma) \sin \beta'_1 \right) - \cos \alpha'_1 (\cos \beta_1 + \cos \beta'_1) - \cos \beta_1 + \cos \beta'_1 \right| \quad (3.140)$$

reduces to

$$S(\gamma) = \left| -\sqrt{2} - \sqrt{2} \cos \gamma \right|, \quad (3.141)$$

where the familiar maximum value of $2\sqrt{2}$ is reached for $\gamma = 0$. For $\gamma = \pi/2$ the value of S approaches zero and returns to the maximum value $2\sqrt{2}$ at $\gamma = 2\pi$. The experimentally obtained values, depicted in Fig. 3.44, evidently reproduced the quantum-

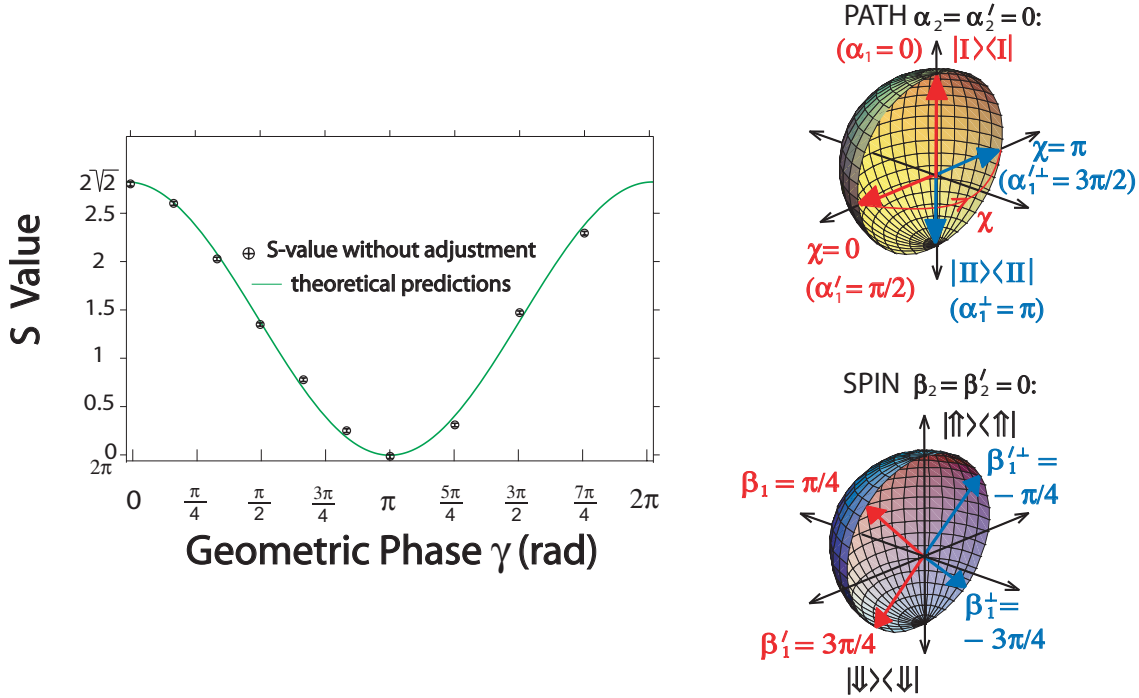


Figure 3.44: S (left) Value under variation of Berry phase γ for the common Bell angles $\alpha_1 = 0$, $\alpha'_1 = \frac{\pi}{2}$, $\beta_1 = \frac{\pi}{4}$, $\beta'_1 = \frac{3\pi}{4}$ (and azimuthal parts fixed at $\alpha'_2 = \beta_2 = \beta'_2 = 0$). (right) Bloch sphere description for corresponding measurement direction of spin and path.

mechanical predictions for S over the entire range of the geometric phase γ from 0 to 2π .

Discussion

Keeping the azimuthal angles fixed, an appropriate adjustment of the polar Bell angles determined by the geometric phase ($\beta_1 = \arctan(\cos \gamma)$), yields a sinusoidal oscillation of the S-value ($2 \leq S \leq 2\sqrt{2}$, with period π , see Fig.3.41). maximum S-value of $2\sqrt{2}$ can be observed, for all values of the geometric phase γ , if the difference of the azimuthal angles (angle between the analysis planes) equals the geometric phase ($\alpha'_2 = \gamma$), while the polar Bell angles remain unchanged at the typical values for testing of a Bell inequality (Fig.3.43(a), *S-value azimuthal adjusted*).

Due to the inherent phase instability of the neutron interferometer, it is necessary

to perform a reference measurement for each setting of γ and δ . This is achieved by turning off the RF-flipper inside the inteferometer, yielding a reference interferogram. The oscillations plotted in Fig. 3.37 and Fig. 3.38 are normalized, by the contrast of the reference measurement, and the phase of the reference interferogram is taken into account (relative phase between the oscillations).

At this point it should be noted that the average contrast of ~ 50 per cent (obtained for $\delta = \pi/2$ with maximum intensity of ~ 25 neutrons/sec.) is below the threshold of 70.7%, required to observe a violation of a Bell inequality. Violation of a Bell-like inequality, for a spin-path entanglement in neutron interferometry, has already been reported in [Hasegawa et al., 2003], the argument here is the influence of the geometric phase on the S -value. Consequently a normalization as performed does not influence the validity of the results presented here.

Next some systematic errors in our experiment are discussed, in particular in the state preparation and in the projective spin measurement. Under ideal conditions no interference fringes should be obtained in the H-beam, due to orthogonal spin states in the interfering sub-beams. Nevertheless we have observed intensity modulations with a contrast of a few per cent. This indicates, that the state preparation (by RF-flipper) was not perfect in some sense. The expectation values for the joint measurements Eqs.(3.118)-(3.108) can be deduced for an arbitrary (spin) state, in the path of the IFM where the RF-flipper is located,

$$|\Psi_{\text{Meas.}}(\gamma)\rangle = \frac{1}{\sqrt{2}} \left(|I\rangle \otimes |\uparrow\rangle + e^{i\chi} |II\rangle \otimes e^{i\gamma} \left(\sin \frac{\theta}{2} |\uparrow\rangle + \cos \frac{\theta}{2} |\downarrow\rangle \right) \right). \quad (3.142)$$

Here θ is determined by the fringe contrast in the H-beam. These systematic deviations from the theoretical initial state have been taken into account in the calculation of the final S value.

The asymmetry in the curve of the projective measurement along the $\pm \hat{\mathbf{x}}$ direction of the path measurement, denoted as \hat{P}_{+x}^{P} : $(\alpha'_1 = \pi/2, \alpha'_2 = 0)$ and \hat{P}_{-x}^{P} : $(\alpha'_1 = 3\pi/2, \alpha'_2 = 0)$ in Fig. 3.37 is considered to result from a misalignment of the static magnetic fields, at the position of the coil, such as the stray field of the first guide field, the second guide field and the two fields ($\hat{\mathbf{x}}$, $\hat{\mathbf{z}}$)-direction produces by the coil itself.

To summarize: In this Section a technique to balance the influence of the geometric phase generated by one subspace of the system, considering a Bell-like inequality, has

been presented. This is achieved by an appropriate adjustment of the polar Bell angles (keeping the measurement planes fixed) or one azimuthal angle (keeping the polar Bell angles at the well-known values), determined by a laborious measurement procedure. It is demonstrated, in particular, that a geometric phase in one subspace does not lead to a loss of entanglement, determined by a violation of a Bell-like inequality. The experimental data are in good agreement with theoretical predictions presented in [Bertlmann et al., 2004], demonstrating the correctness of the procedure as a matter of principle. A summary of the present work can be found in [Sponar et al., 2010a].

4

Polarimetric Experiments

In this Chapter neutron polarimetric experiments are the main focus of attention. Neutron polarimetry has several advantages compared to perfect crystal interferometry. It is insensitive to ambient mechanical and thermal disturbances and therefore provides better phase stability. Efficiencies of the manipulations, including state splitting and recombination, are considerably high (typically $> 98\%$) resulting in a better contrast compared to interferometry. In addition, while single-crystal interferometers accept neutrons only within an angular range of a few arc seconds, which leads to a significant decrease in intensity, polarimeters accept beams with a broad momentum distribution. Neutron polarimetry has been used to demonstrate fundamental quantum-mechanical properties. Just to mention the noncommutation of the Pauli spin operator [Hasegawa and Badurek, 1999], geometric phase measurements [Wagh et al., 2000, Klepp et al., 2005, Klepp et al., 2008], test of an alternative model for non-local correlations [Hasegawa et al., 2011], or in a more recent experiment demonstration of a universally valid uncertainty relation [Erhart et al., 2011]. Another advantage lies in the fact that polarimetry is applicable to other quantum systems in atomic physics, aside from neutrons.

4.1 Zero Field Precession in Neutron Polarimetry

In this Section a method, which has already been introduced in Section 3.3.3, is illuminated by an exhaustive experimental analysis. In a neutron polarimetric experiment, it is demonstrated in detail, how one can tune a zero-field phase γ and a Larmor phase α independently, using an appropriate combination of DC- and RF spin-turners, mounted on translation stage.

4.1.1 Theorie

For a neutron exposed to a stationary magnetic field the motion of the polarization vector, being the expectation value of the spin operators, is described by the Bloch-equation exhibiting Larmor precession (see for more details Sec. 2.1.1)

$$\frac{d\vec{P}}{dt} = -\gamma\vec{P} \times \vec{B}, \quad (4.1)$$

where the polarization vector \vec{P} is given by $\vec{P} = \langle \Psi | \vec{\sigma} | \Psi \rangle$, and γ is the gyromagnetic ratio given by $2\mu/\hbar$, and μ is the magnetic moment of the neutron, respectively. This is the equation of motion of a classical magnetic dipole in a magnetic field, which shows the precession about the magnetic field \vec{B} with the Larmor frequency $\omega_L = |2\mu B/\hbar|$. An important property of the Larmor precession angle α , which is obtained with a frequency ω_L and the propagation time T as

$$\alpha = \omega_L T, \quad (4.2)$$

is that α solely depends on the strength of the applied magnetic field. Larmor precession is utilized for spin-rotators in neutron polarimetric and interferometric experiments [Rauch and Werner, 2000].

A complete different physical situation arises, when a neutron interacts with a time-dependent, rather oscillating, magnetic field. Here photon exchange occurs and the total energy of neutron is no longer a conserved quantity (see Sec. 2.1.2 for detailed description). The total energy of the neutron decreases (or increases) by $\hbar\omega_R$ during the interaction with the RF-field [Alefeld et al., 1981, Gähler and Golub, 1987, Summhammer, 1993, Grigoriev et al., 2004]. As a consequence, an additional phase a so-called *zero-field phase*

$$\gamma = \omega_R T \quad (4.3)$$

is accumulated during the interaction with the time dependent magnetic field. Note that this zero-field phase is independent of the applied guide field and purely depends on the frequency of the rotating (or rather oscillating) field applied i.e. the RF spin-flipper. This effect also occur in field free regions and therefore it referred to as zero-field precession in literature [Golub et al., 1994, Kraan et al., 2001], and related to the spinor precession known from zero-field spin-echo experiments [Gähler and Golub, 1987, Grigoriev et al., 2004]. The advantage of the zero-field phase γ is that is independent of field inhomogeneities.

4.1.2 Polarimetric setup

The experiment was carried out at the neutron polarimetry facility at the 250-kW TRIGA research reactor of the Atomic Institute in Vienna. A schematic view of the experimental setup is shown in Fig. 4.1 The incident neutron beam is monochromatized (with a mean wave length of $\lambda = 1.99 \text{ \AA}$ which corresponds to a velocity of $\sim 1990 \text{ m/s}$) by the use of

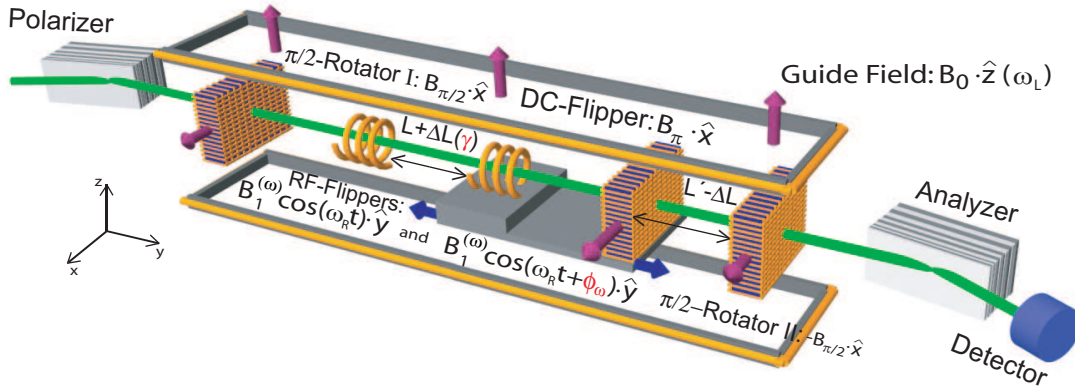


Figure 4.1: Experimental setup for demonstrations of zero-field and Larmor spin precessions. From a polarized incident beam the first $\pi/2$ spin-rotator generates a superposition of $|\uparrow\rangle$, $|\downarrow\rangle$. The first RF-flipper induces the energy shift $\hbar\omega_R$ for each spin eigenstate $|\downarrow\rangle$, $|\uparrow\rangle$ which leads to the zero-field spin precession until the second RF-flipper. The guide field, permeated along the beam path, leads to the Larmor spin precession. The second $\pi/2$ spin-rotator together with the analyzer enables to exhibit the intensity modulation due to the spin precessions.

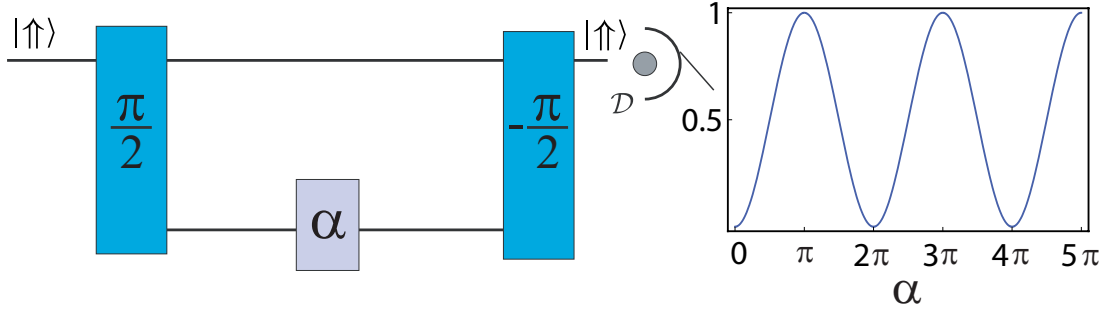


Figure 4.2: Neutron polarimeter scheme.

a pyrolytic graphite crystal and polarized (average degree of polarization over 98%) by reflection from a bent Co-Ti supermirror array. The diameter of the beam is confined to about 4mm in diameter by a Cd diaphragm. The polarization vector \vec{P}_1 , of the initial state $|\Psi_{\text{in}}\rangle = |\uparrow\uparrow\rangle$, is perpendicular to the beam trajectory and defines the $+\hat{z}$ -direction. A second supermirror array is used to analyze the final polarization \vec{P}_f . Depolarization of the neutron beam is minimized by applying a guide fields along the entire beam trajectory.

In our neutron polarimeter, as introduced in Section 2.2.2 and schematically illustrated in Fig. 4.2, the first DC- $\pi/2$ spin-rotator induces a $+\pi/2$ spin-rotation around the $+\hat{x}$ axis, thereby creating a coherent superposition of orthogonal eigenstates, by transforming the initial state $|\Psi_i\rangle = |\uparrow\uparrow\rangle$ according to

$$|\Psi_i\rangle \xrightarrow{\text{DC}\frac{\pi}{2}} |\Psi'\rangle = \frac{1}{\sqrt{2}} \left(|\uparrow\uparrow\rangle - i|\downarrow\downarrow\rangle \right). \quad (4.4)$$

Before the second DC- $\pi/2$ -rotation probes it, different phase shifts of these two states are accumulated, due to further spinor manipulations (which add up to a phase factor α), denoted as

$$|\Psi'\rangle \xrightarrow{\text{PS}:\alpha} |\Psi''\rangle = \frac{1}{\sqrt{2}} \left(|\uparrow\uparrow\rangle - ie^{i\alpha}|\downarrow\downarrow\rangle \right), \quad (4.5)$$

with a corresponding polarization vector in the xy -plane given by

$$\vec{P}'' = (\sin \alpha, -\cos \alpha, 0). \quad (4.6)$$

Between the two DC- $\pi/2$ spin-rotators, three spin-flippers are placed in the beam: two of them are RF spin-flippers and the other is a DC spin-flipper. In addition, one of the RF

and the DC flipper are mounted on a single translator, allowing to tune the propagation time of neutrons between the two RF spin-flippers. The polarization vector after passing through all spin-flippers is expected to lie in the xy -plane, resulting from the interference between the states $|\uparrow\rangle$ and $|\downarrow\rangle$. The second DC- $\pi/2$ spin-rotator reverses the action of the first one by a $-\pi/2$ spin-rotation around the $+\hat{x}$ axis for a forthcoming polarization analysis along the $+\hat{z}$ direction by the second supermirror, used to resolve the different phase shifts accumulated through spin-flips. Finally, a polarization change of the emerging neutron beam is observed.

4.1.3 Experimental results

Larmor precession

The first experiment exhibits pure Larmor precession: both RF-flippers are turned off and only the DC-flipper and the two DC- $\pi/2$ spin-rotators are in operation, which is depicted in Fig. 4.3. In this case, the superposed states $|\uparrow\rangle$ and $|\downarrow\rangle$ (and the flipped states later) simply propagate until (after) the DC-flipper. These states $|\uparrow\rangle$ and $|\downarrow\rangle$ are the eigenstates of the guide field: no additional spinor rotation occurs. Then the superposed state $|\Psi''\rangle$ obtains a Larmor phase α due to the guide field, which is given by

$$\alpha = \omega_L(T_1 - T_2) = \omega_L((T_1^0 + \Delta T) - (T_2^0 - \Delta T)) = \alpha_0 + 2\omega_L\Delta T, \quad (4.7)$$

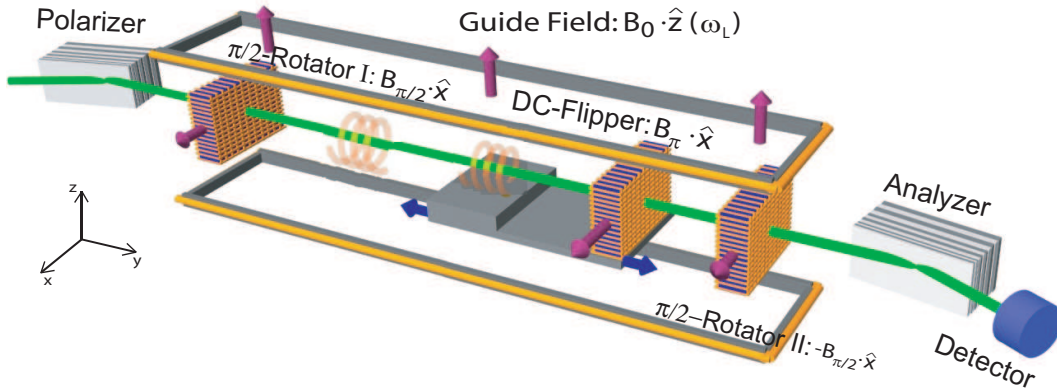


Figure 4.3: Experimental setup for observation of pure Larmor spin precessions, consisting only of two DC- $\pi/2$ spin-rotators and a DC spin-flipper on a translation stage.

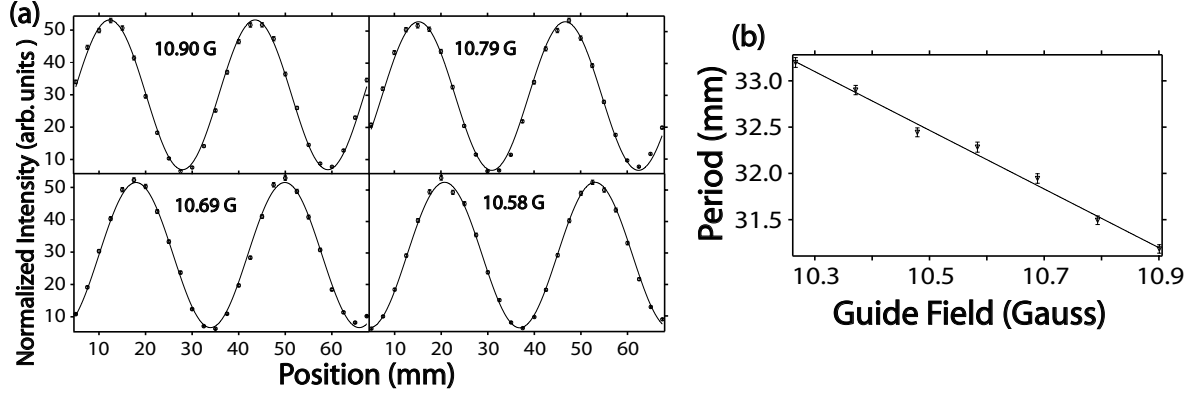


Figure 4.4: (a) Typical intensity oscillations with least square fits for the Larmor spin precession. Curves are shown with the guide field $B_0 = 10.90, 10.79, 10.69$ and 10.58 G. (b) Dependence of the period on the strength of the guide field depicted for seven values of the guide field.

with $\alpha_0 = \omega_L(T_1^0 - T_2^0 + T_3^0)$. T_1 , T_2 , and ΔT are the propagation time before and after the DC flipper and the time shift for T_1 , T_2 due to the position change of the DC flipper. After the beam passes the DC- $\pi/2$ spin-rotator and the analyzer, clear sinusoidal intensity modulations are obtained. Typical experimental data with least square fits are shown Fig. 4.4 (a): the strength of the guide magnetic field was set to $B_0 = 10.90, 10.79, 10.69$ and 10.58 G. The shift of the oscillations is due to $\omega_L T$ (as predicted for α_0 in Eq.(4.7)). In addition, the dependence of the period of the oscillations on the strength of the guide field is plotted in Fig. 4.4 (b). A linear dependence, of which inclination is in good agreement with the theoretically predicted value, is observed.

Zero field precession

Next, characteristics of the zero-field precession are investigated: additionally both RF-flippers are turned on now, which can be seen in Fig. 4.5. In this case, the superposed states $|\uparrow\rangle$ and $|\downarrow\rangle$ are once flipped, and finally again flipped back. Then, the spin precession angle α' is expected to be given with the propagation time, T_1 , T_2 , and T_3 after each spin flipper by

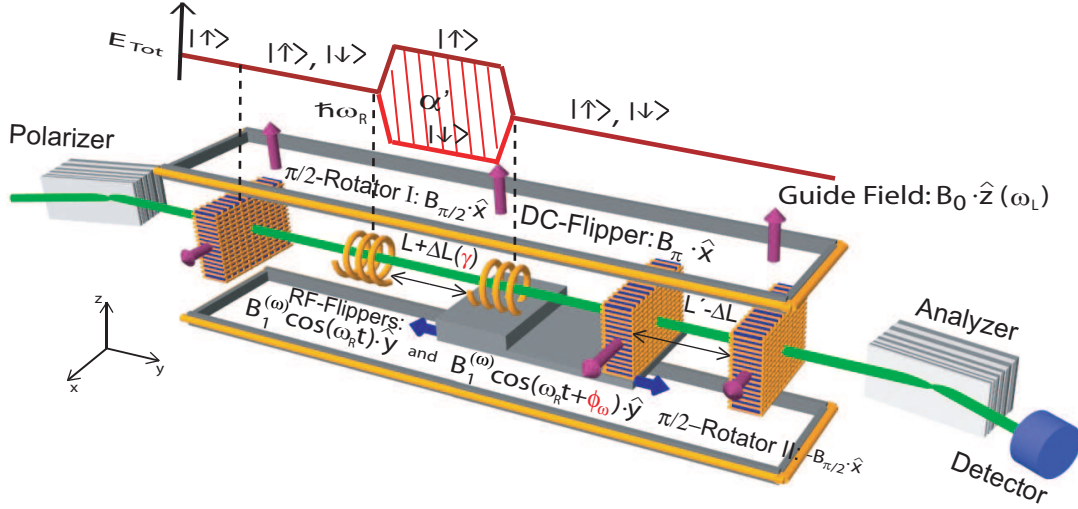


Figure 4.5: Experimental setup for pure zero phase observation, consisting not only of two DC- $\pi/2$ spin-rotators and a DC spin-flipper, but additionally two RF spin-flipper (the second RF-flipper is also mounted on the translation stage).

$$\begin{aligned}
 \alpha' &= \omega_L(T_1 - T_2 + T_3) + \omega_R T_1 \\
 &= \omega_L((T_1^0 + \Delta T) - T_2^0 + (T_3^0 - \Delta T)) + \omega_R(T_1^0 + \Delta T) \\
 &= \alpha'_0 + \omega_R \Delta T,
 \end{aligned} \tag{4.8}$$

with $\alpha'_0 = \omega_L(T_1^0 - T_2^0 + T_3^0) + \omega_R T_1^0$. In this setup, no Larmor precession is expected to be induced by the change of ΔT , since a positive and a negative change of T_1 and T_3 completely compensate each other by shifting the position of the DC flipper and the second RF-flipper.

In order to prove the frequency dependence of the precession, the frequency of the RF-flippers is varied with keeping the strength of the guide field by $B_0 = 10.59$ G. Typical intensity modulations are plotted in Fig. 4.6 (a) at the RF-flipper frequencies of $\omega_R = 30.9, 30.6, 30.3,$ and 30.0 kHz. Clear sinusoidal oscillations of high contrast are again obtained. A slight decrease of the amplitude is solely due to the fact that the frequency ω_R is not exactly on resonance for flip-mode any longer. The shift of the oscillations is due to $\omega_R T$ (see, α'_0 in Eq.(4.8)). In addition, a dependence of the period on the frequency is plotted

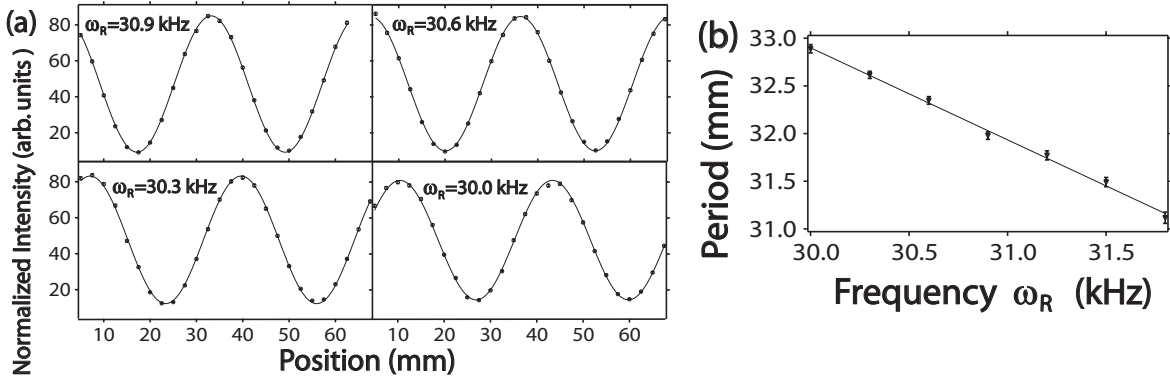


Figure 4.6: (a) Typical intensity oscillations with least square fits for the zero-field spin precession. Curves are shown at the RF-flipper frequencies $\omega_R = 30.9, 30.6, 30.3$ and 30.0 kHz. (b) Dependence of the period on the frequency depicted for seven values of the frequency. A clear linear dependence agrees well with the theoretical predictions (see, Eq.(4.8)).

in Fig. 4.6 (b). A linear dependence is observed and its inclination is in good agreement with the theory, which confirms the precession angle defined in Eq.(4.8).

The setup is constructed in such a way that no spin rotation due to Larmor precession will occur, since the Larmor precessions before and after the second RF-flipper, i.e., ΔT_1

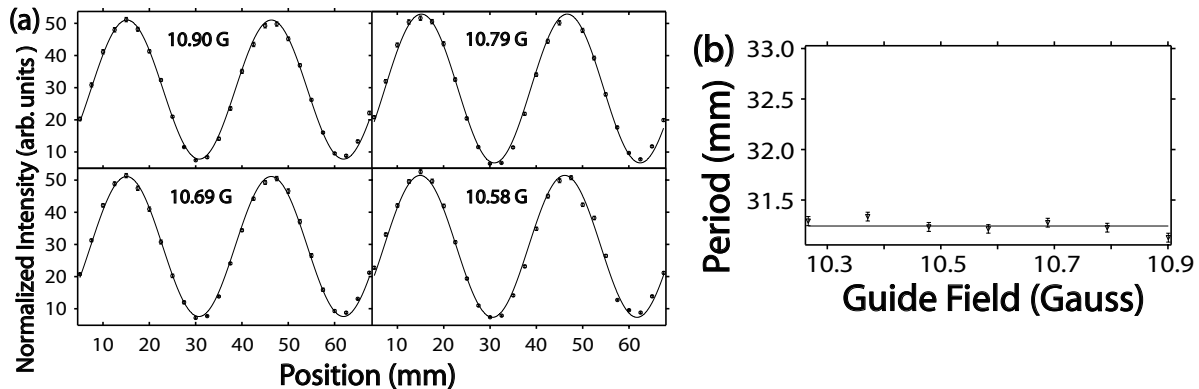


Figure 4.7: (a) Typical intensity oscillations with least square fits for the zero-field precession. Curves are shown with the guide field $B_0 = 10.90, 10.79, 10.69$ and 10.58 G. All curves are identical as expected. (b) The period is plotted versus the strength of the guide field for seven values. The period is constant independent of the strength of the guide field.

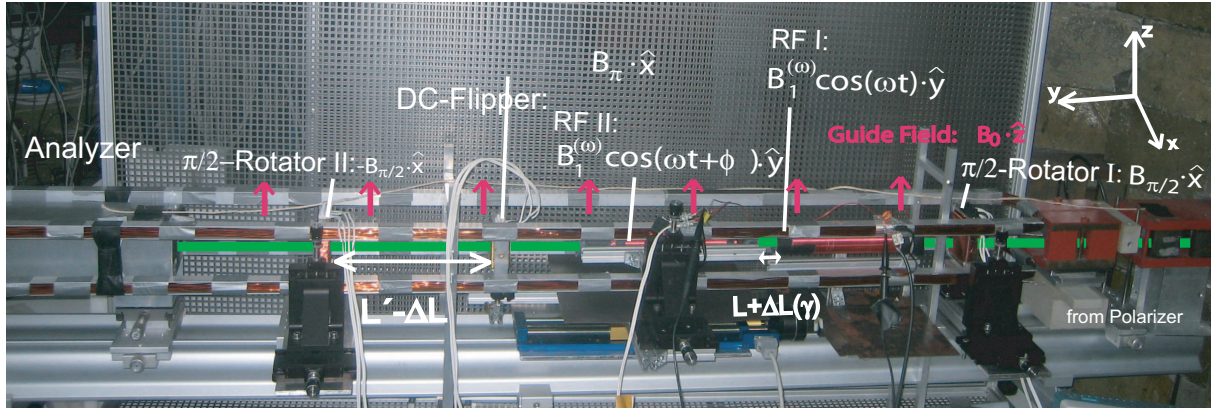


Figure 4.8: Photo of the actual setup for independent Larmor and zero-field phase measurement at the tangential beam tube at the 250 kW TRIGA research reactor of the Atomic Institute of the Austrian Universities in Vienna.

and ΔT_3 , are compensating each other with all flippers turned on (see Eq.(4.8)). This independence of the Larmor precession can also be accessed in the experimental setup. In particular, the frequency of the RF-flippers is tuned at the resonance $\omega_0 = 31.8 \text{ kHz}$ and the strength of the guide field is varied at $B_0 = 10.90, 10.79, 10.69$ and 10.58 G . Typical experimental data with least square fits are depicted in Fig. 4.7(a): identical sinusoidal oscillations are obtained, confirming no spin rotation due to the Larmor precessions. In addition, the period is plotted versus the strength of the guide field in Fig. 4.7(b). Independent behavior of the period from the strength is seen as expected by Eq.(4.8).

The results are in good agreement with theoretically predicted behavior: the frequency of the oscillating field affects only the zero-field precession and the strength of the field only the Larmor precession. The strategy, of displacing RF- and DC flipper by the same amount, allows for individual control of both precessions. This is an advantage for the separate (phase) manipulation of two-spaces, i.e., spin and energy space (see Section 4.2) or spin and momentum space (see Section 4.3). A photograph of the setup including all neutron optical devices, required in this experiment, is seen in Fig. 4.8.

The zero-field precession is independent of the strength of the guide field and purely depends on the frequency of the RF spin-flipper, where an energy shift occurs. A summary of this experiment is found in [Sponar et al., 2008a].

4.2 Violation of Bell's Inequality in Neutron Polarimetry

In this Section violation of a Bell-like inequality in a neutron polarimetric experiment is presented. The proposed inequalities, in Clauser-Horne-Shimony-Holt (CHSH) formalism, rely on the correlations between the spin and energy degree of freedom of single-neutrons. The entangled states are generated using the neutron polarimeter setup introduced in the last Section (4.1). The S value is deduced to be $2.333 \pm 0.005 \not\leq 2$, which violates the Bell-CHSH inequality by more than 66 standard deviations.

4.2.1 Theory

In this experiment the neutron's wavefunction exhibits entanglement between the spinor and energy degree of freedom [Sponar et al., 2008b], expressed as

$$|\Psi_{\text{Bell}}\rangle = \frac{1}{\sqrt{2}} \left(|E_0 + \hbar\omega\rangle \otimes |\uparrow\rangle + |E_0 - \hbar\omega\rangle \otimes |\downarrow\rangle \right). \quad (4.9)$$

Here $|\uparrow\rangle$ and $|\downarrow\rangle$ denote the neutron's up and down spin eigenstates, referring to the chosen quantization axis, describing a spin superposition prepared by a DC- $\pi/2$ spin-turner. $|E_0 + \hbar\omega\rangle$ and $|E_0 - \hbar\omega\rangle$ are the energy eigenstates after interaction with a time-dependent magnetic field within a radio frequency (RF)-flipper, due to absorption or emission of photons of energy $\hbar\omega$. E_0 is the initial total energy of the neutron and ω is the frequency of the oscillating magnetic field.

As in common Bell experiments a joint measurement of two observables, i.e. spin and energy, is performed: First projection operators onto a spin superposition state, specified by an angle parameter α , are defined as

$$\hat{P}_{\pm}^{(S)}(\alpha) = \frac{1}{\sqrt{2}} (|\uparrow\rangle \pm e^{-i\alpha} |\downarrow\rangle) (\langle\uparrow| \pm e^{i\alpha} \langle\downarrow|). \quad (4.10)$$

Similarly projection operators onto an energy superposition state, using an angle parameter γ , are given by

$$\hat{P}_{\pm}^{(E)}(\gamma) = \frac{1}{\sqrt{2}} (|E_0 + \hbar\omega\rangle \pm e^{-i\gamma} |E_0 - \hbar\omega\rangle) (\langle E_0 + \hbar\omega| \pm e^{i\gamma} \langle E_0 - \hbar\omega|). \quad (4.11)$$

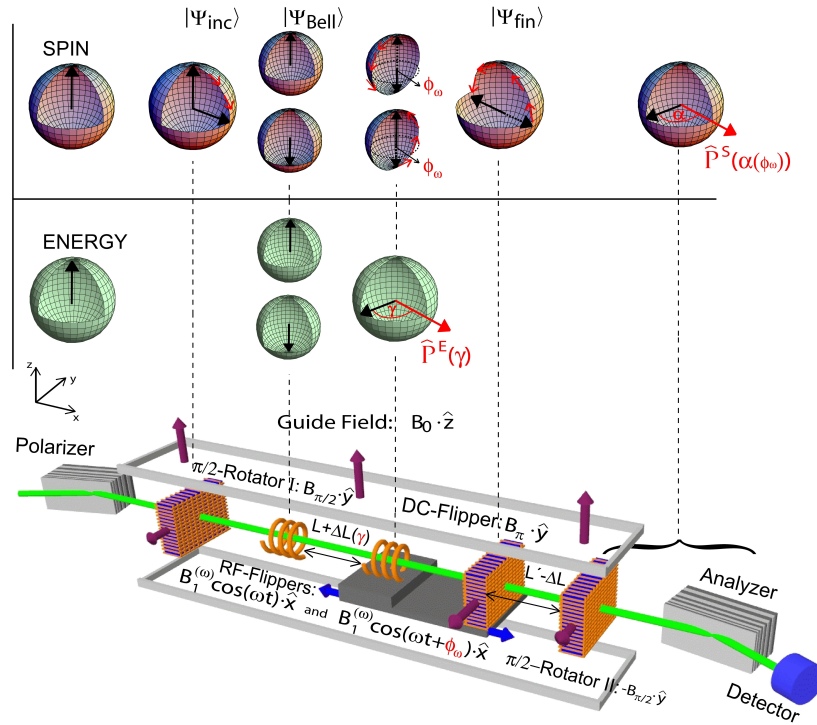


Figure 4.9: Experimental apparatus for observation of quantum correlations between the spin and energy degree of freedom, expressed by a Bell-like CHSH inequality. The incident neutron beam is polarized by a supermirror polarizer. A DC- $\pi/2$ spin-turner creates a spin superposition followed by an RF-flipper, preparing the entanglement of spin and energy. The position change of the translation stage (displacement of second RF-flipper together with DC spin-flipper) and the phase difference between the two oscillating RF-fields adjust the parameters α and γ for the Bell measurement. Finally, the spin is projected back to the initial direction using a second DC- $\pi/2$ spin-turner for a spin polarization analysis followed by a count rate detection. The Bloch-sphere description depicts the evolutions of each quantum state in spin and energy subspaces. It includes measurement settings of α and γ , determining the projection operators used for joint measurement of spin and energy. The effect of the DC-flipper on the translation stage is to suppress a change in the total Larmor precession angle, which explained in detail in the main text.

The angle parameters α and γ are the azimuthal angles on the Bloch spheres corresponding to the spin and energy degree of freedom, respectively. They are depicted in Fig. 4.9.

Introducing the observables

$$\hat{A}^{(S)}(\alpha) = \hat{P}_+^{(S)}(\alpha) - \hat{P}_-^{(S)}(\alpha) \quad (4.12)$$

and

$$\hat{B}^{(E)}(\gamma) = \hat{P}_+^{(E)}(\gamma) - \hat{P}_-^{(E)}(\gamma) \quad (4.13)$$

one can define an expectation value for a joint measurement of spin and energy along the directions α and γ

$$E(\alpha, \gamma) = \langle \Psi(t) | \hat{A}^{(S)} \otimes \hat{B}^{(E)} | \Psi(t) \rangle = \cos(\alpha + \gamma). \quad (4.14)$$

The individual probabilities, for measurement direction in the plane of the superposition state, are given by

$$P_{++} = P_{--} = \frac{1}{4}(1 + \cos(\alpha + \gamma)) \quad (4.15)$$

and

$$P_{+-} = P_{-+} = \frac{1}{4}(1 - \cos(\alpha + \gamma)) \quad (4.16)$$

with

$$P_{\text{equal}} = P_{++} + P_{--} = \frac{1}{2}(1 + \cos(\alpha + \gamma)) \quad (4.17)$$

and

$$P_{\text{diff}} = P_{+-} + P_{-+} = \frac{1}{2}(1 - \cos(\alpha + \gamma)). \quad (4.18)$$

Finally the correlation coefficient, which is the quantum-mechanical expectation values for a projective joint measurement along α and β , $E^{S=\frac{1}{2}}(\alpha, \beta)$ is calculated as

$$E(\alpha, \beta) = P_{\text{equal}} - P_{\text{diff}} = \cos(\alpha + \gamma). \quad (4.19)$$

For a Bell-like inequality in CHSH-formalism [Clauser et al., 1969] four expectation values as defined in Eq.(4.14), with the associated directions α_1, α_2 and γ_1, γ_2 for joint measurements of spin and energy, are required which yields

$$S_{CHSH}(\alpha_1, \alpha_2, \gamma_1, \gamma_2) = |E(\alpha_1, \gamma_1) - E(\alpha_2, \gamma_1) + E(\alpha_1, \gamma_2) + E(\alpha_2, \gamma_2)|. \quad (4.20)$$

The boundary of Eq.(4.20) is given by the value 2 for any noncontextual hidden variable theory, whereas QM predicts a maximal value $S_{CHSH}^{\text{MAX}} = 2\sqrt{2}$ for $\alpha_1 = 0$, $\alpha_2 = \pi/2$, $\gamma_1 = \pi/4$ and $\gamma_2 = -\pi/4$.

The experiment was carried out at the tangential beam port of the 250 kW TRIGA research reactor of the Atomic Institute in Vienna. A schematic view of the experimental arrangement is shown in Fig. 4.9.

4.2.2 Measurement procedure

State preparation

A neutron beam of mean wavelength $\lambda = 1.99 \text{ \AA}$, reflected from a pyrolytic graphite monochromator and propagating in the $+\hat{\mathbf{x}}$ -direction, is polarized along the $\hat{\mathbf{z}}$ -direction using a bent Co-Ti supermirror array. The first DC-coil, functioning as a $\pi/2$ spin-turn device about the $+\hat{\mathbf{y}}$ -axis, rotates the spin into the $\hat{\mathbf{x}}$ -direction. Thus a coherent superposition of the two orthogonal spin eigenstates, denoted as $|\uparrow\rangle$ and $|\downarrow\rangle$, referred to the quantization axis along the static magnetic field $\hat{\mathbf{z}}$ -direction, in equal portions is created, yielding an incident state denoted as

$$|\Psi_{\text{inc}}\rangle \xrightarrow{\text{DC}\frac{\pi}{2}} |\Psi_{S_x}\rangle = \frac{1}{\sqrt{2}} \left(|\uparrow\rangle + |\downarrow\rangle \right) \otimes |E_0\rangle. \quad (4.21)$$

Note that in this particular experiment, unlike in the previous Section 4.1, the propagation direction of the neutron beam has been addressed as $+\hat{\mathbf{x}}$ -direction, in order to avoid an additional phase factor $-i$ in the superposed state in Eq.(4.21) compared to Eq.(4.4) from the Section 4.1. The entanglement between the spinor and energy degree of freedom is created exploiting the operation of a subsequent RF-flipper [Sponar et al., 2008b] with an oscillating field $B(t) = B_1^{(\omega)} \cos(\omega t) \cdot \hat{\mathbf{x}}$. Fulfilling the resonance condition ($\omega = 2|\mu|B_0/\hbar$) for the oscillating field and the guide field, the $\hat{\mathbf{z}}$ -component of the total magnetic field can be completely suppressed within the rotating frame of the oscillating field. The effective field, perpendicular to the initial polarization, is adjusted to $B_1^{(\omega)} = \pi\hbar/(2\tau|\mu|)$ initiating a spin-flip process. Here μ is the magnetic moment of the neutron and τ is the time the neutron requires to traverse the RF-field region. Interacting with a time-dependent magnetic field, the total energy of the neutron is no longer conserved due to absorption and emission of photons of energy $\hbar\omega$, depending on the spin state [Summhammer, 1993, Golub et al., 1994]. The RF-flipper is operating at a frequency of $\omega/2\pi = 32 \text{ kHz}$ and accordingly the guide field is tuned to $B_0 \sim 1.1 \text{ mT}$. The entangled state vector can be represented as a Bell state

$$|\Psi_{S_x}\rangle \xrightarrow{\text{RF}\pi} |\Psi_{\text{Bell}}\rangle = \frac{1}{\sqrt{2}} \left(|E_0 + \hbar\omega\rangle \otimes |\uparrow\rangle + |E_0 - \hbar\omega\rangle \otimes |\downarrow\rangle \right), \quad (4.22)$$

which is illustrated using a Bloch sphere description in Fig 4.9.

Projective measurements and count rate detection

The second RF-flipper and an auxiliary DC-flipper are mounted on a (single) translation stage. By choosing the same frequency for the two RF-flippers the energy difference between the two spin components is compensated. The oscillating field of the second RF-flipper is given by $B(t) = B_1^{(\omega)} \cos(\omega t + \phi_\omega) \cdot \hat{\mathbf{x}}$. This procedure is described by the action of the projection operator for the energy recombination $\hat{P}^{(E)} = |E_0\rangle(\langle E_0 + \hbar\omega| + \langle E_0 - \hbar\omega|)$. Applied to Eq.(4.22), and considering the second RF-flipper (energy recombination) and the DC-flipper, this operator yields the final state

$$|\Psi_{\text{Bell}}\rangle \xrightarrow{\text{RF}\pi(\phi_\omega)} |\Psi_{\text{fin}}\rangle = \frac{1}{\sqrt{2}} \left(e^{-i\phi_\omega} |\uparrow\rangle + e^{i\omega T} e^{i\phi_\omega} |\downarrow\rangle \right) \otimes |E_0\rangle. \quad (4.23)$$

Here $\omega T = \gamma$ is the phase acquired in energy subspace, where T is the propagation time for the distance $L + \Delta L$ between the two RF-flippers and ϕ_ω is the tunable phase of the oscillating field of the second RF-flipper.

The stationary guide field $B_0 \cdot \hat{\mathbf{z}}$ induces an additional phase due to Larmor precession within the guide field region. However this phase contribution remains constant during the experiment and can therefore be adjusted by finding the zero-position of γ scans (displacement of translation stage). The corresponding polarization vector is given by

$$\vec{p}_{\text{fin}} = \left(\cos(\gamma + \alpha), \sin(\gamma + \alpha), 0 \right), \quad (4.24)$$

with the spin phase $\alpha = 2\phi_\omega$, originating from the phase of the oscillating field of the second RF-flipper (a detailed description of the spin phase acquired due to a spinor evolutions from the north to the south pole of the Bloch sphere, and back, is given in [Wagh et al., 2000]). The phases α and γ are associated with the measurement directions on the equatorial plane of the Bloch spheres, required for joint measurements of spin and energy.

Compensation of the Larmor phase is accomplished by the auxiliary DC-flipper placed subsequently to the second RF-flipper. No additional phase shift, induced by Larmor precession, resulting from the change of ΔL is observed. Phase contributions with the same sign occur in the regions $L + \Delta L$ (between first and second RF-flippers) and $L' - \Delta L$ (between DC-flipper and second DC- $\pi/2$ spin-turner) compensating each other. Therefore the total Larmor rotation angle ($\propto \omega_L(L + L')$) remains constant although the position

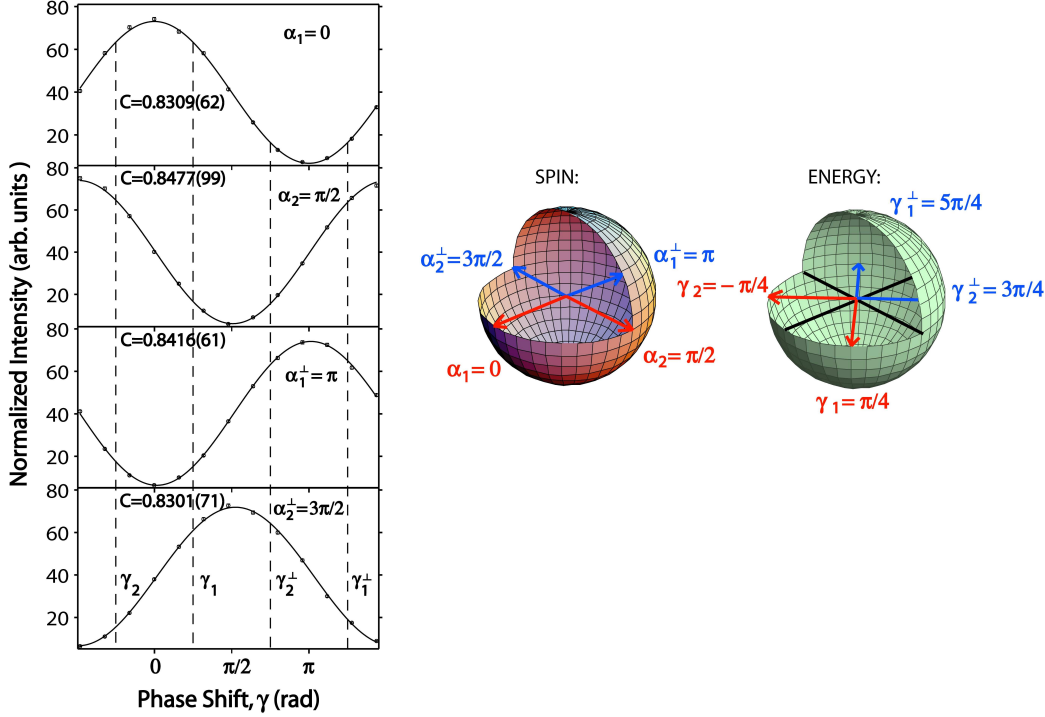


Figure 4.10: Typical interference oscillations, due to a variation of γ , for $\alpha_1 = 0$, $\alpha_2 = \pi/2$, ($\alpha_1^\perp = \pi$, $\alpha_2^\perp = 3\pi/2$), together with Bloch sphere description of the measurement direction for spin and energy. One period corresponds to a displacement of $31.28(6)$ mm of the translation stage. The dashed lines mark the γ values of $\gamma_1 = \pi/4$, $\gamma_2 = -\pi/4$ ($\gamma_1^\perp = 5\pi/4$, $\gamma_2^\perp = 3\pi/4$), where a maximum violation of the Bell-like CHSH inequality is expected. The joint measurements of expectation values exhibit $S_{CHSH} = 2.333 \pm 0.002$.

of the translator is altered. Consequently only γ , the phase of the energy subspace, is affected by a displacement of the translation stage.

The second DC- $\pi/2$ spin-turner reverses the action of the first one by a $-\pi/2$ spin-rotation around the $+\hat{y}$ axis for a forthcoming polarization analysis along the $+\hat{z}$ direction by the second supermirror. This is expressed by applying a projection operator for the spin $\hat{P}^{(S)} = |\uparrow\rangle\langle\uparrow|$. Finally the stationary intensity oscillations are given by

$$N(\alpha, \gamma) = \frac{1}{2} \left(1 + C \cos(\alpha + \gamma) \right), \quad (4.25)$$

where C is the contrast, which is 100% ($C=1$) under ideal circumstances. Here C was experimentally determined as $83.8 \pm 0.4\%$, which is depicted in Fig 4.10. The physical

reasons for the loss in contrast are explained later. Thus the expectation value, defined in Eq.(4.14), can be rewritten using the normalized count rates obtained with the measurement settings of α and γ denoted as

$$E(\alpha, \gamma) = \frac{N(\alpha, \gamma) + N(\alpha^\perp, \gamma^\perp) - N(\alpha, \gamma^\perp) - N(\alpha^\perp, \gamma)}{N(\alpha, \gamma) + N(\alpha^\perp, \gamma^\perp) + N(\alpha, \gamma^\perp) + N(\alpha^\perp, \gamma)}, \quad (4.26)$$

with $\alpha^\perp = \alpha + \pi$ and $\gamma^\perp = \gamma + \pi$. Therefore, from the contrast $C=0.838$ a value of $2.37(0.838 \cdot 2\sqrt{2} \sim 2.37)$ is expected for S_{CHSH} for $\alpha_1 = 0$, $\alpha_2 = \pi/2$, $\gamma_1 = \pi/4$ and $\gamma_2 = -\pi/4$.

Typical oscillations, observed when the position of the translation stage (second RF-flipper) is varied (γ -scans), are plotted in Fig 4.10 for different settings of α . One period corresponds to a displacement of the translator stage of 31.28 ± 0.06 mm. The γ -scan for $\alpha_1 = 0$ was used to determine the position of the translation stage corresponding to the values $\gamma_1 = \pi/4, \gamma_2 = -\pi/4$ ($\gamma_1^\perp = 5\pi/4, \gamma_2^\perp = 3\pi/4$) which are, together with the spin phase settings $\alpha_1 = 0, \alpha_2 = \pi/2$ ($\alpha_1^\perp = \pi, \alpha_2^\perp = 3\pi/2$), required for determining the S -value for a maximal violation of the Bell-like CHSH inequality.

Experimental results

The actual Bell measurement consists of successive count rate measurements using appropriate settings of the phase of the oscillating field of the second RF-flipper (tuning the spin phase α) and position of the second RF-flipper mounted on the translation stage (tuning the energy phase γ). The four expectation values $E(\alpha_i, \gamma_j)$ ($i, j = 1, 2$), for joint measurement of spin and energy degree of freedom, are determined from the associated count rates, using Eq.(4.26). They are listed in Tab. 4.1 After three complete measurement sets (to reduce statistical errors) a final value $S_{\text{CHSH}}=2.333 \pm 0.002$ was determined which is notably above the value of 2, predicted by noncontextual hidden variable theories and close to 2.37, a value derived by taking a contrast of 83.8% of the interferograms into account.

A slight deviation of the measured S_{CHSH} value of 2.333 ± 0.002 from the expected value of 2.37 can be explained by inhomogeneities of the guide field B_0 , which results in fluctuations of the energy phase γ , as well as imperfections of the spin phase manipulation. (Varying the phase ϕ_ω of the oscillating field of the second RF-flipper e.g. by $\pi/4$ should

Table 4.1: Results of the spin-energy correlation measurements.

| $\alpha_i (\alpha_i^\perp)$ | $\gamma_j (\gamma_j^\perp)$ | $E(\alpha_i, \gamma_j)$ | $(i, j = 1, 2)$ |
|-------------------------------------|------------------------------|--|-----------------|
| $\alpha_1 = 0 (\pi)$ | $\gamma_1 = \pi/4 (5\pi/4)$ | $E(\alpha_1, \gamma_1) = 0.594 \pm 0.001$ | |
| $\alpha_2 = \pi/2 (3\pi/2)$ | $\gamma_1 = \pi/4 (5\pi/4)$ | $E(\alpha_2, \gamma_1) = 0.575 \pm 0.001$ | |
| $\alpha_1 = 0 (\pi)$ | $\gamma_2 = -\pi/4 (3\pi/4)$ | $E(\alpha_1, \gamma_2) = -0.571 \pm 0.001$ | |
| $\alpha_2 = \pi/2 (3\pi/2)$ | $\gamma_2 = -\pi/4 (3\pi/4)$ | $E(\alpha_2, \gamma_2) = 0.593 \pm 0.001$ | |
| $S_{\text{CHSH}} = 2.333 \pm 0.002$ | | | |

theoretically yield a phase shift of the intensity modulations of $\pi/2$, as predicted by Eq.(4.40), whereas in practice we measured additional shifts around one and two degrees from the desired settings.) Due to the deviation of the measured S_{CHSH} value from the predicted value it is useful to introduce an error estimation of the calculated value of 2.37, which consists of three parts: The error of the contrast measurement ($83.8 \pm 0.4\%$), inhomogeneities of the guide field B_0 , and imperfections of the spin phase manipulation. These contributions lead to a final error of the calculated value estimated by ~ 0.036 . This error (2.37 ± 0.036) is one magnitude larger compared to the error of the Bell measurement (2.333 ± 0.002). The former reflects all systematic imperfections of the setup, whereas the latter is solely a statistic error derived from the count rates, which are very high (up to 32000 cnts per point) due to a long measurement time.

In the experiment neutrons are detected by a BF_3 detector with an inherent efficiency of $>99\%$, which is larger than the well known threshold efficiency $\eta_{\text{crit}} = 2(\sqrt{2} - 1) \sim 0.83$ required to close the detection loophole with maximally entangled states [Garg and Mermin, 1987, Larsson, 1998].

The average contrast of $C = 83.8\%$, of the observed intensity oscillations, exceeds the minimum visibility $C_{\text{crit}} = 70.7\% (\sqrt{2}/2)$ necessary to exhibit a violation of the CHSH inequality. The maximal S -value that can be achieved experimentally is proportional to the contrast and in our case given by $C \cdot S_{\text{CHSH}}^{\text{MAX}} = 2.37 > 2$ since $C > C_{\text{crit}}$.

The main reason for the rather low contrast with respect to the high flip efficiencies of the DC and RF-flippers is a broad momentum distribution of $\sim 2\%$ (known from multiple time-of-flight measurements) induced by the mosaic structure of our monochromator

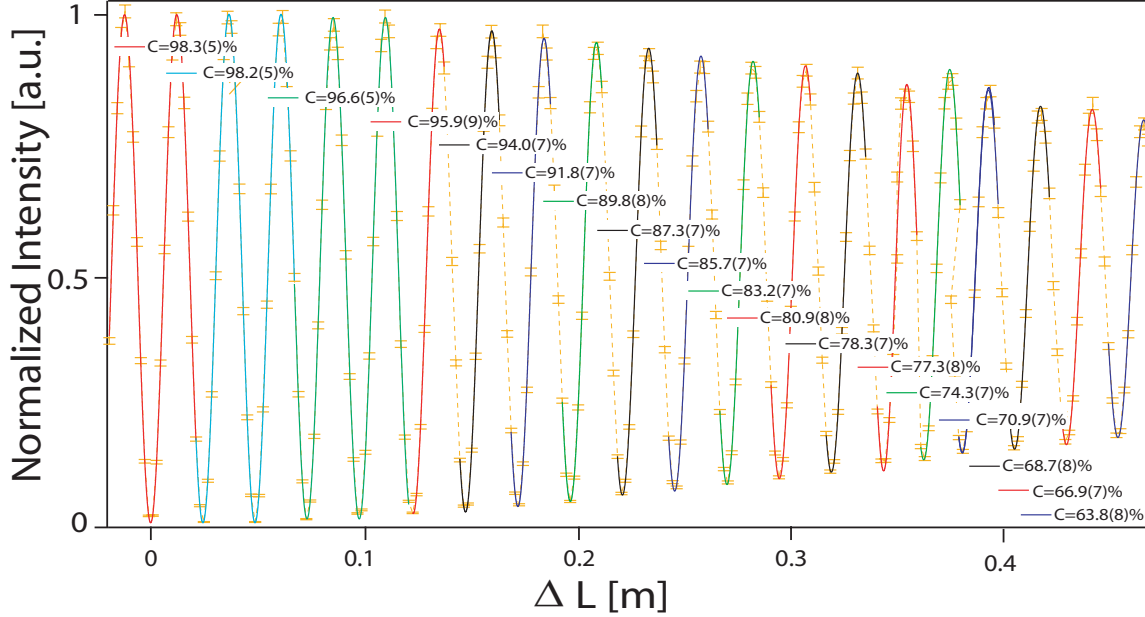


Figure 4.11: Contrast measurement using an arrangement consisting of two DC- $\pi/2$ spin-rotators and DC flipper on a translation stage in between.

crystal. This corresponds to a broad distribution of the propagation-time, and therefore the distribution of the spin-rotation angle (in the $\hat{\mathbf{x}}\hat{\mathbf{y}}$ -plane) is widened after each full rotation of the polarization vector, which results a noticeable decrease in contrast. This effect has been investigated in an additional experiment, where a DC-flipper was placed between two DC- $\pi/2$ spin-rotators, similar to a spin echo setup. In a symmetric configuration, where the DC-flipper is placed exactly at half the distance between the two DC- $\pi/2$ spin-rotators ($\Delta L = 0$), a maximum contrast of more than 98 per cent is achieved, which is plotted in Fig 4.11. When the DC-flipper is displaced (ΔL increased) the contrast decreases as expected.

To summarize, in this Section violation of a Bell-like CHSH inequality in the field of neutron polarimetry has been demonstrated. The measured correlations between the neutron's spinor and energy degree of freedom contribute to a result $S_{\text{CHSH}} = 2.333 \pm 0.002$, which exceeds the Bell limit, demarcating noncontextual hidden variable theories, by more than 166 standard deviations, which has been reported in [Sponar et al., 2010b].

4.3 GHZ-States in Neutron Polarimetry

In this Section a triply entangled Greenberger-Horne-Zeilinger(GHZ)-like state, prepared in a neutron polarimetric experiment, is analyzed. Entanglement is achieved different between the spin, total energy and momentum degree of freedom. The proposed inequality, derived by Mermin, yields a value $M = 3.936(2) \not\leq 2$, which exhibits a clear violation of the classical limit. The result verifies the predictions of quantum mechanics which are at variance with noncontextual hidden variable theories.

4.3.1 Theoretical Background

In this experiment three degrees of freedom, namely total-energy, momentum and spin, are used and manipulated separately. Note that these degrees of freedom are independent degrees of freedom.

Spin-momentum entanglement

As already seen from Eq.(2.47) in Section 2.1.2 the solutions of the Schrödinger equation for neutrons propagating in $+x$ -direction, with in magnetic potential induced by a static magnetic pointing in $+z$ -direction is given by

$$\psi = a|\uparrow\rangle + b|\downarrow\rangle = f_+(x, t) \cos \frac{\vartheta}{2} |\uparrow\rangle + f_-(y, t) e^{i\beta} \sin \frac{\vartheta}{2} |\downarrow\rangle \quad (4.27)$$

where

$$f_{\pm}(x, t)_{\pm} = \int a_{\pm}(k \mp \Delta k) e^{i((k \mp \Delta k) \cdot x - \omega(k)t)}, \quad (4.28)$$

describes the wave packets of the up and down spin components. The azimuthal angle β , being the relative phase between $|\uparrow\rangle$ and $|\downarrow\rangle$ equals $2x\Delta k$. From this one can conclude that it is only in momentum-space where the relative phase shifts between $|\uparrow\rangle$ and $|\downarrow\rangle$, from the static accelerator field are induced. The neutron state vector evolves within a Hilbert space that is formed by two subspaces: Spin space and momentum or k -space. This product space is denoted as $\mathcal{H} = \mathcal{H}_S \otimes \mathcal{H}_k$. Consequently another two-level system consisting of accelerated and decelerated part with the basis states $|k_+\rangle$ and $|k_-\rangle$ occurs with representation given by

$$|\Psi_{\text{Bell}'}\rangle = \frac{1}{\sqrt{2}} \left(|k_-\rangle \otimes |\uparrow\rangle + |k_+\rangle \otimes |\downarrow\rangle \right), \quad (4.29)$$

where $|k_{\pm}\rangle$ is the eigenvector of the momentum operator $\hat{P}_{\pm} = \hbar\hat{k}_{\pm}$ with

$$\hat{k}_{\pm}|k_{\pm}\rangle = k_{\pm}|k_{\pm}\rangle. \quad (4.30)$$

Mermin-like inequality

Since a contradiction between quantum mechanics and local hidden variable theory for the GHZ state is found only found for perfect situations (which cannot be realized experimentally), an inequality is used to demonstrate the peculiarities of the GHZ state. Mermin analyzed the GHZ argument in detail and derived an inequality pertinent for an experimental test of local hidden variable theories [Mermin, 1990]. Since our GHZ-like state consists of an entanglement between degrees of freedom in a single-neutron system we test noncontextual hidden variable theories using a sum of four expectation values defined as

$$M = E(\sigma_x^{(S)}\sigma_x^{(k)}\sigma_x^{(E)}) - E(\sigma_x^{(S)}\sigma_y^{(k)}\sigma_y^{(E)}) - E(\sigma_y^{(S)}\sigma_x^{(k)}\sigma_y^{(E)}) - E(\sigma_y^{(S)}\sigma_y^{(k)}\sigma_x^{(E)}), \quad (4.31)$$

where $\sigma_{x,y}^{(i)}$ are the Pauli operators in spin, total energy and momentum subspace. The value of M is bounded by 2 for any noncontextual hidden variable theory, whereas quantum mechanics predicts an upper limit of 4 for a GHZ state. The Pauli operators used in Eq.(4.31) can be decomposed as

$$\begin{aligned} \sigma_x^{(i)} &= \hat{P}^{(i)}(0) - \hat{P}^{(i)}(\pi) \\ \sigma_y^{(i)} &= \hat{P}^{(i)}\left(\frac{\pi}{2}\right) - \hat{P}^{(i)}\left(\frac{3\pi}{2}\right), \end{aligned} \quad (4.32)$$

with $\hat{P}(\alpha)^{(S)}$, $\hat{P}(\beta)^{(k)}$ and $\hat{P}(\gamma)^{(E)}$ being the projection operators onto an up down superposition on the equatorial plane in spin, momentum and energy subspace. The azimuthal angle is given by an angle parameter α , β and γ , respectively. The operators are defined as

$$\begin{aligned} \hat{P}^{(S)}(\alpha) &= \frac{1}{\sqrt{2}}(|\uparrow\rangle + e^{-i\alpha}|\downarrow\rangle)(\langle\uparrow| + e^{i\alpha}\langle\downarrow|) \\ \hat{P}^{(k)}(\beta) &= \frac{1}{\sqrt{2}}(|k_+\rangle + e^{-i\beta}|k_-\rangle)(\langle k_+| + e^{i\beta}\langle k_-|) \\ \hat{P}^{(E)}(\gamma) &= \frac{1}{\sqrt{2}}(|E_0\rangle + e^{-i\gamma}|E_-\rangle)(\langle E_0| + e^{i\gamma}\langle E_-|), \end{aligned} \quad (4.33)$$

where α , β and γ are the azimuthal angles on the Bloch spheres depicted, having only the values 0 and π or $\pi/2$ and $3\pi/2$, since only σ_x and σ_y occur in Eq.(4.31) (see Fig. 4.12). Each expectation Value $E(\sigma_x^{(S)}\sigma_{x,y}^{(k)}\sigma_{x,y}^{(E)})$ is experimentally determined by a combination of normalized count rates, using appropriate setting of α , β and γ : for instance

$$\begin{aligned} E(\sigma_x^{(S)}\sigma_y^{(k)}\sigma_y^{(E)}) &= E(\alpha : (0; \pi), \beta : (\frac{\pi}{2}; \frac{3\pi}{2}), \gamma : (\frac{\pi}{2}; \frac{3\pi}{2})) \\ &= \langle \Psi_{\text{GHZ}} | (\hat{P}(0)^{(S)} - \hat{P}(\pi)^{(S)}) \otimes (\hat{P}(\frac{\pi}{2})^{(k)} - \hat{P}(\frac{3\pi}{2})^{(k)}) \otimes (\hat{P}(\frac{\pi}{2})^{(E)} - \hat{P}(\frac{3\pi}{2})^{(E)}) | \Psi_{\text{GHZ}} \rangle = \frac{A}{B} \end{aligned} \quad (4.34)$$

with

$$\begin{aligned} A &= \left(N(0, \frac{\pi}{2}, \frac{\pi}{2}) - N(\pi, \frac{\pi}{2}, \frac{\pi}{2}) - N(0, \frac{\pi}{2}, \frac{3\pi}{2}) + N(\pi, \frac{\pi}{2}, \frac{3\pi}{2}) \right. \\ &\quad \left. - (N(0, \frac{3\pi}{2}, \frac{\pi}{2}) - N(\pi, \frac{3\pi}{2}, \frac{\pi}{2}) + N(0, \frac{3\pi}{2}, \frac{3\pi}{2}) + N(\pi, \frac{3\pi}{2}, \frac{3\pi}{2})) \right) \end{aligned} \quad (4.35)$$

and

$$\begin{aligned} B &= \left(N(0, \frac{\pi}{2}, \frac{\pi}{2}) + N(\pi, \frac{\pi}{2}, \frac{\pi}{2}) + N(0, \frac{\pi}{2}, \frac{3\pi}{2}) + N(\pi, \frac{\pi}{2}, \frac{3\pi}{2}) \right. \\ &\quad \left. + N(0, \frac{3\pi}{2}, \frac{\pi}{2}) - N(\pi, \frac{3\pi}{2}, \frac{\pi}{2}) + N(0, \frac{3\pi}{2}, \frac{3\pi}{2}) + N(\pi, \frac{3\pi}{2}, \frac{3\pi}{2}) \right), \end{aligned} \quad (4.36)$$

where for example $N(0, \pi/2, \pi/2)$ is the count rate for spin phase $\alpha = 0$, momentum phase $\beta = \pi/2$ and total energy phase $\gamma = \pi/2$.

4.3.2 Polarimetric experiment

Renewed polarimetric setup

First it should be emphasized, that this experiment was carried out on a renewed optical bench, but with the same wavelength of $\sim 2 \text{ \AA}$, as the previous experiments. During this reconstruction at the tangential beam port of the 250 kW TRIGA research reactor of the Atomic Institute in Vienna, the polarizing supermirrors have been removed from the shielding and mounted outside, to be accessible for the experimentalists. Furthermore, a third beam line, together with the rearranged depol-beam line, has been installed opposite the actual beam line. A detail description of the reconstruction process, now allowing for

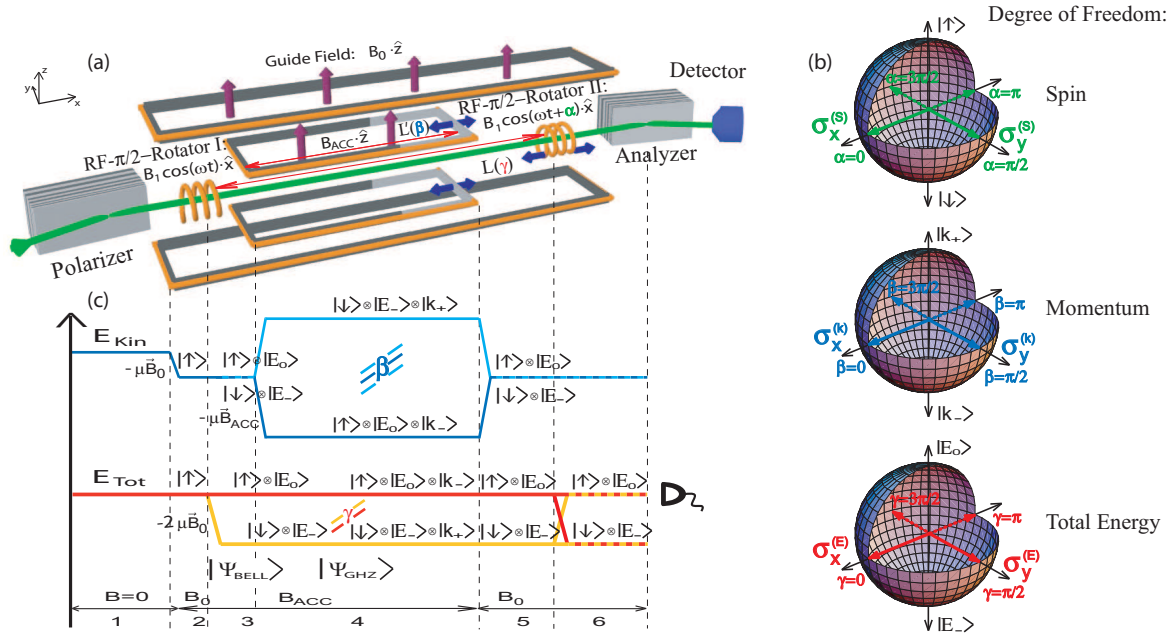


Figure 4.12: (a) Experimental apparatus for observation of stronger-than-classic correlation between the spinor, momentum and energy degree of freedom. (b) Bloch-sphere description includes measurement settings of α , β and γ , determining the projection operators, used for joint measurement. The incident neutron beam is polarized by a supermirror polarizer. (c) Energy level diagram for momentum and total energy. A $\pi/2$ -RF spin-turner creates the spin energy entanglement followed by accelerator coil in Helmholtz configuration, preparing the GHZ-like state consisting of an entanglement between spin, energy and momentum degree of freedom.

much higher contrast (up to $\sim 98.5\%$), can be found in [Schmitzer, 2009]. Results of the first experiment carried out on this beam line, i.e. test of an alternative model for non-local correlations, demonstrated to be incompatible with quantum predictions, are summarized in [Hasegawa et al., 2011].

State preparation

In the present experiment the spin-energy entanglement is achieved by a single RF- $\pi/2$ spin-rotator. Interacting with a time-dependent magnetic field, denoted as $B(t) =$

$B_1^{(\omega_{\text{rf}})} \cos(\omega t) \cdot \hat{\mathbf{x}}$ the total energy of the neutron is no longer conserved. Photons of energy $\hbar\omega_{\text{rf}}$ are emitted or absorbed depending on the spin state [Summhammer, 1993]. The RF-flipper is operating at a frequency of $\omega_{\text{rf}}/2\pi = 40$ kHz and accordingly the guide field is tuned to $B_0 \cdot \hat{\mathbf{z}} \sim 1,3$ mT. A schematic view of the experimental arrangement is shown in Fig.4.12 (a). The effective field, perpendicular to the initial polarization, is adjusted such that it induces a spin flip with a probability of $1/2$ ($B_1^{(\omega_{\text{rf}})} = \pi\hbar/(2\tau|\mu|)$, with μ as magnetic moment and τ as propagation time in RF-field region). Therefore only the flipped spin component is affected by the energy manipulation yielding an entangled state vector, which can be represented as a Bell state

$$|\Psi_{\text{Bell}}\rangle = \frac{1}{\sqrt{2}} \left(|E_0\rangle \otimes |\uparrow\rangle + |E_-\rangle \otimes |\downarrow\rangle \right), \quad (4.37)$$

where $|\uparrow\rangle$ and $|\downarrow\rangle$ denote the neutron's up and down spin eigenstates, referring to the chosen quantization axis, induced by the uniform guide field $B_0 \cdot \hat{\mathbf{z}}$, and $E_- = E_0 - \hbar\omega_{\text{rf}}$. Here E_0 and E_- are considered to be a two-state system, which will be described, without loss of generality, as a two-level system with its associated Hilbert Space \mathcal{H}_E as already demonstrated in Section 4.2. The entire bipartite Hilbert space is given as a product space consisting of the space for total energy and the space for the spin, denoted as $\mathcal{H} = \mathcal{H}_S \otimes \mathcal{H}_E$.

Together with the time dependent interaction within the first RF-coil and the static magnetic pointing in $+z$ -direction, denoted as B_{acc} , the total system $\mathcal{H} = \mathcal{H}_S \otimes \mathcal{H}_E \otimes \mathcal{H}_k$ can be described by a GHZ-like state given by

$$|\Psi_{\text{GHZ}}\rangle = \frac{1}{\sqrt{2}} \left(|\uparrow\rangle \otimes |k_-\rangle \otimes |E_0\rangle + |\downarrow\rangle \otimes |k_+\rangle \otimes |E_0\rangle \right). \quad (4.38)$$

4.3.3 Experimental results

The experiment was carried out at the renewed 2 Å beam line at the tangential beam port of the 250 kW TRIGA research reactor of the renewed Atomic Institute of the Austrian Universities, Vienna. A neutron beam incident from a pyrolytic graphite monochromator, is polarized along the $\hat{\mathbf{z}}$ -direction by reflection from a bent Co-Ti supermirror array. In our experiment the measurement apparatus consists of the second RF-spin-rotator, the accelerator Field B_{acc} both in combination with the Co-Ti supermirror.

Spin phase

The spin-phase measurement direction α is turned the phase of the oscillating field within the second RF spin-rotator denoted as $B_1^{(\omega_{\text{rf}})} \cos(\omega_{\text{rf}}t + \alpha) \cdot \hat{\mathbf{x}}$, being the physical action of the projection operator Eq.(4.33). As all spin states to be analyzed lie in the $\hat{\mathbf{x}}\hat{\mathbf{y}}$ -plane again a $\pi/2$ spinor-rotation is performed ($B_1 = \pi\hbar/(2\tau|\mu|)$). Typical intensity modulations when scanning α are depicted in Fig4.13, where an average contrast of 0.9844(9) was achieved.

Momentum phase

The measurement direction of the momentum phase is tuned by the propagation time within the accelerator coil. The acquired phase in momentum space is given by $\beta = \int B_{\text{acc}} ds$. However in practice the strength of the magnetic field was varied, instead of the length, due to experimental convenience. However, both approaches lead to the same phase contributions. The accelerator coil, just like the uniform guide field, is realized in Helmholtz configuration, for higher field homogeneity and an accurate alignment of accelerator and guide field.

Energy phase

The measurement direction of the energy phase is tuned by the position of the second RF- $\pi/2$ spin-rotator, mounted on a motorized translation stage, thereby varying the distance between the two RF- $\pi/2$ spin-rotators. Unlike in our previous experiment [Sponar et al., 2010b] this requirement is not provided inherently by the setup and therefore the Larmor precession angle has to be compensated. Thus, a change of the position of RF2 by ΔL , induces an undesired additional relative phase between the two spin eigenstates, due to Larmor precession within the guide field, denoted as $\delta = \omega_L \Delta L/v$. Here ω_L is the Larmor frequency and v the velocity of the neutrons $\sim 2000\text{m/s}$. So to retrieve a pure tuning of the energy phase γ this additional Larmor phase contribution has to be compensated. This is done by appropriately tuning the phase of the oscillating magnetic field in RF1, yielding an reversed spin phase shift of $-\delta$. As this compensation depends on the relative position (ΔL) of RF2, the associated Larmor precession angle has to be determined in an individual measurement using two DC- instead of RF- $\pi/2$ spin rotators.

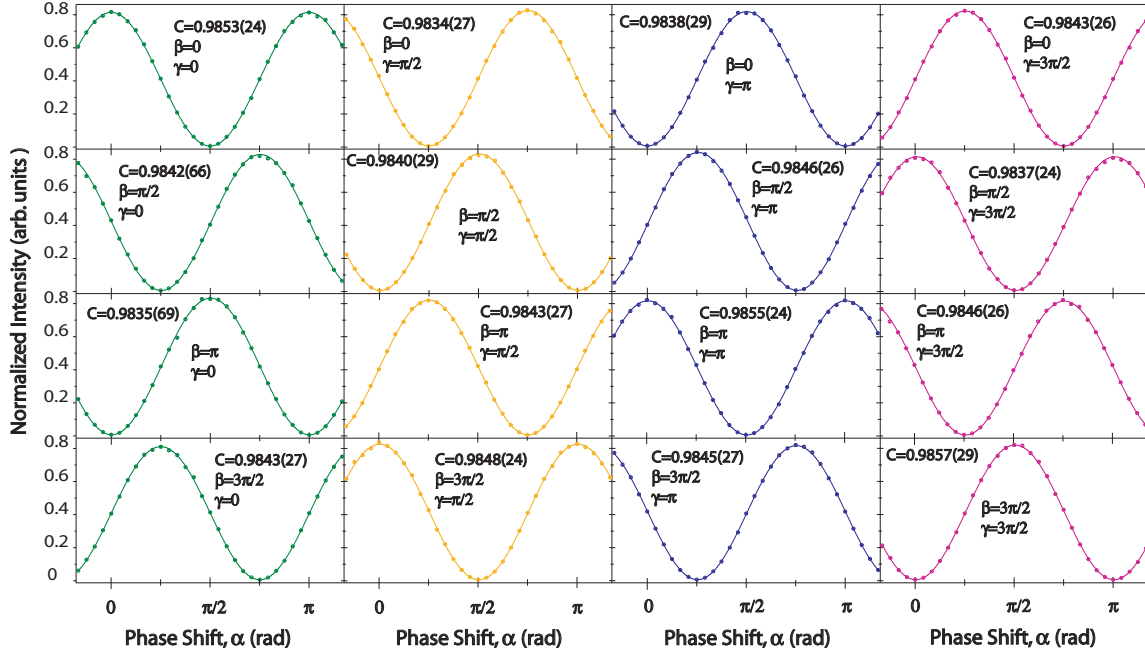


Figure 4.13: Typical intensity oscillation when varying the spin phase α for different setting of the momentum phase β and energy phase γ .

By shifting the position of DC2 (ΔL) pure Larmor precession is observed, from which the Larmor precession angle, in terms of ΔL , is determined.

If the resonance condition would be exactly $\omega_{\text{rf}} = \omega_L$, Larmor- and energy-phase, for spin- and energy-subspace respectively, would make phase contributions for the state, of the same amount but opposite directions. Thus, when varying L there should be no intensity modulation. In practice this does not hold, due to the so called Bloch-Siegert shift [Bloch and Siegert, 1940] which originates from the second rotating field, when an oscillating field is decomposed in two counter rotating fields. A static field $B_0 \cdot \hat{\mathbf{z}}$ and a perpendicular oscillating field $B^{(1)} = B_{\text{rf}}^{(\omega)} \cos(\omega t + \alpha) \cdot \hat{\mathbf{x}}$ with amplitude

$$B_{\text{rf}}^{(\omega)} = \frac{\pi \hbar}{2\tau |\mu|} \quad \text{and} \quad \omega = \frac{2|\mu|B_0}{\hbar} \left(1 + \frac{B_1^2}{16B_0^2}\right), \quad (4.39)$$

The second DC $\pi/2$ spin-turner converts the $\hat{\mathbf{x}}$ -component of the polarization back to the $\hat{\mathbf{z}}$ -direction to be analyzed by the second supermirror. This is expressed by applying a projection operator for the spin $\hat{P}^{(S)} = |\uparrow\rangle\langle\uparrow|$. Finally the stationary intensity

Table 4.2: Experimentally determined expectation values and the resulting M value.

| Observable | Settings | | | Determined Values |
|--|-------------------|-------------------|-------------------|----------------------|
| | α | β | γ | |
| $\sigma_x^{(S)} \sigma_x^{(k)} \sigma_x^{(E)}$ | $(0; \pi)$ | $(0; \pi)$ | $(0; \pi)$ | 0.9843(10) |
| $\sigma_x^{(S)} \sigma_y^{(k)} \sigma_y^{(E)}$ | $(0; \pi)$ | $(\pi/2; 3\pi/2)$ | $(\pi/2; 3\pi/2)$ | 0.9839(10) |
| $\sigma_y^{(S)} \sigma_x^{(k)} \sigma_y^{(E)}$ | $(\pi/2; 3\pi/2)$ | $(0; \pi)$ | $(\pi/2; 3\pi/2)$ | 0.9840(10) |
| $\sigma_y^{(S)} \sigma_y^{(k)} \sigma_x^{(E)}$ | $(\pi/2; 3\pi/2)$ | $(\pi/2; 3\pi/2)$ | $(0; \pi)$ | 0.9837(11) |
| $M=3.936(2)$ | | | | |

oscillations are given by

$$N(\alpha, \beta, \gamma) = \cos^2(\alpha + \beta + \gamma) = \frac{1}{2}(1 + C \cos(2(\alpha + \beta + \gamma))), \quad (4.40)$$

with C being the contrast, experimentally determined as 0.9844(9).

By tuning the momentum phase β and the energy phase γ at $0, \pi/2, \pi$ and $3\pi/2$, sixteen spin phase α scans were carried out for a determination of M , according to Eq.(4.31), yielding a final value $M = 3.936(2)$. The individual results for each expectation value are summarized in Tab. 4.2.

In conclusion, the obtained violation of a Mermin-like inequality for a triply entangled GHZ-like state in a single-neutron system clearly confirm the prediction of quantum mechanics in explicit terms, seen in the final value $M = 3.936(2) \gg 2$. The deviation of less than 2 per cent from the theoretical value $M_{\text{th}} = 4$ is worth noting here.

5

Conclusion and Outlook

Multi-entanglement has been studied in perfect Si-crystal interferometer experiments as well as polarimetric measurements. Entanglement of various degrees of freedom has been prepared and analyzed in detail.

In Section 3.2 a technique of coherent energy manipulation in neutron interferometry has been presented. By utilizing the interferometer in combination with two RF fields time-independent interference patterns have been observed.

After successful preparation and manipulation of a triply entangled GHZ-like state (i.e. entanglement of spin, path and energy degree of freedom), presented in Section 3.3, further investigation in the field of multi-entanglement in neutron interferometry are anticipated. In a next step preparation of a W-state, which requires three RF-flippers inside a neutron interferometer operating at different frequencies, is expected. In addition, generation of these typical triply entangled (pure) states will allow further mixture of these states. For instance measurements of gradual translation from the GHZ-state to the W-state are of special interest. At the second stage, neutron interferometer measurements will be carried out in order to determine and distinguish a variety of entangled states, by means of state tomography or entanglement witness [Bertlmann et al., 2008].

In Section 3.4 a technique to balance the influence of the geometric phase generated by one subspace of the system, considering a Bell-like inequality, has been presented. This

is achieved by an appropriate adjustment of the polar Bell angles or one azimuthal angle, determined by a laborious measurement procedure.

Concerning neutron polarimetry, in addition to the experiments with spin-energy entangled states, induced by RF-flippers (see Section 4.2 for violation of a Bell-like inequality and Section 4.3 for GHZ-like states), multi-energy splitting, using *Ramsey's resonance method of separated oscillating fields*, will be topic of a forthcoming experiment. Here a polarized neutron beam passes through N successive RF coils, each having a spin flip probability p less than 1 (i.e. $p = 1/2$). Applying this scheme, the number of energy levels is doubled after each flipper, finally yielding 2^N states. Multi-energy splitting is expected to be of great interest both from theoretical and experimental points of view. A numerical simulation of the described scheme can be found in [Grigoriev et al., 2003].

Another polarimetric experiment planned in near future, addresses the effect of *pre- and post-selected ensemble*, which is subject of the concept of *weak measurements* [Aharonov et al., 1988]. A weak measurement is an imperfect measurement with finite precision. The non-disturbing character of these measurements is based on the trade-off relation between precision and disturbance. Due to the high efficiency of spin manipulation neutron polarimetry is an ideal candidate for *weak measurements*.

Bibliography

- [Aharonov and Anandan, 1987] Y. Aharonov and J. Anandan, *Phase change during a cyclic quantum evolution*, Phys. Rev. Lett. **58**, 1593 (1987).
- [Aharonov et al., 1988] Y. Aharonov, D. Z. Albert, and L. Vaidman, *How the result of a measurement of a component of the spin of a spin-1/2 particle can turn out to be 100*, Phys. Rev. Lett. **60**, 1351 (1988).
- [Alefeld et al., 1981] B. Alefeld, G. Badurek, and H. Rauch, *Observation of the neutron magnetic resonance energy shift*, Z. Phys. B **41**, 231 (1981).
- [Allman et al., 1997] B. E. Allman, H. Kaiser, S. A. Werner, A. G. Wagh, V. C. Rakhecha, and J. Summhammer, *Observation of geometric and dynamical phases by neutron interferometry*, Phys. Rev. A **56**, 4420 (1997).
- [Arndt et al., 1999] M. Arndt, O. Nairz, J. Vos-Andreae, C. Keller, G. van der Zouw, and A. Zeilinger, *Wave-particle duality of C60 molecules*, Nature (London) **401**, 680 (1999).
- [Aspect, 1999] A. Aspect, *Bell's inequality test: more ideal than ever*, Nature (London) **398**, 189 (1999).
- [Aspect et al., 1981] A. Aspect, P. Grangier, and G. Roger, *Experimental tests of realistic local theories via Bell's theorem*, Phys. Rev. Lett. **47**, 460 (1981).
- [Aspect et al., 1982a] A. Aspect, J. Dalibard, and G. Roger, *Experimental test of Bell's inequalities using time-varying analyzers*, Phys. Rev. Lett. **49**, 1804 (1982).

- [Aspect et al., 1982b] A. Aspect, P. Grangier, and G. Roger, *Experimental realization of Einstein-Podolsky-Rosen-Bohm gedankenexperiment: A new violation of Bell's inequalities*, Phys. Rev. Lett. **49**, 91 (1982).
- [Badurek et al., 1983] G. Badurek, H. Rauch, and J. Summhammer, *Time-dependent superposition of spinors*, Phys. Rev. Lett. **51**, 1015 (1983).
- [Badurek et al., 1986] G. Badurek, H. Rauch, and D. Tuppinger, *Neutron interferometric double-resonance experiment*, Phys. Rev. A **34**, 2600 (1986).
- [Badurek et al., 2000] G. Badurek, R. J. Buchelt, G. Kroupa, M. Baron, and M. Villa, *Permanent magnetic field-prism polarizer for perfect crystal neutron interferometers*, Physica B **283**, 389 (2000).
- [Bartosik et al., 2009] H. Bartosik, J. Klepp, C. Schmitzer, S. Sponar, A. Cabello, H. Rauch, and Y. Hasegawa, *Experimental test of quantum contextuality in neutron interferometry*, Phys. Rev. Lett. **103**, 040403 (2009).
- [Basu et al., 2001] S. Basu, S. Bandyopadhyay, G. Kar, and D. Home, *Bell's inequality for a single spin-1/2 particle and quantum contextuality*, Phys. Lett. A **279**, 281 (2001).
- [Bell, 1964] J. S. Bell, *On the Einstein-Podolsky-Rosen paradox*, Physics (Long Island City, N.Y.) **1**, 195 (1964).
- [Bell, 1966] J. S. Bell, *On the problem of hidden variables in quantum mechanics*, Rev. Mod. Phys. **38**, 447 (1966).
- [Berry, 1984] M. V. Berry, *Quantal phase factors accompanying adiabatic changes*, Proc. R. Soc. Lond. A **392**, 45 (1984).
- [Bertlmann et al., 2004] R. A. Bertlmann, K. Durstberger, Y. Hasegawa, and B. C. Hiesmayr, *Berry phase in entangled systems: A proposed experiment with single neutrons*, Phys. Rev. A **69**, 032112 (2004).
- [Bertlmann et al., 2008] R. A. Bertlmann and P. Krammer, *Geometric entanglement witnesses and bound entanglement*, Phys. Rev. A **77**, 024303 (2008).

- [Bertlmann and Zeilinger, 2002] R. A. Bertlmann and A. Zeilinger, *Quantum [Un]speakables, from Bell to quantum information*, (Springer Verlag, Heidelberg, 2002).
- [Bitter and Dubbers, 1987] T. Bitter and D. Dubbers, *Manifestation of Berry's topological phase in neutron spin rotation*, Phys. Rev. Lett. **59**, 251 (1987).
- [Bloch and Siegert, 1940] F. Bloch and A. Siegert, *Magnetic resonance for nonrotating fields*, Phys. Rev. **57**, 522 (1940).
- [Bohm, 1951] D. Bohm, *Quantum theory*, Prentice-Hall, Englewood Cliffs N.J. (1951).
- [Bohr, 1935] N. Bohr, *Can quantum-mechanical description of physical reality be considered complete?* Phys. Rev. **48**, 696 (1935).
- [Bonse and Hart, 1965] U. Bonse and M. Hart, *An X-ray interferometer*, Appl. Phys. Lett. **6**, 155 (1965).
- [Bouwmeester et al., 1999] D. Bouwmeester, J.-W. Pan, M. Daniell, H. Weinfurter, and A. Zeilinger, *Observation of three-photon Greenberger-Horne-Zeilinger entanglement*, Phys. Rev. Lett. **82**, 1345 (1999).
- [Clauser, 1976] J. F. Clauser, *Experimental investigation of a polarization correlation anomaly*, Phys. Rev. Lett. **36**, 1223 (1976).
- [Clauser et al., 1969] J. F. Clauser, M. A. Horne, A. Shimony, and R. A. Holt, *Proposed experiment to test local hidden-variable theories*, Phys. Rev. Lett. **3**, 880 (1969).
- [Cronin et al., 2009] A. D. Cronin, J. Schmiedmayer, and D. E. Pritchard, *Optics and interferometry with atoms and molecules*, Rev. Mod. Phys. **81**, 1051 (2009).
- [Du et al., 2003] J. Du, P. Zou, M. Shi, L. C. Kwek, J.-W. Pan, C. H. Oh, A. Ekert, D. K. L. Oi, and M. Ericsson, *Observation of geometric phases for mixed states using NMR interferometry*, Phys. Rev. Lett. **91**, 100403 (2003).
- [Einstein et al., 1935] A. Einstein, B. Podolsky, and N. Rosen, *Can quantum-mechanical description of physical reality be considered complete?* Phys. Rev. **47**, 777 (1935).

- [Erhart et al., 2011] J. Erhart, S. Sponar, G. Sulyok, G. Badurek, M. Ozawa, and Y. Hasegawa, *Experimental demonstration of a universally valid uncertainty relation for error and disturbance in successive spin-measurements*, submitted to Nature (2011).
- [Ericsson et al., 2005] M. Ericsson, D. Achilles, J. T. Barreiro, D. Branning, N. A. Peters, and P. G. Kwiat, *Measurement of geometric phase for mixed states using single photon interferometry*, Phys. Rev. Lett. **94**, 050401 (2005).
- [Filipp et al., 2005] S. Filipp, Y. Hasegawa, R. Loidl, and H. Rauch, *Noncyclic geometric phase due to spatial evolution in a neutron interferometer*, Phys. Rev. A **72**, 021602 (2005).
- [Filipp and Sjöqvist, 2003a] S. Filipp and E. Sjöqvist, *Off-diagonal generalization of the mixed-state geometric phase*, Phys. Rev. A **68**, 042112 (2003).
- [Filipp and Sjöqvist, 2003b] S. Filipp and E. Sjöqvist, *Off-diagonal geometric phase for mixed states*, Phys. Rev. Lett. **90**, 050403 (2003).
- [Freedman and Clauser, 1972] S. J. Freedman and J. F. Clauser, *Experimental test of local hidden-variable theories*, Phys. Rev. Lett. **28**, 938 (1972).
- [Fry and Thompson, 1976] E. S. Fry and R. C. Thompson, *Experimental test of local hidden-variable theories*, Phys. Rev. Lett. **37**, 465 (1976).
- [Gähler and Golub, 1987] R. Gähler and R. Golub, *A neutron resonance spin echo spectrometer for quasi-elastic and inelastic scattering*, Phys. Lett. A **123**, 43 (1987).
- [Garg and Mermin, 1987] A. Garg and N. D. Mermin, *Detector inefficiencies in the Einstein-Podolsky-Rosen experiment*, Phys. Rev. D **35**, 3831 (1987).
- [Golub et al., 1994] R. Golub, R. Gähler, and T. Keller, *A plane wave approach to particle beam magnetic resonance*, Am. J. Phys. **62**, 779 (1994).
- [Grangier, 2001] P. Grangier, *Count them all*, Nature (London) **409**, 774 (2001).
- [Greenberger et al., 1989] D. M. Greenberger, M. A. Horne, and A. Zeilinger, *Bell's theorem, quantum theory, and concepts of the universe*, edited by M. Kafatos, Kluwer Academics, Dordrecht (1989).

- [Greenberger et al., 1990] D. M. Greenberger, A. Shimony, M. A. Horne, and A. Zeilinger, *Bell's theorem without inequalities*, Am. J. Phys. **58**, 1131 (1990).
- [Grigoriev et al., 2003] S. Grigoriev, Y. Chetverikov, W. Kraan, and M. Rekveldt, *Neutron multiwave interference experiments with many resonance coils*, Physica B **335**, 243 (2003).
- [Grigoriev et al., 2004] S. V. Grigoriev, W. H. Kraan, and M. T. Rekveldt, *Four-wave neutron-resonance spin echo*, Phys. Rev. A **69**, 043615 (2004).
- [Häffner et al., 2005] H. Häffner, W. Hänsel, C. F. Roos, J. Benhelm, D. C. al kar, M. Chwalla, T. Körber, U. D. Rapol, M. Riebe, P. O. Schmidt, C. Becher, O. Gühne, W. Dür, and R. Blatt, *Scalable multiparticle entanglement of trapped ions*, Nature (London) **438**, 643 (2005).
- [Hasegawa and Badurek, 1999] Y. Hasegawa and G. Badurek, *Noncommuting spinor rotation due to balanced geometrical and dynamical phases*, Phys. Rev. A **59**, 4614 (1999).
- [Hasegawa et al., 1996] Y. Hasegawa, M. Zawisky, H. Rauch, and A. I. Ioffe, *Geometric phase in coupled neutron interference loops*, Phys. Rev. A **53**, 2486 (1996).
- [Hasegawa et al., 2001] Y. Hasegawa, R. Loidl, M. Baron, G. Badurek, and H. Rauch, *Off-diagonal geometric phase in a neutron interferometer experiment*, Phys. Rev. Lett. **87**, 070401 (2001).
- [Hasegawa et al., 2002] Y. Hasegawa, R. Loidl, G. Badurek, M. Baron, N. Manini, F. Pistolesi, and H. Rauch, *Observation of off-diagonal geometric phases in polarized-neutron-interferometer experiments*, Phys. Rev. A **65**, 052111 (2002).
- [Hasegawa et al., 2003] Y. Hasegawa, R. Loidl, G. Badurek, M. Baron, and H. Rauch, *Violation of a Bell-like inequality in single-neutron interferometry*, Nature (London) **425**, 45 (2003).
- [Hasegawa et al., 2006] Y. Hasegawa, R. Loidl, G. Badurek, M. Baron, and H. Rauch, *Quantum contextuality in a single-neutron optical experiment*, Phys. Rev. Lett. **97**, 230401 (2006).

- [Hasegawa et al., 2007] Y. Hasegawa, R. Loidl, G. Badurek, S. Filipp, J. Klepp, and H. Rauch, *Evidence for entanglement and full tomographic analysis of Bell states in a single-neutron system*, Phys. Rev. A **76**, 052108 (2007).
- [Hasegawa et al., 2010] Y. Hasegawa, R. Loidl, G. Badurek, K. Durstberger-Rennhofer, S. Sponar, and H. Rauch, *Engineering of triply entangled states in a single-neutron system*, Phys. Rev. A **81**, 032121 (2010).
- [Hasegawa et al., 2011] Y. Hasegawa, C. Schmitzer, H. Bartosik, J. Klepp, S. Sponar, K. Durstberger-Rennhofer, and G. Badurek, *Neutron polarimetric test of contextual model of quantum mechanics a la Leggett*, submitted to Nature Physics (2011).
- [Heisenberg, 1927] W. Heisenberg, *Über den anschaulichen Inhalt der quantentheoretischen Kinematik und Mechanik*, Z. Phys. **43**, 172 (1927).
- [Home and Sengupta, 1984] D. Home and S. Sengupta, *Bell's inequality and non-contextual dispersion-free states*, Phys. Lett. A **102**, 4 (1984).
- [Jaynes and Cummings, 1963] E. T. Jaynes and F. W. Cummings, *Comparison of quantum and semiclassical radiation theories with application to the beam maser*, Proc. IEEE **51**, 89 (1963).
- [Keith et al., 1991] D. W. Keith, C. R. Ekstrom, Q. A. Turchette, and D. E. Pritchard, *An interferometer for atoms*, Phys. Rev. Lett. **66**, 2693 (1991).
- [Klepp et al., 2005] J. Klepp, S. Sponar, Y. Hasegawa, E. Jericha, and G. Badurek, *Non-cyclic Pancharatnam phase for mixed state $SU(2)$ evolution in neutron polarimetry*, Phys. Lett. A **342**, 48 (2005).
- [Klepp et al., 2008] J. Klepp, S. Sponar, S. Filipp, M. Lettner, G. Badurek, and Y. Hasegawa, *Observation of nonadditive mixed-state phases with polarized neutrons*, Phys. Rev. Lett. **101**, 150404 (2008).
- [Kraan et al., 2001] W. Kraan, S. Grigoriev, R. Kreuger, F. Mulder, and M. Rekveldt, *Line integral corrections in spin-echo small angle neutron scattering instrument*, Physica B **27**, 23 (2001).

- [Kwiat et al., 1995] P. G. Kwiat, K. Mattle, H. Weinfurter, A. Zeilinger, A. V. Sergienko, and Y. Shih, *New high-intensity source of polarization-entangled photon pairs*, Phys. Rev. Lett. **75**, 4337 (1995).
- [Larsson, 1998] J.-A. Larsson, *Bell's inequality and detector inefficiency*, Phys. Rev. A **57**, 3304 (1998).
- [Leibfried et al., 2005] D. Leibfried, E. Knill, S. Seidelin¹, J. Britton, R. B. Blakestad, J. Chiaverini, D. B. Hume, W. M. Itano, J. D. Jost, C. Langer, R. Ozeri, R. Reichle, and D. J. Wineland, *Creation of a six-atom 'Schrödinger cat' state*, Nature (London) **438**, 639 (2005).
- [Lu et al., 2007] C.-Y. Lu, X.-Q. Zhou, O. Gühne, W.-B. Gao, J. Zhang, Z.-S. Yuan, A. Goebel, T. Yang, and J.-W. Pan, *Experimental entanglement of six photons in graph states*, Nature Physics **3**, 91 (2007).
- [Manini and Pistoiesi, 2000] N. Manini and F. Pistoiesi, *Off-diagonal geometric phases*, Phys. Rev. Lett. **85**, 3067 (2000).
- [Marton et al., 1953] L. Marton, J. A. Simpson, and J. A. Suddeth, *Electron beam interferometer*, Phys. Rev. **90**, 490 (1953).
- [Matsukevich et al., 2008] D. N. Matsukevich, P. Maunz, D. L. Moehring, S. Olmschenk, and C. Monroe, *Bell inequality violation with two remote atomic qubits*, Phys. Rev. Lett. **100**, 150404 (2008).
- [Mermin, 1990] N. D. Mermin, *Extreme quantum entanglement in a superposition of macroscopically distinct states*, Phys. Rev. Lett. **65**, 1838 (1990).
- [Mermin, 1993] N. D. Mermin, *Hidden variables and the two theorems of John Bell*, Rev. Mod. Phys. **65**, 803 (1993).
- [Moehring et al., 2004] D. L. Moehring, M. J. Madsen, B. B. Blinov, and C. Monroe, *Experimental Bell inequality violation with an atom and a photon*, Phys. Rev. Lett. **93**, 090410 (2004).

- [Muskat et al., 1987] E. Muskat, D. Dubbers, and O. Schärpf, *Dressed neutrons*, Phys. Rev. Lett. **58**, 2047 (1987).
- [Nairz et al., 2004] O. Nairz, M. Arndt, and A. Zeilinger, *Quantum Interference Experiments with Large Molecules*, Am. J. Phys. **71**, 319 (2003).
- [Nielsen and Chuang, 2000] M. A. Nielsen and I. Chuang, *Quantum Computation and Quantum Information*, Cambridge University Press Cambridge (2000).
- [Ota et al., 2009] Y. Ota, Y. Goto, Y. Kondo, and M. Nakahara, *Geometric quantum gates in liquid-state NMR based on a cancellation of dynamical phases*, Phys. Rev. A **80**, 052311 (2009).
- [Pan et al., 2000] J. W. Pan, D. Bouwmeester, M. Daniell, H. Weinfurter, and A. Zeilinger, *Observation of three-photon Greenberger-Horne-Zeilinger entanglement*, Nature (London) **403**, 515 (2000).
- [Pipkin, 1978] F. Pipkin, *Atomic physics tests of the basics concepts in quantum mechanics*, in "Advances in Atomic and Molecular Physics", D.R. Bates and B. Bederson, ed., Academic (1978).
- [Rauch and Petrascheck, 1976a] H. Rauch and D. Petrascheck, *Grundlagen für ein Laue-Neutroneninterferometer - Teil 1* (1976).
- [Rauch and Petrascheck, 1976b] H. Rauch and D. Petrascheck, *Grundlagen für ein Laue-Neutroneninterferometer - Teil 2* (1976).
- [Rauch et al., 1974] H. Rauch, W. Treimer, and U. Bonse, *Test of a single crystal neutron interferometer*, Phys. Lett. A **47**, 369 (1974).
- [Rauch et al., 1975] H. Rauch, A. Zeilinger, G. Badurek, A. Wilfing, W. Bauspiess, and U. Bonse, *Verification of coherent spinor rotation of fermions*, Phys. Lett. **54A**, 425 (1975).
- [Rauch and Werner, 2000] H. Rauch and S. A. Werner, *Neutron Interferometry*, Clarendon Press Oxford (2000).

- [Rowe et al., 2001] M. A. Rowe, D. Kielpinski, V. Meyer, C. A. Sackett, W. Itano, C. Monroe, and D. J. Wineland, *Experimental violation of a Bell's inequality with efficient detection*, Nature (London) **409**, 791 (2001).
- [Sakai et al., 2006] H. Sakai, T. Saito, T. Ikeda, K. Itoh, T. Kawabata, H. Kuboki, Y. Maeda, N. Matsui, C. Rangacharyulu, M. Sasano, Y. Satou, K. Sekiguchi, K. Suda, A. Tamii, T. Uesaka, and K. Yako, *Spin correlations of strongly interacting massive fermion pairs as a test of Bell's inequality*, Phys. Rev. Lett. **97**, 150405 (2006).
- [Samuel and Bhandari, 1988] J. Samuel and R. Bhandari, *General setting for Berry's phase*, Phys. Rev. Lett. **60**, 2339 (1988).
- [Schmitzer, 2009] C. Schmitzer, *A neutron polarimetric test of Leggett's contextual model of quantum mechanics*, Vienna University of Technology, Master Thesis (2009).
- [Shore and Knight, 1993] B. W. Shore and P. L. Knight, *The Jaynes-Cummings model*, J. Mod. Optic **40**, 1195 (1993).
- [Simon et al., 2000] C. Simon, M. Żukowski, H. Weinfurter, and A. Zeilinger, *Feasible "Kochen-Specker" experiment with single particles*, Phys. Rev. Lett. **85**, 1783 (2000).
- [Sjöqvist et al., 2000] E. Sjöqvist, A. K. Pati, A. Ekert, J. S. Anandan, M. Ericsson, D. K. L. Oi, and V. Vedral, *Geometric phases for mixed states in interferometry*, Phys. Rev. Lett. **85**, 2845 (2000).
- [Sponar et al., 2008a] S. Sponar, J. Klepp, G. Badurek, and Y. Hasegawa, *Zero-field and Larmor spinor precessions in a neutron polarimeter experiment*, Phys. Lett. A **372**, 3153 (2008).
- [Sponar et al., 2008b] S. Sponar, J. Klepp, R. Loidl, S. Filipp, G. Badurek, Y. Hasegawa, and H. Rauch, *Coherent energy manipulation in single-neutron interferometry*, Phys. Rev. A **78**, 061604(R) (2008).
- [Sponar et al., 2010a] S. Sponar, J. Klepp, R. Loidl, S. Filipp, K. Durstberger-Rennhofer, R. A. Bertlmann, G. Badurek, H. Rauch, and Y. Hasegawa, *Geometric phase in entangled systems: A single-neutron interferometer experiment*, Phys. Rev. A **81**, 042113 (2010).

- [Sponar et al., 2010b] S. Sponar, J. Klepp, C. Zeiner, G. Badurek, and Y. Hasegawa, *Violation of Bell-like inequality for spin-energy entanglement in neutron polarimetry*, Phys. Lett. A **374**, 431 (2010).
- [Summhammer, 1993] J. Summhammer, *Coherent multiphoton exchange between a neutron and an oscillating magnetic field*, Phys. Rev. A **47**, 556 (1993).
- [Summhammer et al., 1983] J. Summhammer, G. Badurek, H. Rauch, U. Kischko, and A. Zeilinger, *Direct observation of fermion spin superposition by neutron interferometry*, Phys. Rev. A **27**, 2523 (1983).
- [Suter et al., 1987] D. Suter, G. Chingas, R. A. Harris, and A. Pines, *Berry's phase in magnetic resonance*, Mol. Phys. **61**, 1327 (1987).
- [Suter et al., 1988] D. Suter, K. T. Mueller, and A. Pines, *Study of the Aharonov-Anandan quantum phase by NMR interferometry*, Phys. Rev. Lett. **60**, 1218 (1988).
- [Tapster et al., 1994] P. R. Tapster, J. G. Rarity, and P. C. M. Owens, *Violation of Bell's inequality over 4 km of optical fiber*, Phys. Rev. Lett. **73**, 1923 (1994).
- [Tittel et al., 1998] W. Tittel, J. Brendel, H. Zbinden, and N. Gisin, *Violation of Bell inequalities by photons more than 10 km apart*, Phys. Rev. Lett. **81**, 3563 (1998).
- [Tomita and Chiao, 1986] A. Tomita and R. Y. Chiao, *Observation of Berry's topological phase by use of an optical fiber*, Phys. Rev. Lett. **57**, 937 (1986).
- [Tong et al., 2003] D. M. Tong, L. C. Kwek, and C. H. Oh, *Geometric phase for entangled states of two spin-1/2 particles in rotating magnetic field*, J. Phys. A **36**, 1149 (2003).
- [Uhlmann, 1991] A. Uhlmann, *Parallel transport along mixed states*, Lett. Math. Phys. **21**, 229 (1991).
- [von Neumann, 1932] J. von Neumann, *Mathematische Grundlagen der Quantenmechanik*, Berlin: Springer (1932).
- [Wagh et al., 2000] A. G. Wagh, G. Badurek, Buchelt Rakhecha, and R. J. Schricker, *Neutron polarimetric separation of geometric and dynamical phases*, Phys. Lett. A **268**, 209 (2000).

- [Wagh et al., 1998] A. G. Wagh, V. C. Rakhecha, P. Fischer, and A. Ioffe, *Neutron interferometric observation of noncyclic phase*, Phys. Rev. Lett. **81**, 1992 (1998).
- [Walther et al., 2005] P. Walther, K. Resch, T. Rudolph, E. Schenck, H. Weinfurter, V. Vedral, M. Aspelmeyer, and A. Zeilinger, *Experimental one-way quantum computing*, Nature (London) **434**, 169 (2005).
- [Weihs et al., 1998] G. Weihs, T. Jennewein, C. Simon, H. Weinfurter, and A. Zeilinger, *Violation of Bell's inequality under strict Einstein locality conditions*, Phys. Rev. Lett. **81**, 5039 (1998).
- [Weinfurter and Badurek, 1990] H. Weinfurter and G. Badurek, *Measurement of Berry's phase for noncyclic evolution*, Phys. Rev. Lett. **64**, 1318 (1990).
- [Wu and Shaknov, 1950] C. S. Wu and I. Shaknov, *The angular correlation of scattered annihilation radiation*, Phys. Rev. **77**, 136 (1950).
- [Zeilinger, 1986] A. Zeilinger, *Testing Bell's inequalities with periodic switching*, Physics Letters A **118**, 1 (1986).
- [Zhao et al., 2004] Z. Zhao, Y. Chen, A. Zhang, T. Yang, H. J. Briegel, and J. W. Pan, *Experimental demonstration of five-photon entanglement and open-destination teleportation*, Nature (London) **430**, 54 (2004).
- [Zhu and Wang, 2003] S.-L. Zhu and Z. D. Wang, *Universal quantum gates based on a pair of orthogonal cyclic states: Application to NMR systems*, Phys. Rev. A **67**, 022319 (2003).

Curriculum Vitae, Publications

Personal details

Name: Stephan Sponar
Address: Steinklammerg.19
Nationality: Austria
Email: stephan.sponar@gmx.net
Place/Date of birth: Vienna, 18.06.1977
Civilian Service: June 2005 - June 2006, Vienna

Education and University Studies

1987-1995 Realgymnasium, Rosasg., 1120 Vienna (Matura May 1995)
1995 - 2005 Physics studies at the Vienna University of Technology, Austria
Jan 2005 Master's Degree (Dipl.-Ing.) in Technical Physics, Vienna University of Technology. Thesis: *Non-cyclic geometric phases in neutron polarimetric experiments* (Supervisor: Prof. Gerald Badurek)
2006-2010 PhD-Studies at the Atominstitut, Vienna University of Technology

Work History

July 1994 Windsurfing Instructor Certification
1996-2004 IT-Services, Hewlett-Packard

Publications (refereed)

S. Sponar, J. Klepp, R. Loidl, S. Filipp, K. Durstberger, R. Bertlmann, G. Badurek, H. Rauch, and Y. Hasegawa: *Geometric phase in entangled systems: A single-neutron interferometer experiment*; Physical Review A, **81**, 042113 (2010).

S. Sponar, J. Klepp, K. Durstberger, R. Loidl, S. Filipp, M. Lettner, R. Bertlmann, G. Badurek, H. Rauch, and Y. Hasegawa: *New aspects of geometric phases in experiments with polarized neutrons*; Journal of Physics A: Mathematical and Theoretical, **43**, 354015 (2010).

S. Sponar, J. Klepp, C. Zeiner, G. Badurek, and Y. Hasegawa: *Violation of a Bell-like inequality for spin-energy entanglement in neutron polarimetry*; Physics Letters A, **374**, 431 (2010).

Y. Hasegawa, R. Loidl, G. Badurek, K. Durstberger, S. Sponar, and H. Rauch: *Engineering of triply entangled states in a single-neutron system*; Physical Review A, **81**, 032121 (2010).

H. Bartosik, J. Klepp, C. Schmitzer, S. Sponar, A. Cabello, H. Rauch, and Y. Hasegawa: *Experimental test of quantum contextuality in neutron interferometry*; Physical Review Letters, **103**, 040403 (2009).

S. Sponar, J. Klepp, R. Loidl, S. Filipp, G. Badurek, Y. Hasegawa, and H. Rauch: *Coherent energy manipulation in single-neutron interferometry*; Physical Review A, **78**, 061604(R) (2008).

S. Sponar, J. Klepp, G. Badurek, and Y. Hasegawa: *Zero-field and Larmor spinor precessions in a neutron polarimeter experiment*; Physics Letters A, **372**, 3153 (2008).

J. Klepp, S. Sponar, S. Filipp, M. Lettner, G. Badurek, and Y. Hasegawa: *Observation of Nonadditive Mixed-State Phases with Polarized Neutrons*; Physical Review Letters, **101**, 150404 (2008).

J. Klepp, S. Sponar, Y. Hasegawa, E. Jericha, and G. Badurek: *Noncyclic Pancharatnam phase for mixed state $SU(2)$ evolution in neutron polarimetry*; Physics Letters A, **342**, 48 (2005).

Publications (Proceedings)

Y. Hasegawa, K. Durstberger, S. Sponar, and H. Rauch: *Kochen-Specker theorem studied with neutron interferometer*; Nuclear Instruments and Methods in Physics Research A, in Press, (2010).

Y. Hasegawa, G. Badurek, S. Filipp, J. Klepp, R. Loidl, S. Sponar, and H. Rauch: *Entanglement between degrees of freedom of single-neutrons*; Nuclear Instruments and Methods in Physics Research A, **611**, 310 (2009).

J. Klepp, S. Sponar, S. Filipp, M. Lettner, G. Badurek, and Y. Hasegawa: *Nonadditivity of Quantum Phases for mixed States*; in: "Proceedings of the Junior Scientist Conference 2008", Vienna University of Technology, Wien, 2008, ISBN: 978-3-200-01612-5, 129.

S. Sponar, J. Klepp, Y. Hasegawa, E. Jericha, and G. Badurek: *Non-Cyclic Geometric Phases in Mixed State Neutron Polarimetry*; Acta Phys. Hung. B, **26**, 165 (2006).